NASA TECHNICAL NOTE

NASA TN D-4439

NASA TN D-4439

STATIC LONGITUDINAL AERODYNAMIC CHARACTERISTICS OF SEVERAL CONFIGURATIONS USED IN THE DEVELOPMENT OF THE LITTLE JOE II-APOLLO TEST VEHICLE AT MACH NUMBERS FROM 0.056 TO 4.65

by Robert H. Moore, Jr.

Manned Spacecraft Center
Houston, Texas

NATIONAL AERONAUTICS AND SPACE ADMINISTRATION • WASHINGTON, D. C. • MAY 1968

STATIC LONGITUDINAL AERODYNAMIC CHARACTERISTICS OF SEVERAL CONFIGURATIONS USED IN THE DEVELOPMENT OF THE LITTLE JOE II-APOLLO TEST VEHICLE AT MACH NUMBERS FROM 0.056 TO 4.65

By Robert H. Moore, Jr.

Manned Spacecraft Center
Houston, Texas

NATIONAL AERONAUTICS AND SPACE ADMINISTRATION

For sale by the Clearinghouse for Federal Scientific and Technical Information
Springfield, Virginia 22151 – CFSTI price $3.00

ABSTRACT

Investigations have been conducted to determine the static longitudinal aerodynamic characteristics of several configurations of the Little Joe-Apollo and Little Joe II-Apollo test vehicles at angles of attack from 0° to 90° at the low-subsonic Mach numbers and at angles of attack from -15° to $+15^\circ$ at the transonic and supersonic Mach numbers. The tests covered Mach numbers from 0.056 to 4.65. The Little Joe-Apollo configuration was unstable at the subsonic and low-supersonic speeds. Test results indicate that the production-model Little Joe II-Apollo configuration (with trailing-edge control surfaces on the booster fins) is stable throughout the Mach number range tested and that the trailing-edge control surfaces are effective for all Mach numbers tested. This configuration was used in the developmental tests of the Apollo launch escape system.

CONTENTS

TABLES

FIGURES

STATIC LONGITUDINAL AERODYNAMIC CHARACTERISTICS OF SEVERAL CONFIGURATIONS USED IN THE DEVELOPMENT OF THE LITTLE JOE II-APOLLO TEST VEHICLE AT MACH NUMBERS FROM 0.056 TO 4.65

By Robert H. Moore, Jr.
Manned Spacecraft Center

SUMMARY

Investigations of the static longitudinal aerodynamic characteristics of several configurations of the Little Joe-Apollo test vehicle and the Little Joe II-Apollo test vehicle were conducted in the NASA Langley Research Center 7- by 10-foot wind tunnel, the Langley 8-foot transonic pressure tunnel, and the Langley Unitary Plan wind tunnel, at Mach numbers from 0.056 to 4.65. The configurations studied included the Little Joe booster combined with a proposed Apollo launch-escape-vehicle configuration, a proposed Little Joe II booster (with two booster-fin sizes) combined with the Apollo launch-escape-vehicle configuration and three service-module configurations, and the production model of the Little Joe booster (with trailing-edge control surfaces on the booster fins) combined with the Apollo launch-escape-vehicle configuration and a service-module configuration. The results of these investigations indicated that the Little Joe-Apollo test-vehicle configuration was unstable, for a typical center-of-gravity location, at subsonic and low-supersonic speeds at angle-of-attack values near 0°, primarily because of the ineffectiveness of booster-fin operation in highly separated flow. As a result of these tests, all further effort was directed toward the development of the Little Joe II booster as the test vehicle.

The results of the investigations of the Little Joe II-Apollo test-vehicle configuration with two booster-fin sizes and three service modules of different lengths indicated that increasing the service-module length only slightly affects the aerodynamic characteristics of the configuration. Also, there is a large rearward shift (approximately 2.5 diameters) in the center-of-pressure location with the addition of the small stabilizing fins and a further shift rearward (approximately 0.5 diameter) with an increase in fin size. The data for the production model of the Little Joe II-Apollo test-vehicle configuration (with trailing-edge control surfaces on the booster fins) indicate that the configuration is stable throughout the Mach number range tested for the typical center-of-gravity location chosen. The data also indicate that the trailing-edge control surfaces are effective for all Mach numbers tested and that the magnitude of the trailing-edge control-surface hinge moment is within an acceptable range.

INTRODUCTION

The Apollo Program has as a goal the landing of man on the moon within the decade. As a part of the overall program, it is necessary to demonstrate the capabilities of the flight systems under critical flight conditions. One of these systems is the Apollo launch escape vehicle (LEV). The LEV consists of a cylindrical rocket package which is attached to a tower mounted on top of the spacecraft. The LEV system is capable of lifting the command module (CM) away from the launch vehicle in the event of a malfunction during the final countdown or during the initial launch phases of the mission.

For developmental tests of the launch escape system, an unsophisticated and economical launch vehicle was required for simulation of the most critical phases of the atmospheric portion of the launch profile. Initial studies indicated that the Little Joe booster used in the Project Mercury spacecraft-development program could be used to simulate some of the launch conditions; however, wind-tunnel tests of the resulting launch configuration, with a CM diameter which was approximately twice the diameter of the booster, indicated that the configuration was unstable (refs. 1 and 2). Effort was, therefore, directed toward developing a new booster to perform the desired developmental Apollo missions. This configuration, designated the Little Joe II booster, was similar in configuration to the Little Joe booster but was larger in diameter. Preliminary investigations were conducted in several facilities of the NASA Langley Research Center to define the basic aerodynamics of the configuration and to confirm design estimates. Several booster lengths and two fin sizes were studied (refs. 3, 4, and 5).

In June 1962, a 30-day study contract was awarded for the development of the fin size and the control surfaces for the Little Joe II booster. As a direct result of these studies, additional wind-tunnel tests were conducted to ascertain the effectiveness of the fins and of the trailing-edge control surfaces and to determine the effects of several small configuration modifications made to the booster vehicle and to the Apollo LEV. The results of these studies are reported in references 6 and 7.

The purpose of this paper is to compile into one document all of the wind-tunnel data obtained during the development of the Little Joe II booster. The investigations at the NASA Langley Research Center were conducted in the Mach number range from 0.056 to 4.65.

SYMBOLS

The six-component aerodynamic force-and-moment data are referenced to the body and stability systems of axes with the origin on the centerline at the model base, as in figure 1. In addition, some of the data are presented about a more realistic center-of-gravity location to assess the effectiveness of the control surfaces.

$A_{b,1}$ area of sting hole in booster airframe, ft^2

$A_{b,2}$ area of rim at base of booster airframe, ft^2

C_A axial-force coefficient corrected for base pressure, $\frac{\text{axial force uncorrected}}{q_\infty S} - C_{A,b}$

$C_{A,b}$ base axial-force coefficient, $-\left[(C_{p,b,1})\left(\frac{A_{b,1}}{S}\right) + (C_{p,b,2})\left(\frac{A_{b,2}}{S}\right)\right]$

C_D drag coefficient, $C_A \cos \alpha + C_N \sin \alpha$

C_h hinge-moment coefficient, $\frac{\text{hinge moment}}{q_\infty S_f \bar{C}_f}$

C_{h_α} hinge-moment curve slope/deg, $\frac{\partial C_h}{\partial \alpha}$

C_{h_δ} hinge-moment curve slope/deg, $\frac{\partial C_h}{\partial \delta}$

C_L lift coefficient, $C_N \cos \alpha - C_A \sin \alpha$

C_m pitching-moment coefficient, $\frac{\text{pitching moment}}{q_\infty SD}$

C_{m_α} pitching-moment curve slope/deg, $\frac{\partial C_m}{\partial \alpha}$

C_{m_δ} pitching-moment curve slope/deg, $\frac{\partial C_m}{\partial \delta}$

C_N normal-force coefficient, $\frac{\text{normal force}}{q_\infty S}$

C_{N_α} normal-force curve slope/deg, $\frac{\partial C_N}{\partial \alpha}$

C_{N_δ}	normal-force curve slope/deg, $\frac{\partial C_N}{\partial \delta}$
$C_{p,b,1}$	pressure coefficient in balance chamber, $\frac{p_{b,1} - p}{q_\infty}$
$C_{p,b,2}$	pressure coefficient at rim of model base, $\frac{p_{b,2} - p}{q_\infty}$
C_l	rolling-moment coefficient, $\frac{\text{rolling moment}}{q_\infty SD}$
$\overline{C}_f$	control-surface mean aerodynamic chord, in.
D	reference diameter (maximum booster diameter), ft
M	free-stream Mach number
p	static pressure of undisturbed stream, lb/ft^2
$p_{b,1}$	static pressure in balance chamber, lb/ft^2
$p_{b,2}$	static pressure at rim of model base, lb/ft^2
q_∞	free-stream dynamic pressure, lb/ft^2
S	reference area, $\frac{\pi D^2}{4}$, ft^2
S_f	area of trailing-edge control surface, ft^2
X, Y, Z	coordinates in the body and stability systems of axes
$\frac{X_{c.p.}}{D}$	longitudinal location of center of pressure based on maximum Apollo CM diameter measured from base of booster
α	angle of attack of model centerline, deg
δ_f	deflection of control surface, deg

Subscripts:

b	base
c.p.	center of pressure
f	control surface
∞	free stream

APPARATUS

Tunnels

The investigations were conducted in the Langley 300-mph 7- by 10-foot wind tunnel, in the Langley 8-foot transonic pressure tunnel, and in the Langley Unitary Plan wind tunnel. The Langley 300-mph 7- by 10-foot wind tunnel is a low-speed, continuous return-flow-type tunnel. The size of the test section is approximately 7 by 10 feet, and the sting support system can rotate $\pm 90°$. Measurements in this tunnel can be made over the Mach number range from approximately 0.05 to approximately 0.30.

The test section of the Langley 8-foot transonic pressure tunnel is square in cross section, with the upper and lower walls axially slotted to permit continuous testing throughout the transonic velocity range. The total pressure of the tunnel air can be varied from a minimum value of approximately 0.25 atmosphere at all test Mach numbers to maximum values of approximately 1.5 atmospheres at transonic Mach numbers and approximately 2.0 atmospheres at Mach numbers ≤ 0.40. The tunnel air is dried to avoid condensation effects.

The Langley Unitary Plan wind tunnel has low Mach number and high Mach number test sections, which are 4 feet square by approximately 7 feet in length. The tunnel is a variable-pressure, continuous return-flow type with asymmetric sliding-block-type nozzles which permit continuous variation of Mach numbers from approximately 1.50 to 2.90 and from 2.30 to 4.70 in the low Mach number and high Mach number test sections, respectively.

Models

Dimensional details of the configurations tested are given in figure 2, and figures 3(a) to 3(c) are photographs of the models. Configuration I was a 0.028-scale model of the Little Joe booster combined with an early proposed version of the Apollo LEV. The booster diameter for the resulting vehicle was one-half the diameter of the Apollo CM. Configuration II was a 0.0292-scale model of a proposed Little Joe II booster combined with the proposed version of the Apollo LEV and a service module (SM). (Three SM lengths were tested with the configuration.) Also, two booster-fin sizes were tested, the areas of which were 75 and 150 ft^2/fin, respectively (full-scale values). Configuration III was a 0.030-scale model of the production-model

Little Joe II booster combined with the Apollo LEV and SM. The four stabilizing fins with trailing-edge control surfaces were spaced 90° apart at the base of the booster airframe. These trailing-edge control surfaces could be deflected to obtain either pitch control or roll control. One fin was instrumented with a small hinge-moment beam to obtain control-surface hinge-moment data. Geometric characteristics of the configurations are summarized in table I.

Instrumentation

A six-component strain-gage balance housed in the model booster airframe was used for determining the overall forces and moments in the models. A static-pressure orifice located within the chamber surrounding the six-component strain-gage balance was included in all the configurations. Also, configurations II and III had eight static-pressure orifices located around the rim of the model base which were manifolded to a single output. Static pressures from these orifices were recorded and used in the base-pressure corrections. A strain-gage beam mounted in the trailing-edge control surface of fin no. 2 was used for determining the hinge moment of the trailing-edge control surfaces in configuration III.

TESTS, CORRECTIONS, AND ACCURACY

Tests

The investigations were conducted at Mach numbers from 0.056 to 4.65 over a Reynolds number range from approximately 0.154×10^6 to 2.5×10^6/foot (based on Apollo CM maximum diameter). The tests in the Langley 7- by 10-foot wind tunnel were conducted over an angle-of-attack range from approximately -2° to 90°, and the tests in the Langley 8-foot transonic pressure tunnel and in the Langley Unitary Plan wind tunnel were conducted over an angle-of-attack range of approximately ±15°.

Corrections

The axial-force coefficient C_A includes the correction for the base axial-force coefficient $C_{A,b}$. The aerodynamic force-and-moment data presented are considered to be free of tunnel-boundary interference. Corrections have been made to the model angles of attack to account for angularity of the airflow in the test sections. In addition, corrections have also been applied for balance-sting deflection caused by aerodynamic loads.

Accuracy

The estimated accuracy of the data, based primarily on the static calibration of the balance and on the repeatability of the data, is tabulated in tables II to IV.

DISCUSSION

Basic aerodynamic characteristics of all configurations tested are shown in figures 4 to 31, and summary longitudinal aerodynamic characteristics for all configurations tested are plotted against Mach number in figures 32 to 38.

Configuration I

The longitudinal aerodynamic characteristics of configuration I, with and without the stabilizing fins, are presented in figures 4 and 5 and are summarized in figure 32. The data in figures 4 and 5 indicate that the addition of stabilizing fins to the booster has only slight apparent effect on the pitching-moment characteristics of the configuration when the moment reference center is located at the base of the booster, except at subsonic Mach numbers (fig. 32(a)). Also, the addition of the stabilizing fins increases the value of C_A and adversely affects the normal-force coefficient by reducing the variation of C_N with α, at the lowest test angles of attack at subsonic speeds.

As indicated by the data in figure 32, for angle-of-attack values near 0°, the center-of-pressure location for the fins-on booster configuration varies considerably with Mach number. The data also indicate that the configuration would be unstable at supersonic speeds for a typical center-of-gravity location. There is a large forward shift in the center-of-pressure location which is associated with the reduced fins-on normal-force coefficient at subsonic and transonic velocities. At angles of attack of approximately 15°, however, the center-of-pressure location for either the fins-on or fins-off configuration remains essentially constant with changes in Mach number and is located at approximately 1.41D to 2.65D or at 4.0D to 4.77D, respectively, forward of the booster base.

In general, the data summarized in figure 32 indicate the following:

1. The general magnitude of the drag estimate was good, except that the sharp drag rise at $M = 0.95$ was not predicted.

2. The variation of normal-force curve slope was predicted fairly well.

3. The center-of-pressure estimate was grossly in error.

The primary reason for the error in the center-of-pressure estimate was the ineffectiveness of the stabilizing fins in the region of highly separated flow rearward of the bulbous forebody, particularly at subsonic and transonic Mach numbers. At these Mach numbers, the downwash from the forebody acting on the fins at low angles of attack resulted in a more forward center-of-pressure location for the fins-on configuration than for the fins-off configuration. The data presented in references 8 and 9 were used to obtain the predicted data presented in figure 32.

Configuration II

The longitudinal aerodynamic characteristics of configuration II are presented in figures 6 to 20 and are summarized in figures 33 and 34. Configuration II was tested with three SM lengths and two stabilizing-fin sizes. The SM lengths were as follows:

1. Short SM (160-inch length, full-scale value)

2. Medium SM (209-inch length, full-scale value)

3. Long SM (242-inch length, full-scale value)

The areas of the two booster stabilizing fins were 75 and 150 ft^2/fin, respectively (full-scale value).

Effect of fin size. - To determine the effect of fin size on the aerodynamics of the configuration, the fin-size investigation for configuration II was conducted with the medium SM length. Basic data for the large-fin, small-fin, and no-stabilizing-fin booster configurations are presented in figures 6 to 14.

The low-subsonic data presented in figures 6, 9, and 12 were obtained through an angle-of-attack range from approximately -2° to 90°. These data were obtained primarily to provide high-angle-of-attack information for the launch conditions. The transonic and supersonic data were obtained through an angle-of-attack range from approximately -5° to 15°. The variation of pitching-moment coefficient with angle of attack for the subsonic data is generally linear up to $\alpha \approx 65^\circ$ and $\alpha \approx 55^\circ$ for $M = 0.056$ and $M = 0.10$ and is linear up to $\alpha \approx 40^\circ$ for $M = 0.20$. The data at $M = 0.30$ are generally linear throughout the angle-of-attack range tested, as are the data for the transonic and supersonic Mach numbers tested.

Adding the fins to the configuration had only slight effect on the variation of pitching-moment coefficient with α, which indicates that the incremental normal force caused by adding the fins was localized at a point very close to the base of the booster. The fin effectiveness, as determined from the slope of the normal-force coefficient data, indicates that the increase in normal-force curve slope is generally proportional to the increase in fin size for the Mach number range tested.

There is a large rearward shift (approximately 2.5D) in the center-of-pressure location with the addition of the small fins to the booster configuration. An additional rearward shift (approximately 0.5D) in the center-of-pressure location occurs with the change from the small fins to the large fins (fig. 33). The addition of the stabilizing fins to the booster also causes a substantial increase in the axial-force coefficient C_A.

Effect of SM length. - The basic data (figs. 6, 7, and 8 and figs. 14 to 20) and the summary data (fig. 34) indicate that there is very little effect on the normal-force coefficient or on the axial-force coefficient with the change in SM length. Increasing the length of the SM moved the center-of-pressure location forward by a small amount ($\leq 0.13D$).

Configuration III

The longitudinal aerodynamic characteristics of configuration III are presented in figures 21 to 31 and are summarized in figures 35 to 38. Configuration III was tested with a booster stabilizing-fin size of 50 ft^2/fin (full-scale value), and there was a trailing-edge control surface on each fin. The area of the trailing-edge control surface was approximately 30 percent of the total fin area. The SM length used for configuration III was 160 inches (full-scale value). During the development of the production-model Little Joe II booster, changes were made to the Apollo LEV configuration. The changes are as follows:

1. The launch-escape-system rocket motor has a 15° nose cant as compared to a 33° nose cant on configuration II.

2. The launch-escape-system rocket is considerably longer and has a slightly larger diameter.

3. The tower structure is mounted higher on the CM and has a different lateral-bracing configuration.

Also, for some of the tests, a stabilizing disk or flow separator was added to the Apollo LEV configuration. This disk was mounted on the rocket motor slightly forward of the conical shroud around the rocket-motor nozzles (fig. 2(e)).

The data presented in figures 21 and 22 are for configuration III with and without the stabilizing disk. The data indicate that the stabilizing disk has little or no effect on the aerodynamic characteristics of the configuration, except for an increase in the axial-force coefficient C_A. The flow separator was introduced as a modification to the Apollo LEV and resulted in improved static-stability characteristics at some Mach numbers. Other design considerations, however, resulted in the removal of the disk from the configuration. Therefore, comparisons of configuration III with and without the disk were made for limited tests only. The pitching-moment coefficient and the normal-force coefficient for the configuration without the disk show a generally linear variation with angle of attack throughout the Mach number range tested. Since the stabilizing fins are located near the base of the booster and since the primary moment reference center is in the plane of the base of the booster, the data in figures 21 to 26 give little or no indication of the effectiveness of the trailing-edge control surfaces. Therefore, the pitching-moment coefficient data presented in figure 27 and summarized in figure 37 have been computed about a typical center-of-gravity location of $X/D = 2.272$; $Z/D = 0$. These data indicate that for this particular center-of-gravity location the configuration is stable throughout the Mach number range tested and that the trailing-edge control surfaces provide adequate control effectiveness, although a decrease in control effectiveness occurs with an increase in Mach number at Mach numbers >0.70.

Hinge-moment characteristics. - The variation of hinge-moment coefficient C_h with angle of attack was approximately linear at control deflections of 0° and -10° at Mach numbers ≤ 0.80. Increasing control deflection or increasing Mach number resulted in a greater nonlinearity in the variation of hinge-moment coefficient with

angle of attack. The hinge-moment curve slope C_{h_α} was negative over the angle-of-attack range, and the magnitude of this parameter was usually less at low angles of attack than at higher angles of attack. The parameter C_{h_α} in figure 36 was measured over an angle-of-attack range of approximately ±2°.

The variation of hinge-moment coefficient with trailing-edge control-surface deflection was approximately linear for the range of control-surface deflections tested, with a maximum deflection of approximately -20° at $\alpha \approx 0°$ and with deflections generally $< -20°$ as the angle of attack increased or decreased from $\alpha = 0°$. The parameter C_{h_δ} in figure 37 was the average value for trailing-edge control-surface deflections from 0° to approximately -10°. The parameter increased in magnitude at the higher subsonic Mach numbers and decreased in magnitude at the supersonic Mach numbers.

Rolling-moment characteristics. - The variation of rolling-moment coefficient with differential deflection of the trailing-edge control surfaces was approximately linear over most of the angle-of-attack range at all Mach numbers, and the magnitude of the rolling-moment coefficient developed by differential deflection of the trailing-edge control surfaces appeared to be adequate. The rolling-moment effectiveness was approximately constant at Mach numbers from 0.30 to 1.20 and increased slightly at the intermediate Mach numbers.

CONCLUDING REMARKS

The results of wind-tunnel tests over a Mach number range from 0.056 to 4.65 of several configurations of the Little Joe and the Little Joe II boosters combined with the Apollo launch-escape-vehicle configuration yield the following conclusions:

Little Joe-Apollo (Configuration I)

1. The configuration is unstable, for a typical center-of-gravity location, at subsonic and low-supersonic speeds for angle-of-attack values near 0°.

2. The booster stabilizing fins contribute to a reduced normal-force curve slope at subsonic speeds because of the total ineffectiveness of booster-fin operation in the region of highly separated flow rearward of the bulbous forebody.

Little Joe II-Apollo (Configuration II)

1. Results of the initial studies of the Little Joe II-Apollo configuration indicate that the vehicle is stable and can perform the developmental missions planned.

2. For the normal operating ranges, the variation of the pitching-moment coefficient is generally linear throughout the angle-of-attack and Mach number ranges tested.

3. The booster stabilizing fins contribute to a large rearward shift (approximately 2.5 diameters) in the center-of-pressure location, and a further rearward shift (approximately 0.5 diameter) results from increasing the fin size.

4. Varying the service-module length from 1.068 diameters to 1.620 diameters has only slight effect on the aerodynamic characteristics of the configuration.

Little Joe II-Apollo (Configuration III)

1. The fins-on configuration is stable throughout the Mach number range tested.

2. The trailing-edge control surfaces are effective in producing adequate longitudinal control and/or roll control at all Mach numbers tested.

3. The variation of trailing-edge control-surface hinge moment with control deflection and the magnitude of the control-surface hinge moment are within an acceptable range.

Manned Spacecraft Center
National Aeronautics and Space Administration
Houston, Texas, December 13, 1967
914-50-10-09-72

REFERENCES

1. Pearson, Albin O.: Static Longitudinal Aerodynamic Characteristics of a 0.028-Scale Model of a Proposed Little Joe-Apollo Space Vehicle at Mach Numbers From 0.50 to 1.20 (U). NASA TM X-692, 1962.

2. Fournier, Roger H.: Static Longitudinal Aerodynamic Characteristics of a 0.028-Scale Model of a Proposed Little Joe-Apollo Space Vehicle at Mach Numbers From 1.50 to 2.16 (U). NASA TM X-730, 1962.

3. Luoma, Arvo A.: Wind-Tunnel Investigation of the Static Longitudinal Aerodynamic Characteristics of Several Configurations of a Proposed Little Joe II-Apollo Space Vehicle at Mach Numbers From 0.30 to 1.20 (U). NASA TM X-827, 1963.

4. Fournier, Roger H.; and Silvers, H. Norman: Static Longitudinal Aerodynamic Characteristics of a 0.028-Scale Model of a Proposed Little Joe II-Apollo Space Vehicle at Mach Numbers From 1.50 to 2.16 (U). NASA TM X-754, 1963.

5. Henderson, William P.: Subsonic Static Longitudinal Aerodynamic Characteristics at Angles of Attack From -2° to 95° of a Proposed Little Joe-Apollo Space Vehicle (U). NASA TM X-751, 1963.

6. Luoma, Arvo A.: Longitudinal Stability and Control, Roll Control, and Hinge Moments of a Little Joe II-Apollo Model at Mach Numbers up to 1.20 (U). NASA TM X-1002, 1964.

7. Fournier, Roger H.; and Vahl, Walter A.: Static Stability and Control Characteristics of a 0.030-Scale Model of a Little Joe II-Apollo Space Vehicle at Mach Numbers From 1.57 to 4.65 (U). NASA TM X-843, 1963.

8. Rainey, Robert W.: Summary of Aerodynamic Characteristics of Low-Lift-Drag-Ratio Reentry Vehicles From Subsonic to Hypersonic Speeds (U). NASA TM X-588, 1961.

9. Rittenhouse, Lewis E.; and Kaupp, H., Jr.: Influence of Several Shape Parameters on the Aerodynamics of Ballistic Re-entry Configurations (U). AEDC TR 60-13, 1960.

TABLE I. - GEOMETRIC CHARACTERISTICS OF THE LITTLE JOE AND LITTLE JOE II BOOSTERS COMBINED WITH THE APOLLO LAUNCH-ESCAPE-VEHICLE CONFIGURATION

(a) Configuration I

Booster body:	
Cross-sectional area (reference area S), ft^2	0.0277
Diameter (reference diameter D), in.	2.250
Apollo LEV:	
Cross-sectional area, ft^2	0.1104
Diameter, in.	4.50
Stabilizing fins (exposed, single-fin values given):	
Airfoil section (parallel to root chord), wedge total angle, deg	11
Area, ft^2	0.0264
Span, in.	2.480
Root chord, in.	1.640
Tip chord, in.	1.170
Sweepback of leading edge, deg	45

TABLE I. - GEOMETRIC CHARACTERISTICS OF THE LITTLE JOE AND LITTLE JOE II BOOSTERS COMBINED WITH THE APOLLO LAUNCH-ESCAPE-VEHICLE CONFIGURATION - Continued

(b) Configuration II

Booster body:	
Cross-sectional area (reference area S), ft^2	0.1104
Diameter (reference diameter D), in.	4.50
Area of sting hole, $A_{b,1}$, ft^2	0.0491
Area of rim, $A_{b,2}$, ft^2	0.0614
Stabilizing fins (exposed, single-fin values given):	
Large fins:	
Airfoil section (parallel to root chord), wedge total angle, deg	11
Area, ft^2	0.127
Span, in.	5.140
Root chord, in.	3.500
Tip chord, in.	2.920
Sweepback of leading edge, deg	45
Small fins:	
Airfoil section (parallel to root chord), wedge total angle, deg	11
Area, ft^2	0.064
Span, in.	3.570
Root chord, in.	2.510
Tip chord, in.	2.120
Sweepback of leading edge, deg	45

TABLE I. - GEOMETRIC CHARACTERISTICS OF THE LITTLE JOE AND LITTLE JOE II BOOSTERS COMBINED WITH THE APOLLO LAUNCH-ESCAPE-VEHICLE CONFIGURATION - Concluded

(c) Configuration III

Booster Body:	
Cross-sectional area (reference area S), ft^2	0.1164
Diameter (reference diameter D), in.	4.620
Area of sting hole, $A_{b,1}$, ft^2	0.0576
Area of rim, $A_{b,2}$, ft^2	0.0588
Stabilizing fins (exposed, single-fin values given):	
Airfoil section (parallel to root chord), wedge total angle, deg	10
Area (includes area of control surface), ft^2	0.0451
Span, in.	2.790
Root chord, in.	2.633
Tip chord, in.	1.320
Aspect ratio	1.20
Sweepback of leading edge, deg	45
Trailing-edge control surface (flap):	
Area, S_f, ft^2	0.0135
Percent of fin area	30
Mean aerodynamic chord, $\overline{C}_f$, in.	0.956

TABLE II. - ESTIMATED ACCURACY OF DATA FOR CONFIGURATION I

Datum	Estimated accuracy in the —	
	8-foot transonic pressure tunnel	Unitary Plan wind tunnel
α, deg . . .	±0.2	±0.10
M	±.005	±.015
C_N	±.017	±.017
C_A	±.006	±.006
C_m	±.020	±.010
C_L	±.006	±.006
C_D	±.020	±.021

TABLE III. - ESTIMATED ACCURACY OF DATA FOR CONFIGURATION II

(a) In the 7- by 10-foot wind tunnel

Datum	Estimated accuracy at —			
	M = 0.056	M = 0.10	M = 0.20	M = 0.30
α, deg . . .	±0.05	±0.05	±0.05	±0.05
C_N	±.613	±.189	±.050	±.023
C_A	±.091	±.028	±.007	±.003
C_m	±.294	±.093	±.024	±.011
C_L	±.090	±.028	±.007	±.003
C_D	±.613	±.189	±.050	±.021

(b) In the 8-foot transonic pressure tunnel[a] and in the Unitary Plan wind tunnel

Datum	Estimated accuracy in the —	
	8-foot transonic pressure tunnel	Unitary Plan wind tunnel
α, deg . . .	±0.1	±0.1
M	±.005	±.015
C_N	±.025	±.024
C_A	±.008	±.008
C_m	±.015	±.014
C_L	±.007	±.007
C_D	±.022	±.018

[a]Accuracies of coefficient data are for Mach numbers ≥0.70. At M = 0.30 and M = 0.50, where the dynamic pressure was substantially lower than at the higher Mach numbers, the accuracy of the aerodynamic coefficients is affected adversely.

TABLE IV. - ESTIMATED ACCURACY OF DATA FOR CONFIGURATION III

(a) In the 7- by 10-foot wind tunnel

Datum	Estimated accuracy at —		
	M = 0.056	M = 0.10	M = 0.30
α, deg . . .	±0.05	±0.05	±0.05
C_N	±.613	±.189	±.023
C_A	±.091	±.028	±.003
C_m	±.294	±.093	±.011
C_L	±.090	±.028	±.003
C_D	±.613	±.189	±.021

TABLE IV. - ESTIMATED ACCURACY OF DATA

FOR CONFIGURATION III - Concluded

(b) In the 8-foot transonic pressure tunnel[a] and in the Unitary Plan wind tunnel

Datum	Estimated accuracy in the —	
	8-foot transonic pressure tunnel	Unitary Plan wind tunnel
α, deg	±0.1	±0.1
M	±.005	---
M = 1.57 to M = 2.80	---	±.015
M = 3.86 and M = 4.65	---	±.050
C_N	±.020	±.050
C_A	±.007	±.005
C_m	±.010	±.050
C_L	±.007	±.006
C_D	±.019	±.050
C_l	±.002	---
$C_h(\delta_f = 0° \text{ and } \delta_f = 10°)$	±.007	---
$C_h(\delta_f = 20°)$	±.011	---
$C_h(\delta_f = 30°)$	±.018	---

[a]Accuracies of coefficient data are for Mach numbers ≥ 0.70. At M = 0.30 and M = 0.50, where the dynamic pressure was substantially lower than at the higher Mach numbers, the accuracy of the aerodynamic coefficients is affected adversely.

NASA-S-67-7332

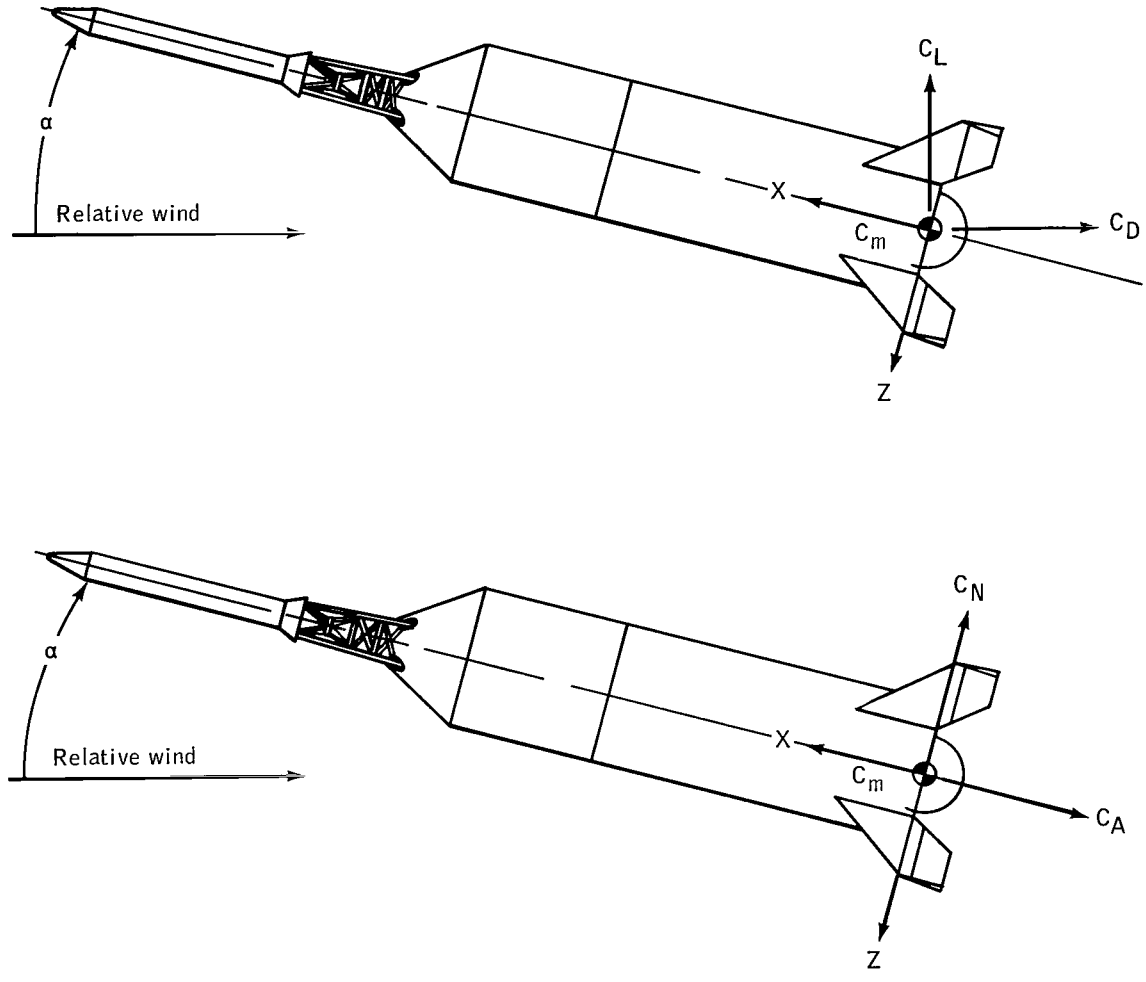

Figure 1.- Sketch showing axis systems used. Arrows indicate positive-to-positive direction of forces, moments, and angles of attack.

NASA-S-67-7325

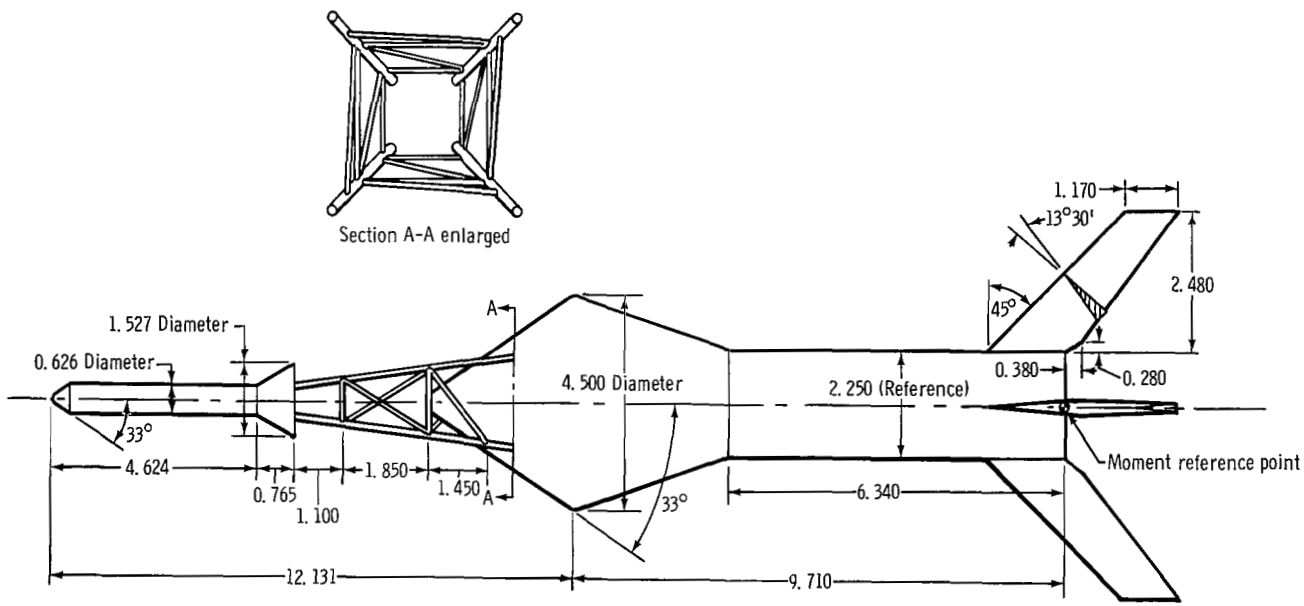

(a) Configuration I.

Figure 2. - Sketch of the configurations tested showing general arrangement and dimensions. All linear dimensions are in inches.

NASA-S-67-7334

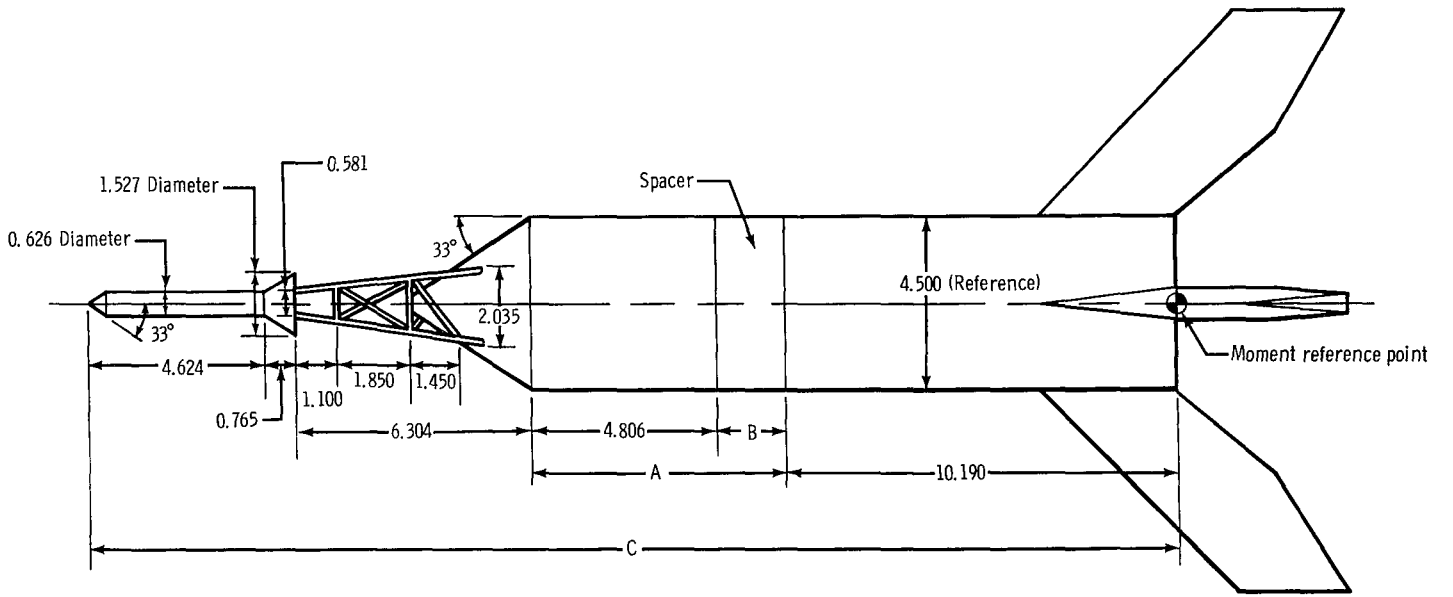

Configuration II dimensions

Service module		Spacer	Overall configuration
Description	Length (dimension A), in.	Length (dimension B), in.	Length (dimension C), in.
Short	4.806	0.000	26.527
Medium	6.558	1.752	28.279
Long	7.288	2.482	29.009

(b) Complete model of configuration II.

Figure 2. - Continued.

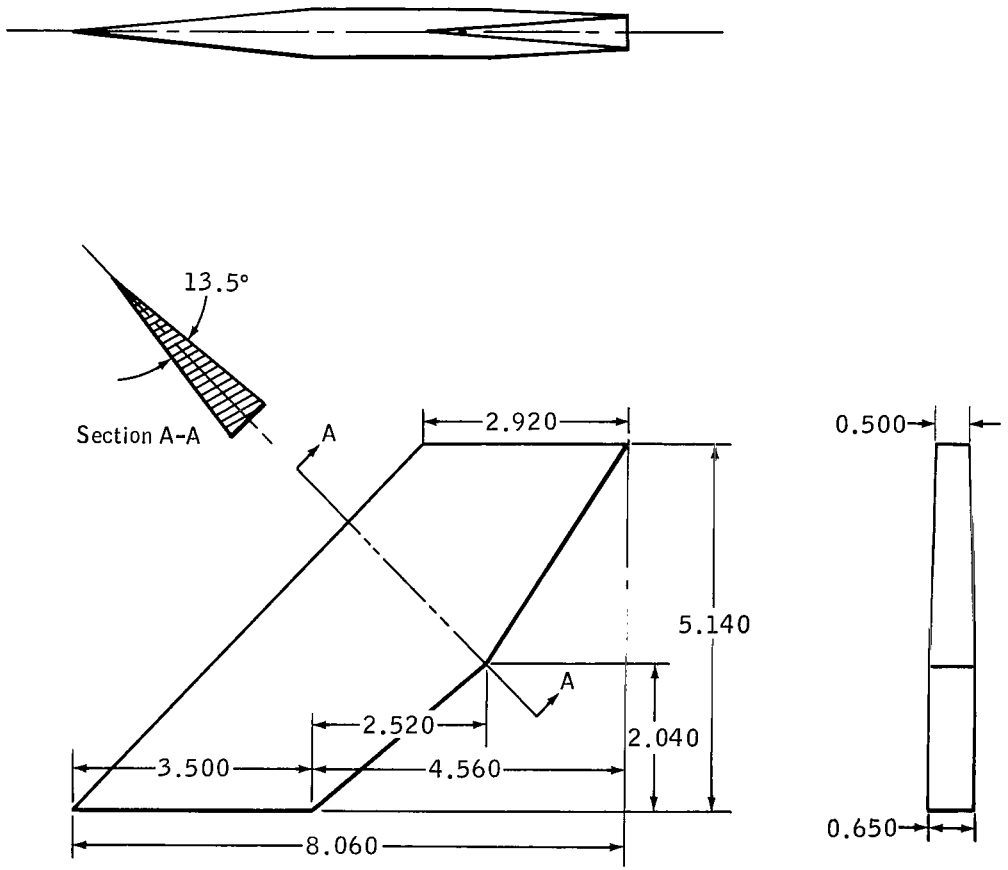

(c) Large-fin detail for configuration II.

Figure 2. - Continued.

NASA- S-67-7326

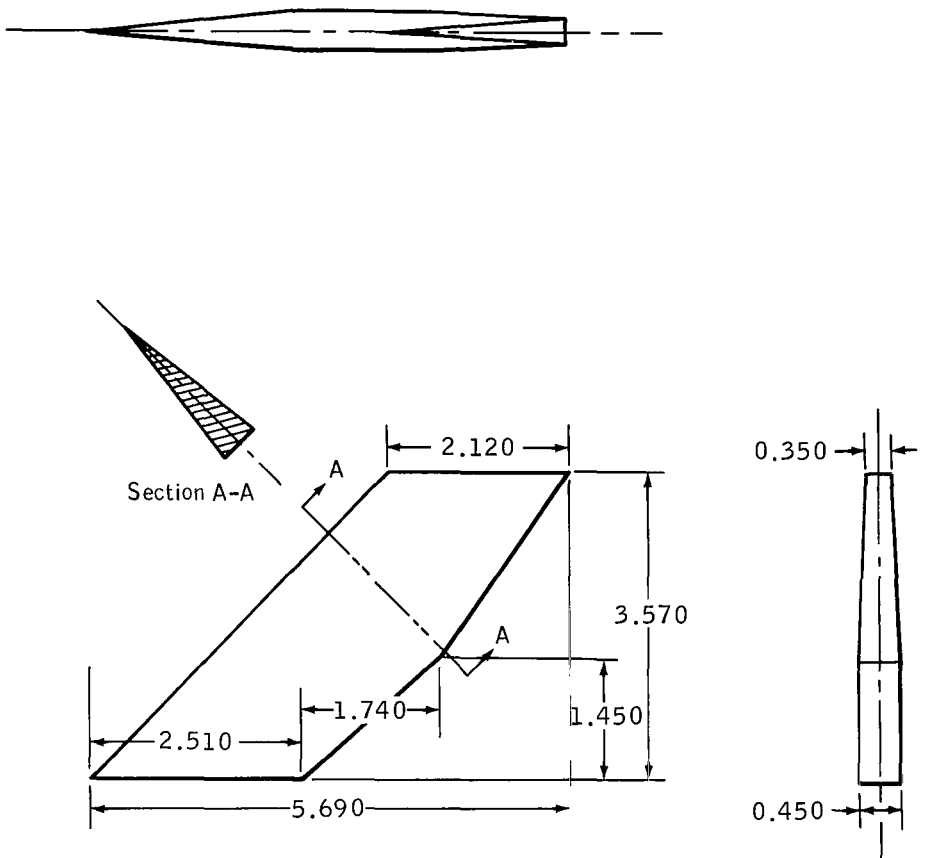

(d) Small-fin detail for configuration II.

Figure 2. - Continued.

NASA-S-67-7333

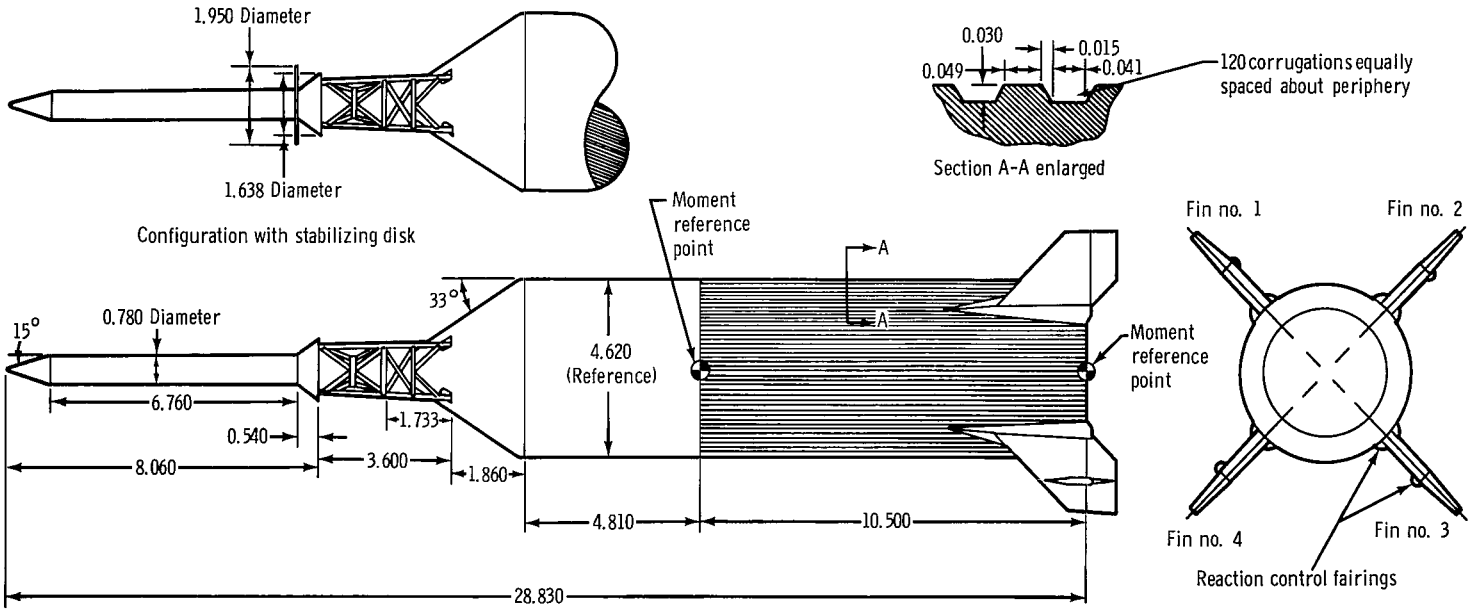

(e) Complete model of configuration III.

Figure 2. - Continued.

NASA-S-67-7328

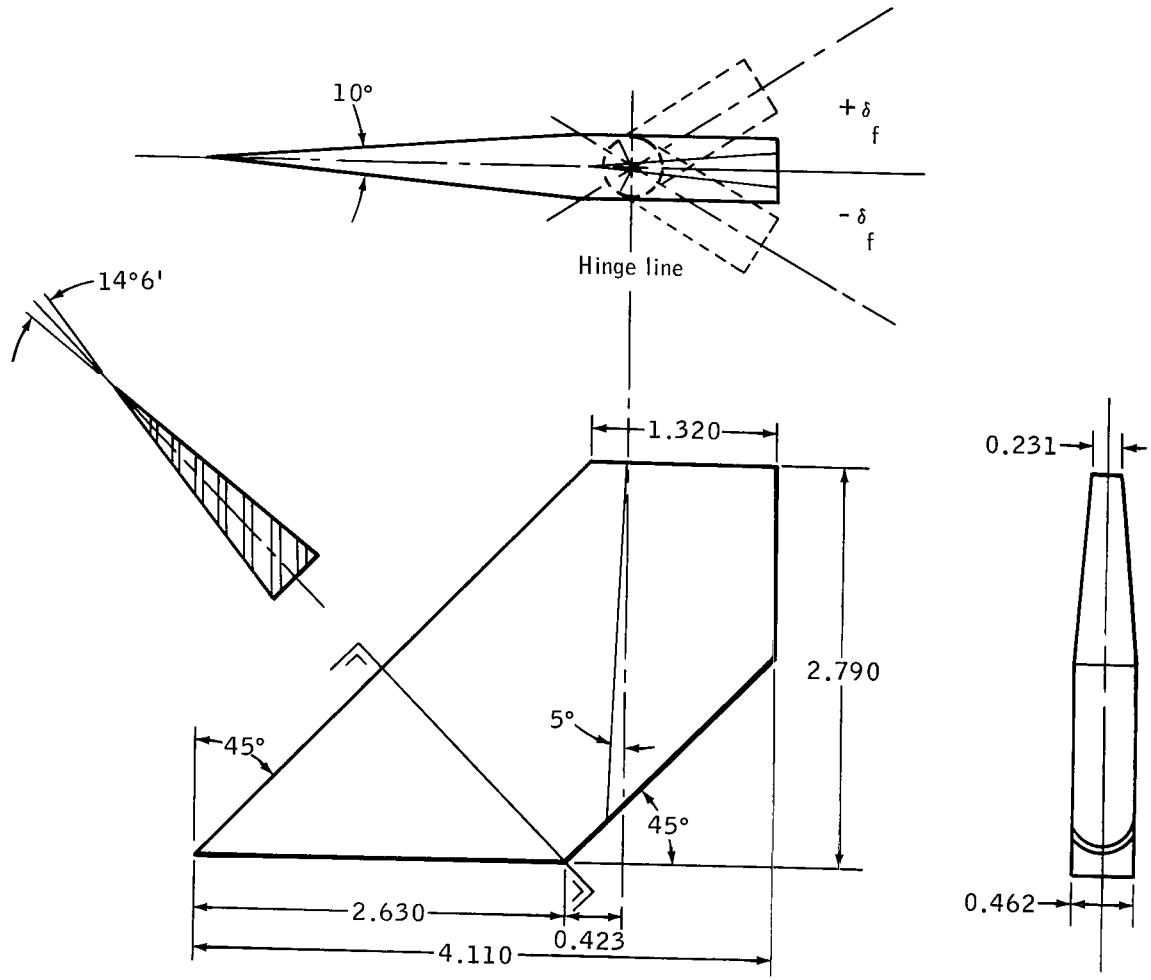

(f) Fin detail for configuration III.

Figure 2. - Concluded.

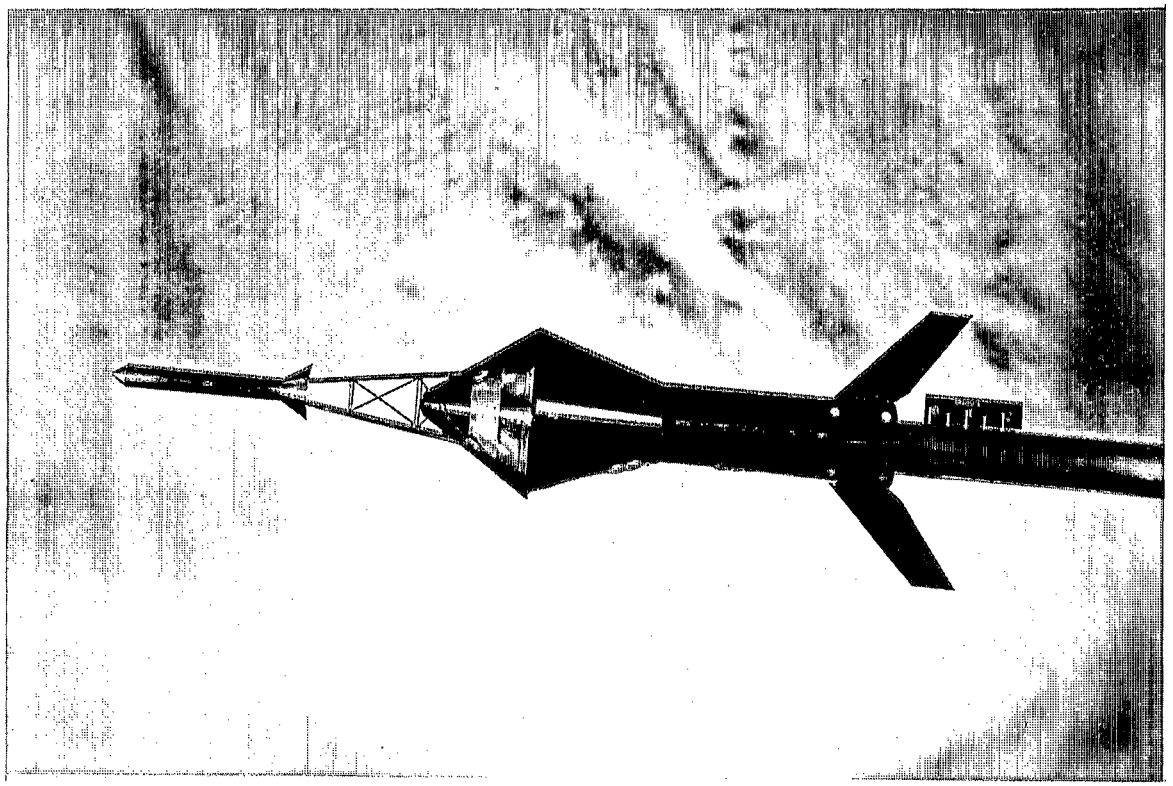

(a) Configuration I installed on a sting.

Figure 3.- Photographs of the configurations tested.

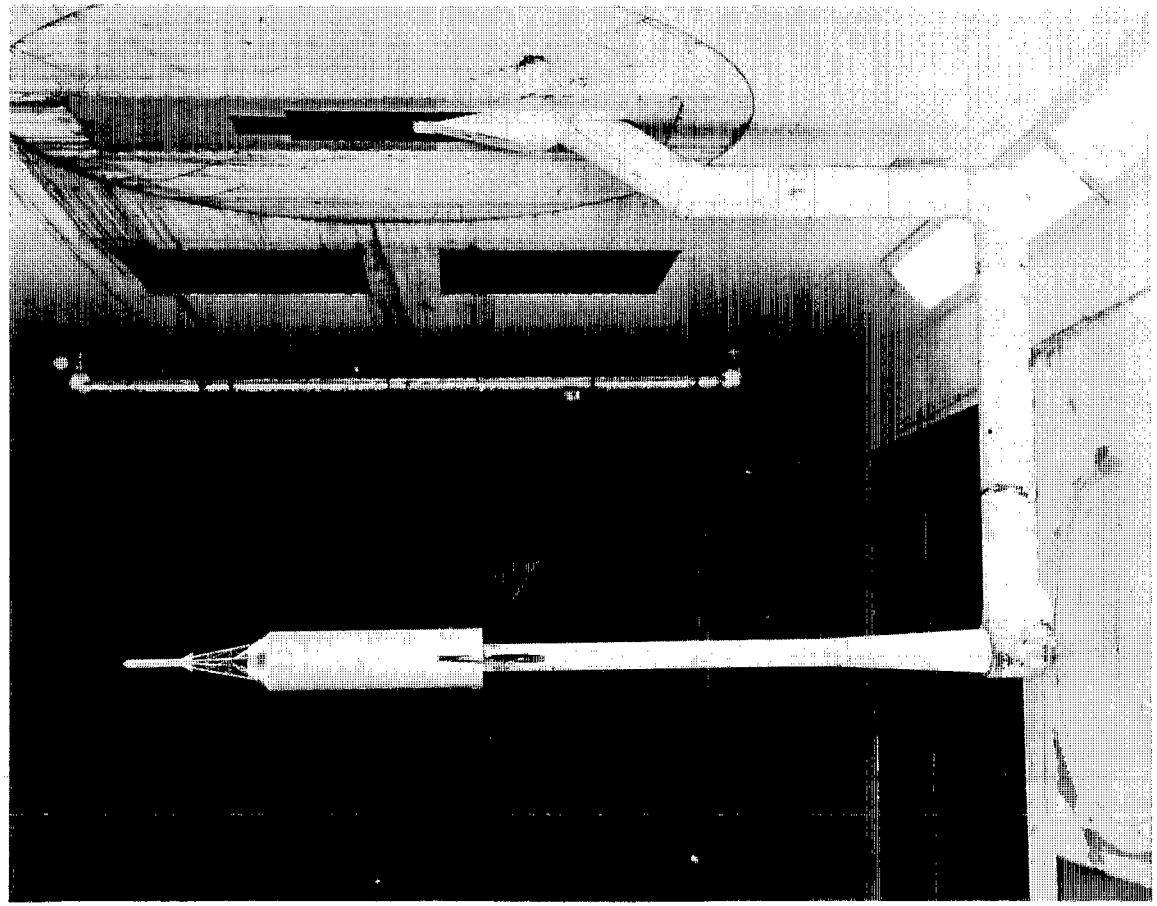

(b) Configuration II installed in a test section.

Figure 3. - Continued.

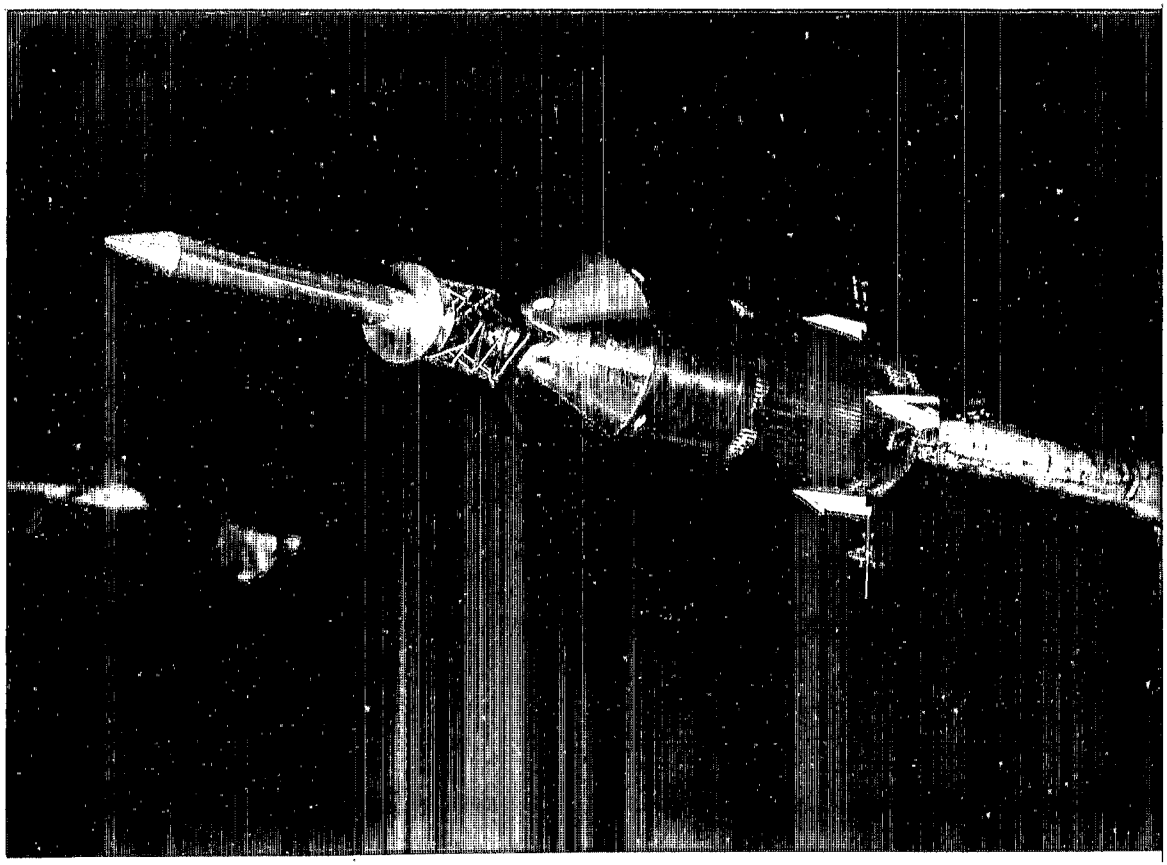

(c) Configuration III installed in a test section.

Figure 3. - Concluded.

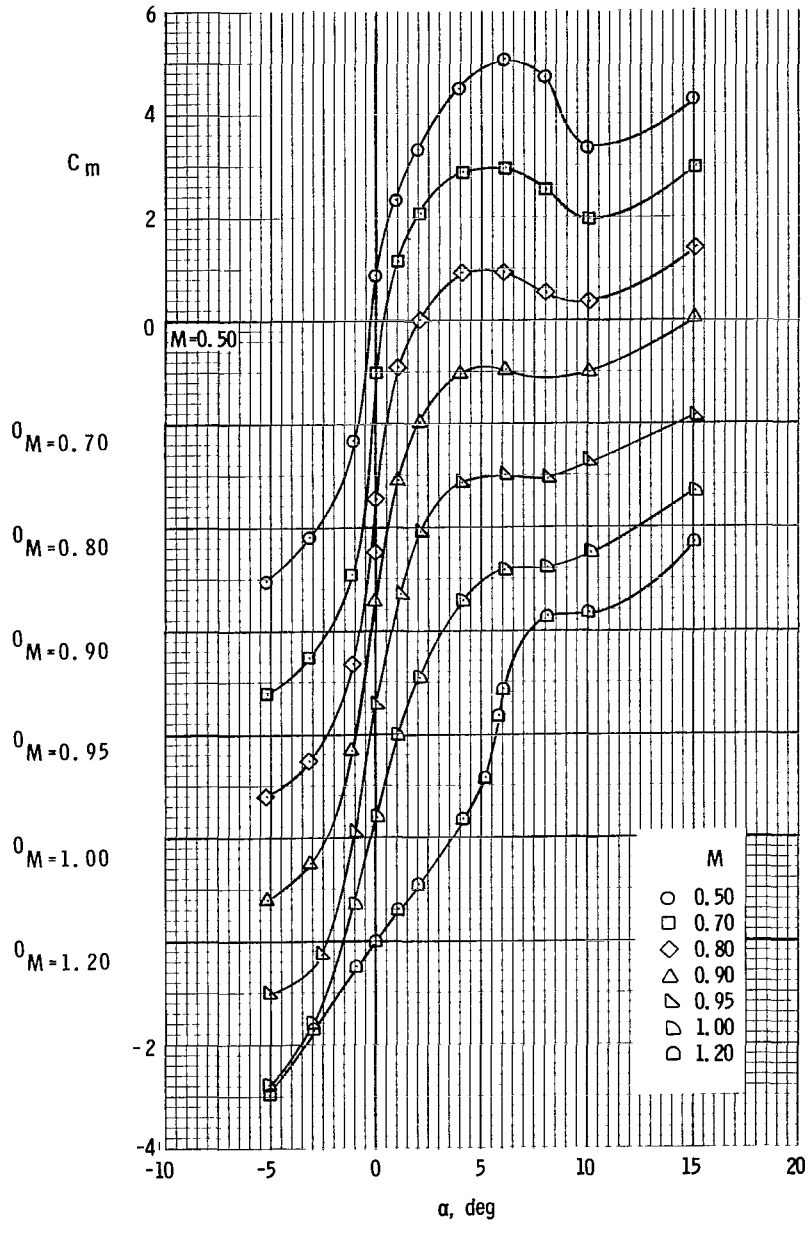

(a) Transonic pitching-moment coefficient.

Figure 4. - Aerodynamic characteristics of configuration I at Mach numbers from 0.50 to 2.16, fins off.

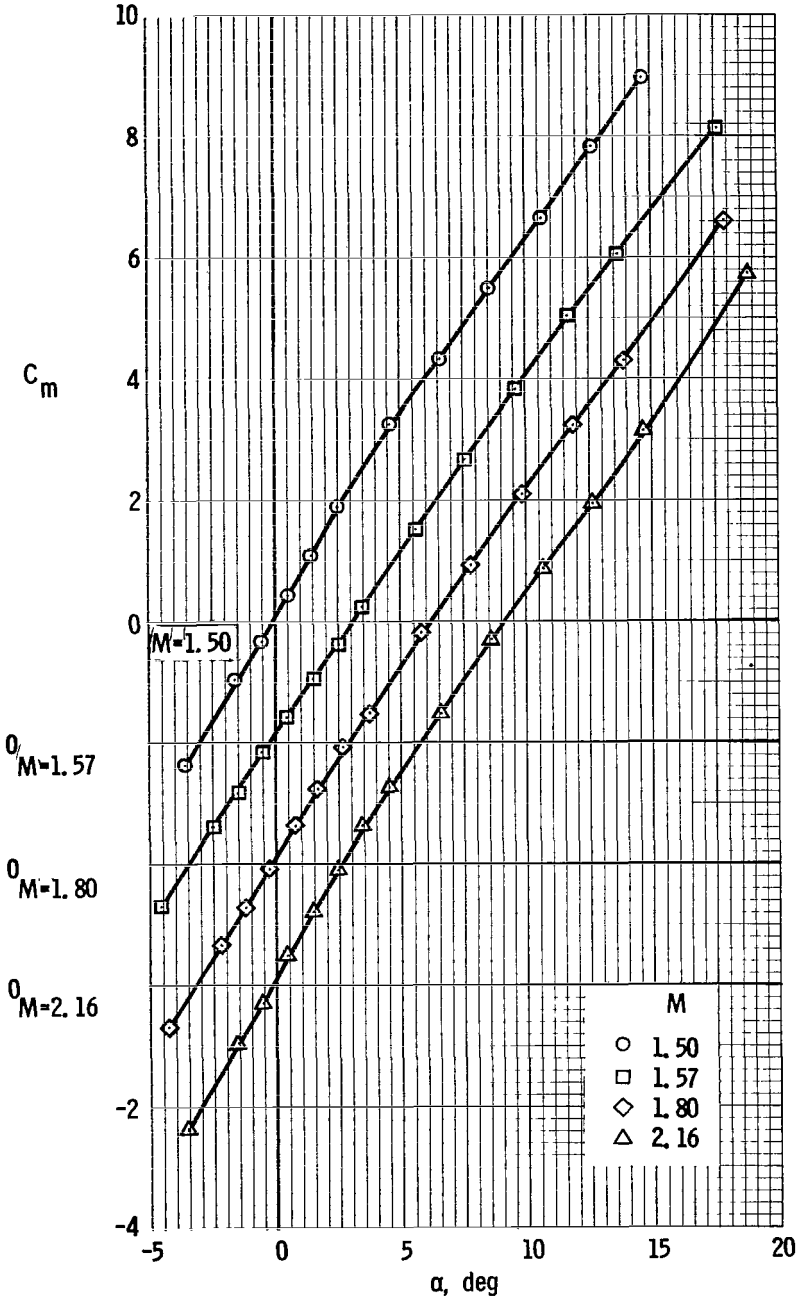

(b) Supersonic pitching-moment coefficient.

Figure 4. - Continued.

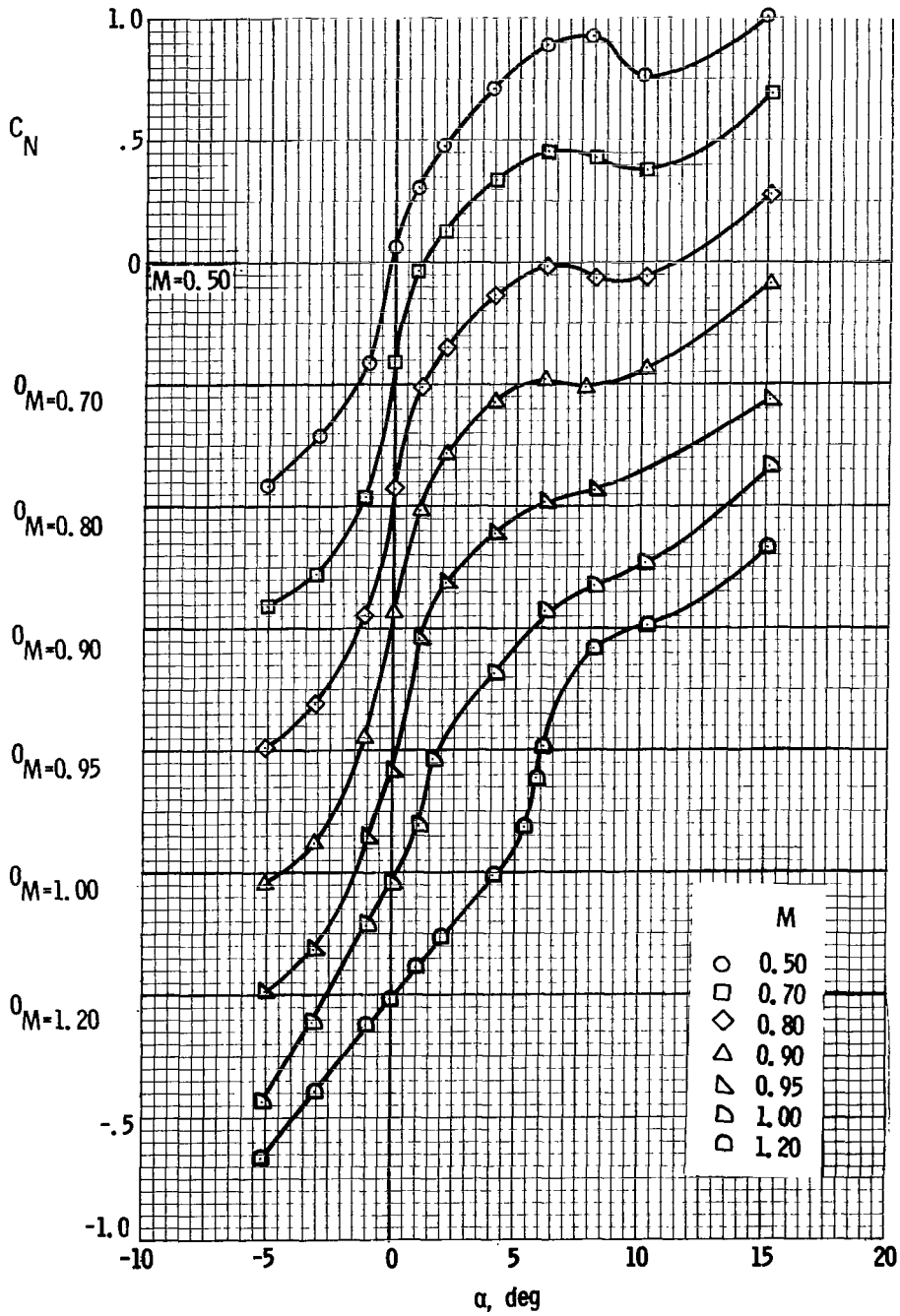

(c) Transonic normal-force coefficient.

Figure 4.- Continued.

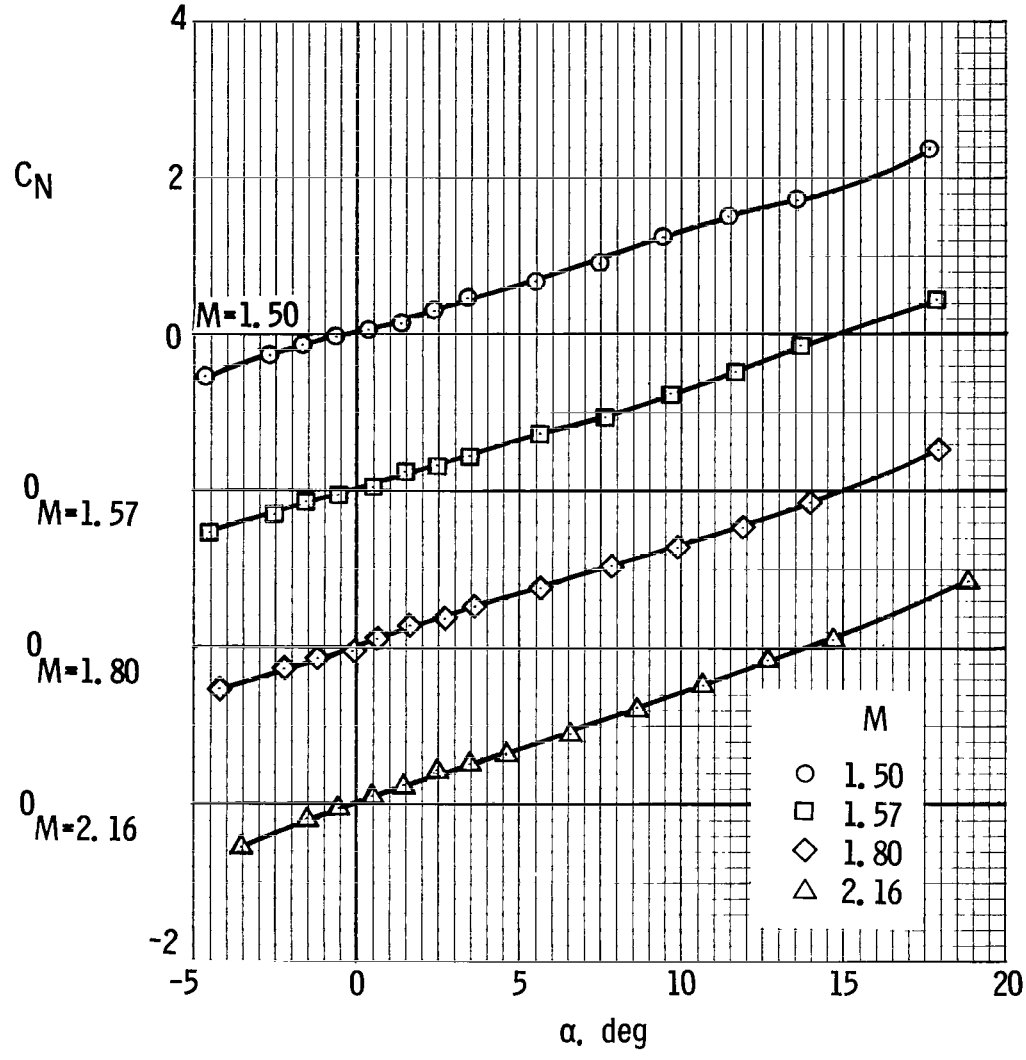

(d) Supersonic normal-force coefficient.

Figure 4. - Continued.

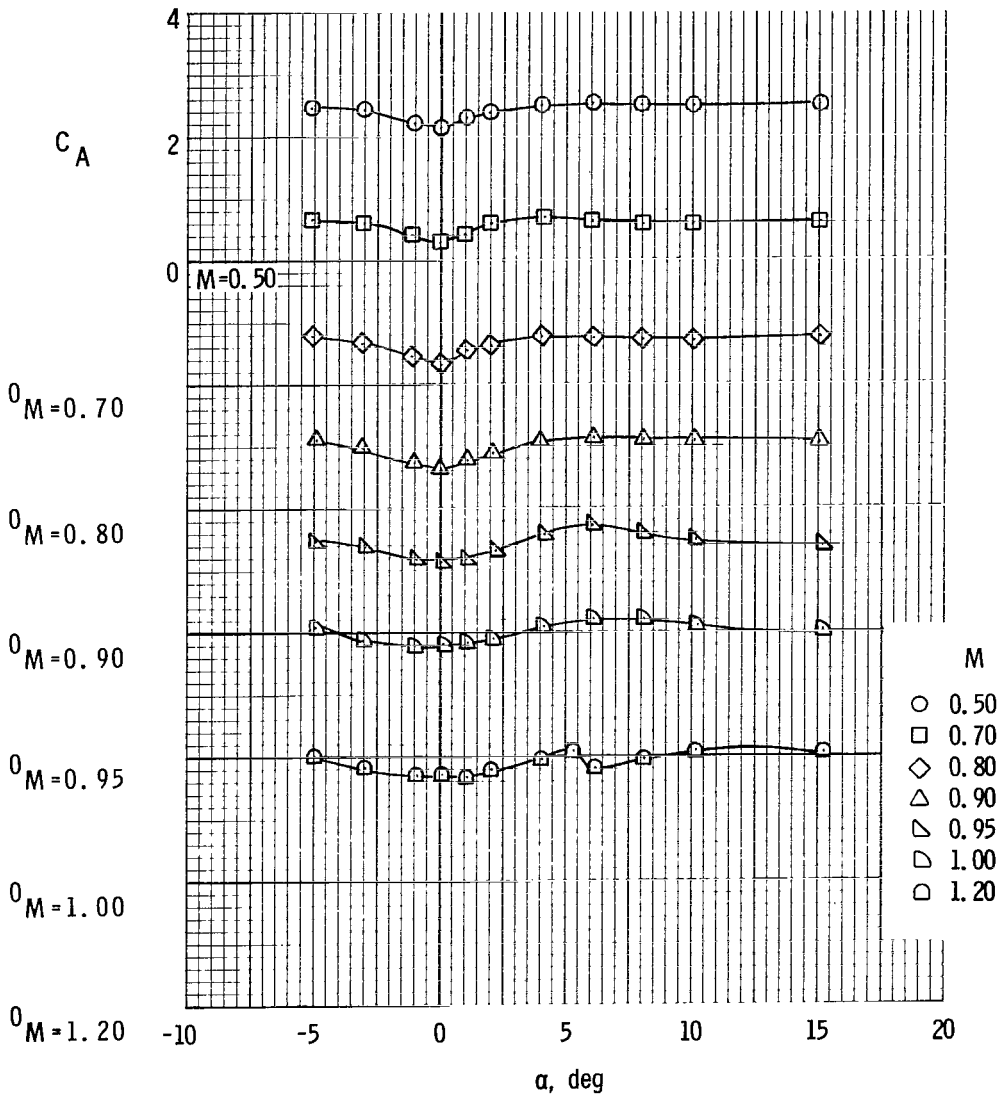

(e) Transonic axial-force coefficient.

Figure 4.- Continued.

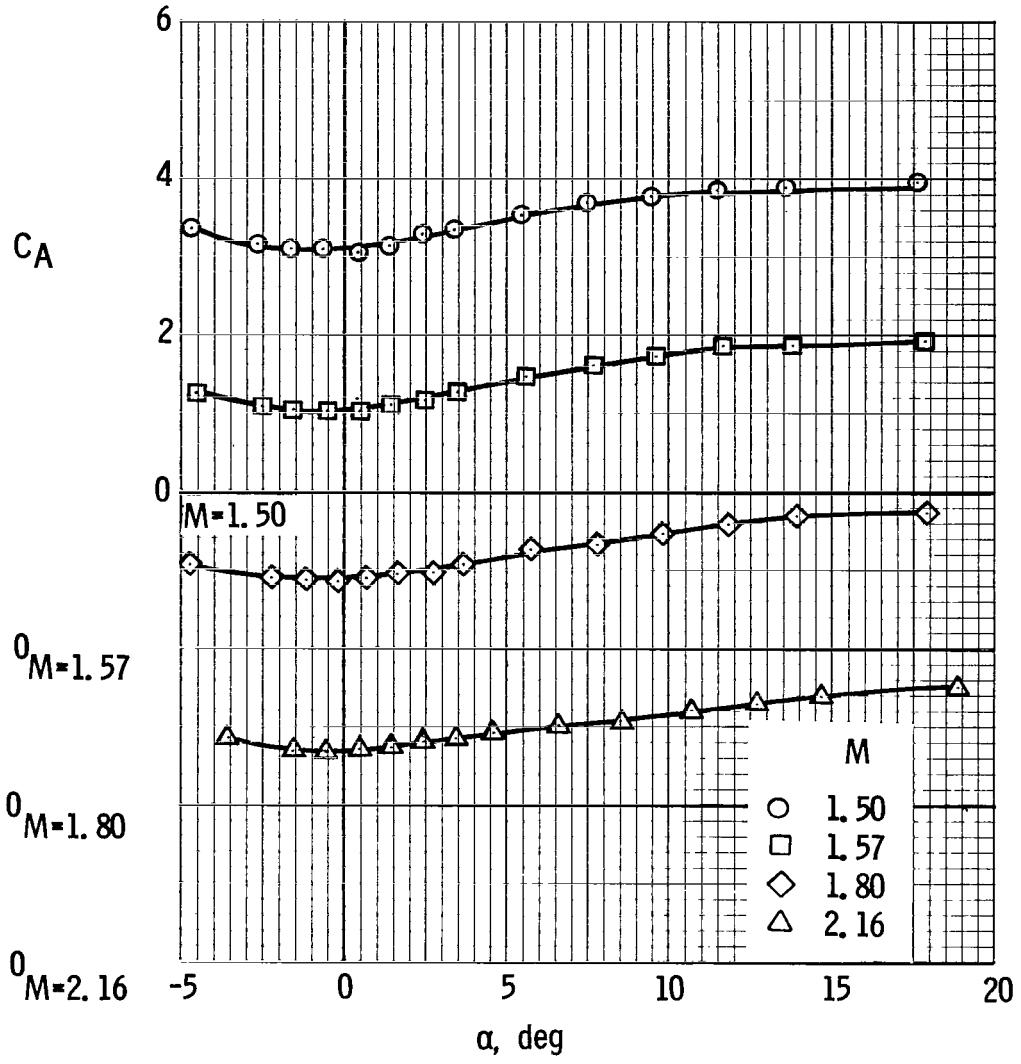

(f) Supersonic axial-force coefficient.

Figure 4. - Continued.

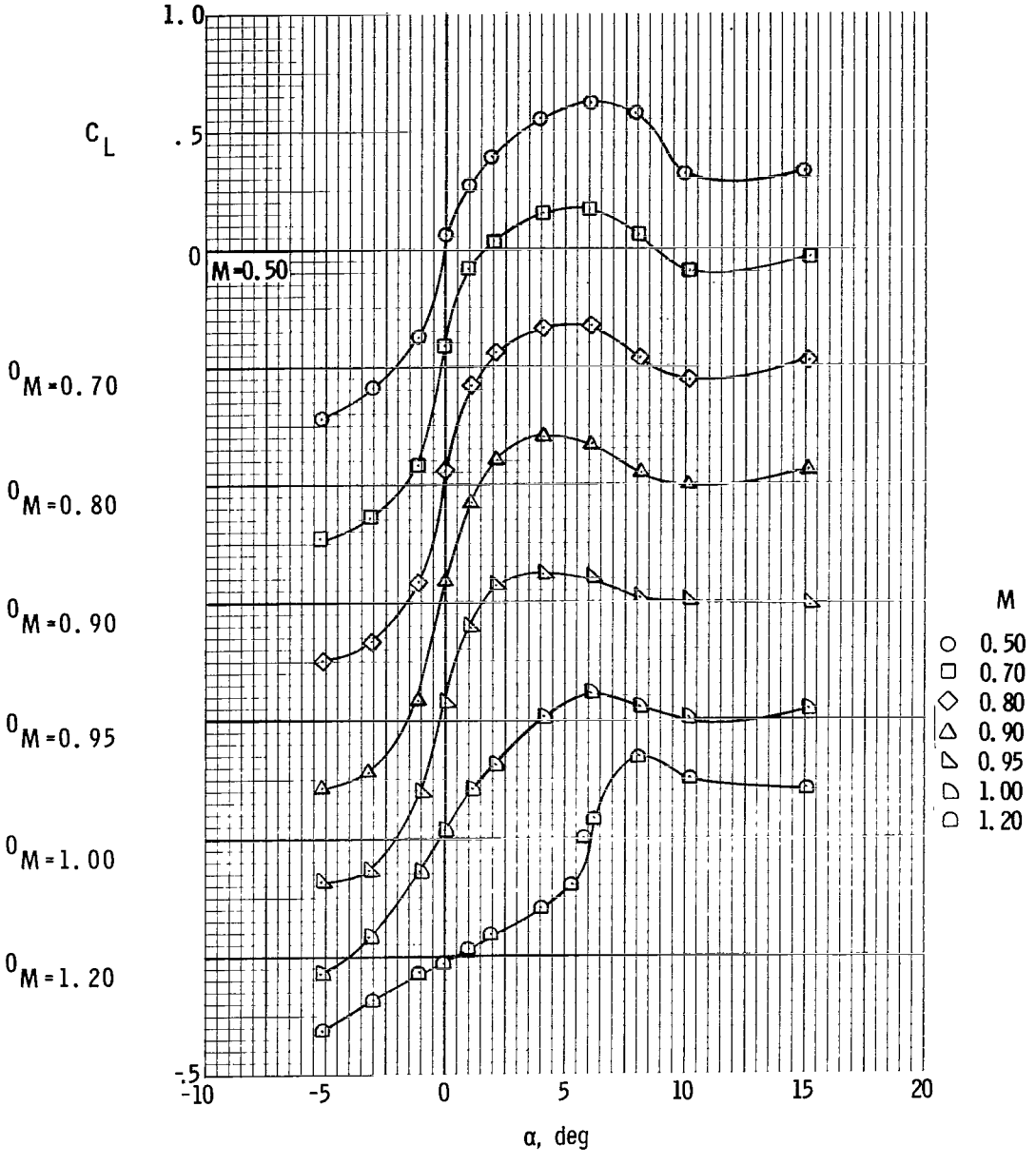

(g) Transonic lift coefficient.

Figure 4.- Continued.

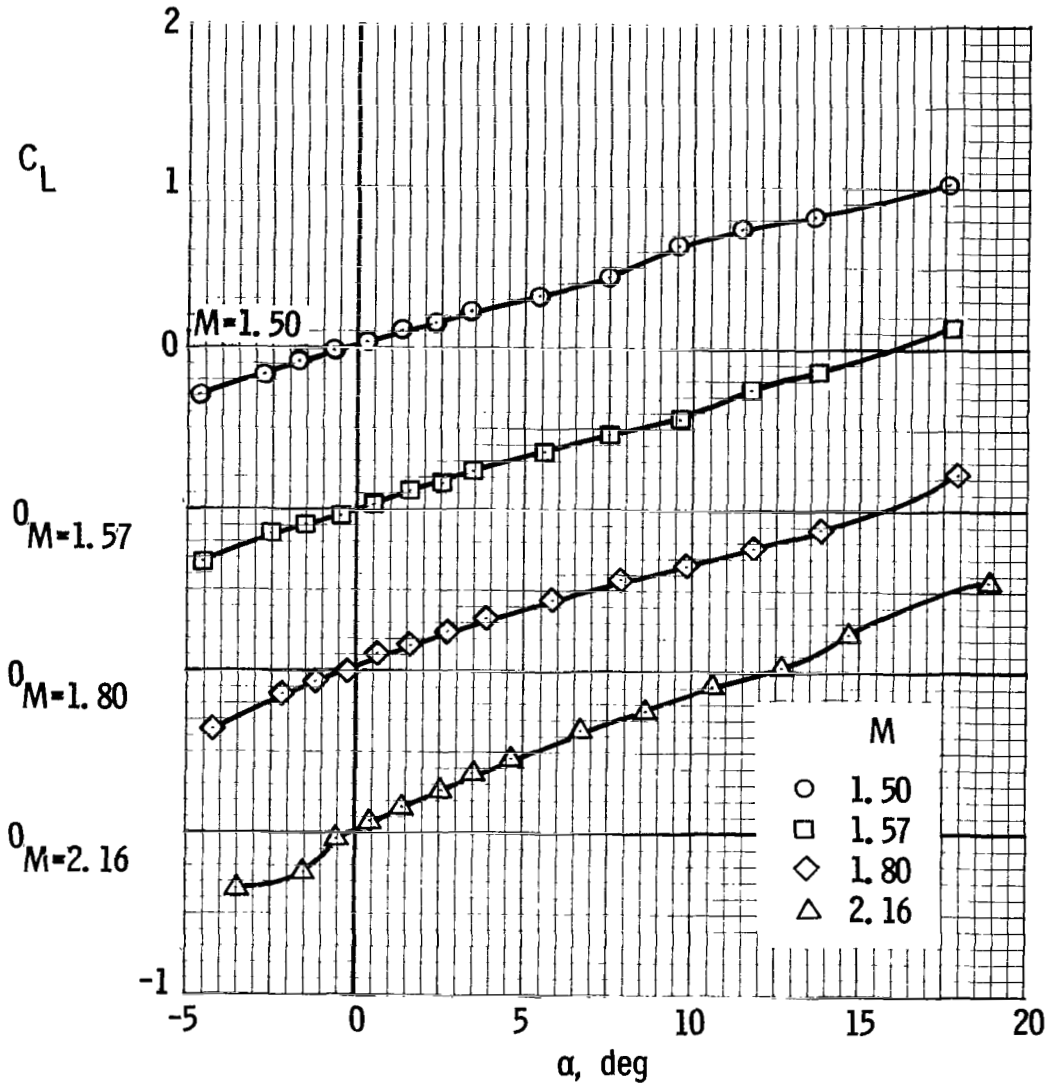

(h) Supersonic lift coefficient.

Figure 4. - Continued.

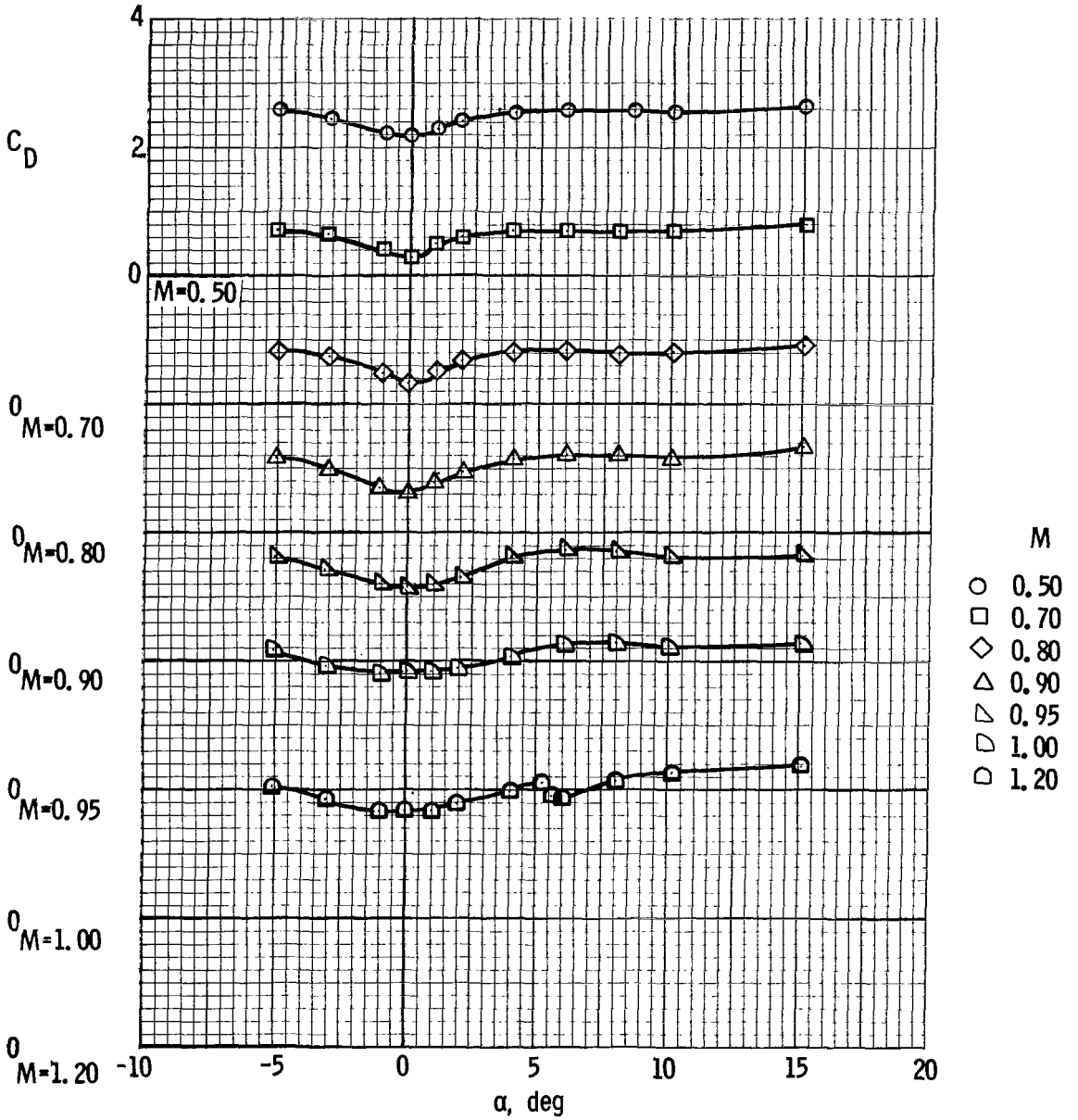

(i) Transonic drag coefficient.

Figure 4. - Continued.

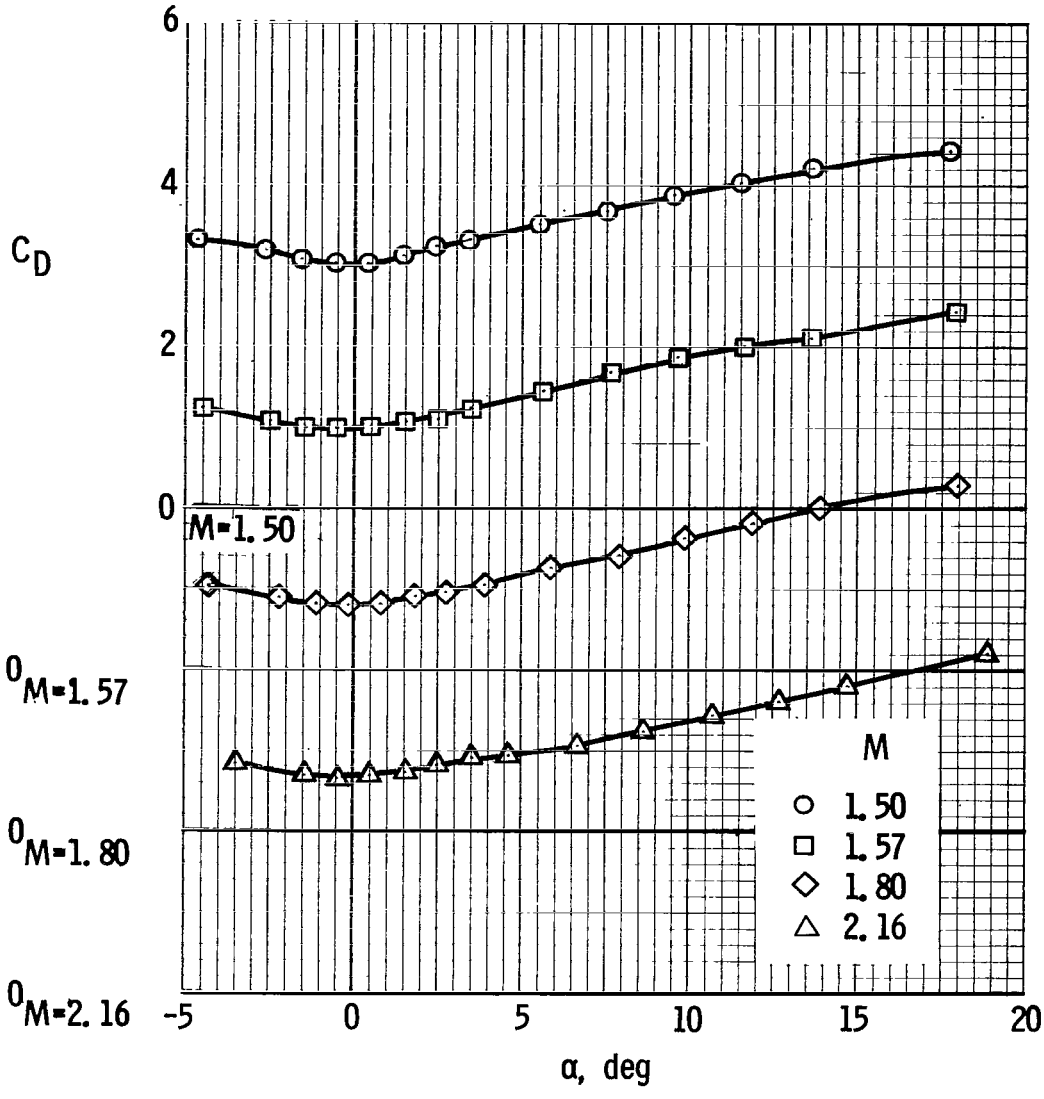

(j) Supersonic drag coefficient.

Figure 4. - Continued.

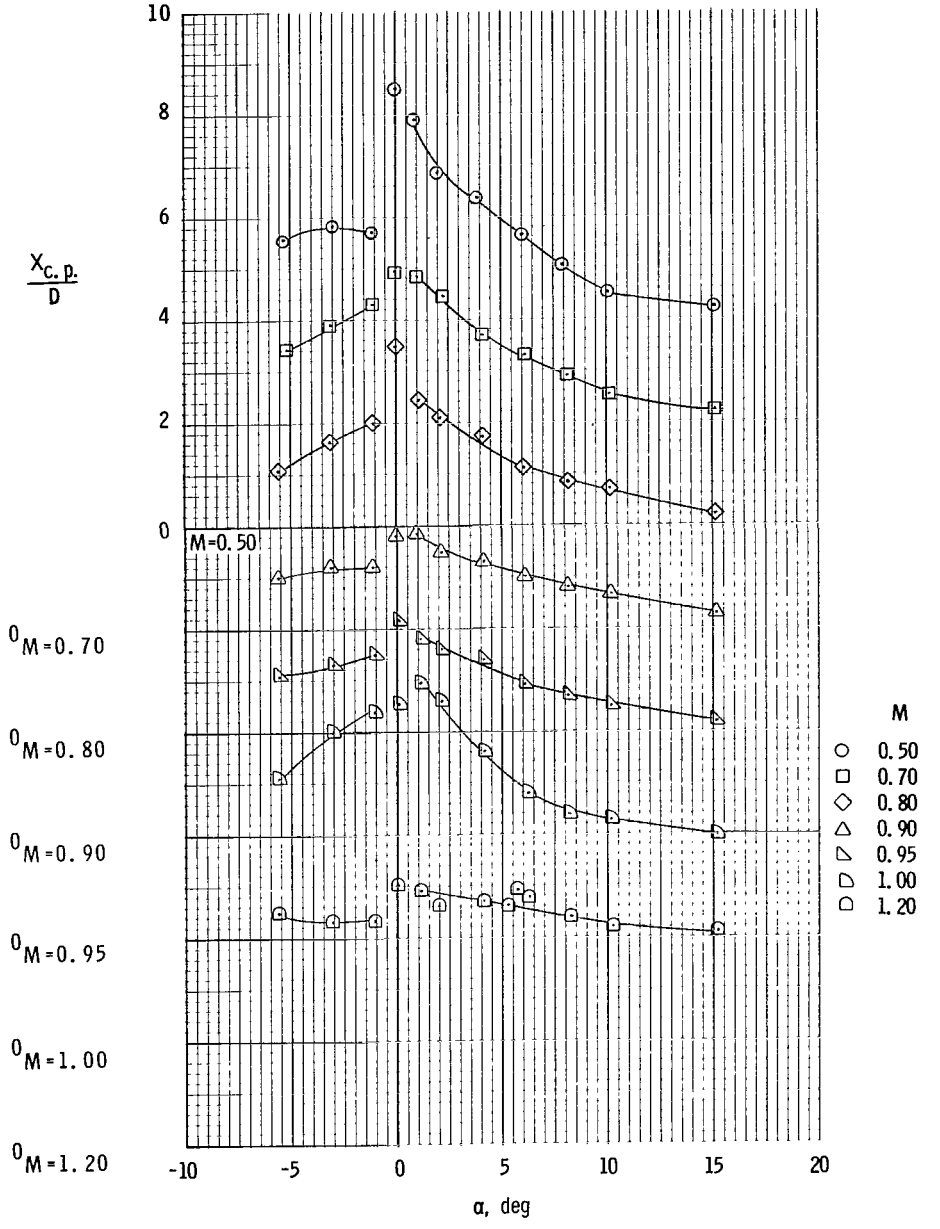

(k) Transonic center of pressure.

Figure 4.- Continued.

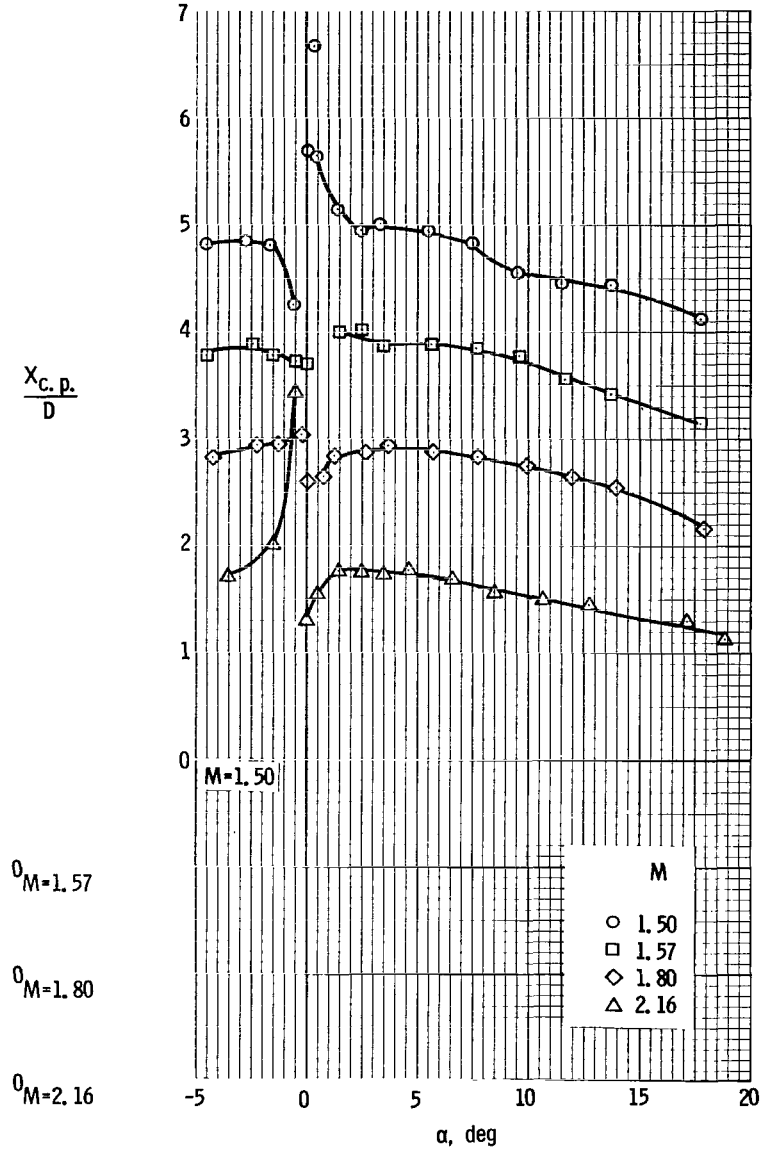

(l) Supersonic center of pressure.

Figure 4.- Concluded.

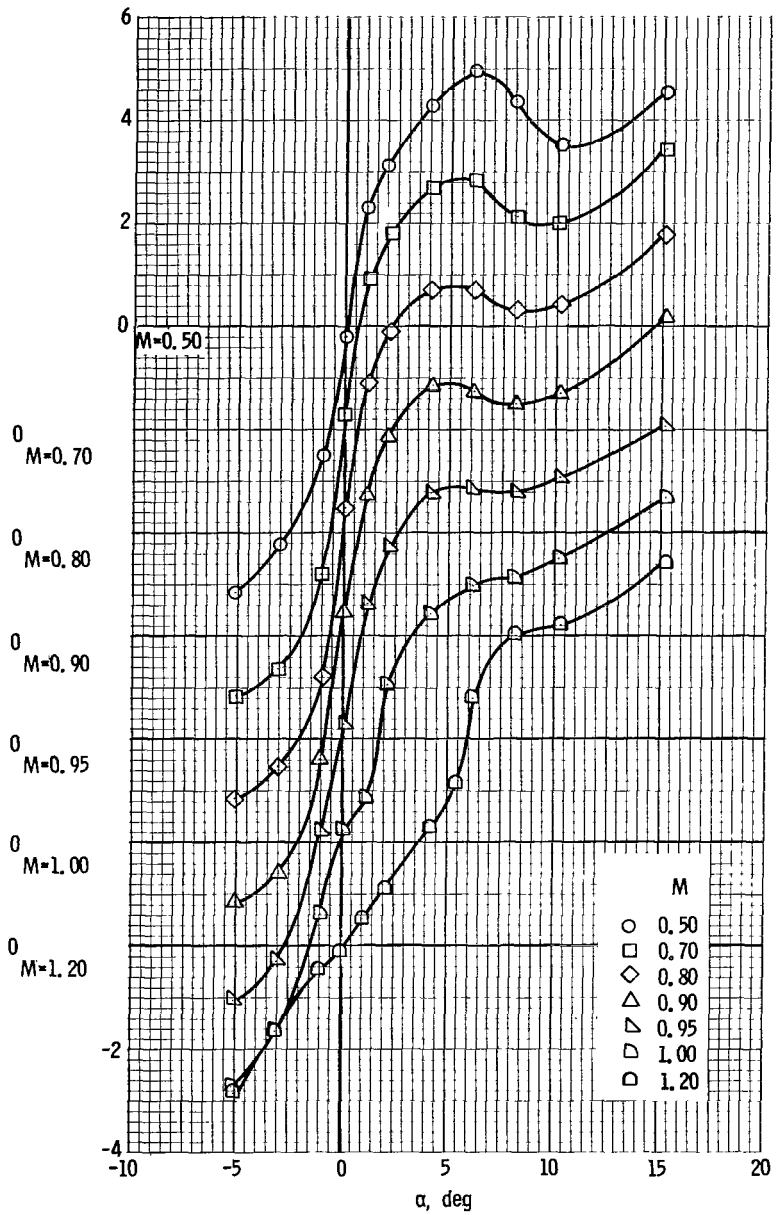

(a) Transonic pitching-moment coefficient.

Figure 5.- Aerodynamic characteristics of configuration I at Mach numbers from 0.50 to 2.16, fins on.

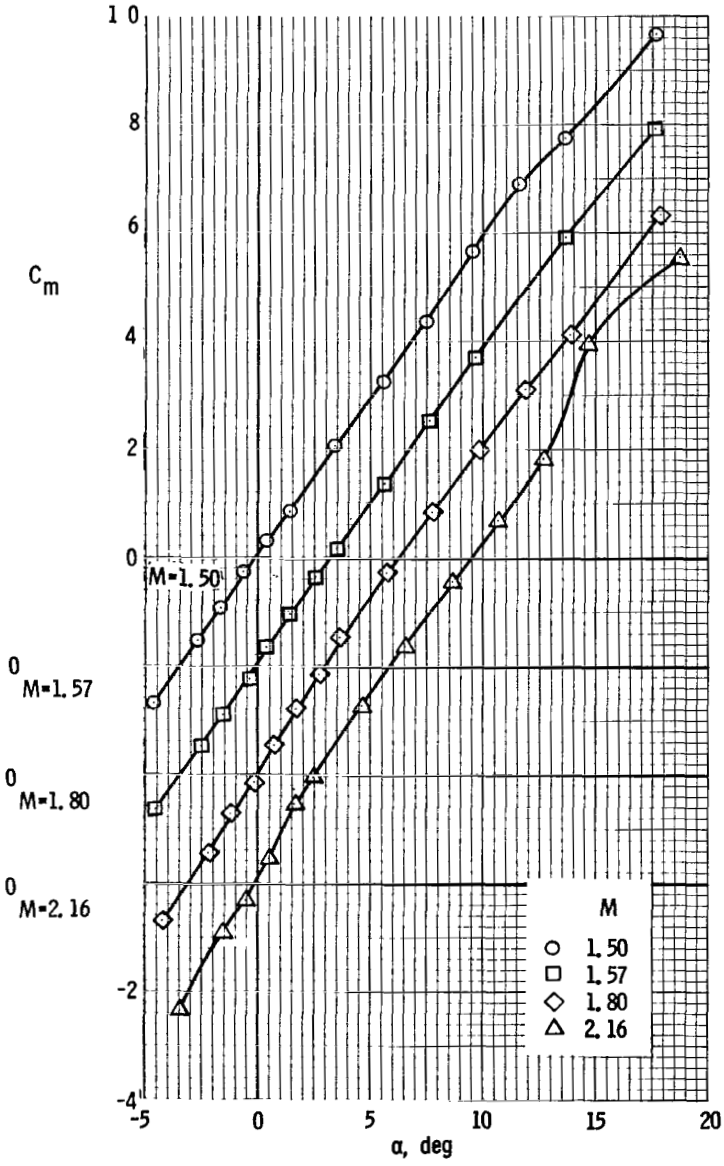

(b) Supersonic pitching-moment coefficient.

Figure 5.- Continued.

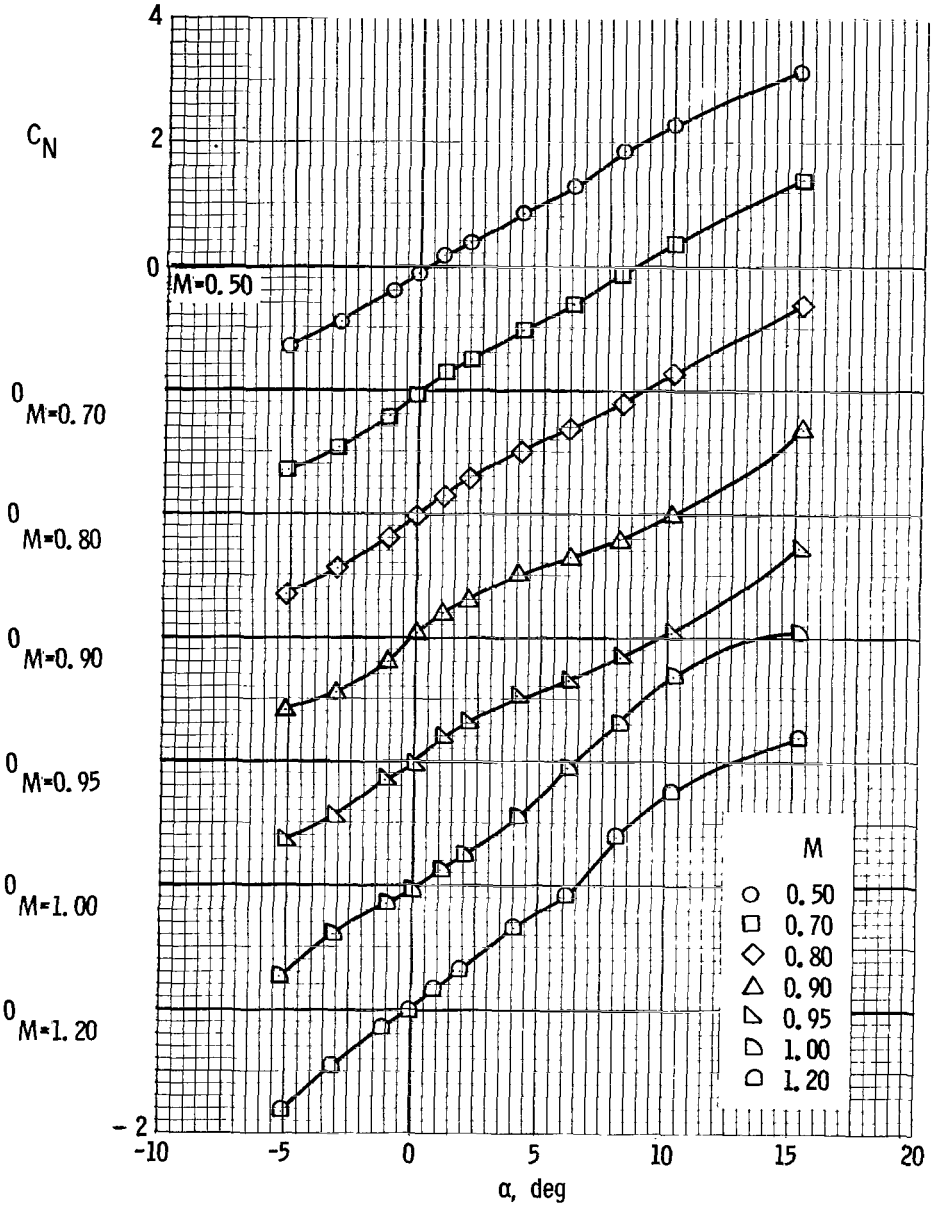

(c) Transonic normal-force coefficient.

Figure 5.- Continued.

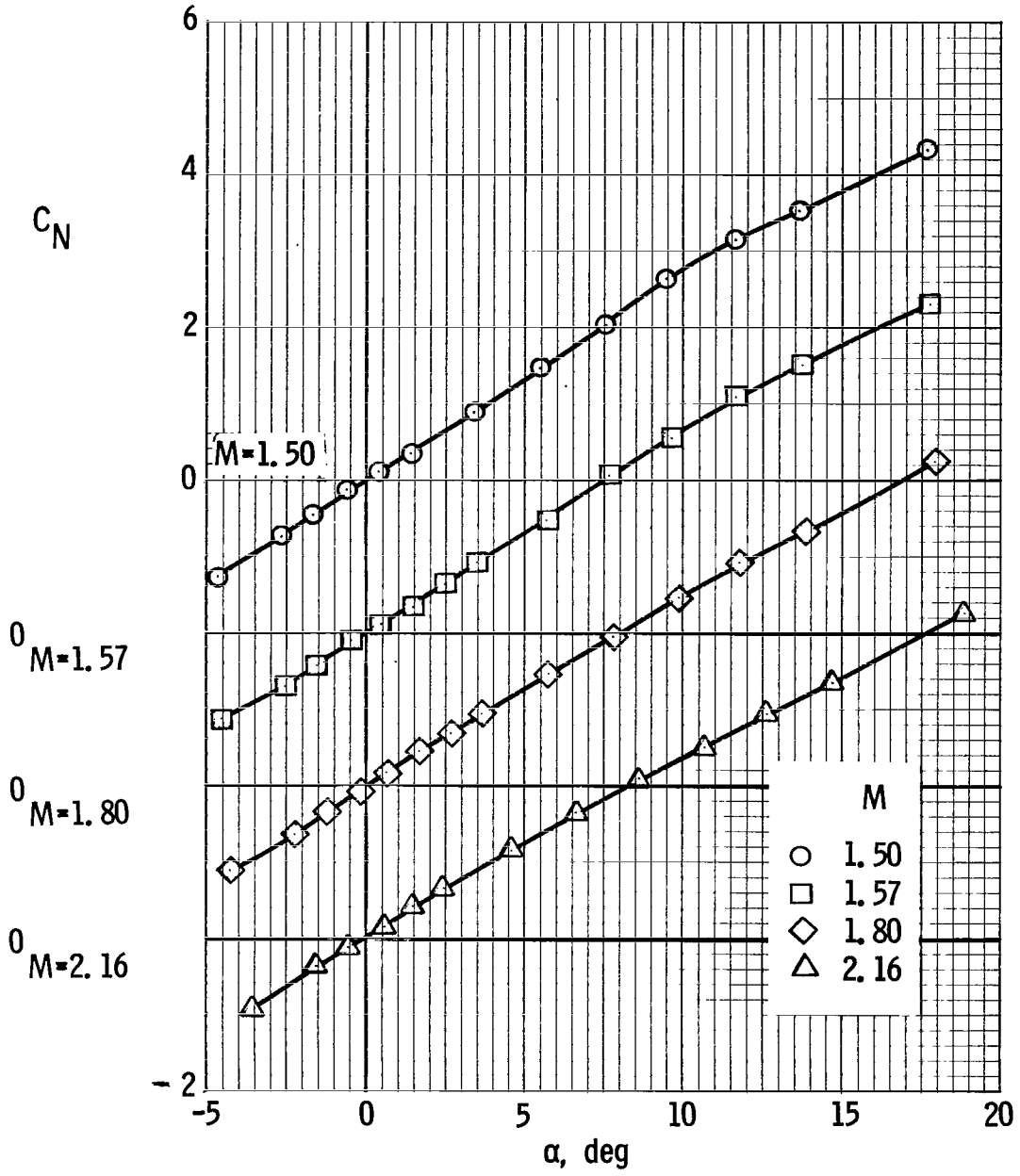

(d) Supersonic normal-force coefficient.

Figure 5.- Continued.

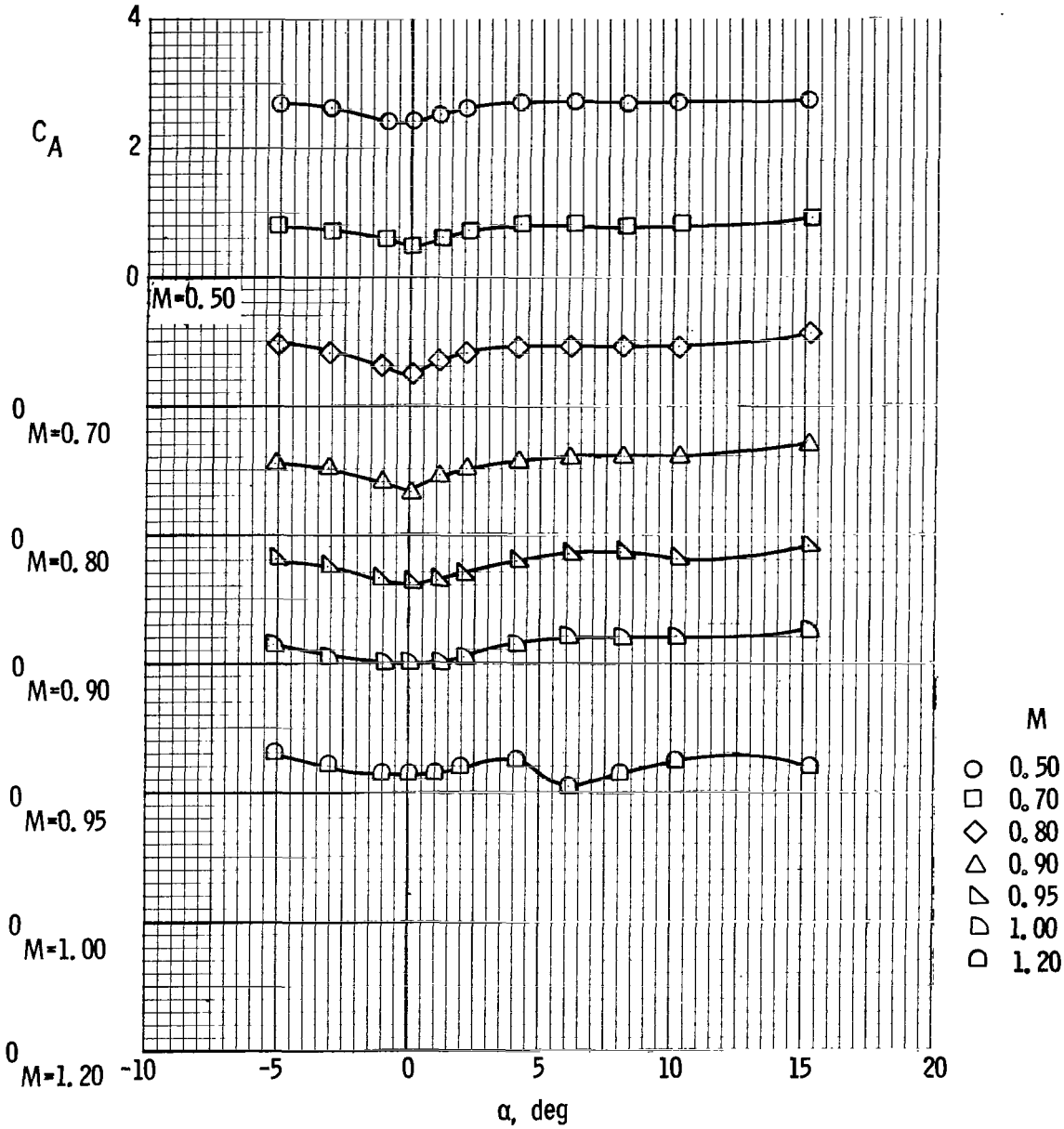

(e) Transonic axial-force coefficient.

Figure 5. - Continued.

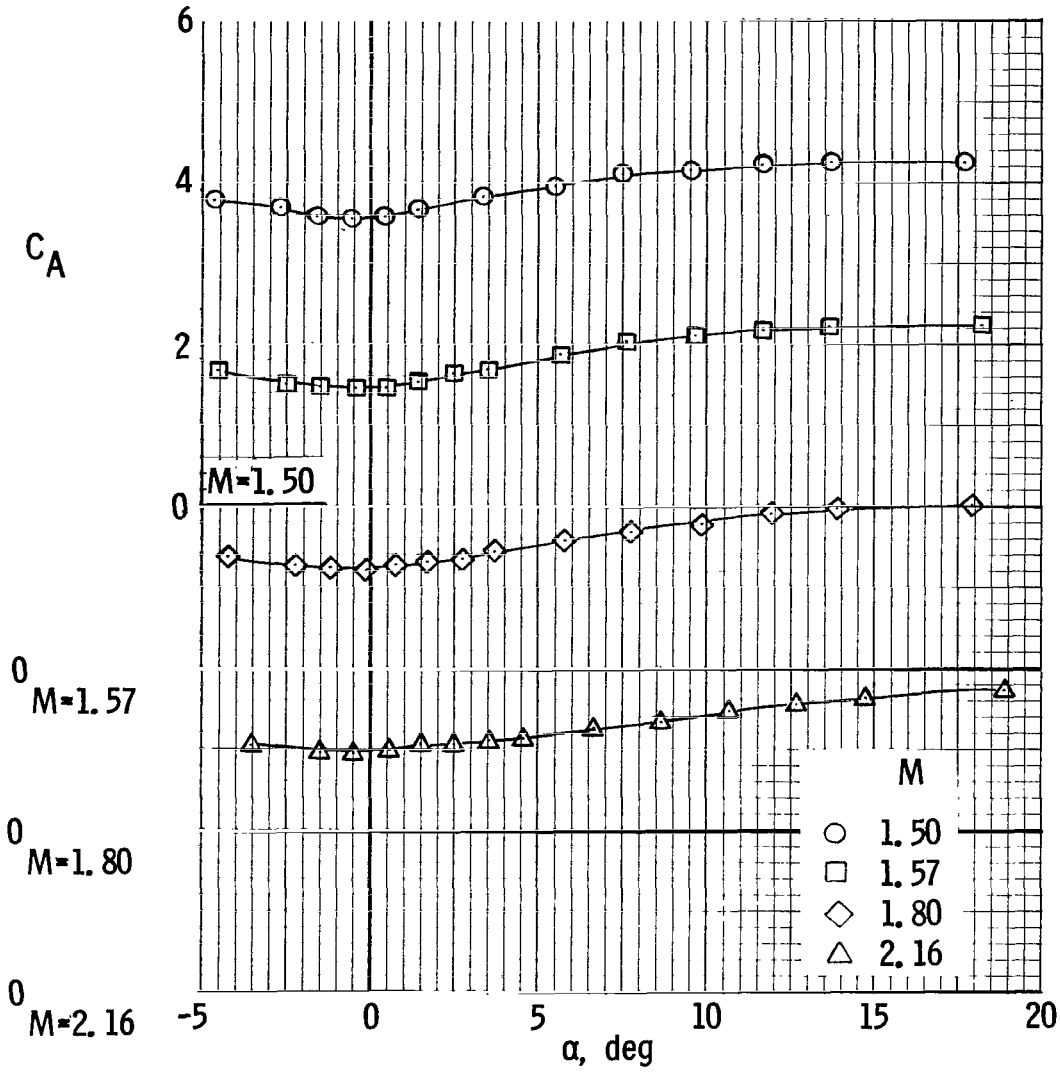

(f) Supersonic axial-force coefficient.

Figure 5. - Continued.

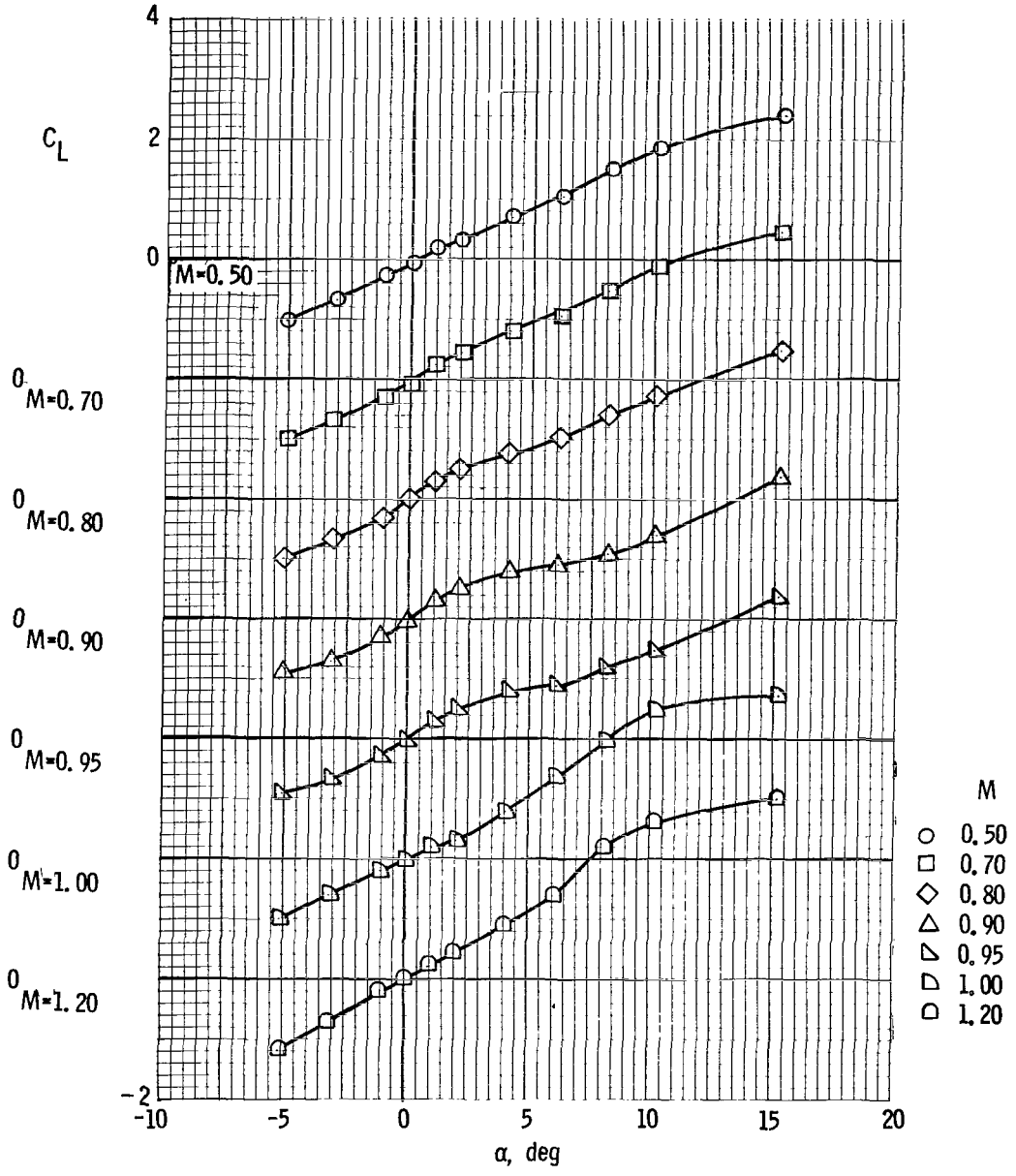

(g) Transonic lift coefficient.

Figure 5. - Continued.

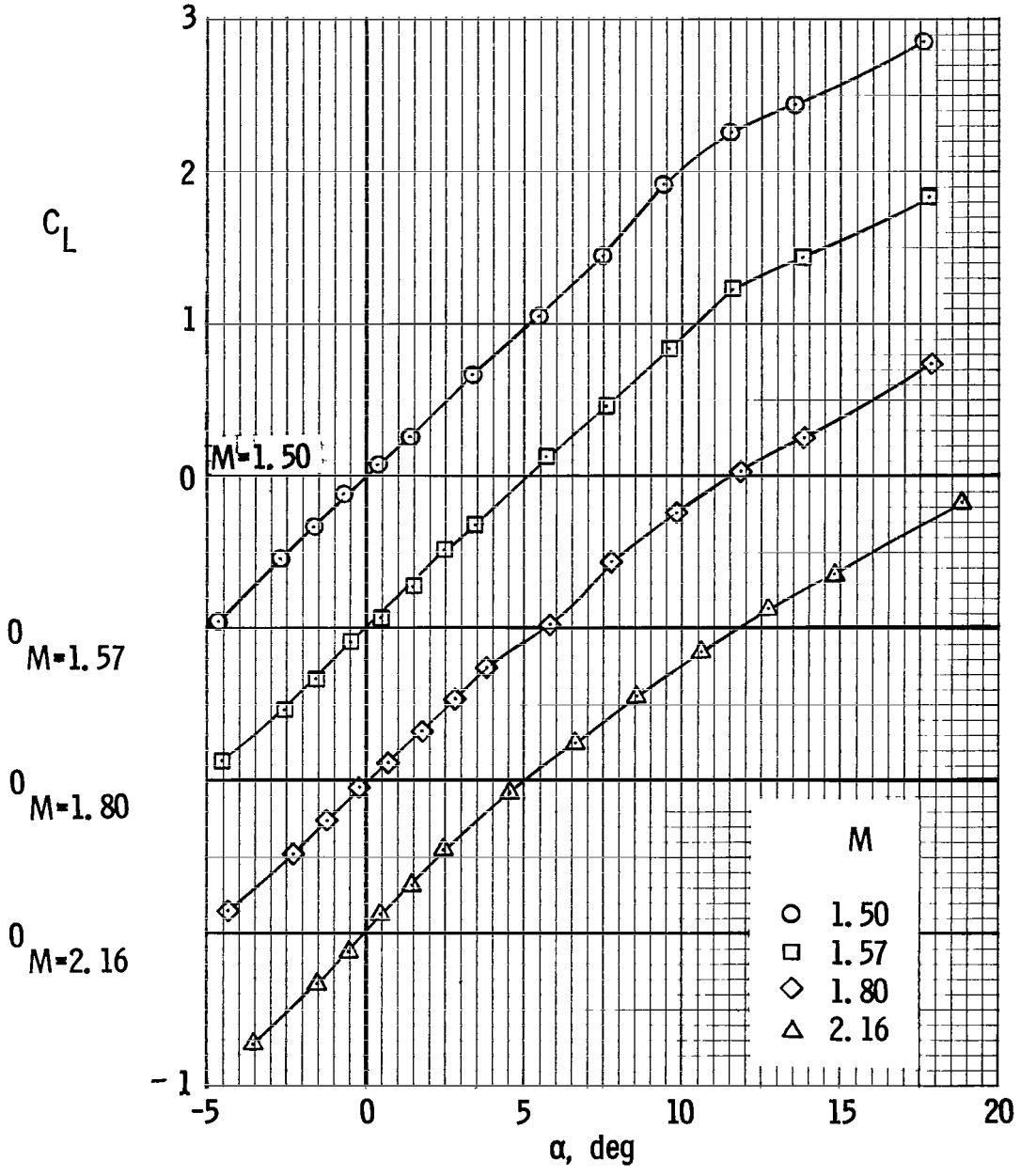

(h) Supersonic lift coefficient.

Figure 5. - Continued.

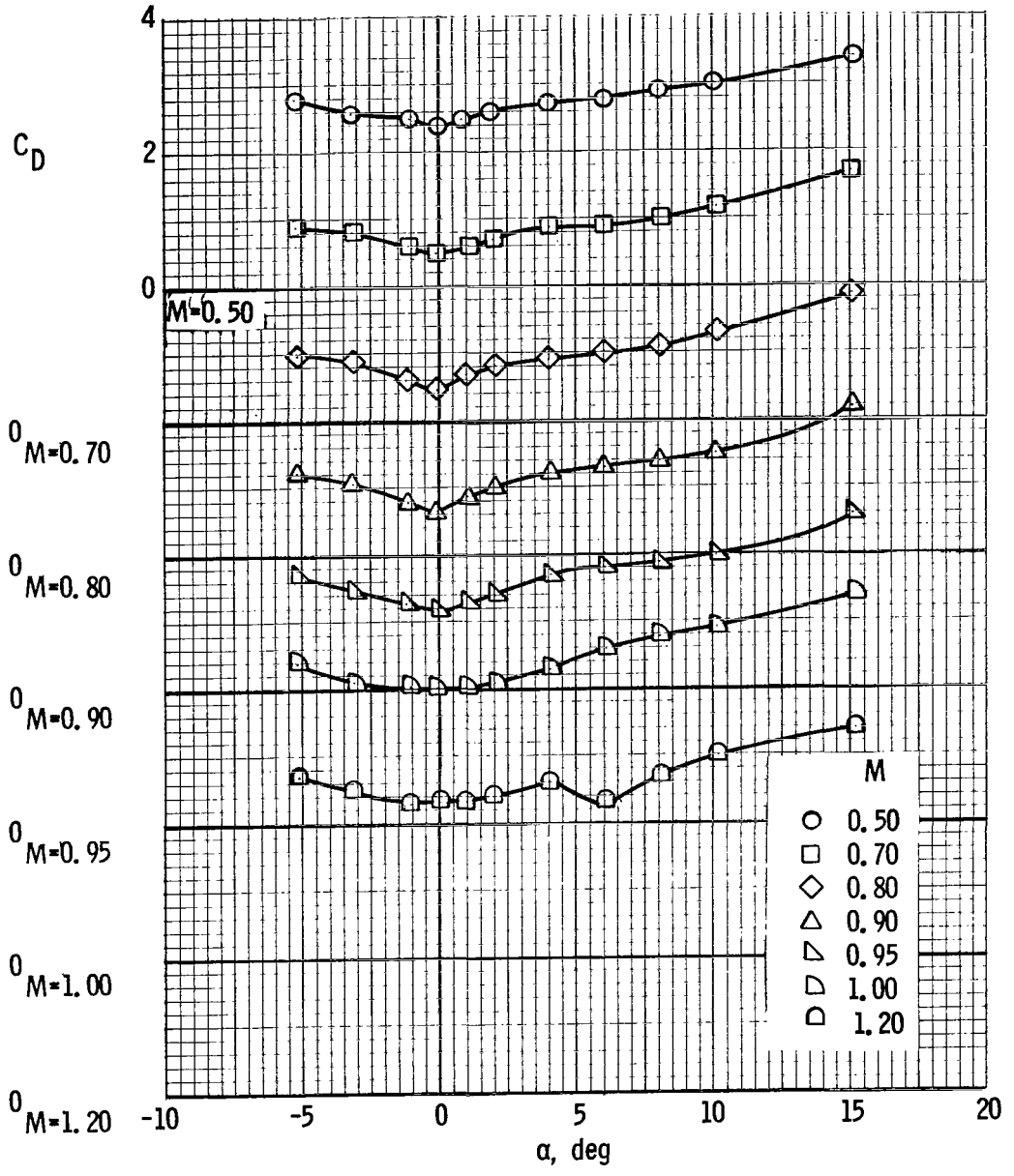

(i) Transonic drag coefficient.

Figure 5.- Continued.

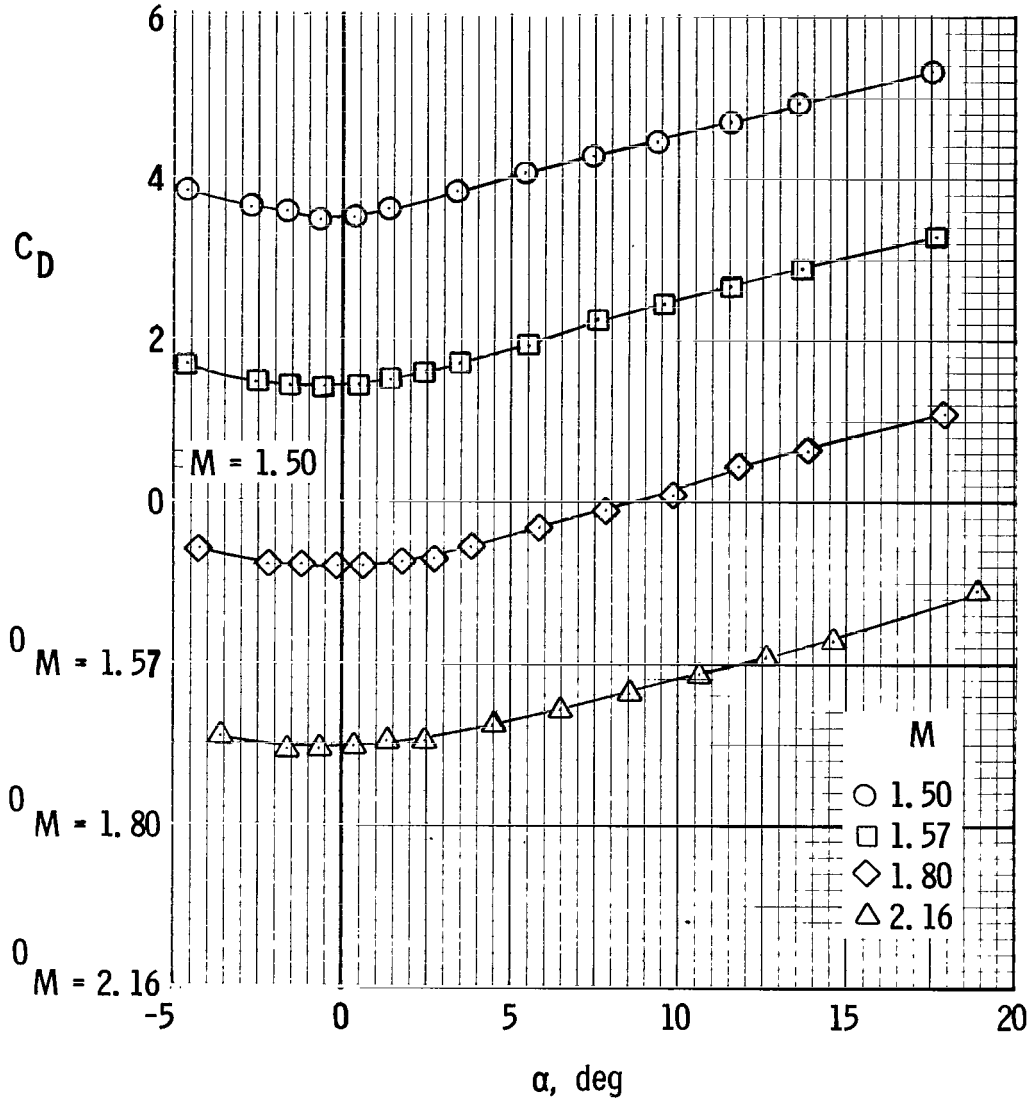

(j) Supersonic drag coefficient.

Figure 5. - Continued.

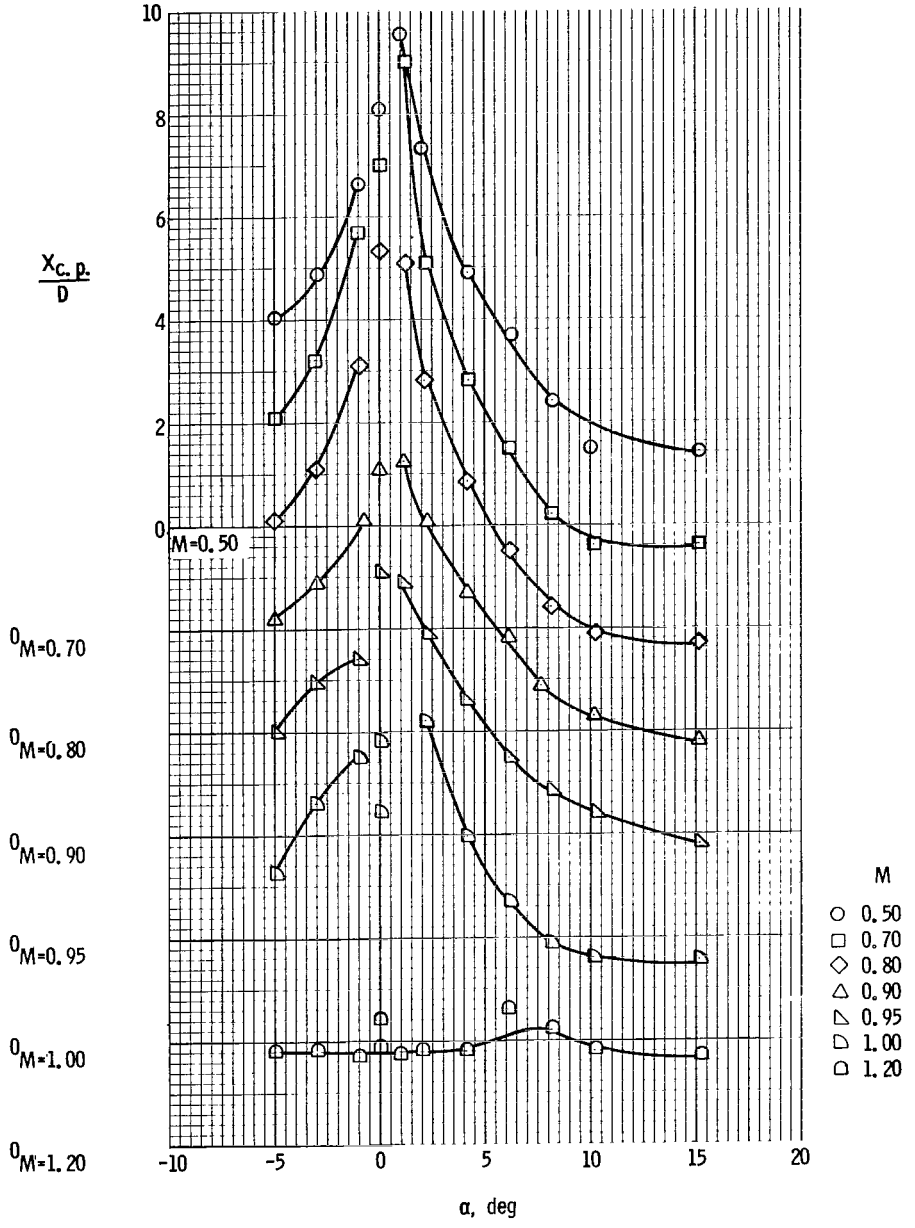

(k) Transonic center of pressure.

Figure 5.- Continued.

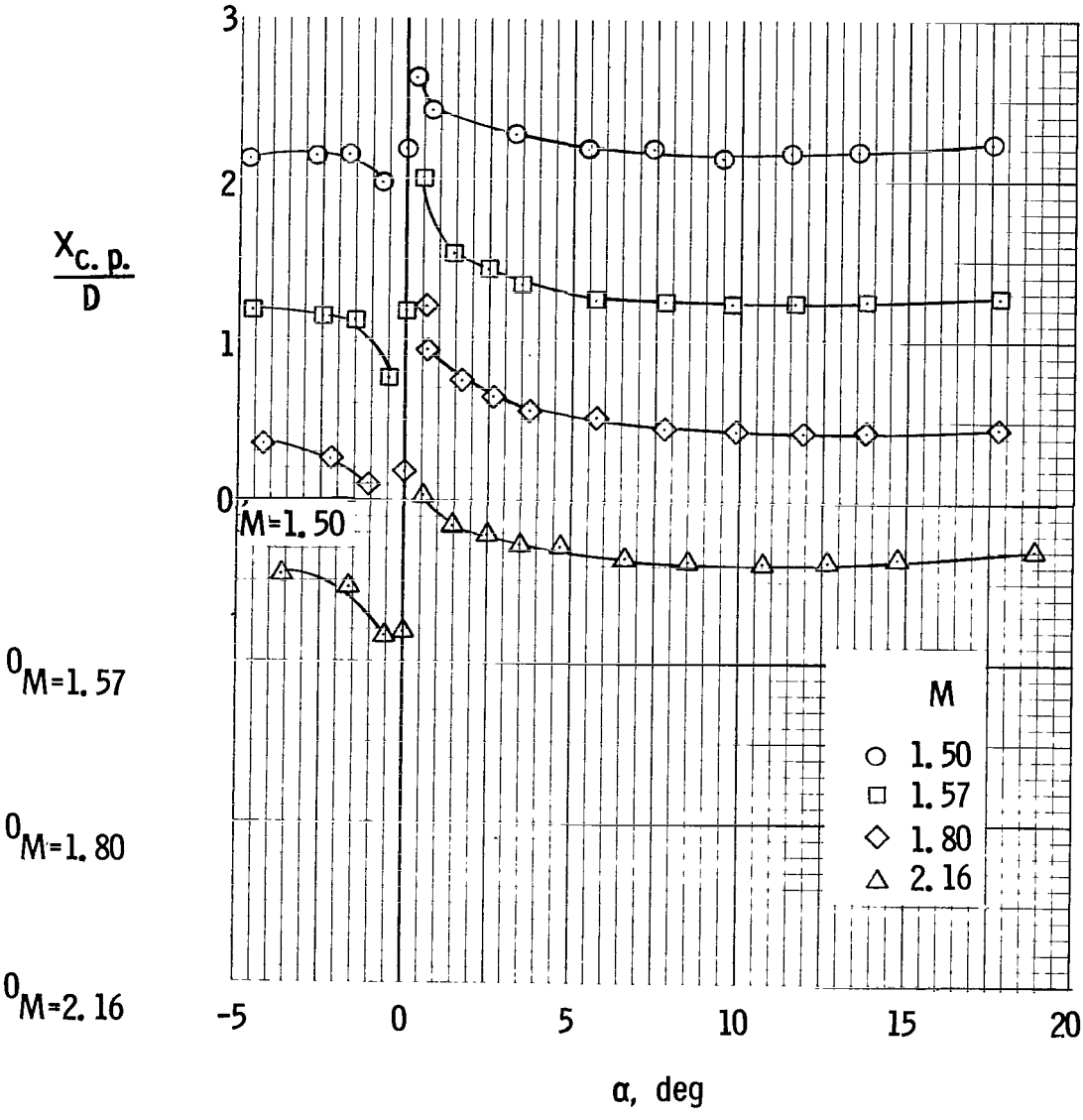

(1) Supersonic center of pressure.

Figure 5. - Concluded.

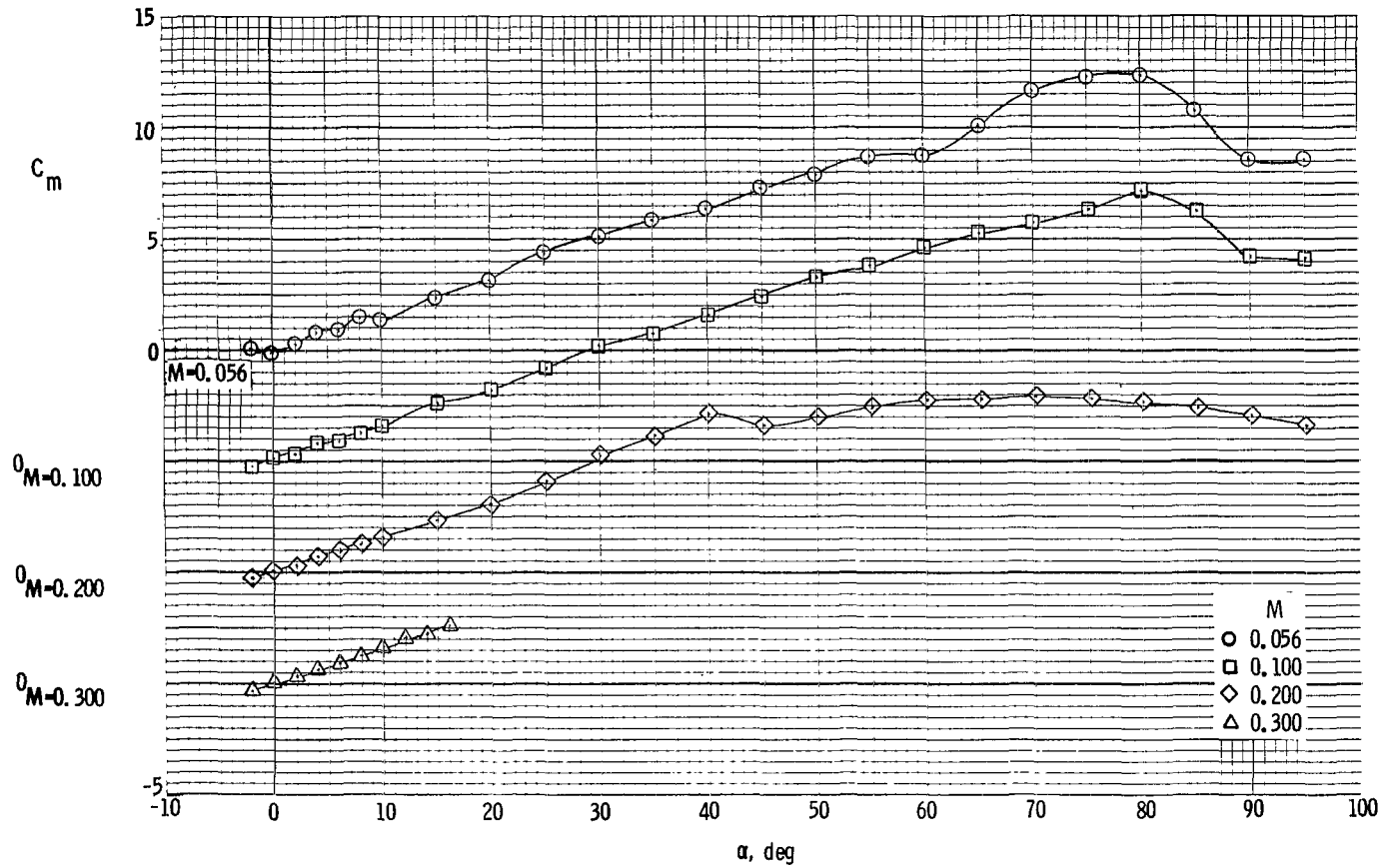

(a) Pitching-moment coefficient.

Figure 6.- Aerodynamic characteristics of configuration II with large fins and medium service module at Mach numbers from 0.056 to 0.30.

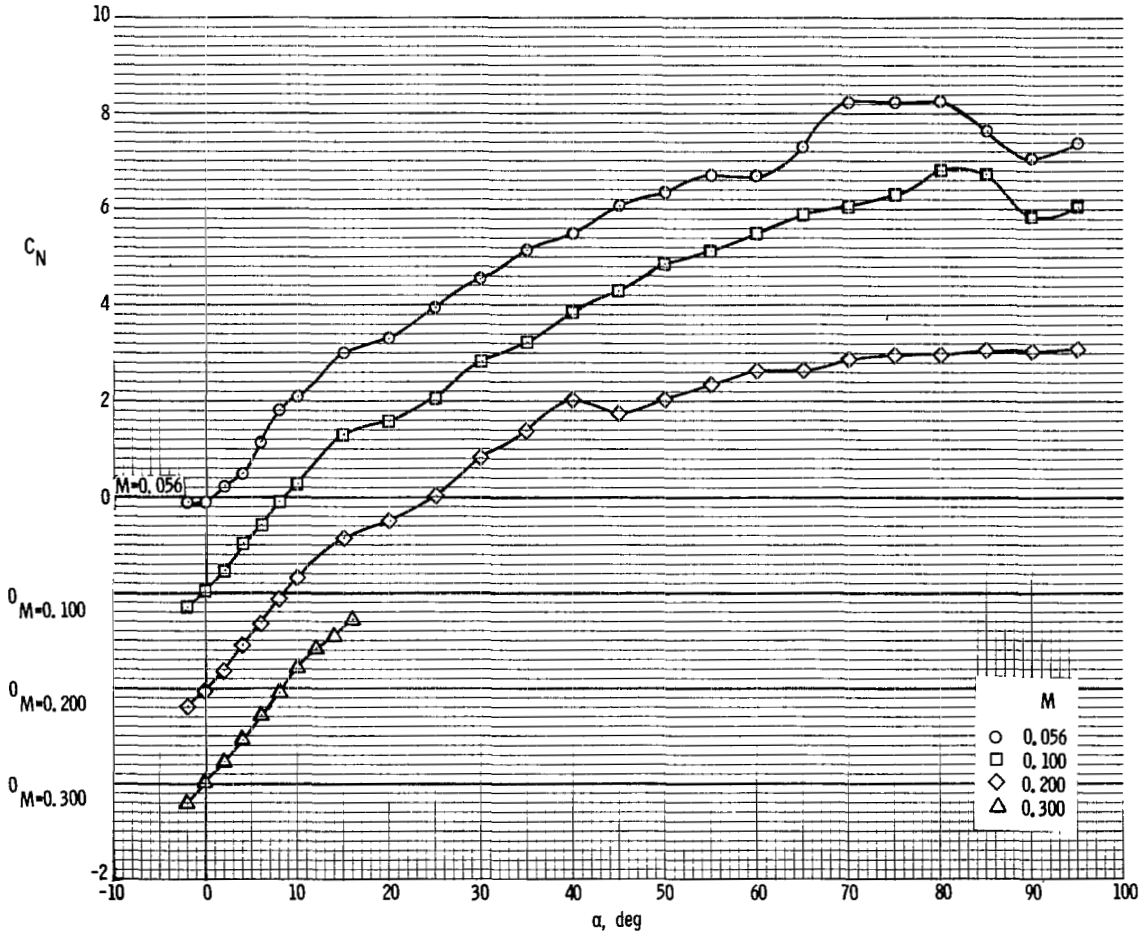

(b) Normal-force coefficient.

Figure 6. - Continued.

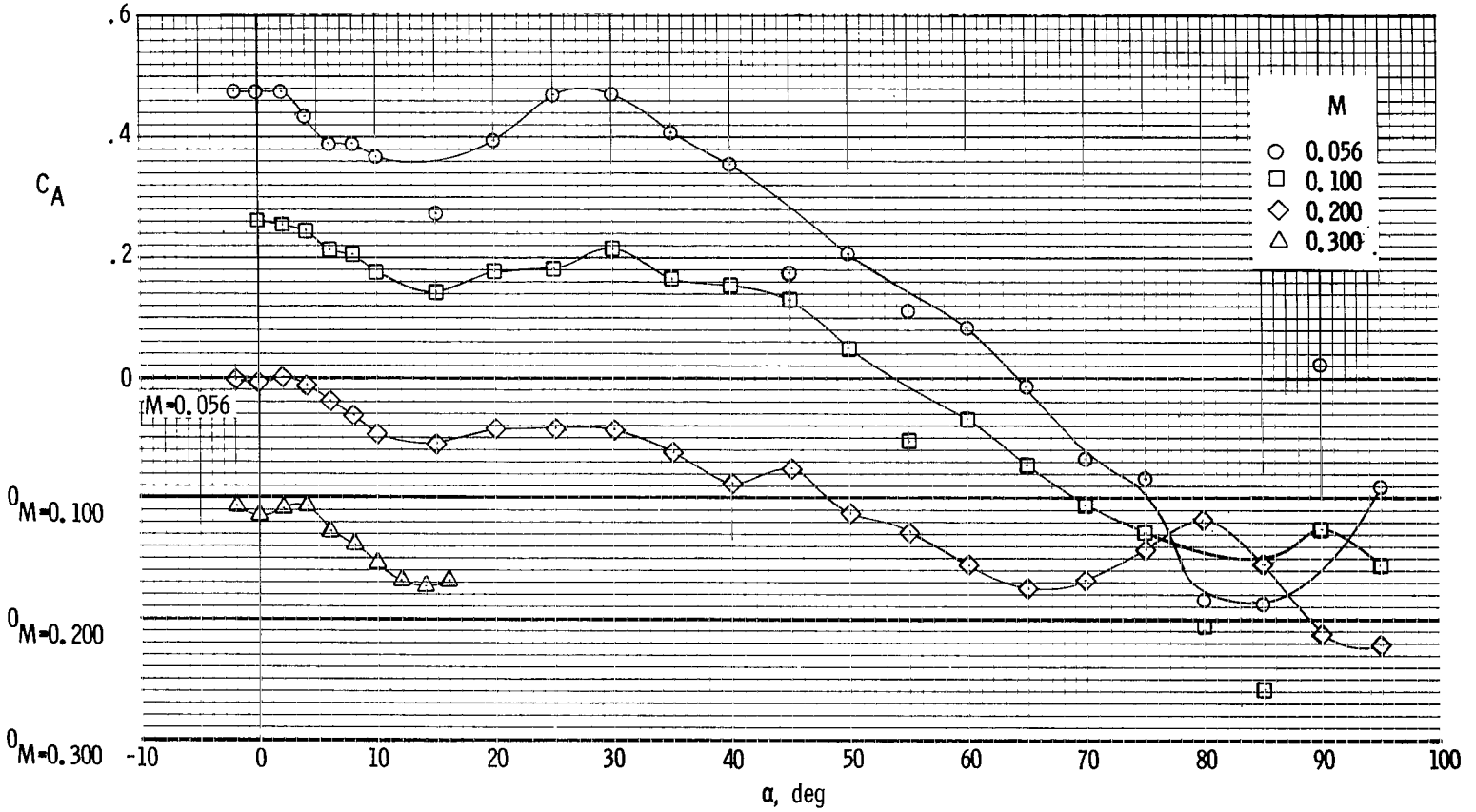

(c) Axial-force coefficient.

Figure 6.- Continued.

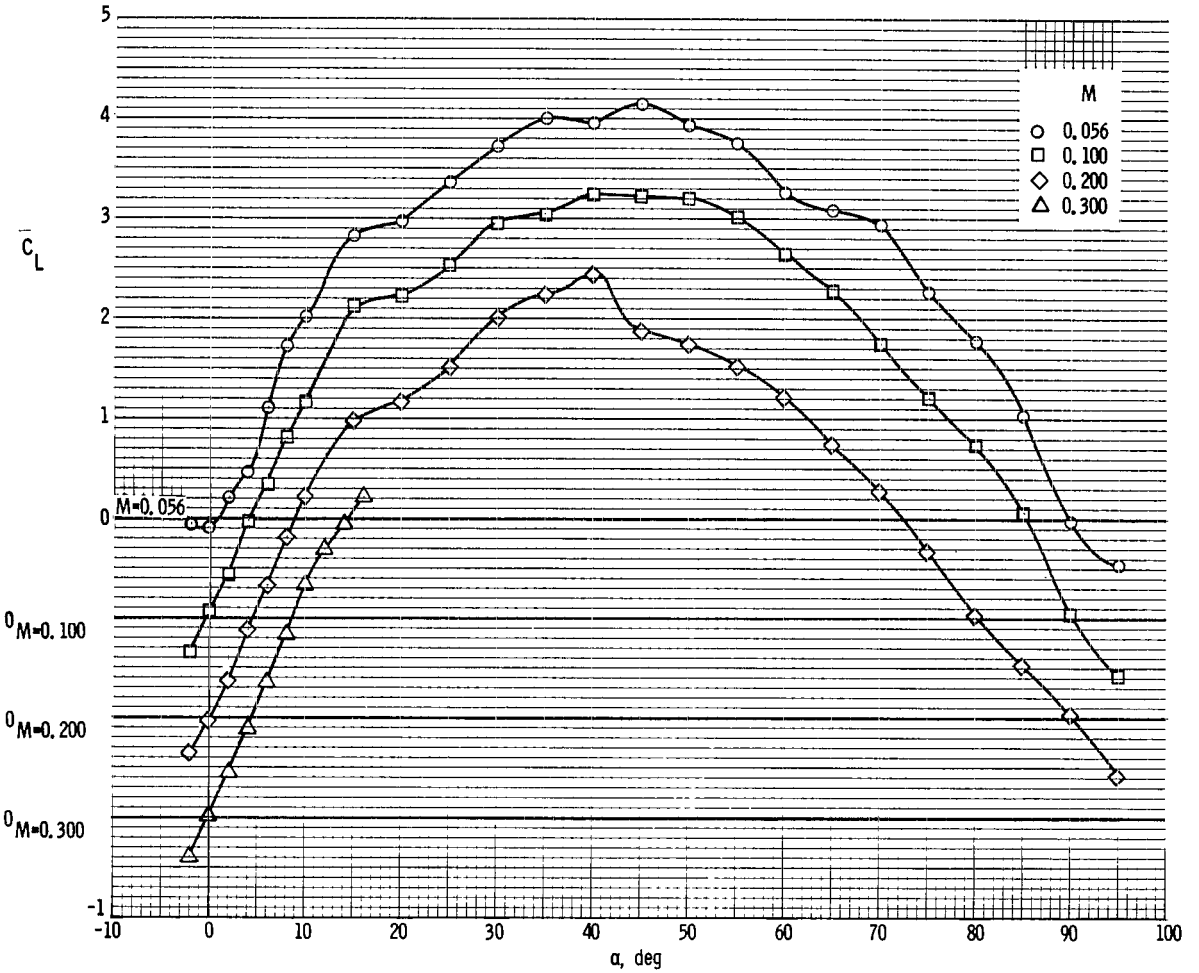

(d) Lift coefficient.

Figure 6.- Continued.

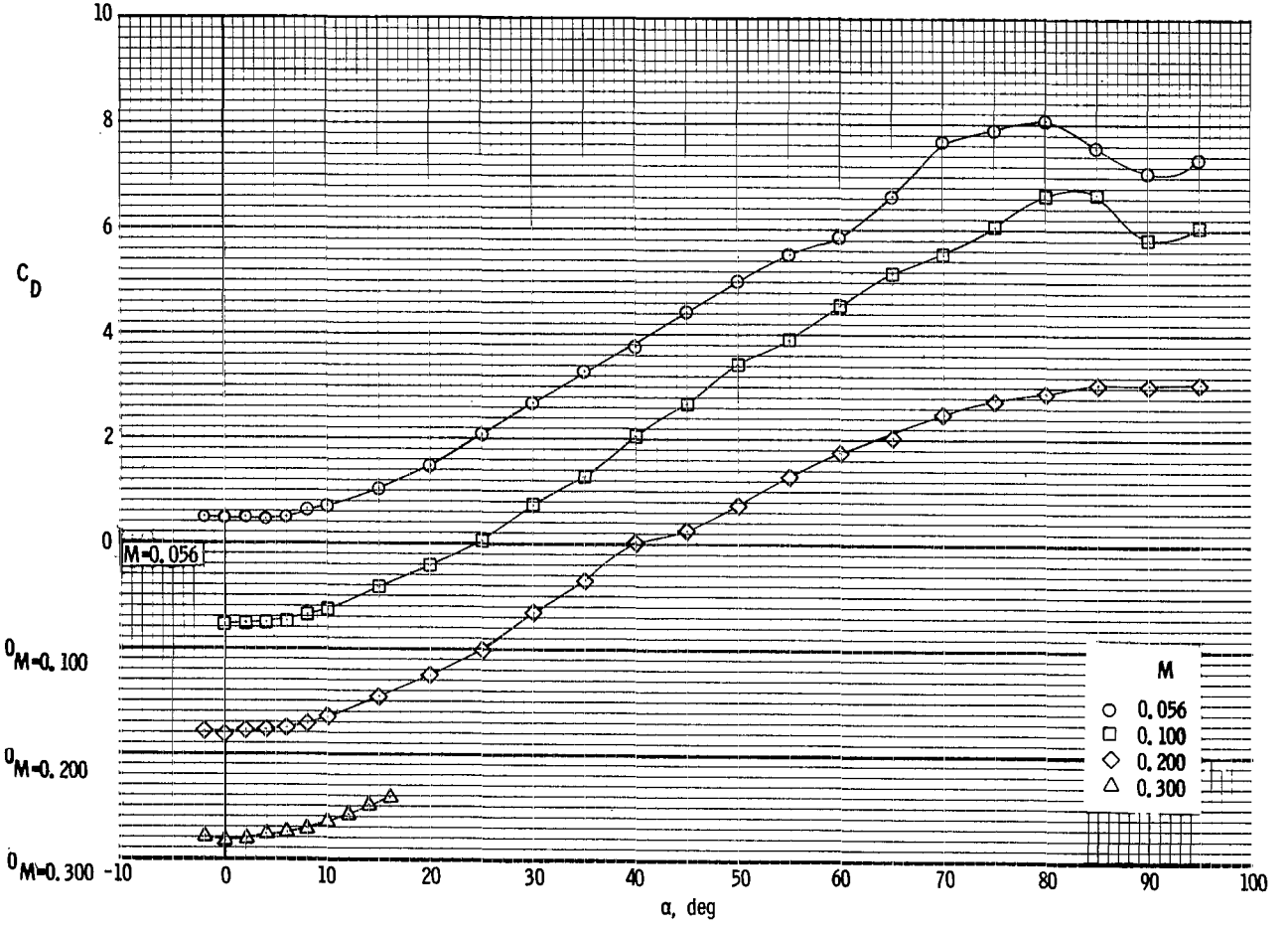

(e) Drag coefficient.

Figure 6. - Continued.

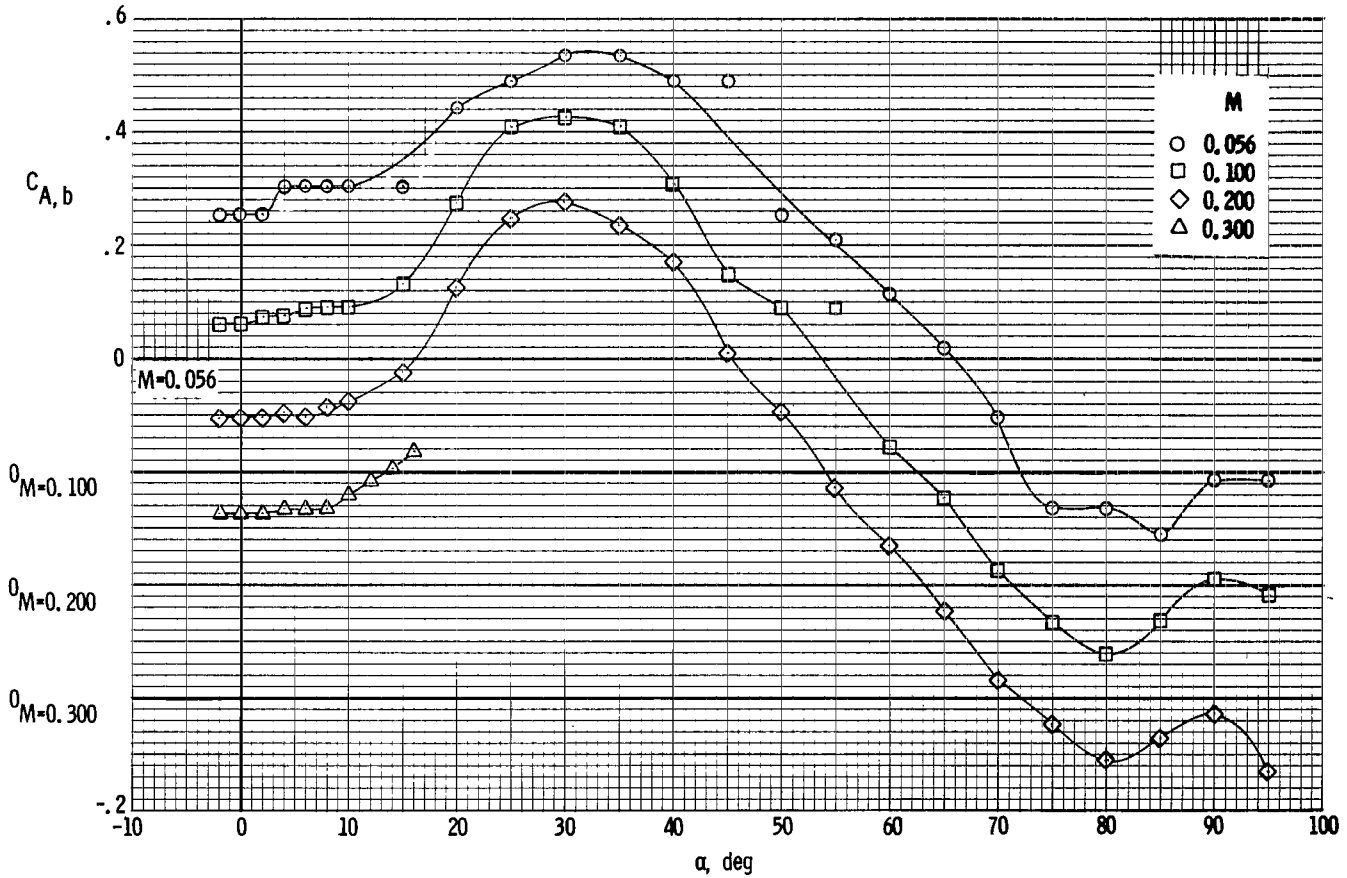

(f) Base axial-force coefficient.

Figure 6.- Concluded.

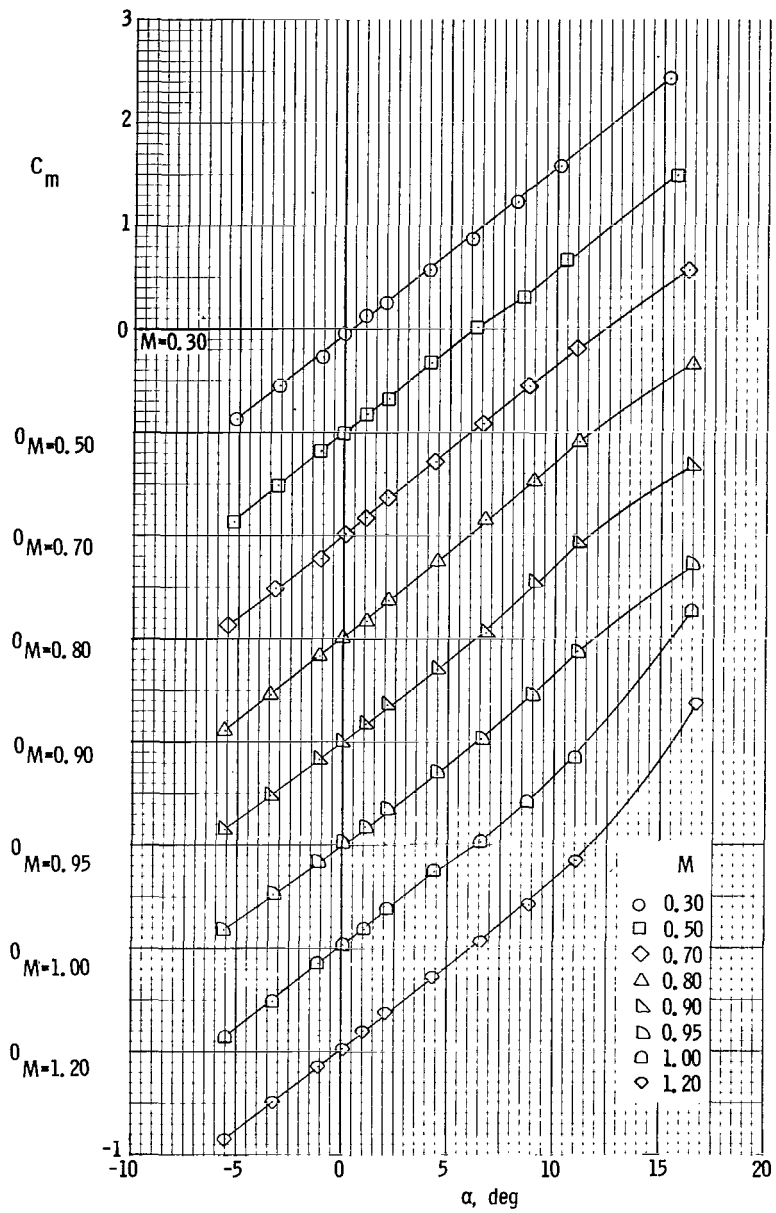

(a) Pitching-moment coefficient.

Figure 7.- Aerodynamic characteristics of configuration II with large fins and medium service module at Mach numbers from 0.30 to 1.20.

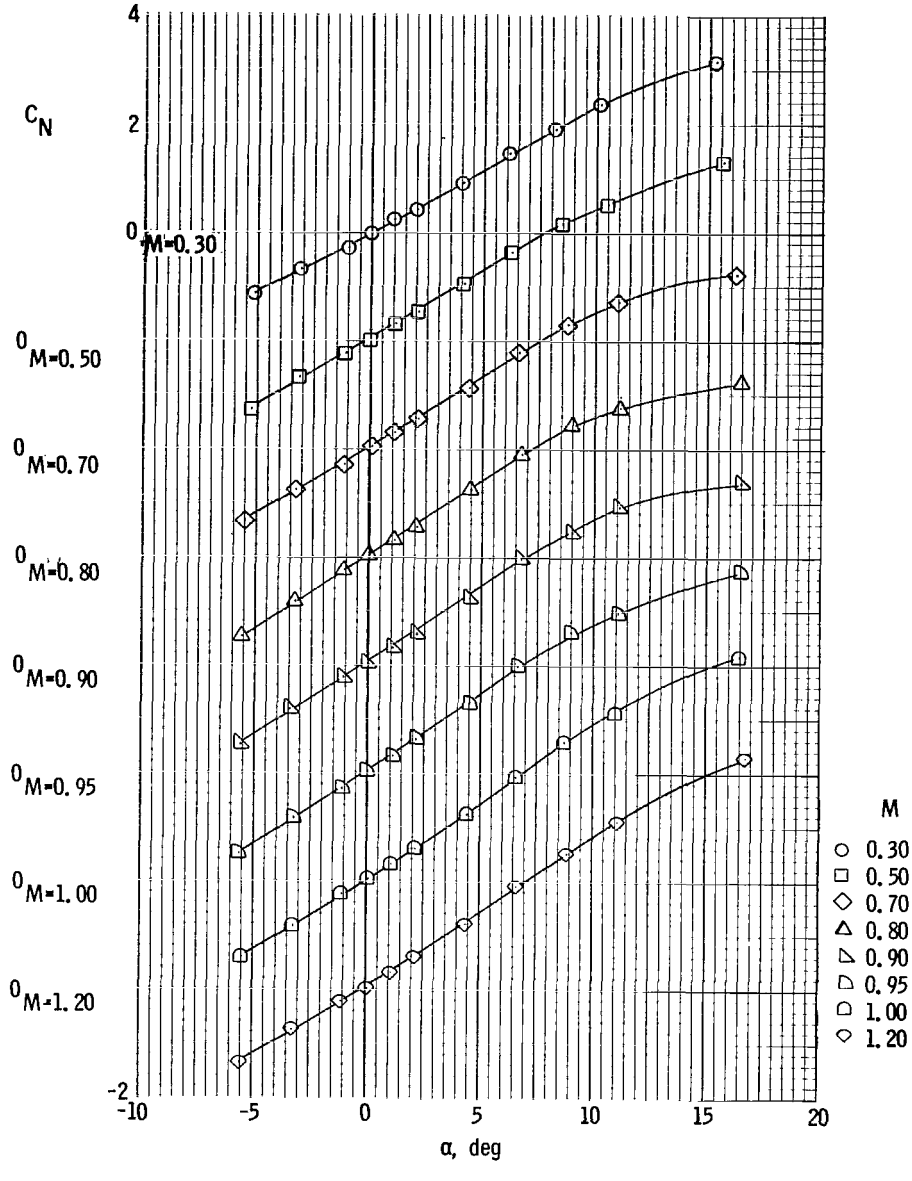

(b) Normal-force coefficient.

Figure 7.- Continued.

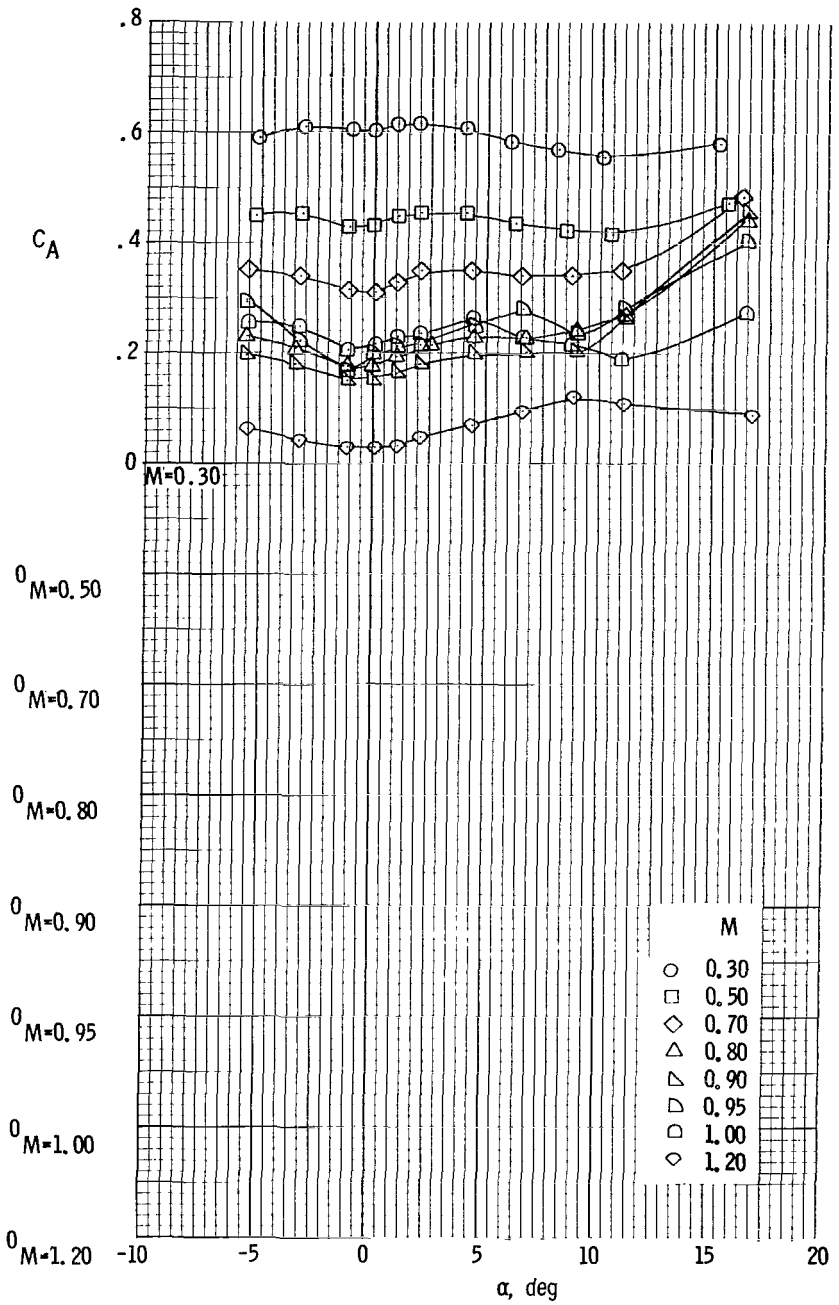

(c) Axial-force coefficient.

Figure 7. - Continued.

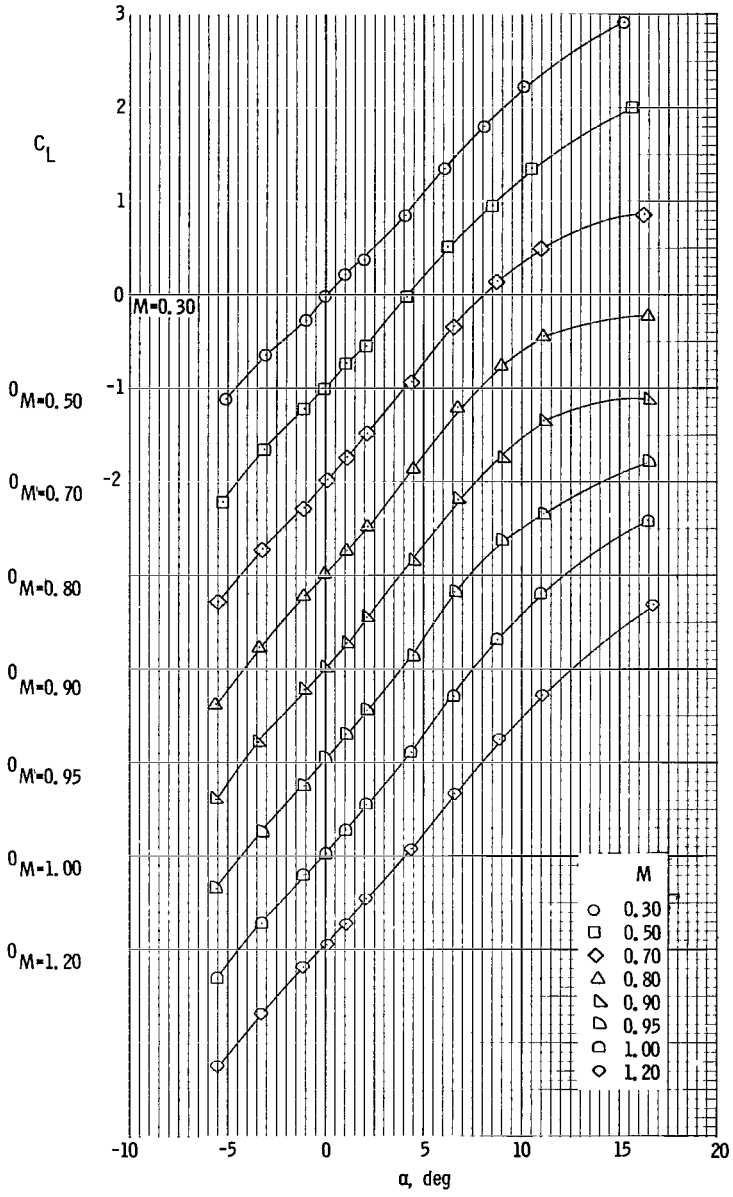

(d) Lift coefficient.

Figure 7. - Continued.

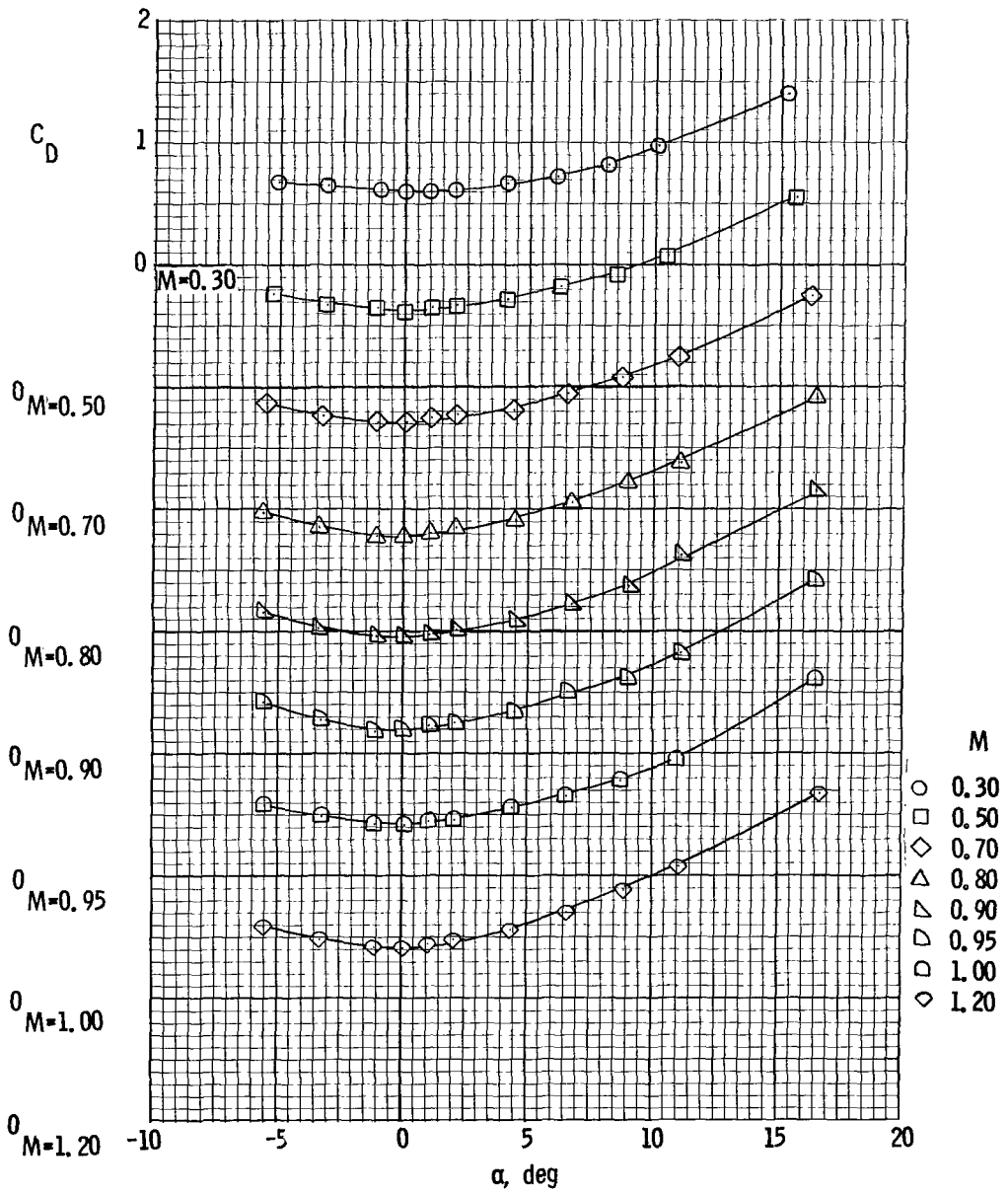

(e) Drag coefficient.

Figure 7.- Continued.

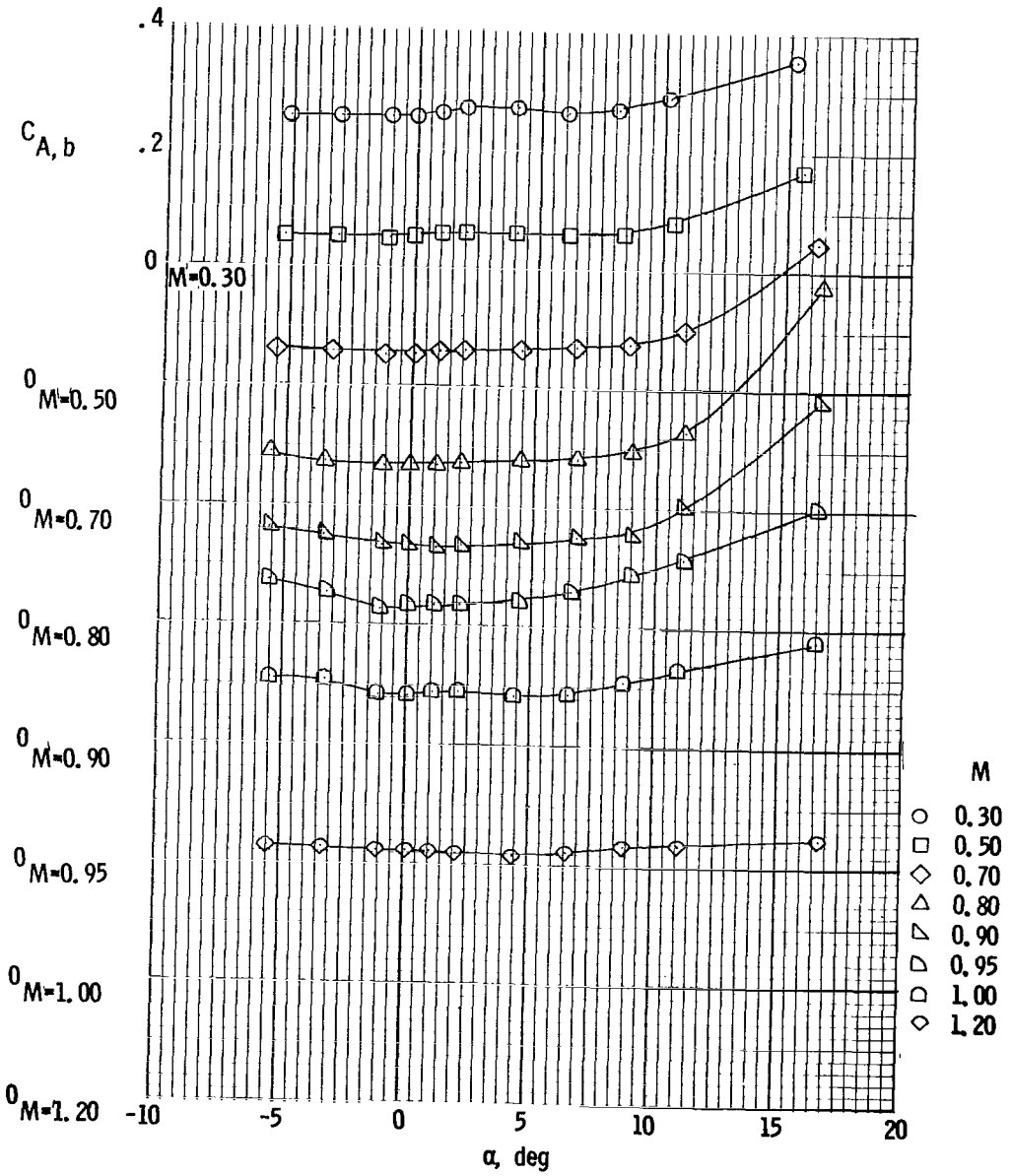

(f) Base axial-force coefficient.

Figure 7. - Concluded.

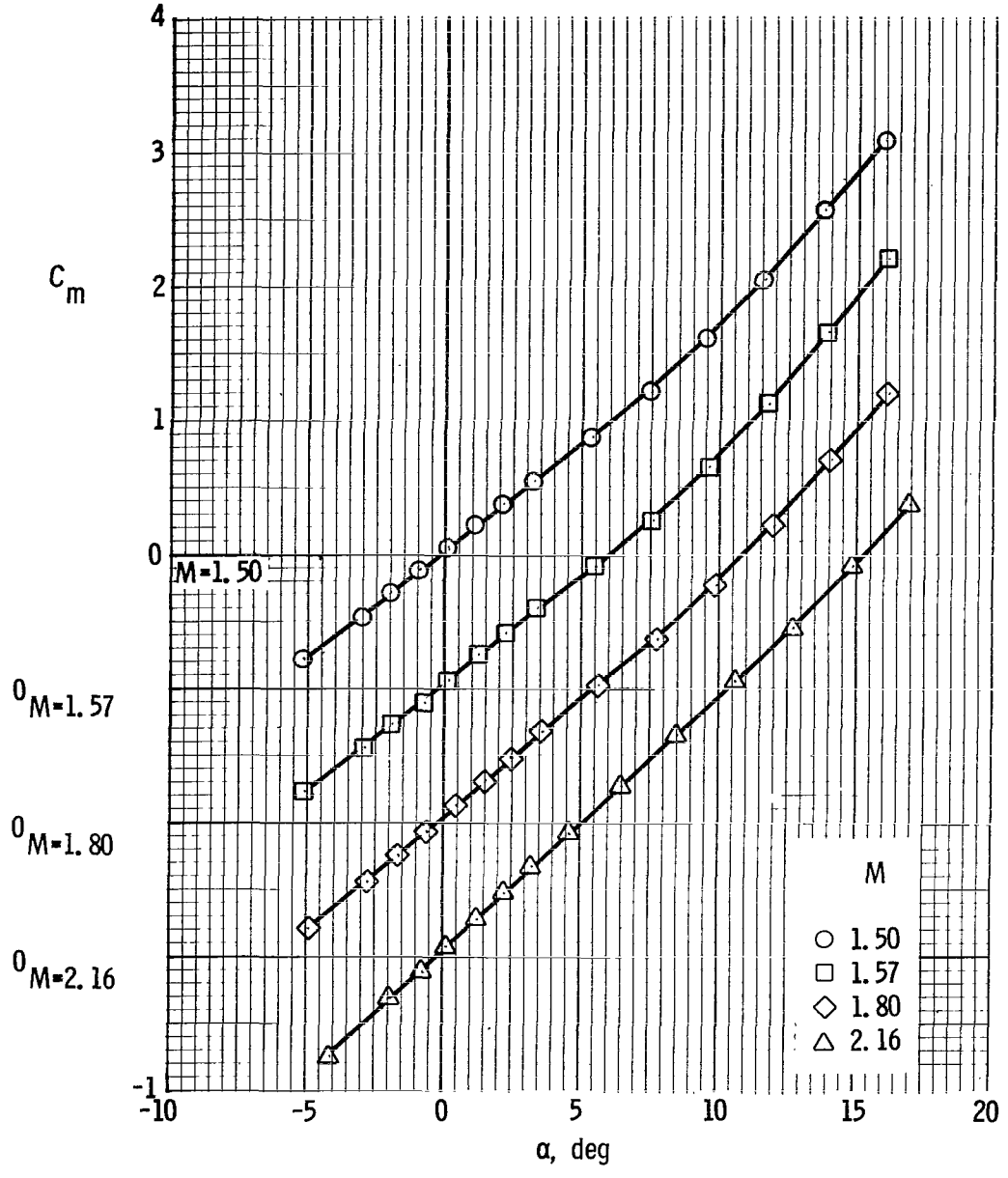

(a) Pitching-moment coefficient.

Figure 8. - Aerodynamic characteristics of configuration II with large fins and medium service module at Mach numbers from 1.50 to 2.16.

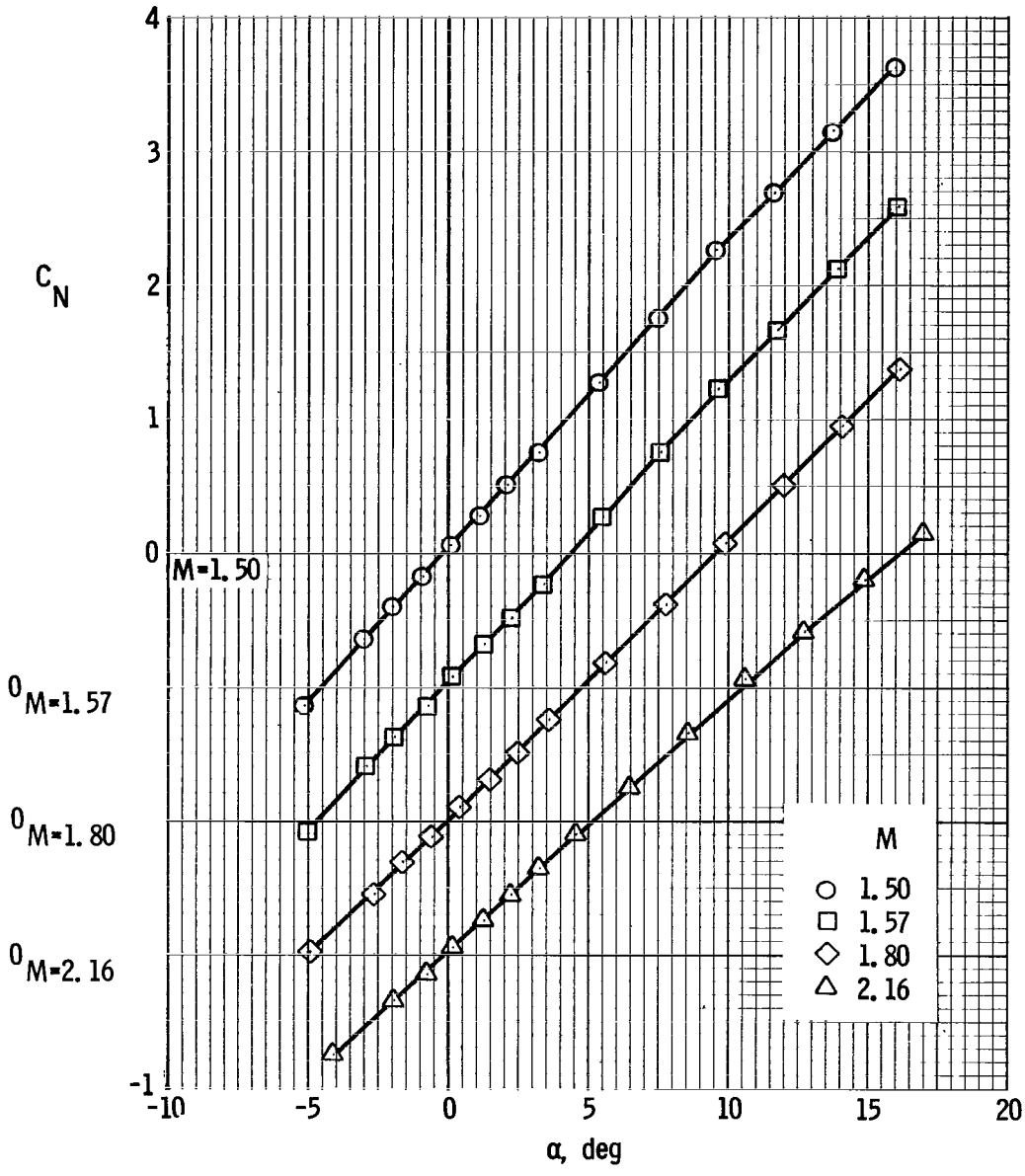

(b) Normal-force coefficient.

Figure 8.- Continued.

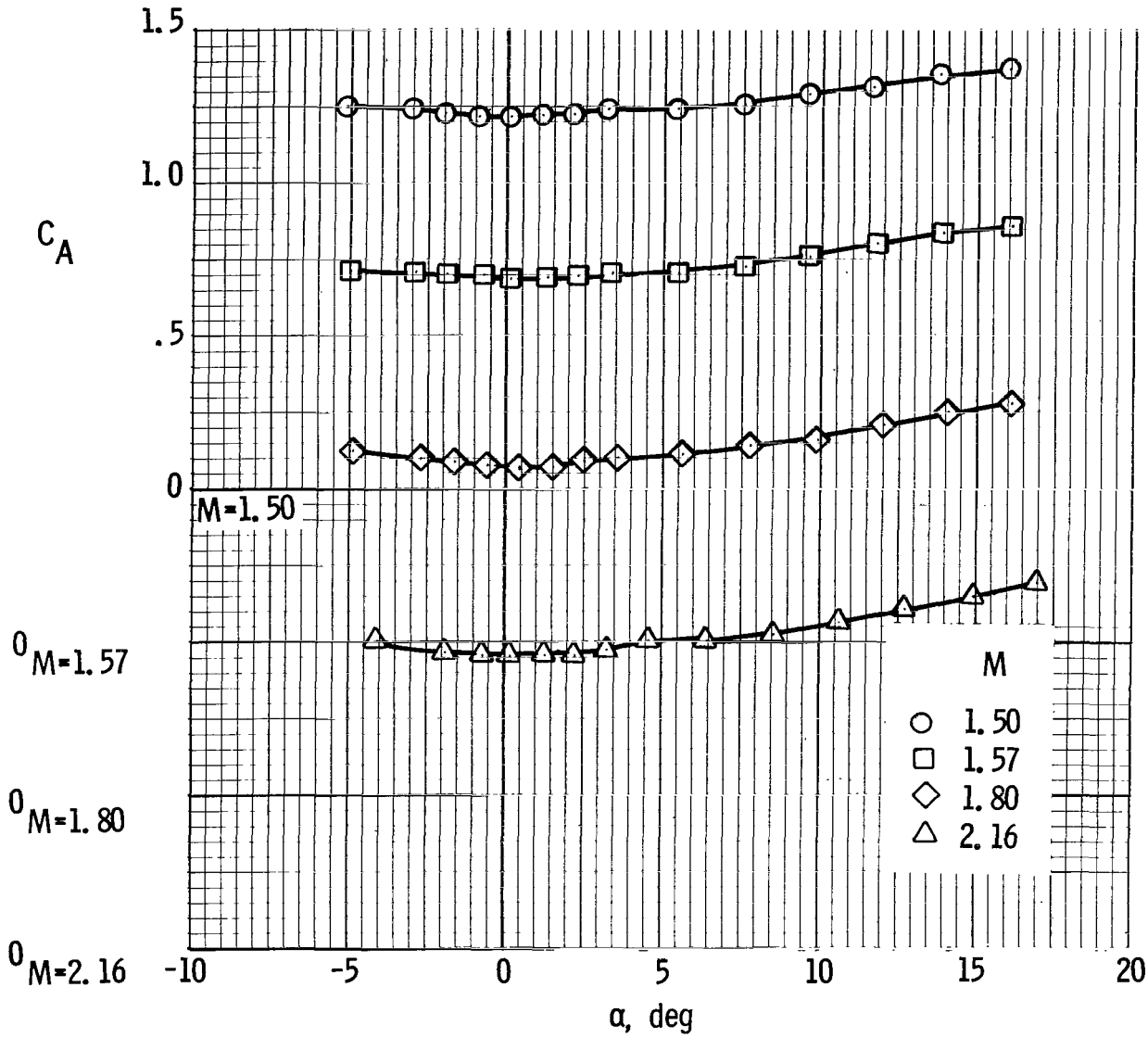

(c) Axial-force coefficient.

Figure 8. - Continued.

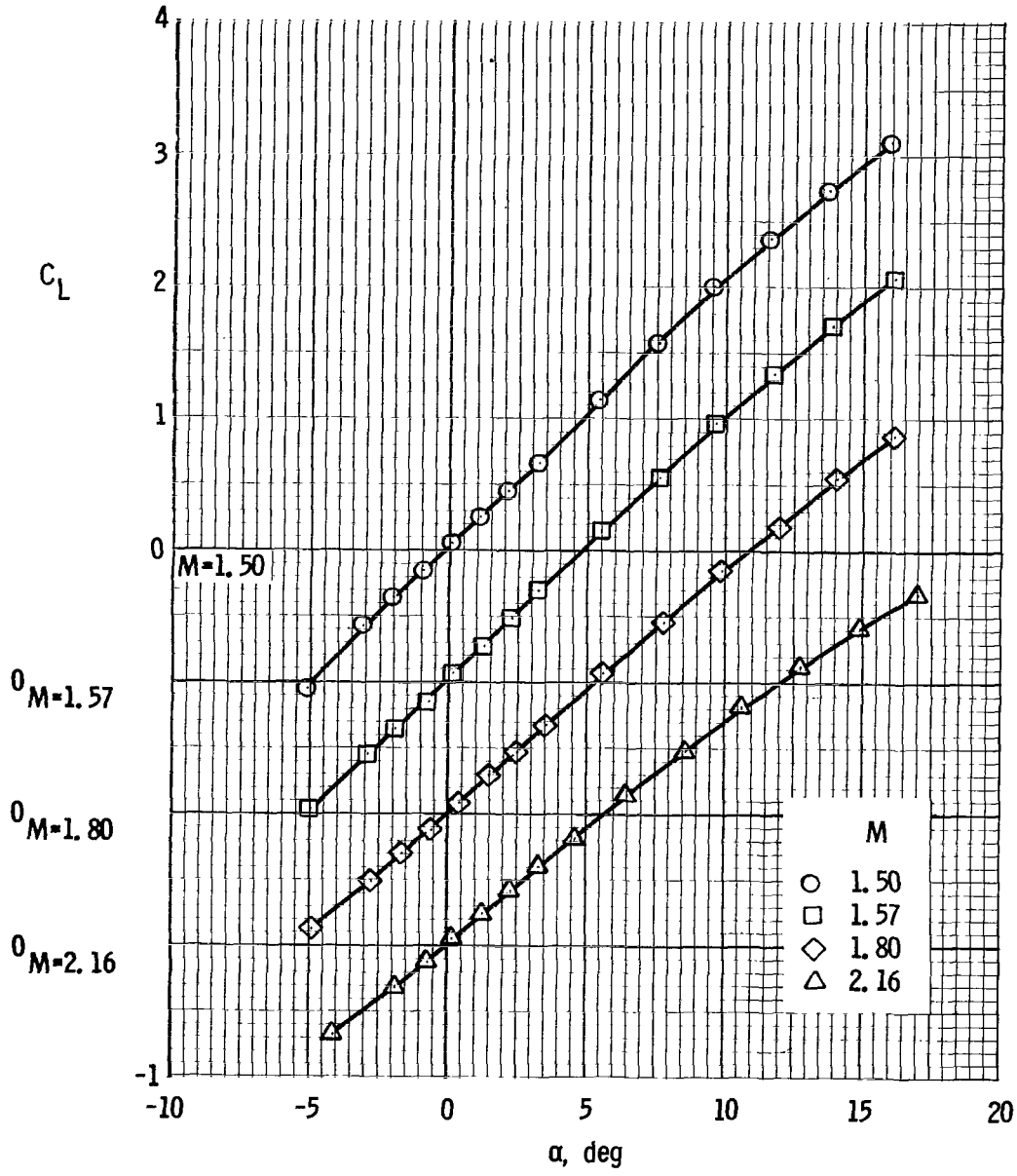

(d) Lift coefficient.

Figure 8.- Continued.

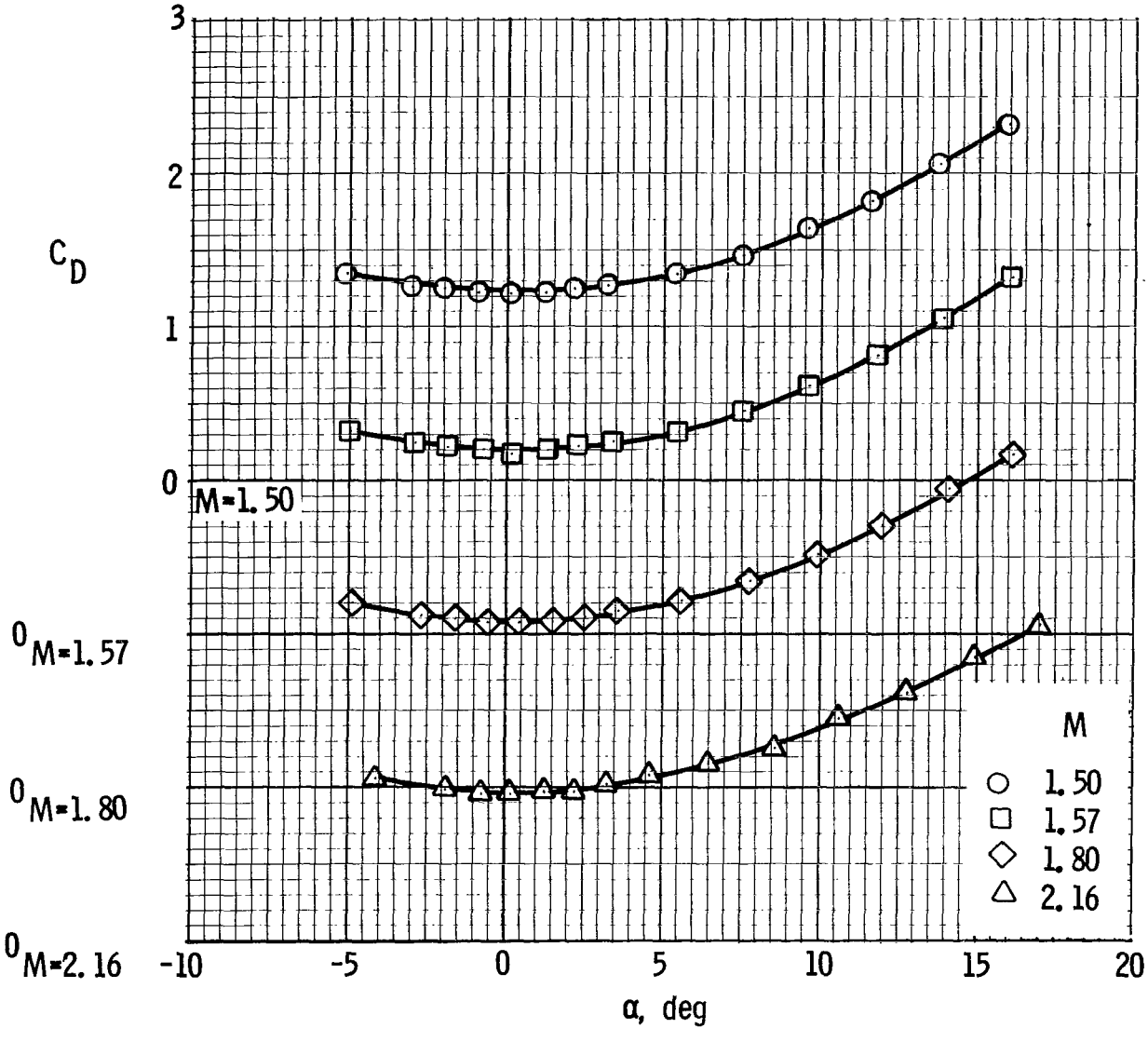

(e) Drag coefficient.

Figure 8. - Continued.

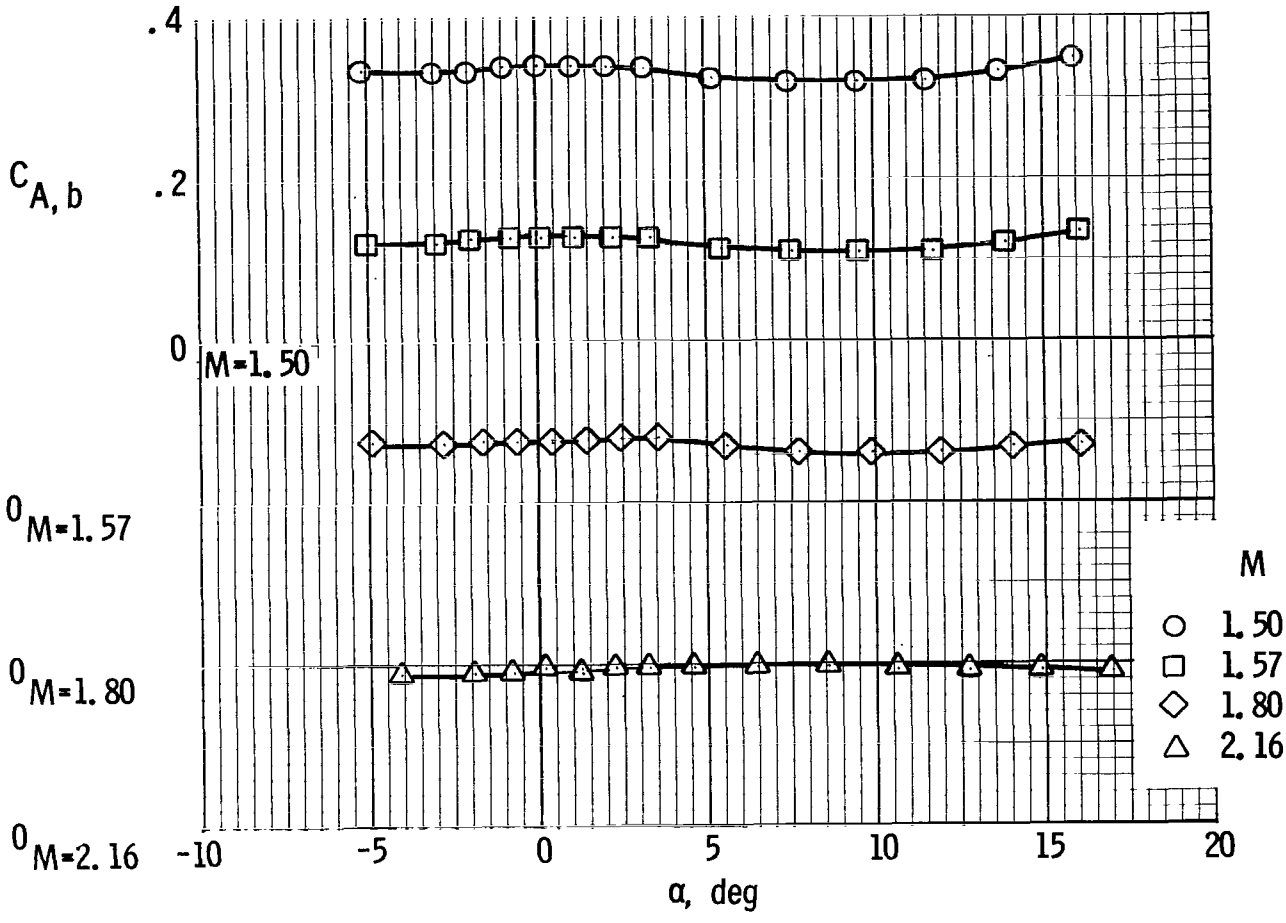

(f) Base axial-force coefficient.

Figure 8. - Concluded.

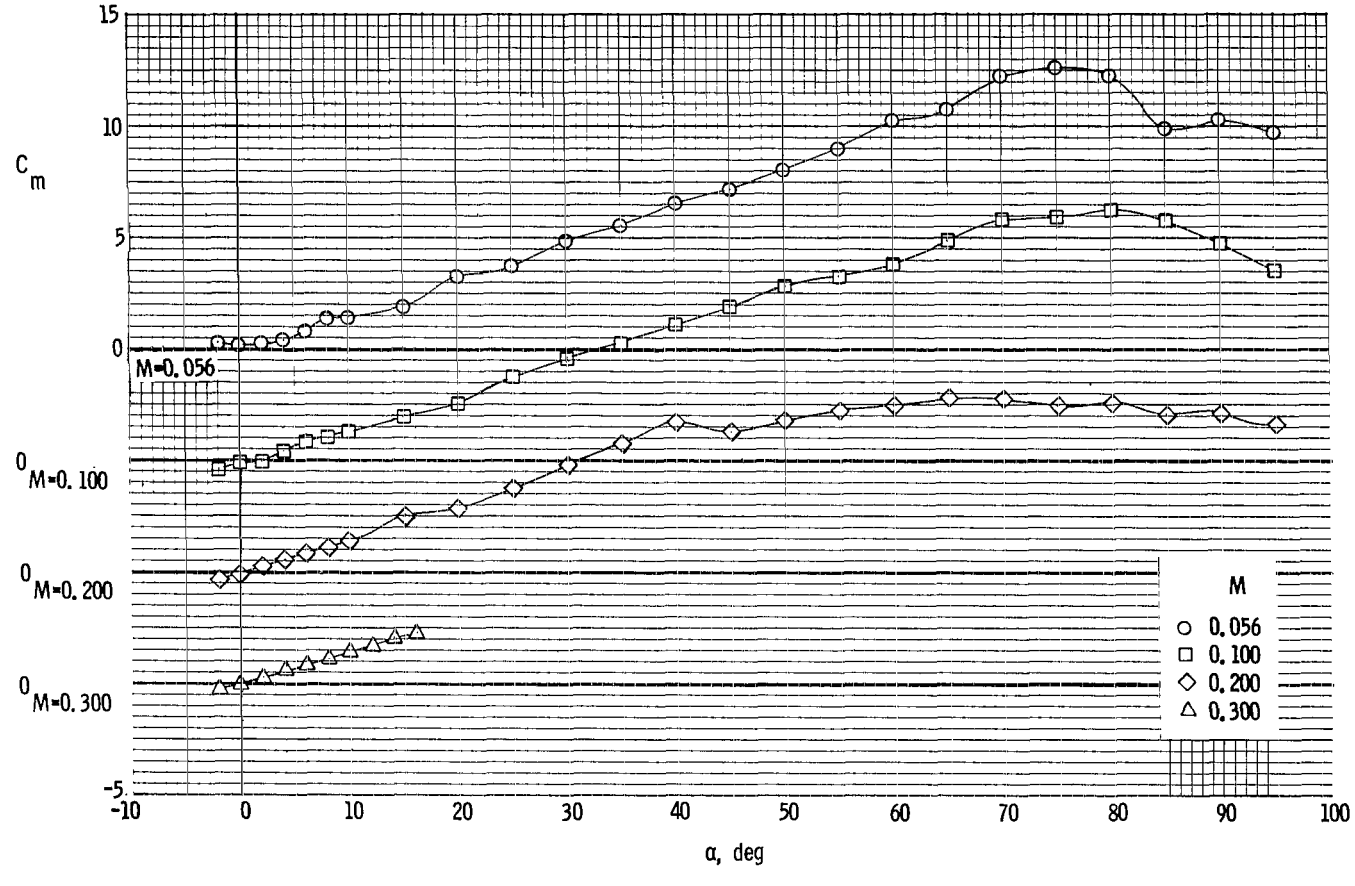

(a) Pitching-moment coefficient.

Figure 9. - Aerodynamic characteristics of configuration II with small fins and medium service module at Mach numbers from 0.056 to 0.30.

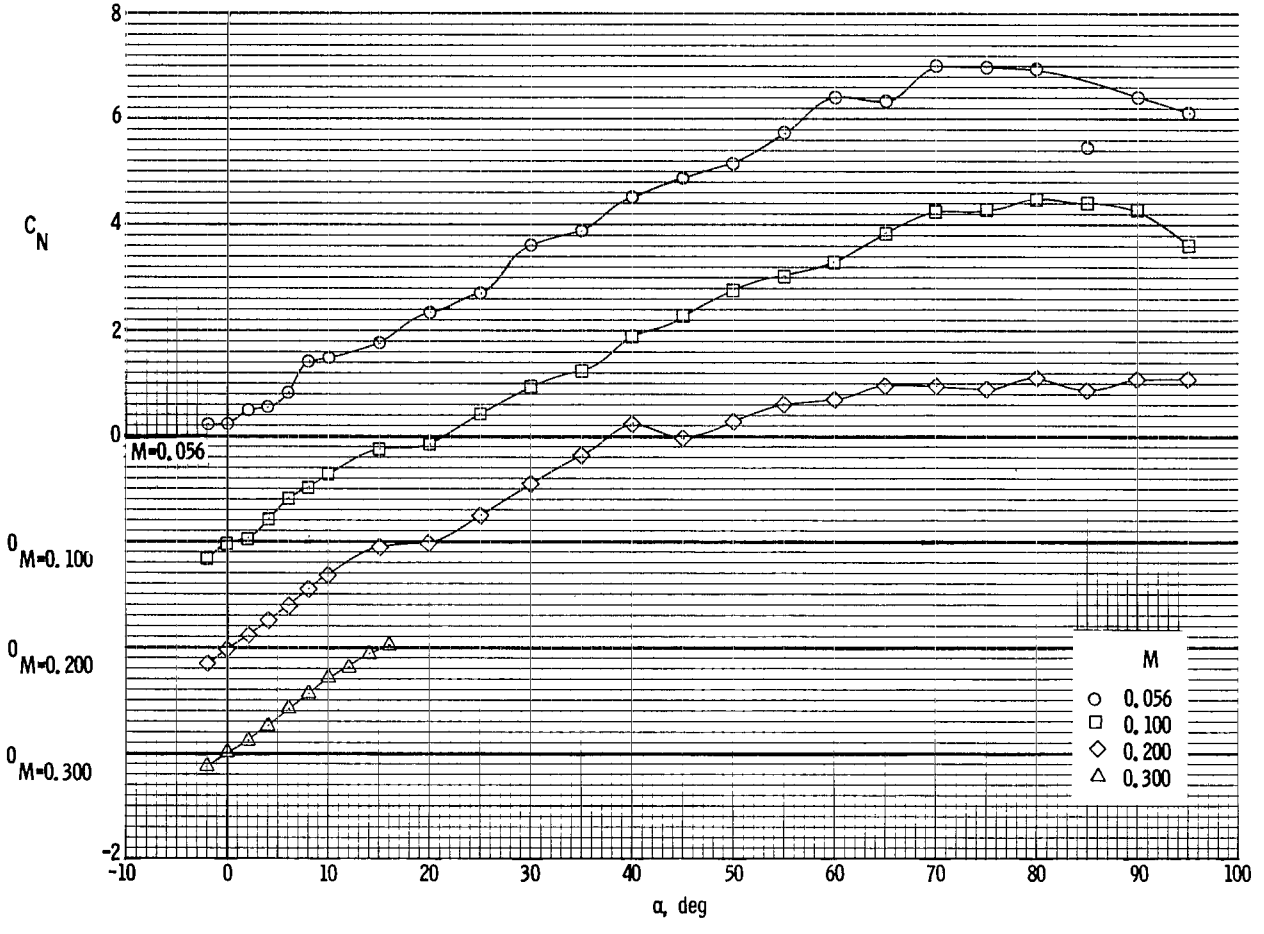

(b) Normal-force coefficient.

Figure 9. - Continued.

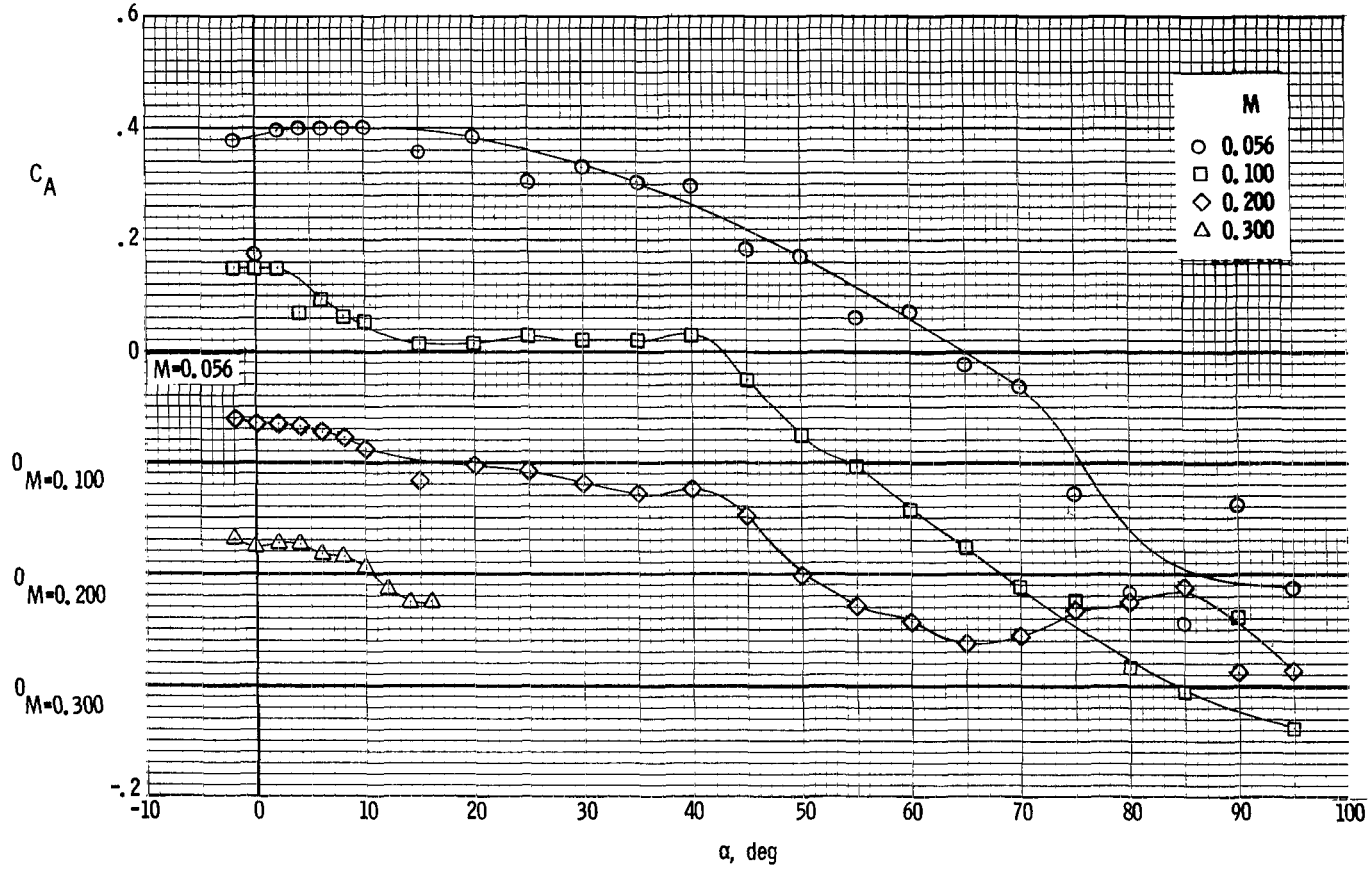

(c) Axial-force coefficient.

Figure 9. - Continued.

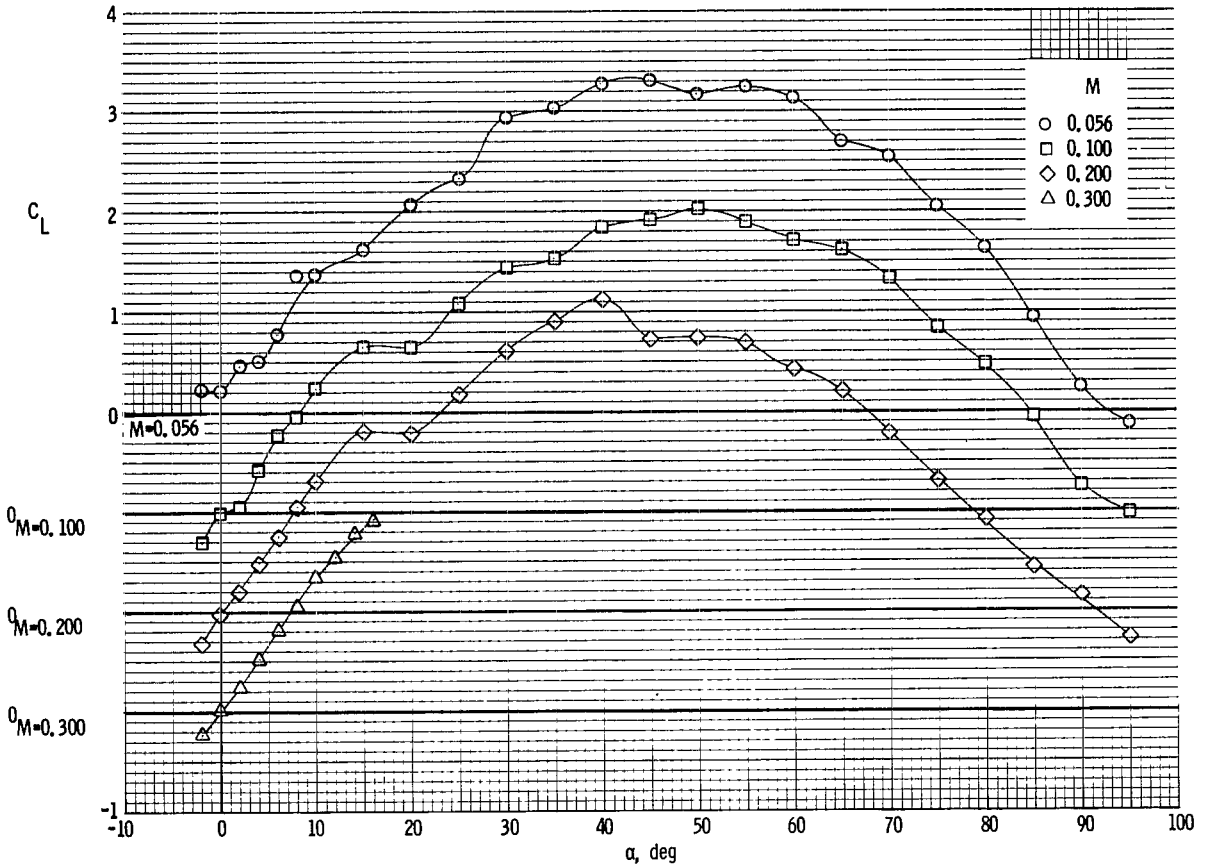

(d) Lift coefficient.

Figure 9. - Continued.

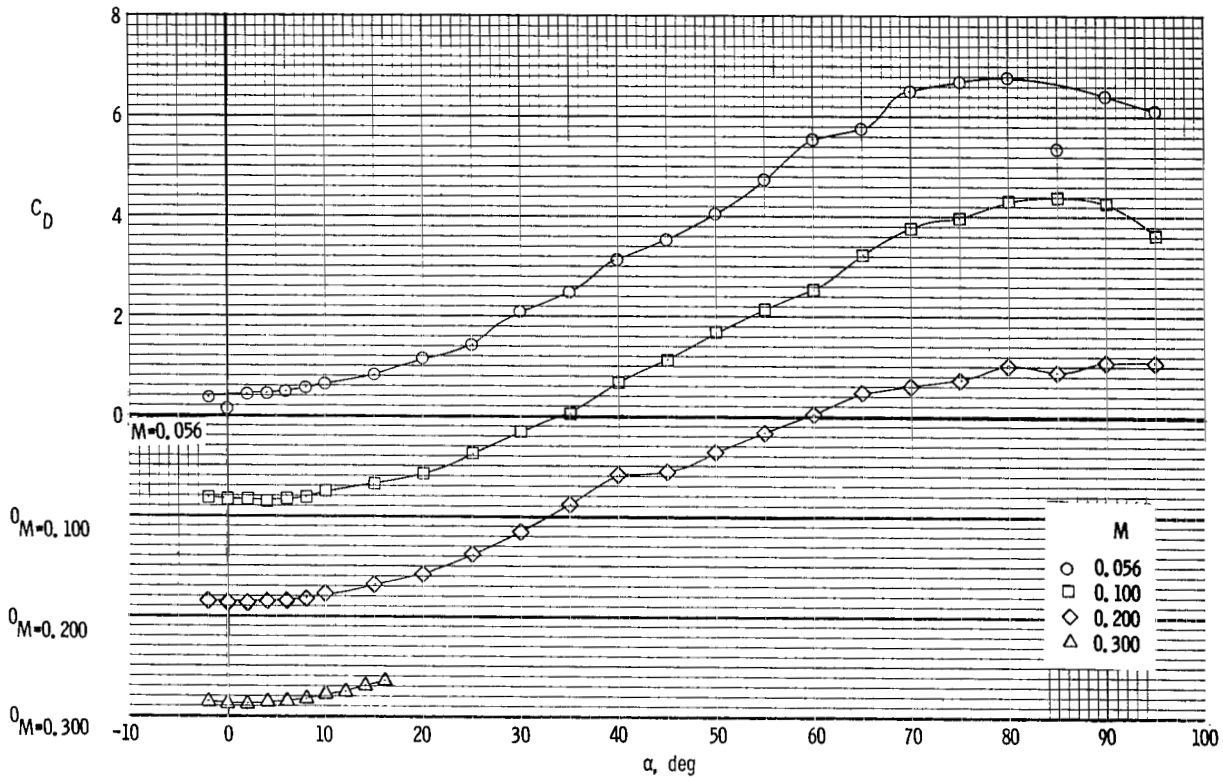

(e) Drag coefficient.

Figure 9. - Continued.

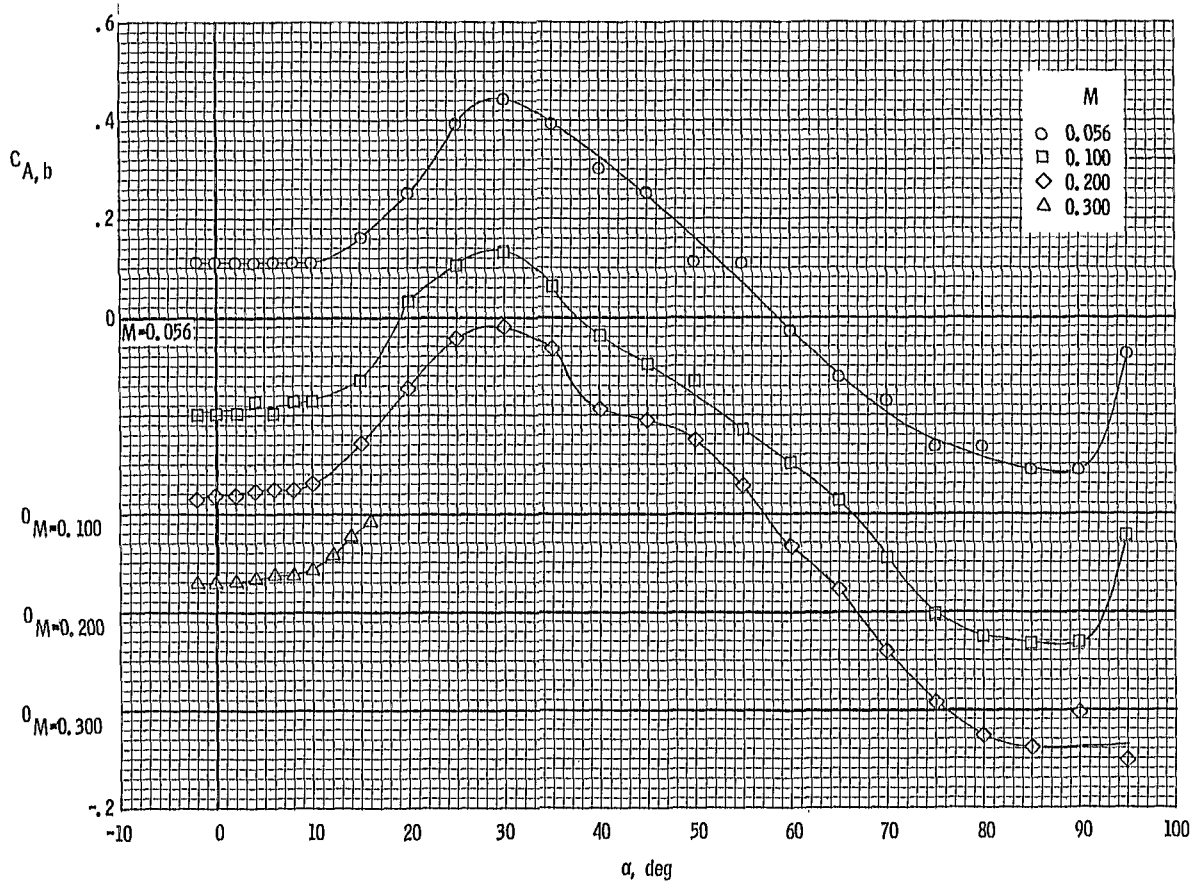

(f) Base axial-force coefficient.

Figure 9. - Concluded.

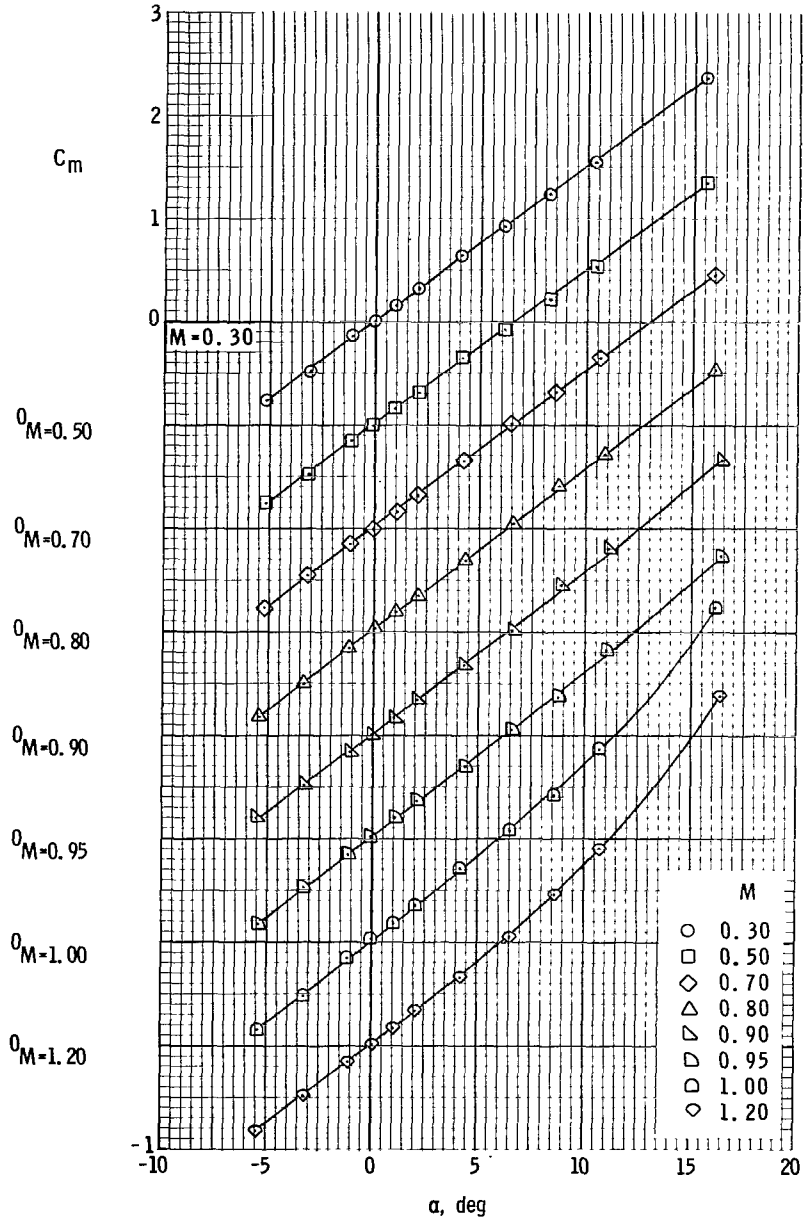

(a) Pitching-moment coefficient.

Figure 10. - Aerodynamic characteristics of configuration II with small fins and medium service module at Mach numbers from 0.30 to 1.20.

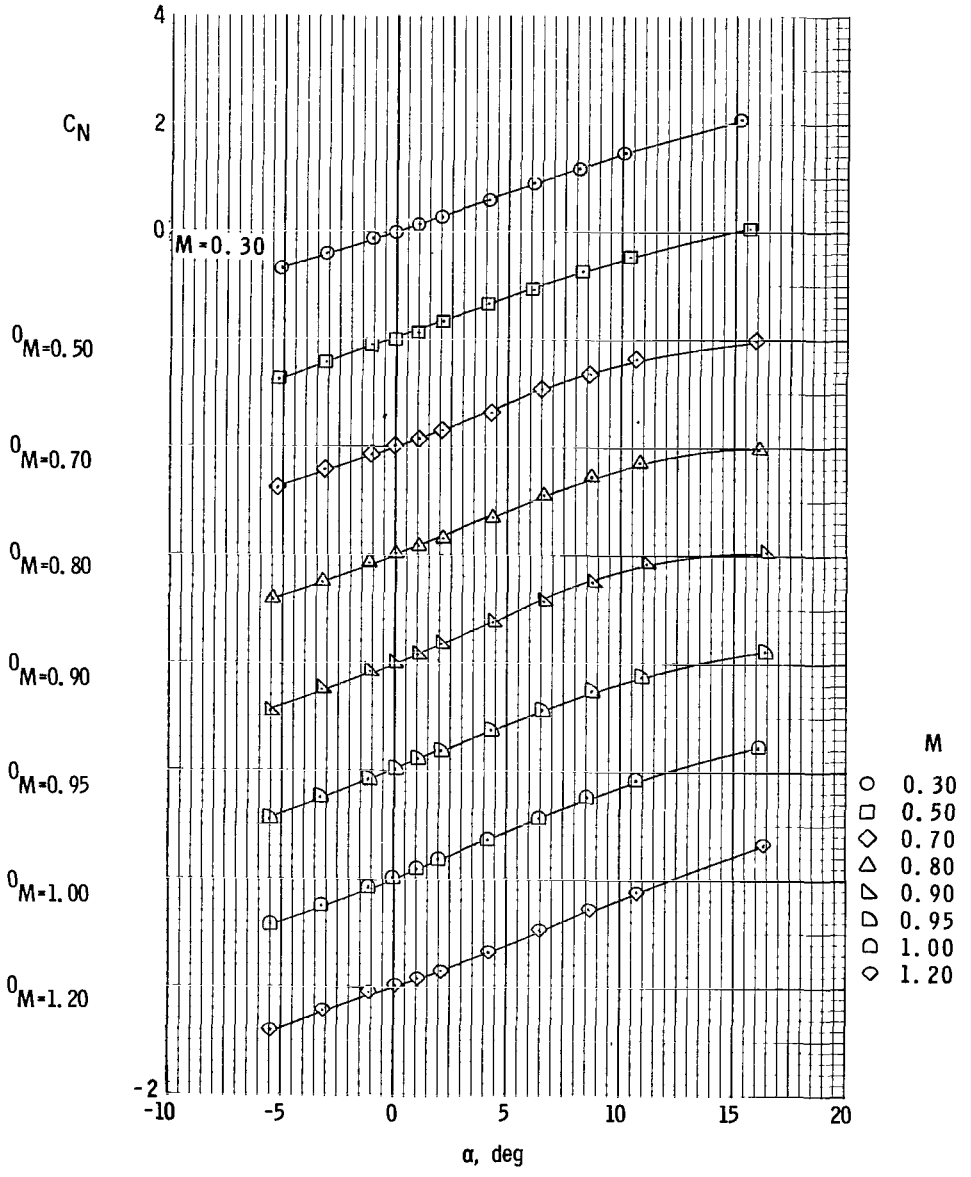

(b) Normal-force coefficient.

Figure 10. - Continued.

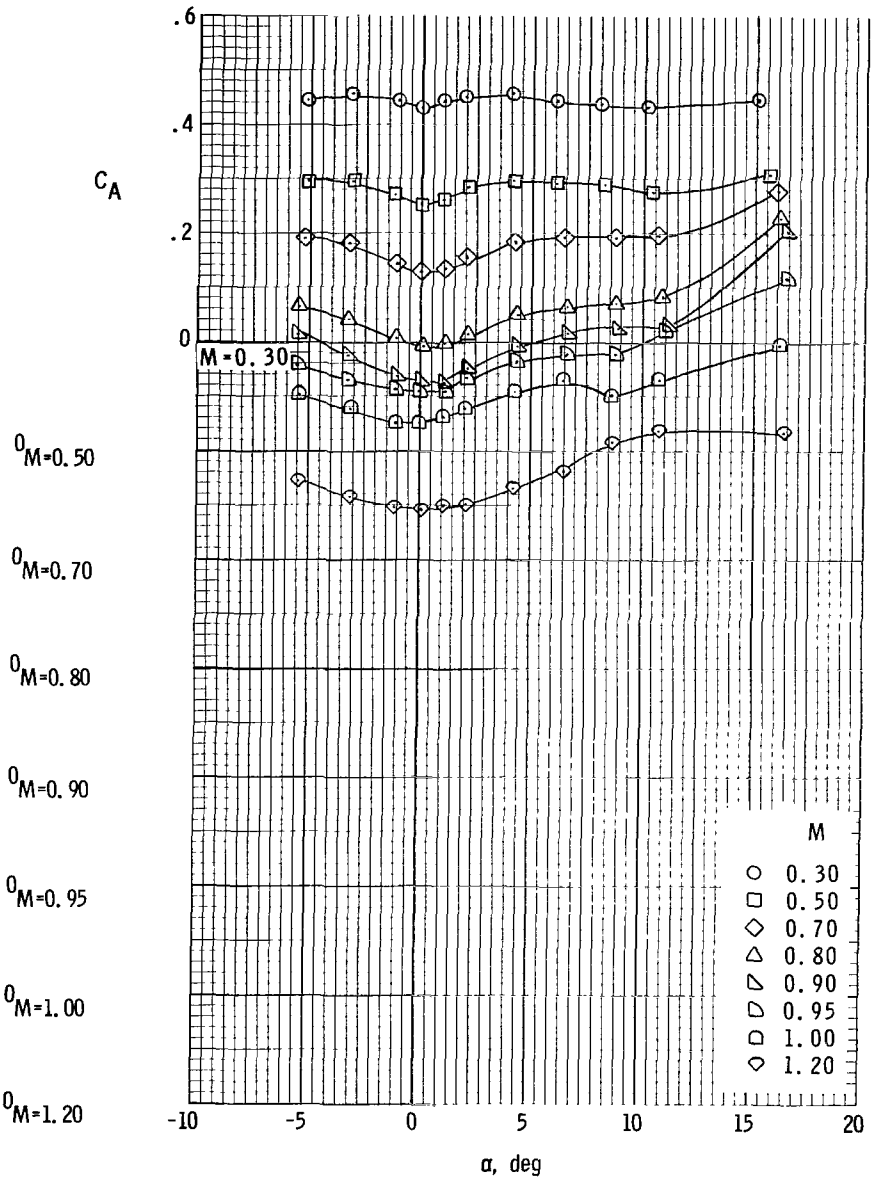

(c) Axial-force coefficient.

Figure 10. - Continued.

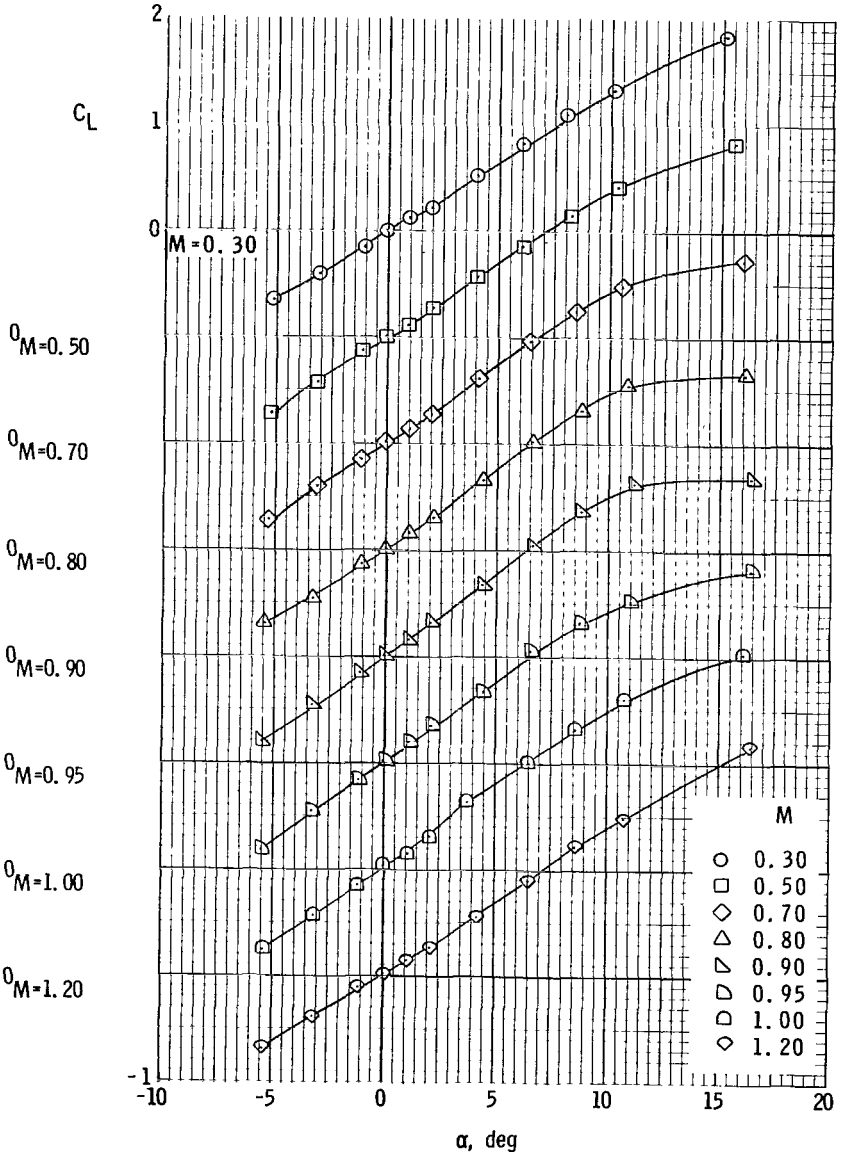

(d) Lift coefficient.

Figure 10. - Continued.

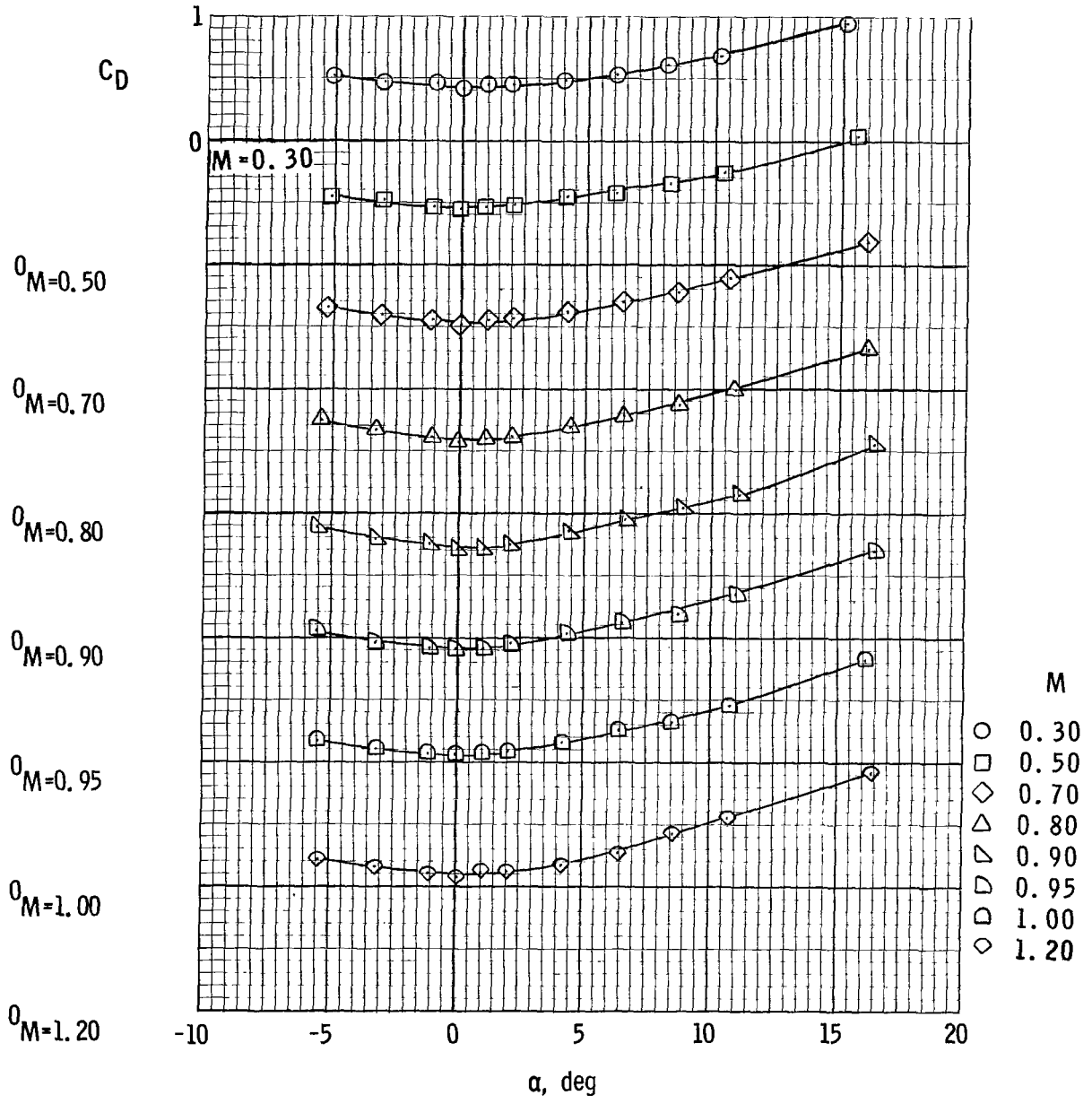

(e) Drag coefficient.

Figure 10. - Continued.

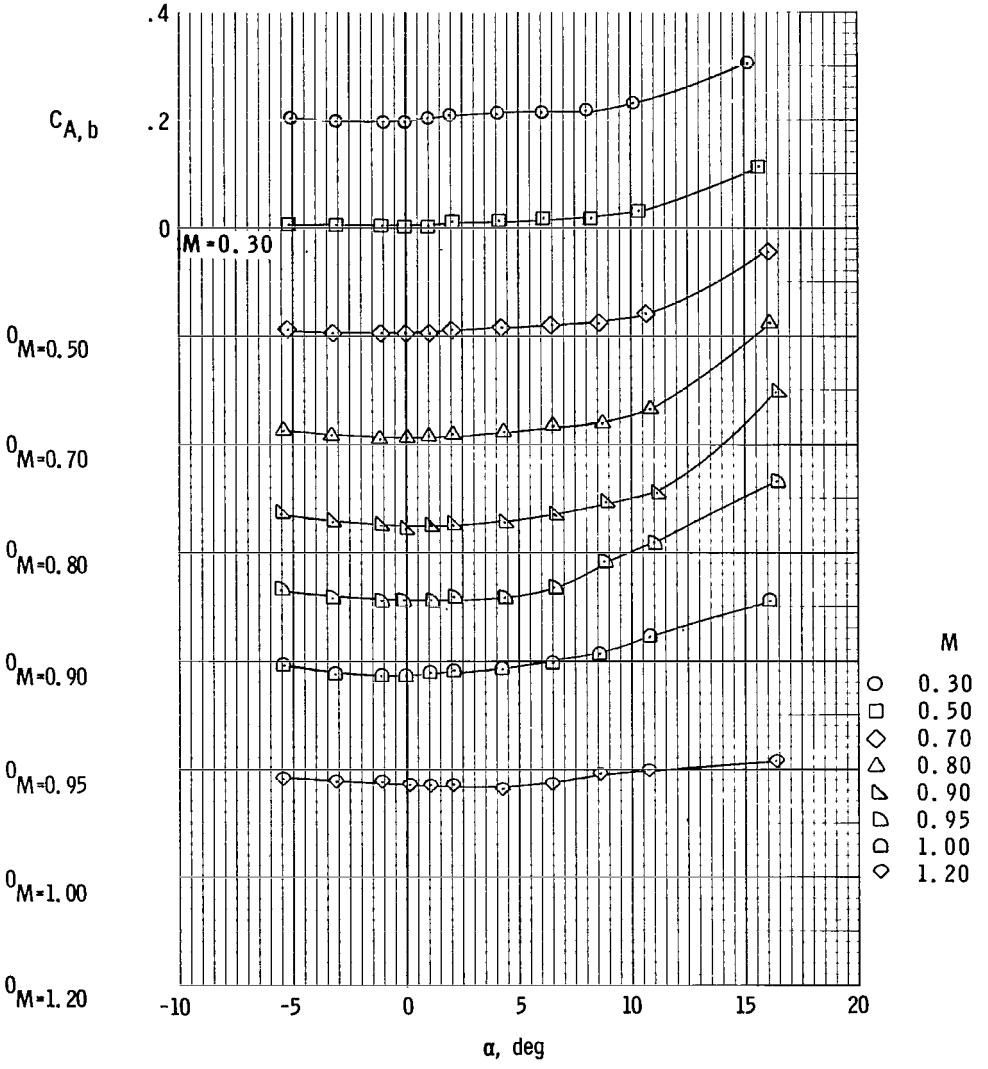

(f) Base axial-force coefficient.

Figure 10. - Concluded.

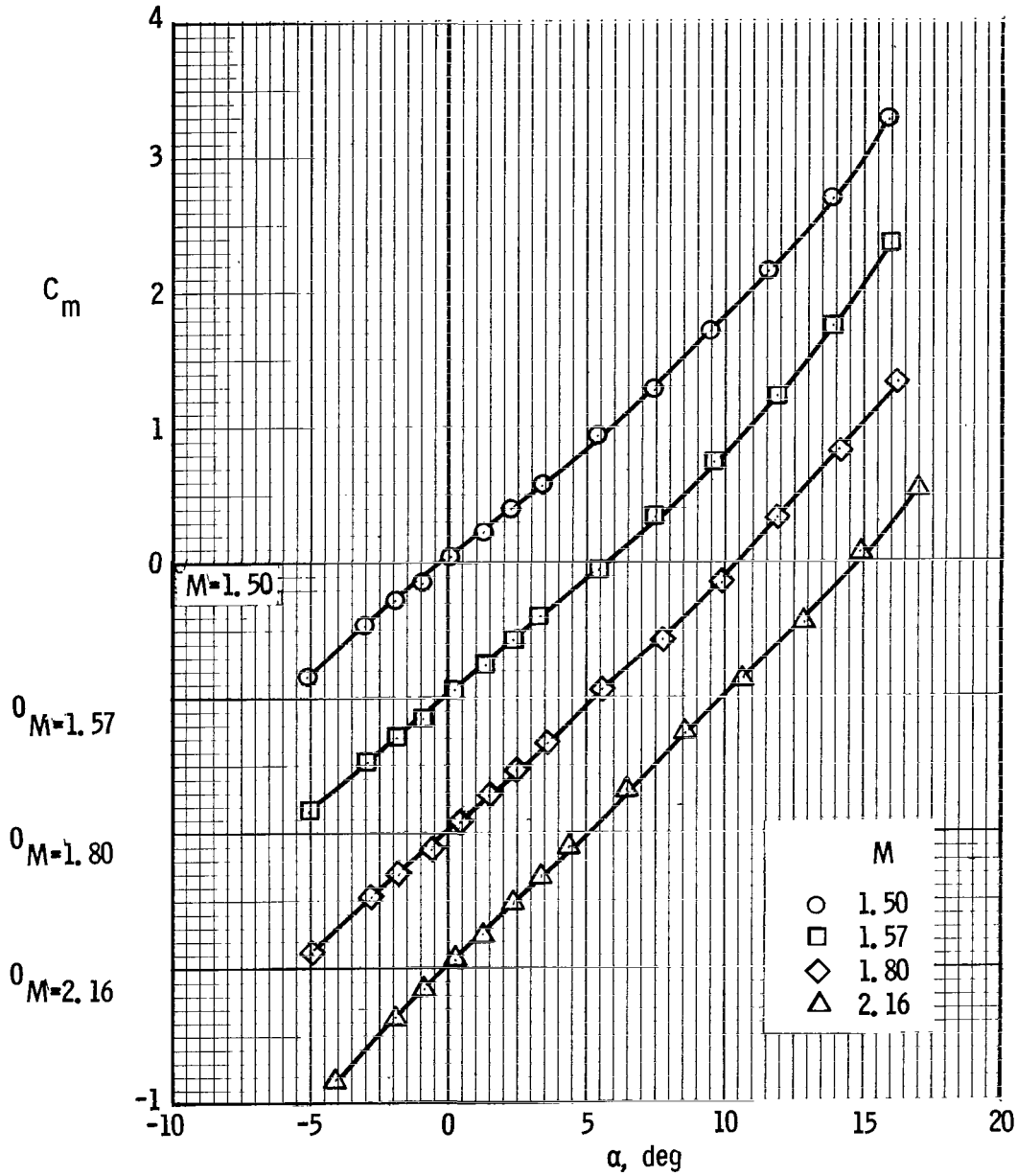

(a) Pitching-moment coefficient.

Figure 11. - Aerodynamic characteristics of configuration II with small fins and medium service module at Mach numbers from 1.50 to 2.16.

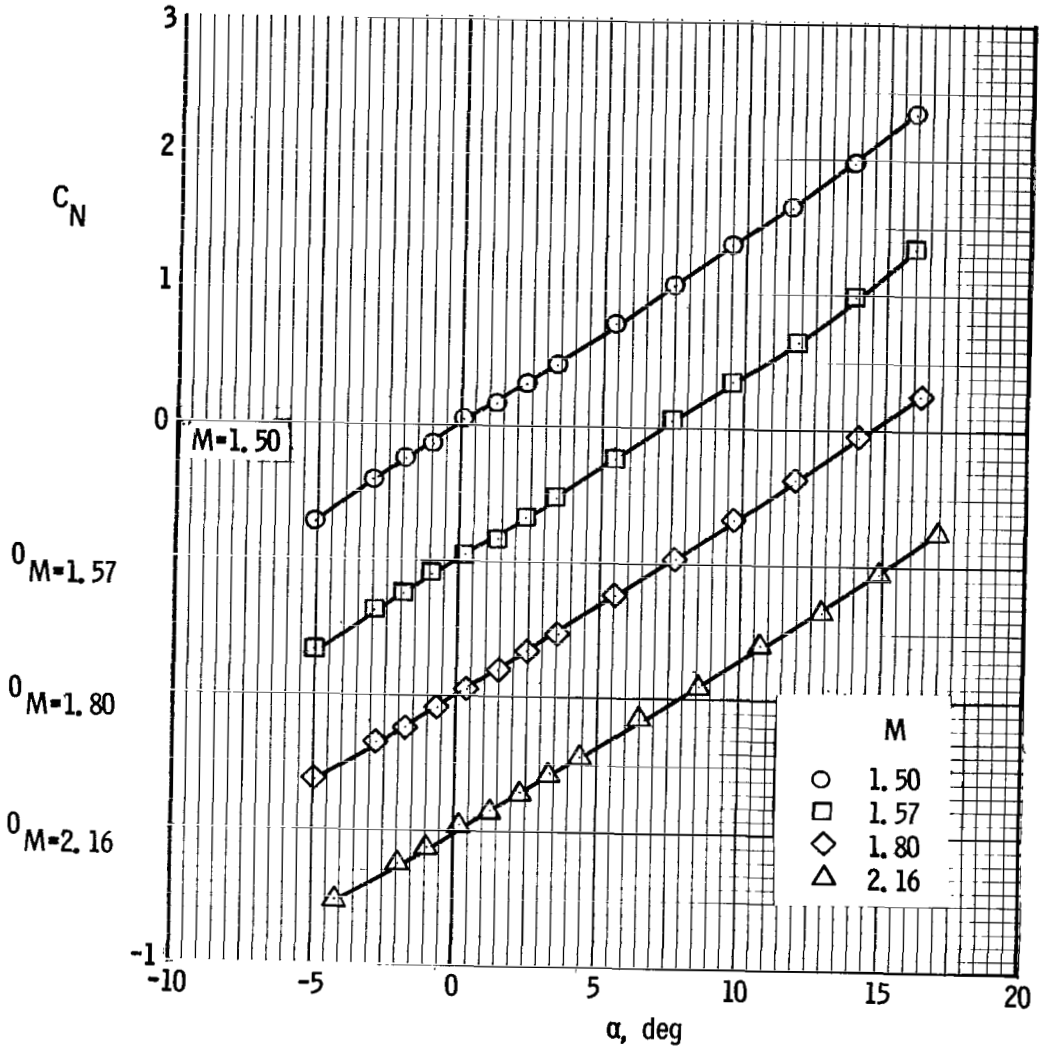

(b) Normal-force coefficient.

Figure 11. - Continued.

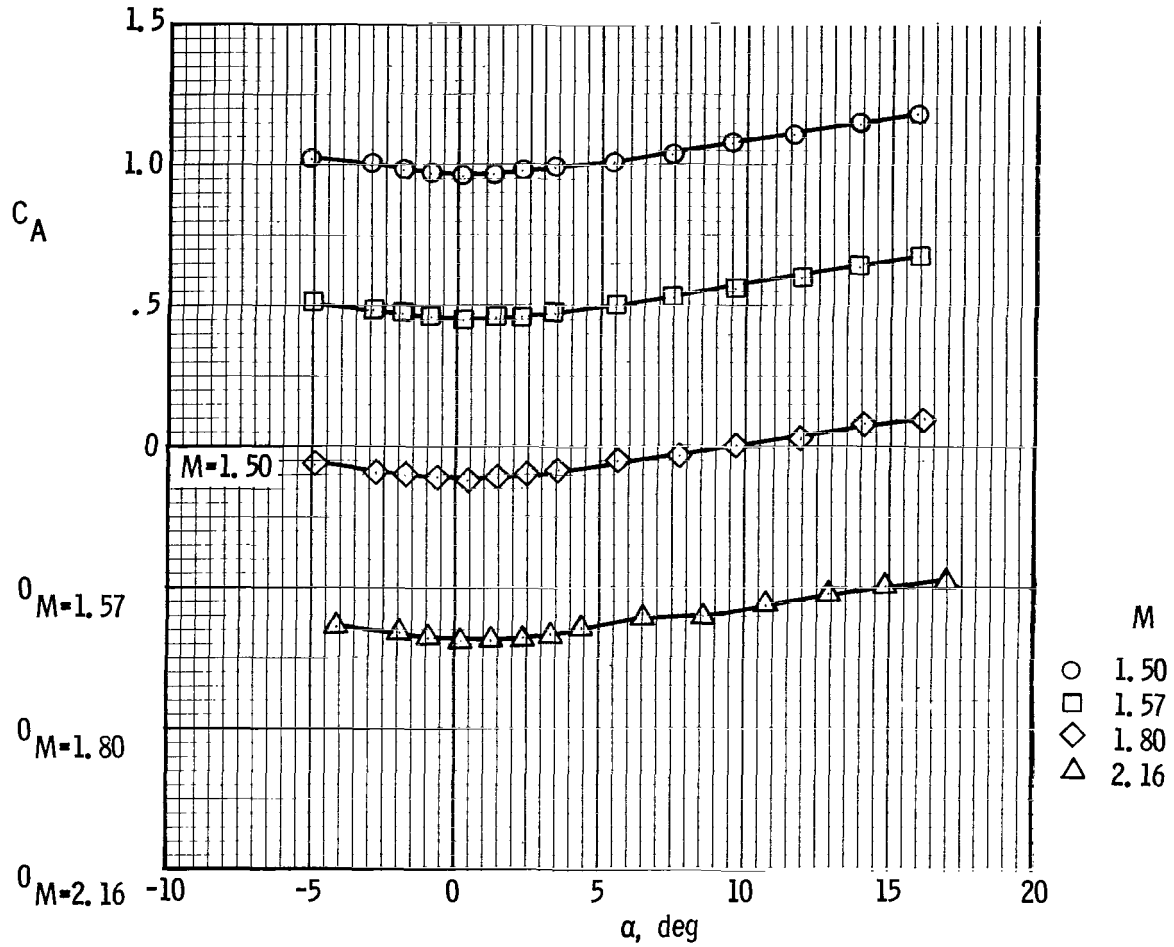

(c) Axial-force coefficient.

Figure 11. - Continued.

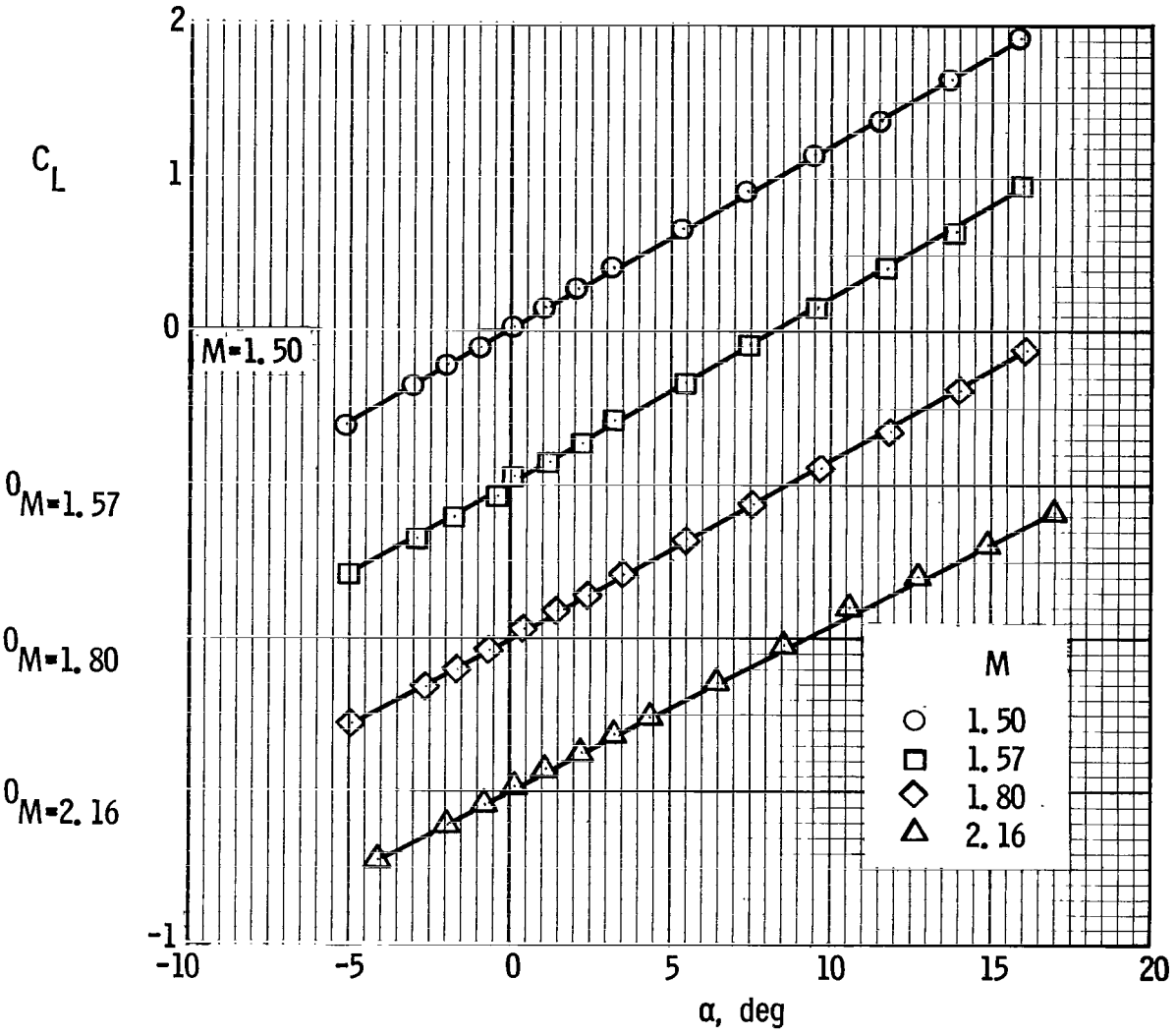

(d) Lift coefficient.

Figure 11. - Continued.

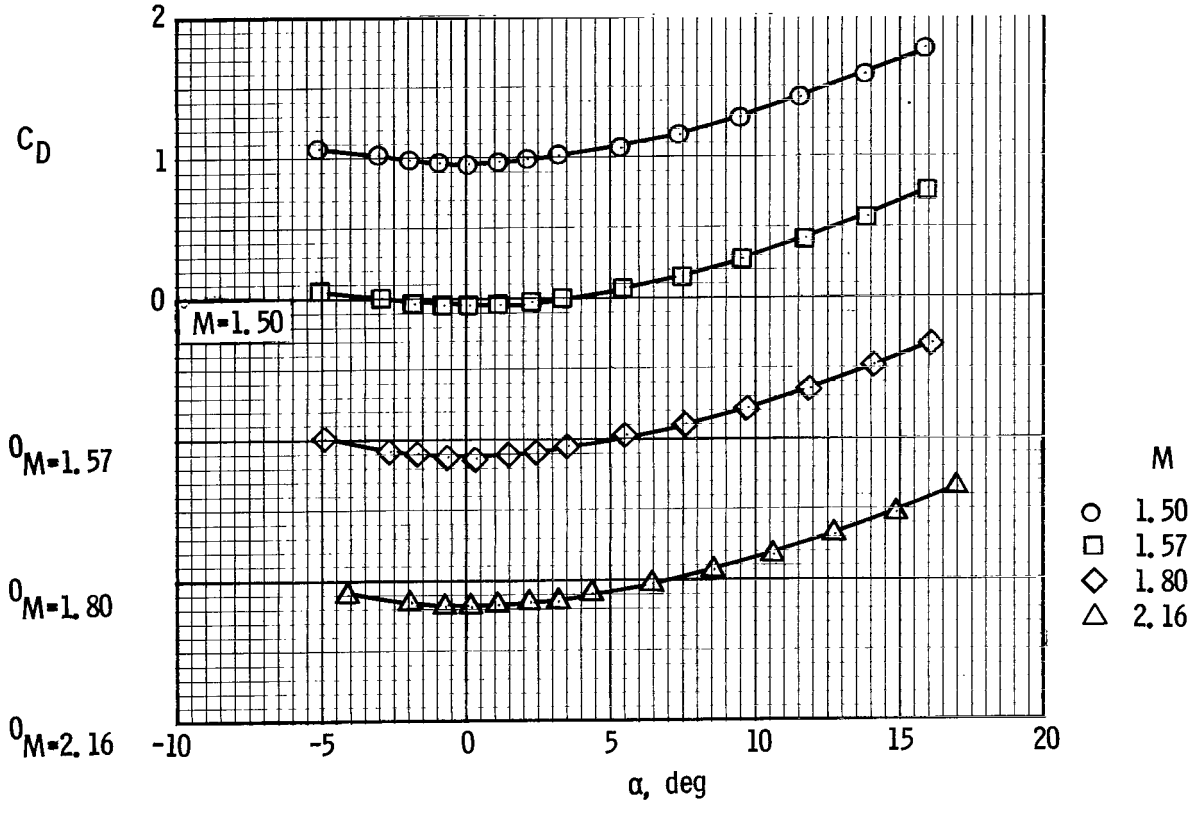

(e) Drag coefficient.

Figure 11. - Continued.

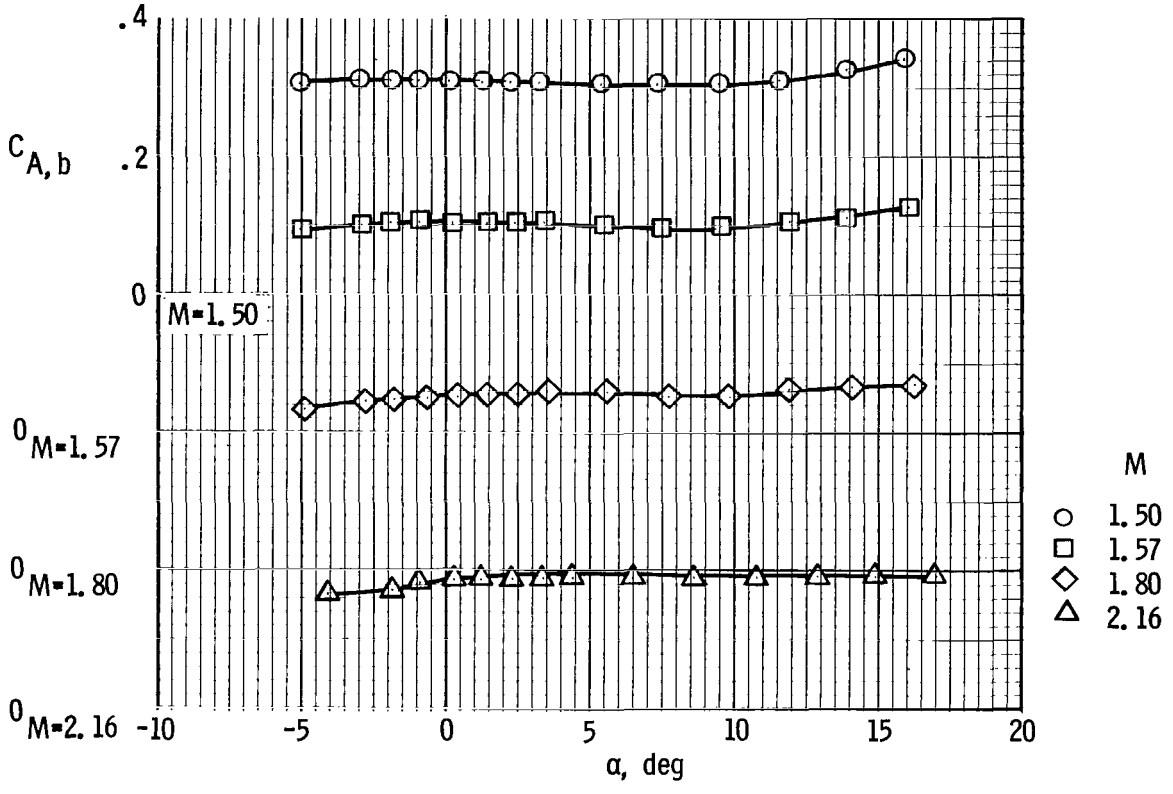

(f) Base axial-force coefficient.

Figure 11. - Concluded.

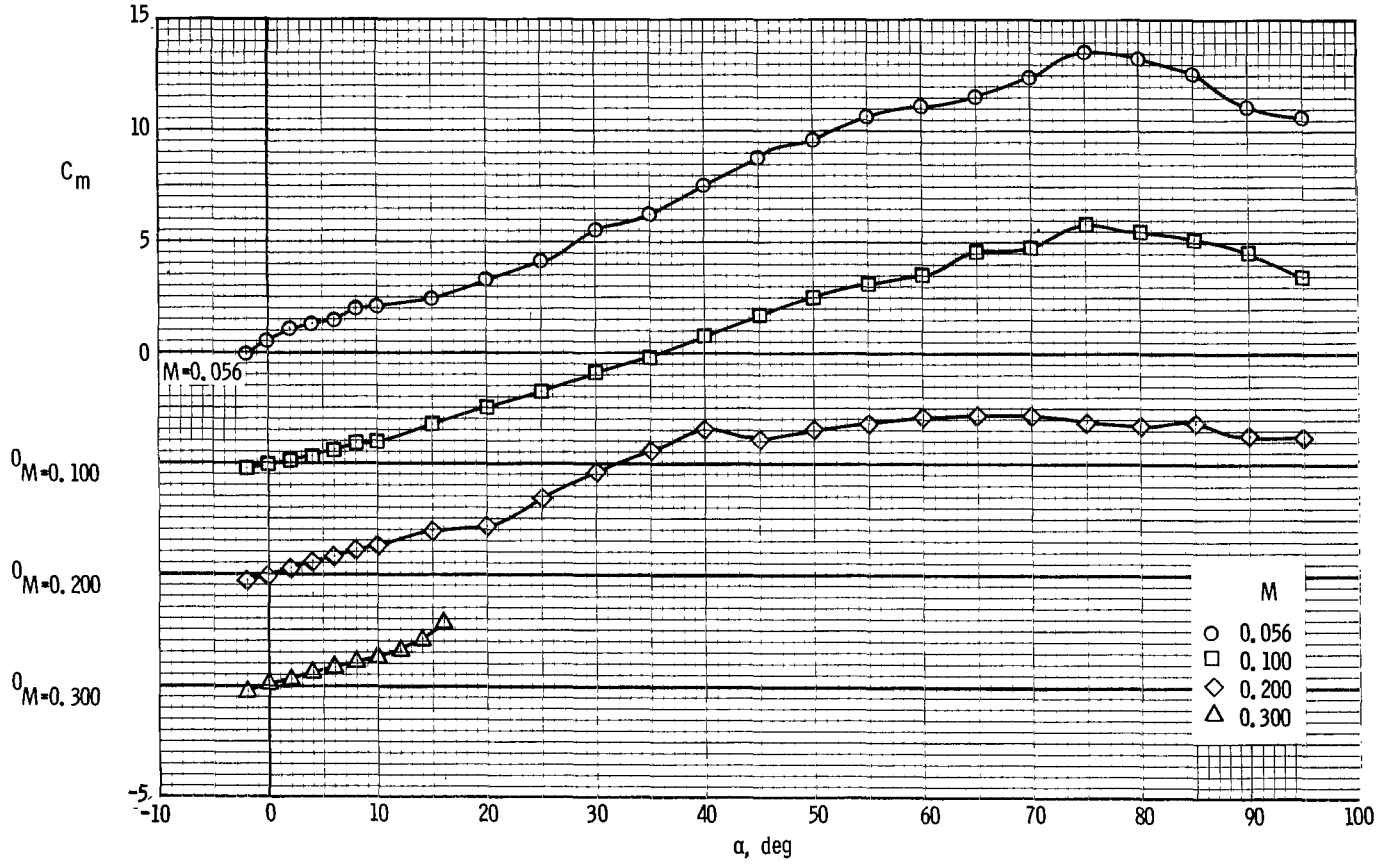

(a) Pitching-moment coefficient.

Figure 12. - Aerodynamic characteristics of configuration II with medium service module at Mach numbers from 0.056 to 0.30, fins off.

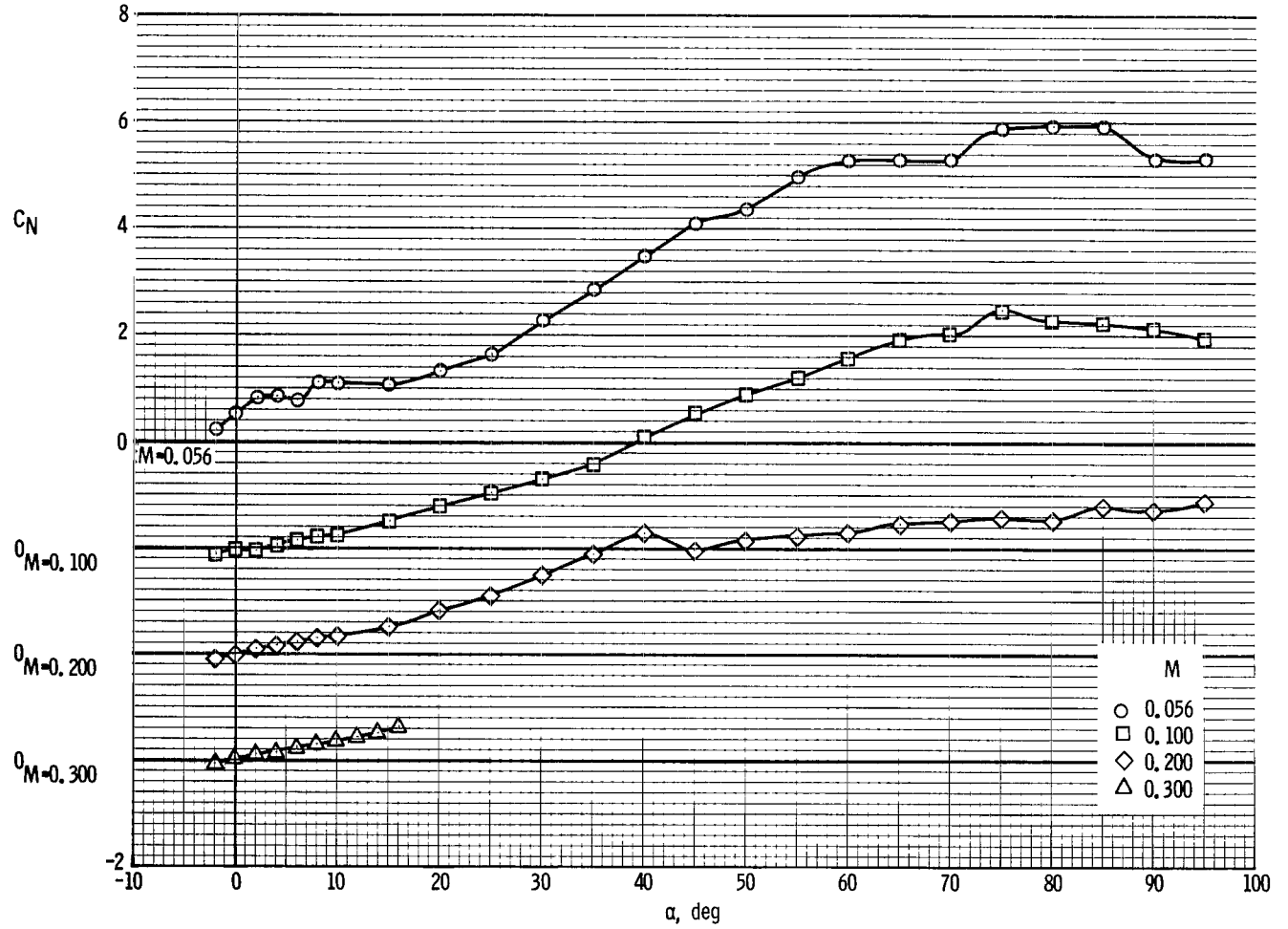

(b) Normal-force coefficient.

Figure 12. - Continued.

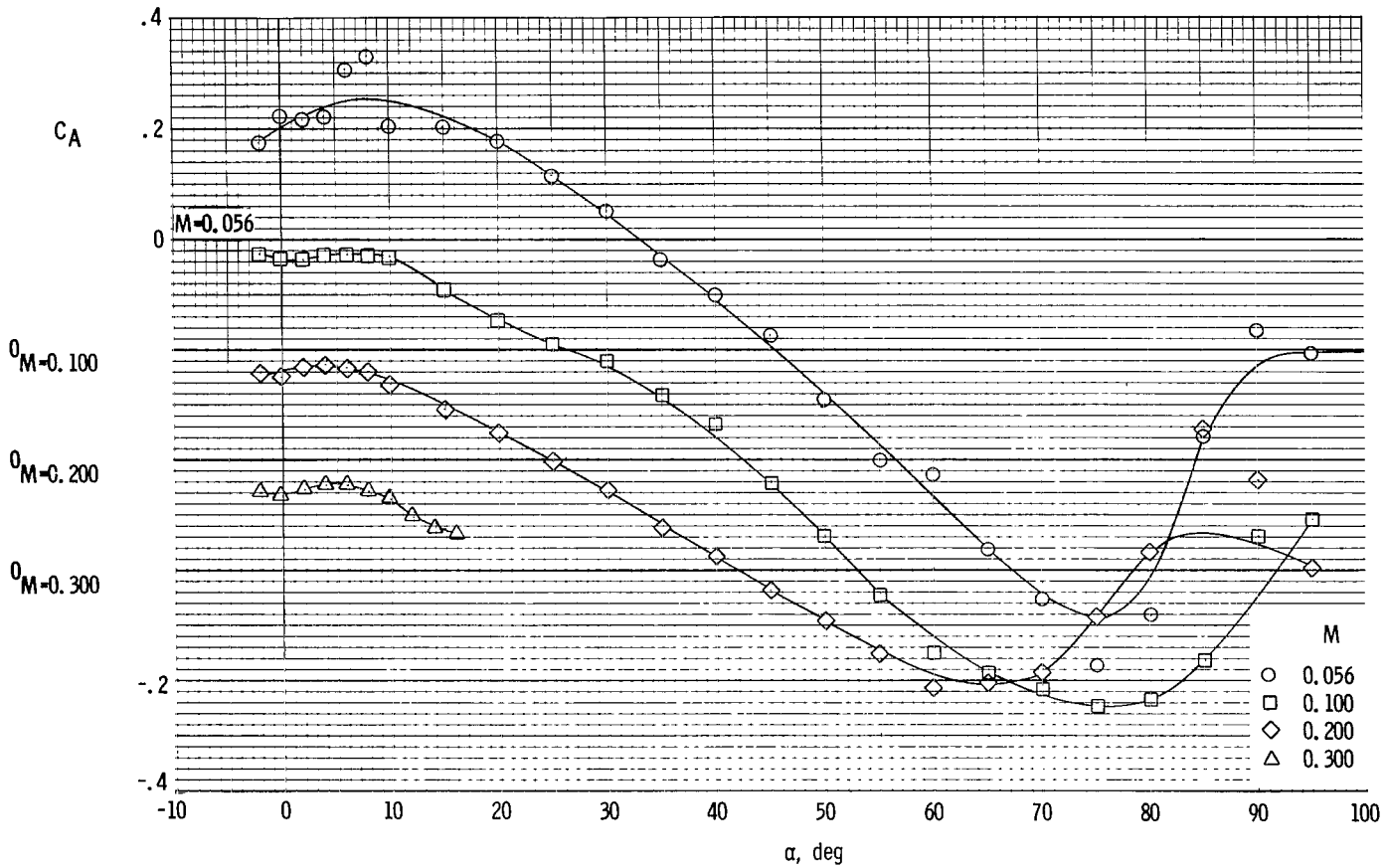

(c) Axial-force coefficient.

Figure 12. - Continued.

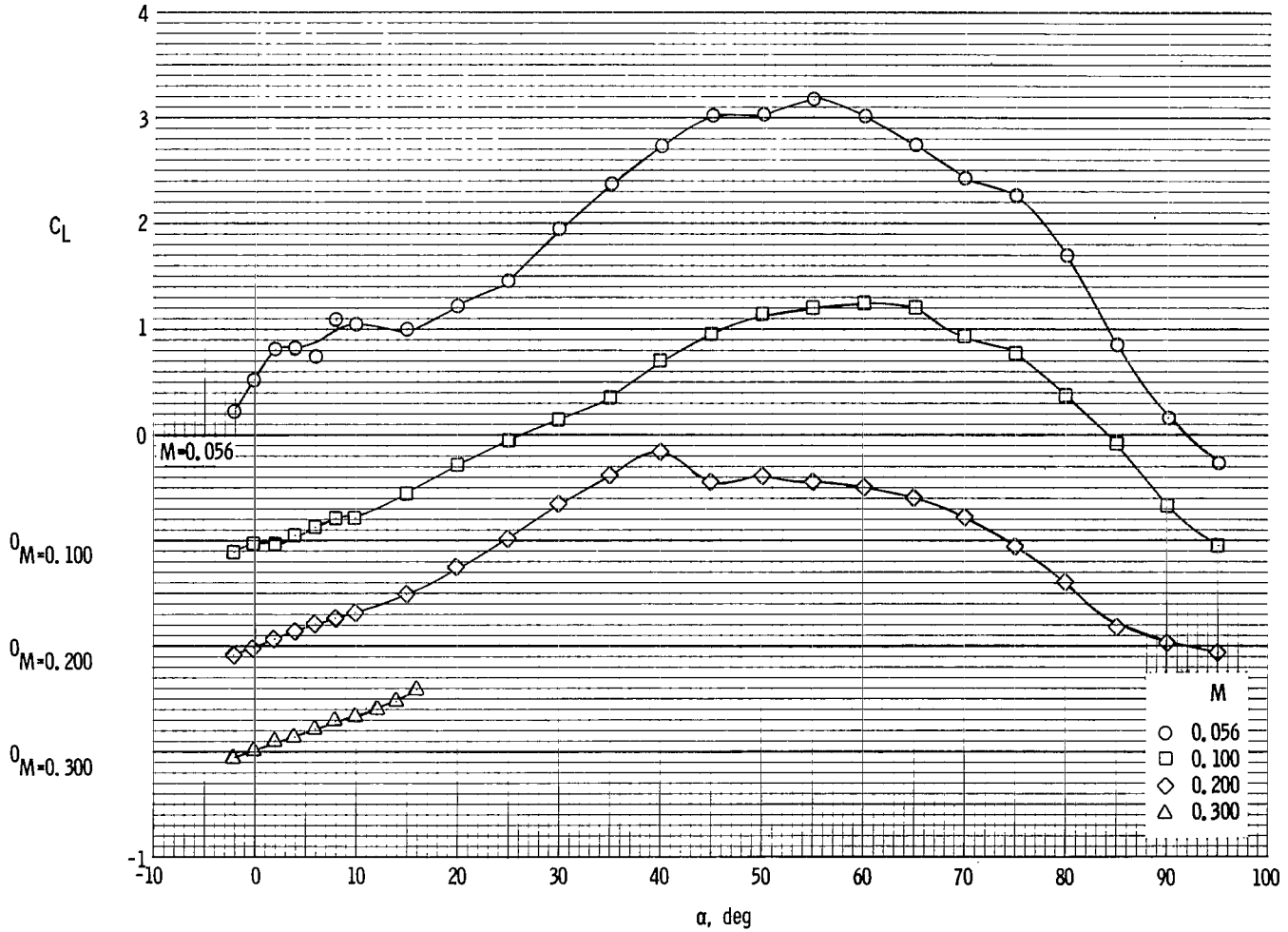

(d) Lift coefficient.

Figure 12. - Continued.

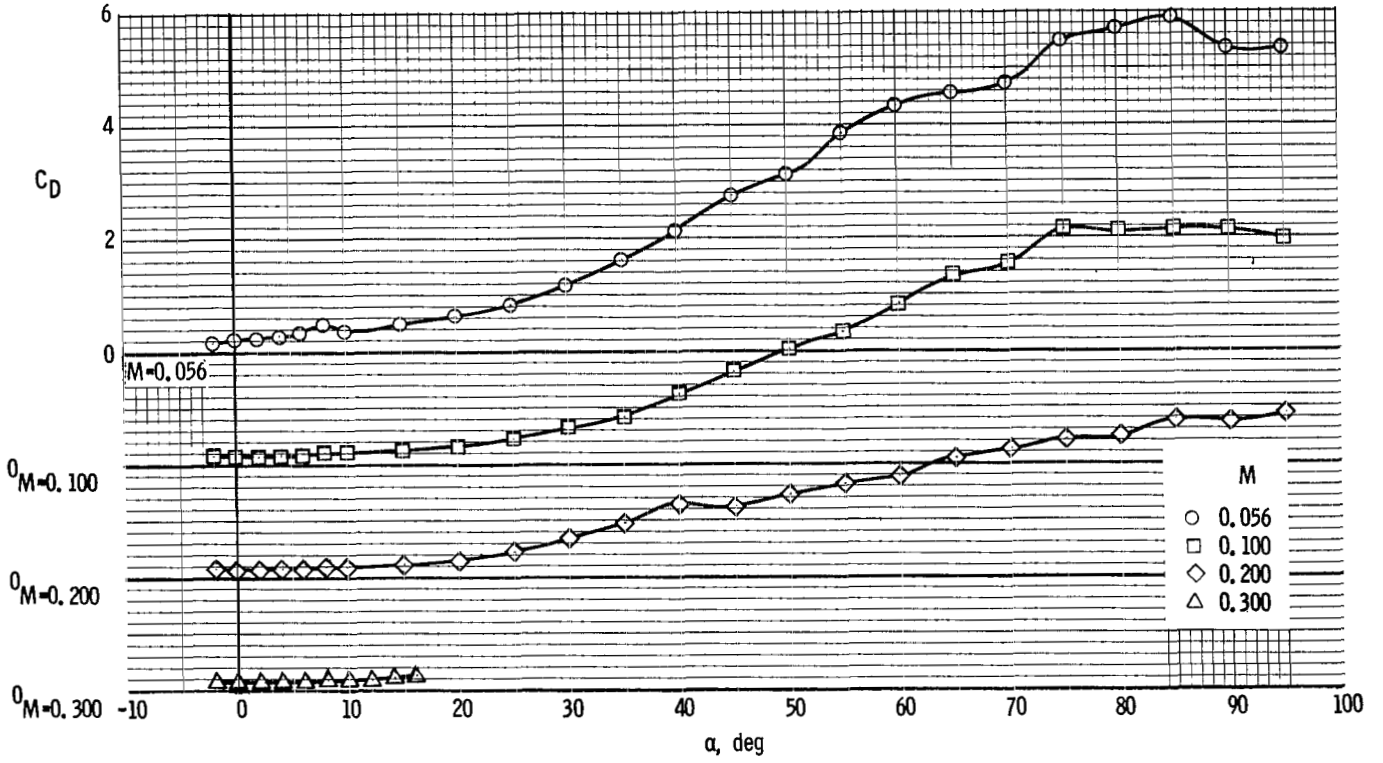

(e) Drag coefficient.

Figure 12. - Continued.

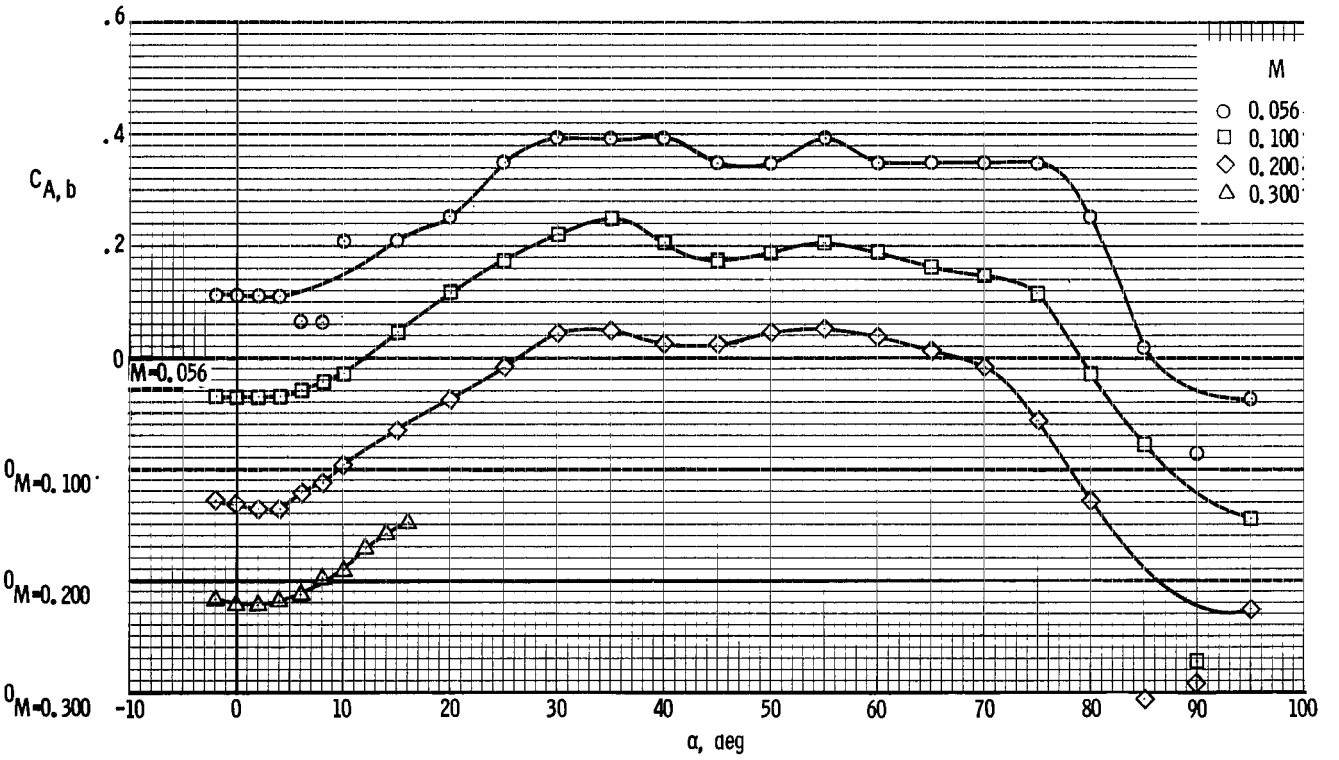

(f) Base axial-force coefficient.

Figure 12. - Concluded.

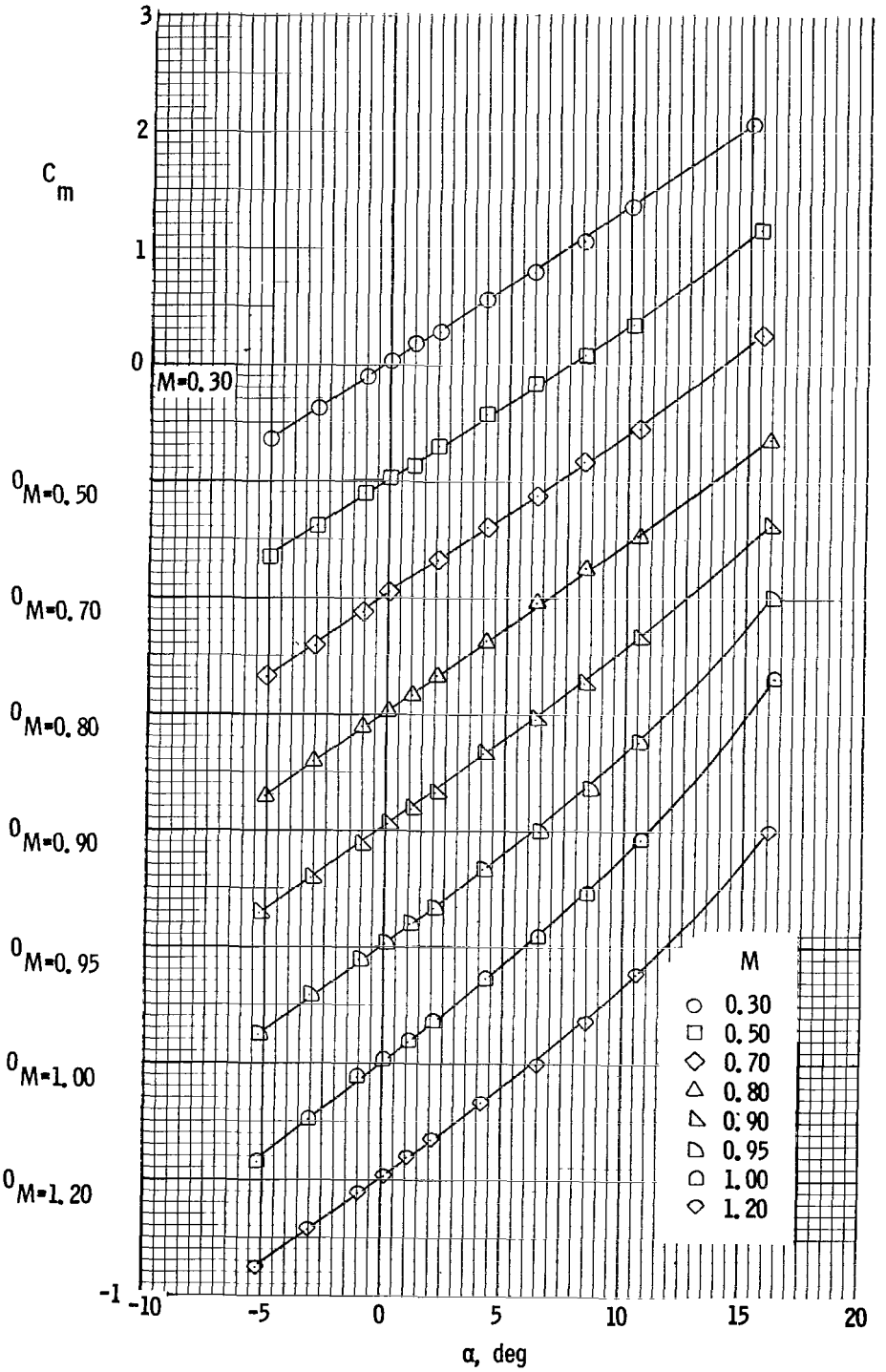

(a) Pitching-moment coefficient.

Figure 13. - Aerodynamic characteristics of configuration II with medium service module at Mach numbers from 0.30 to 1.20, fins off.

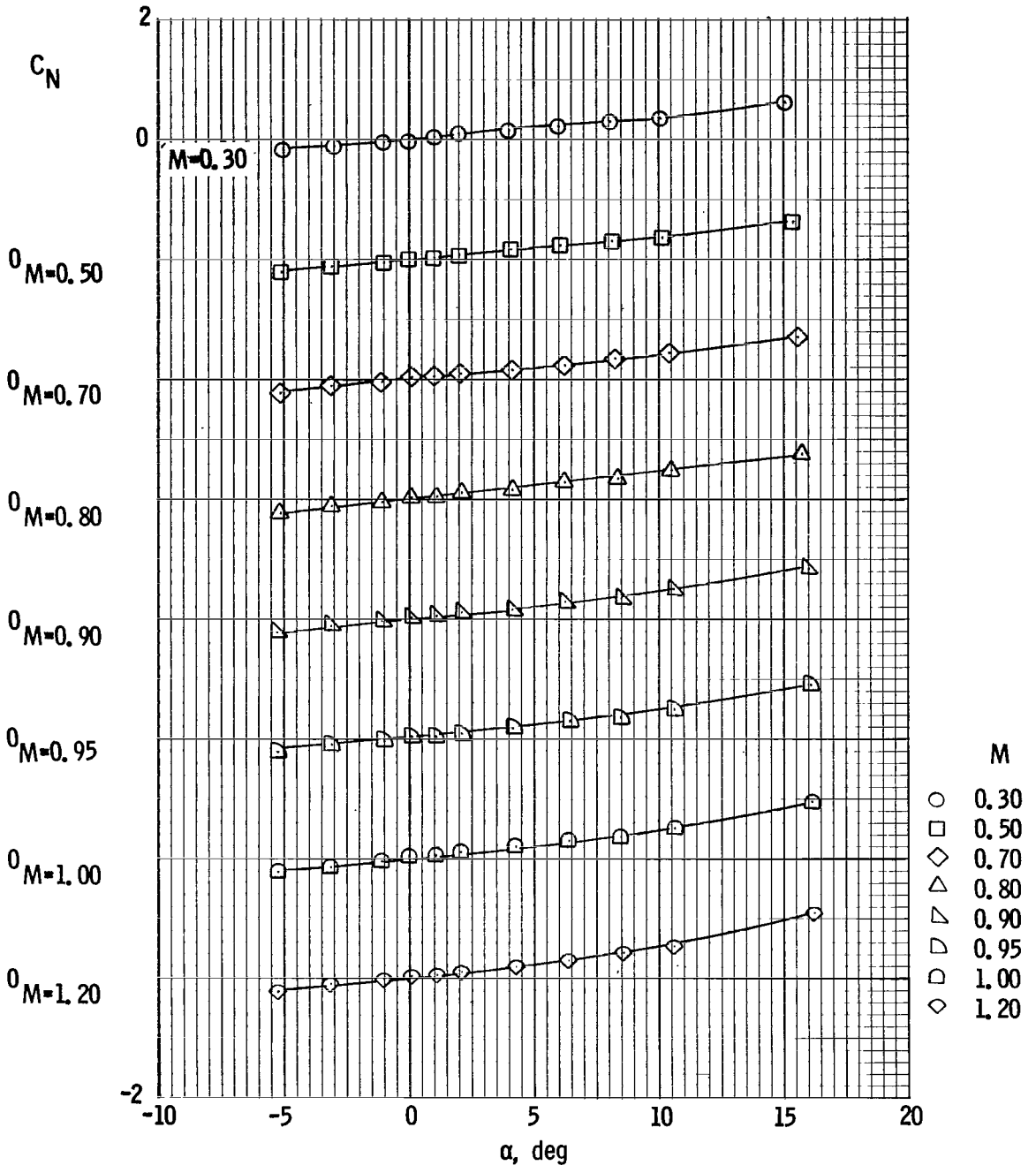

(b) Normal-force coefficient.

Figure 13. - Continued.

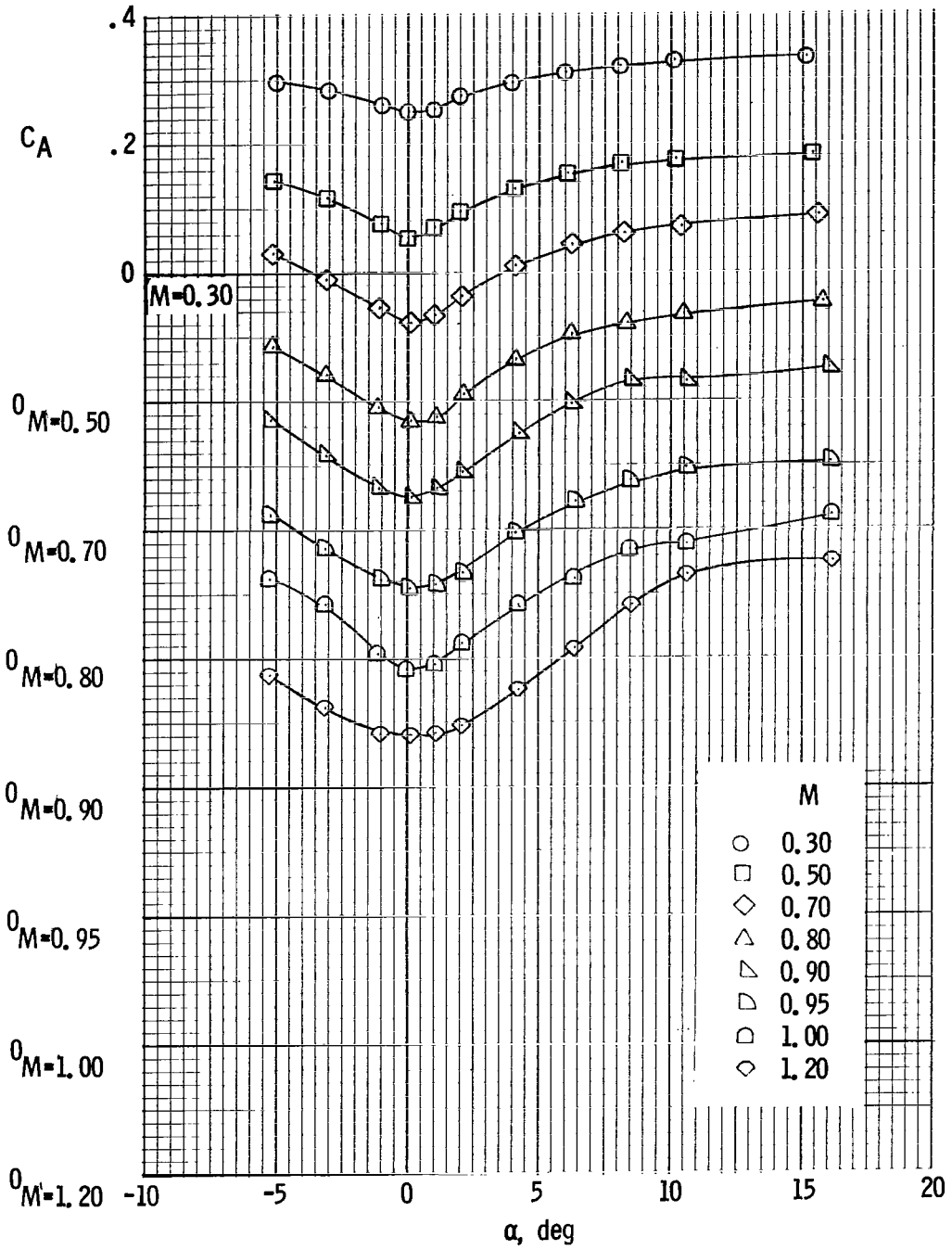

(c) Axial-force coefficient.

Figure 13. - Continued.

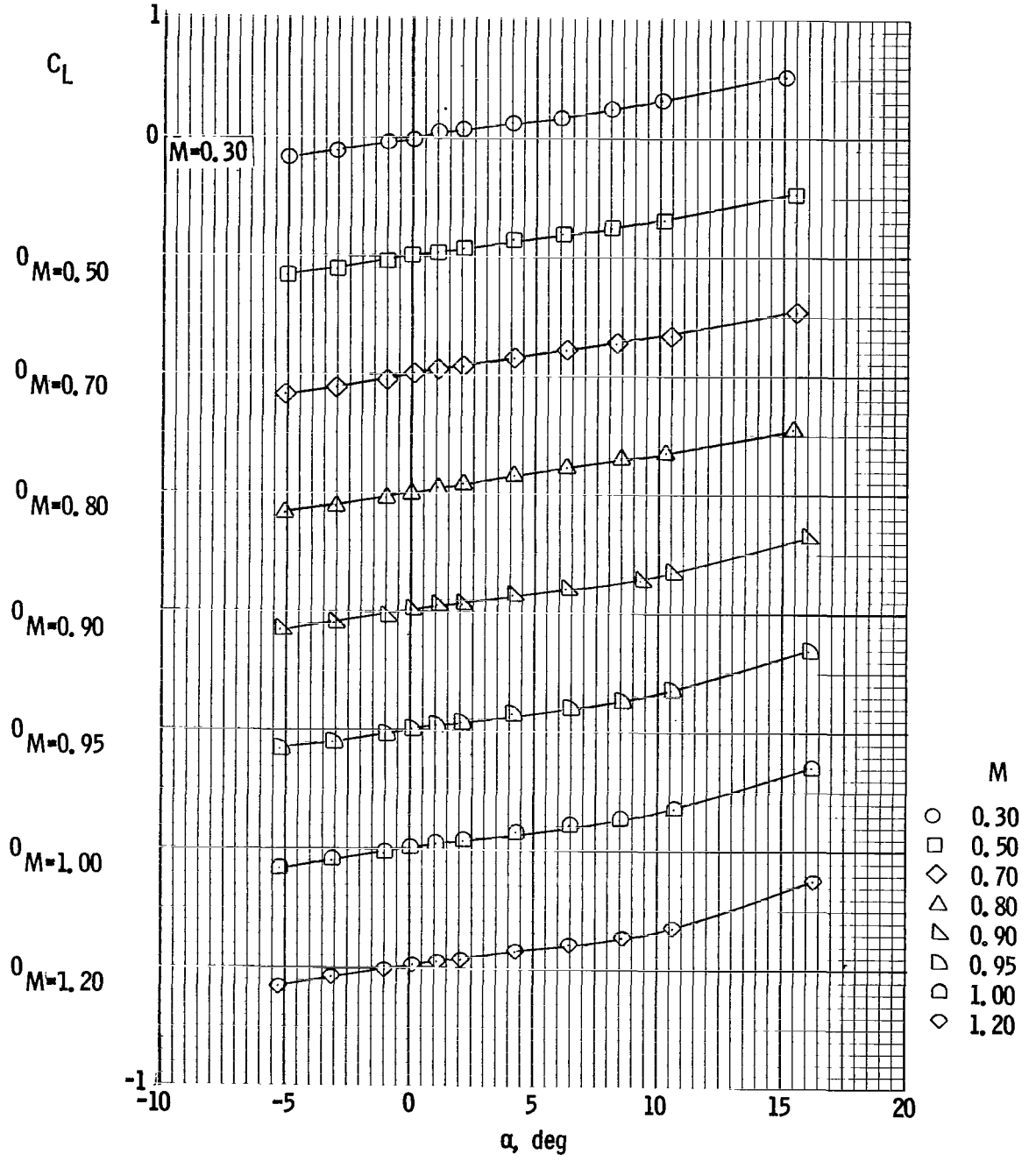

(d) Lift coefficient.

Figure 13. - Continued.

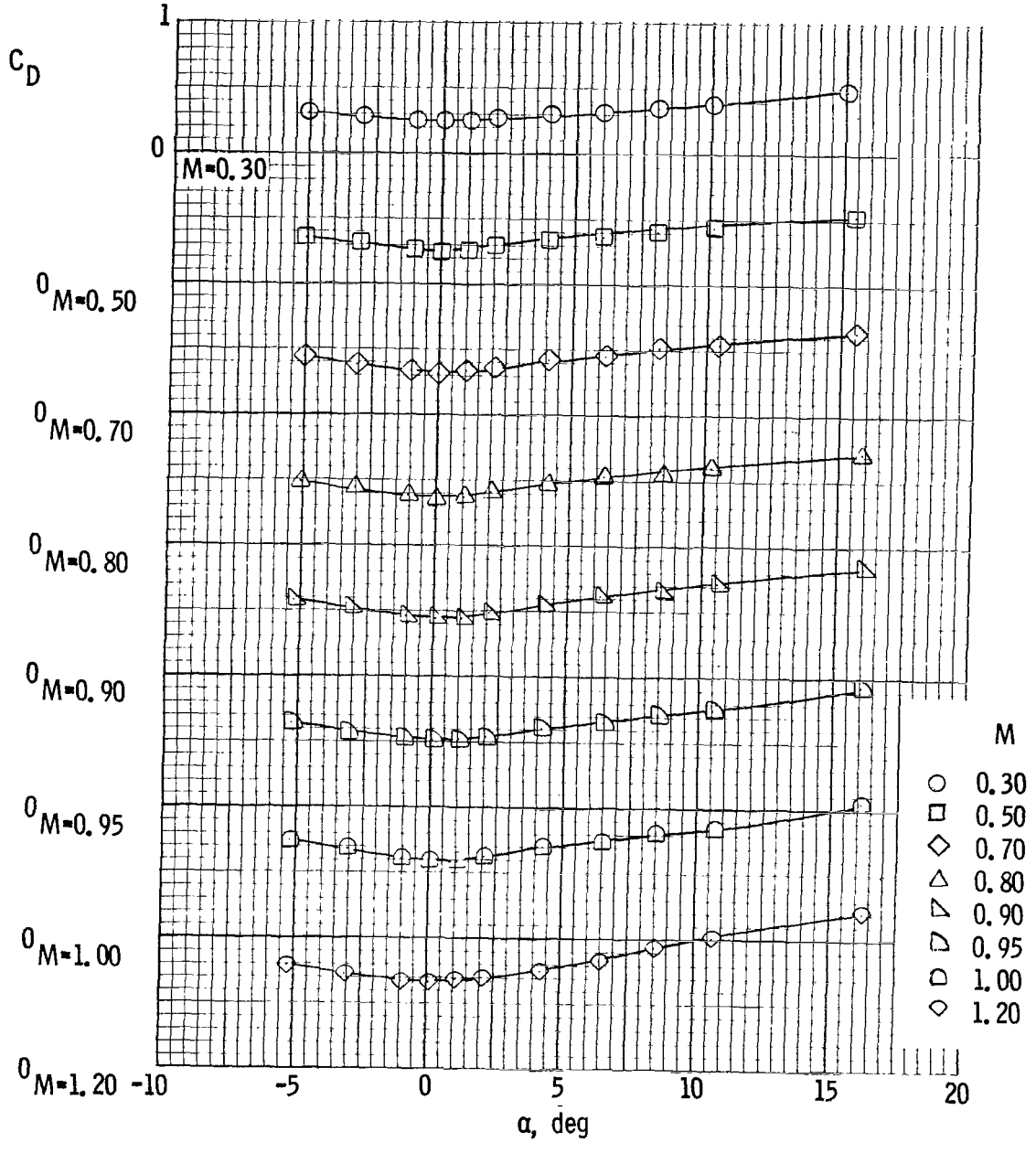

(e) Drag coefficient.

Figure 13. - Continued.

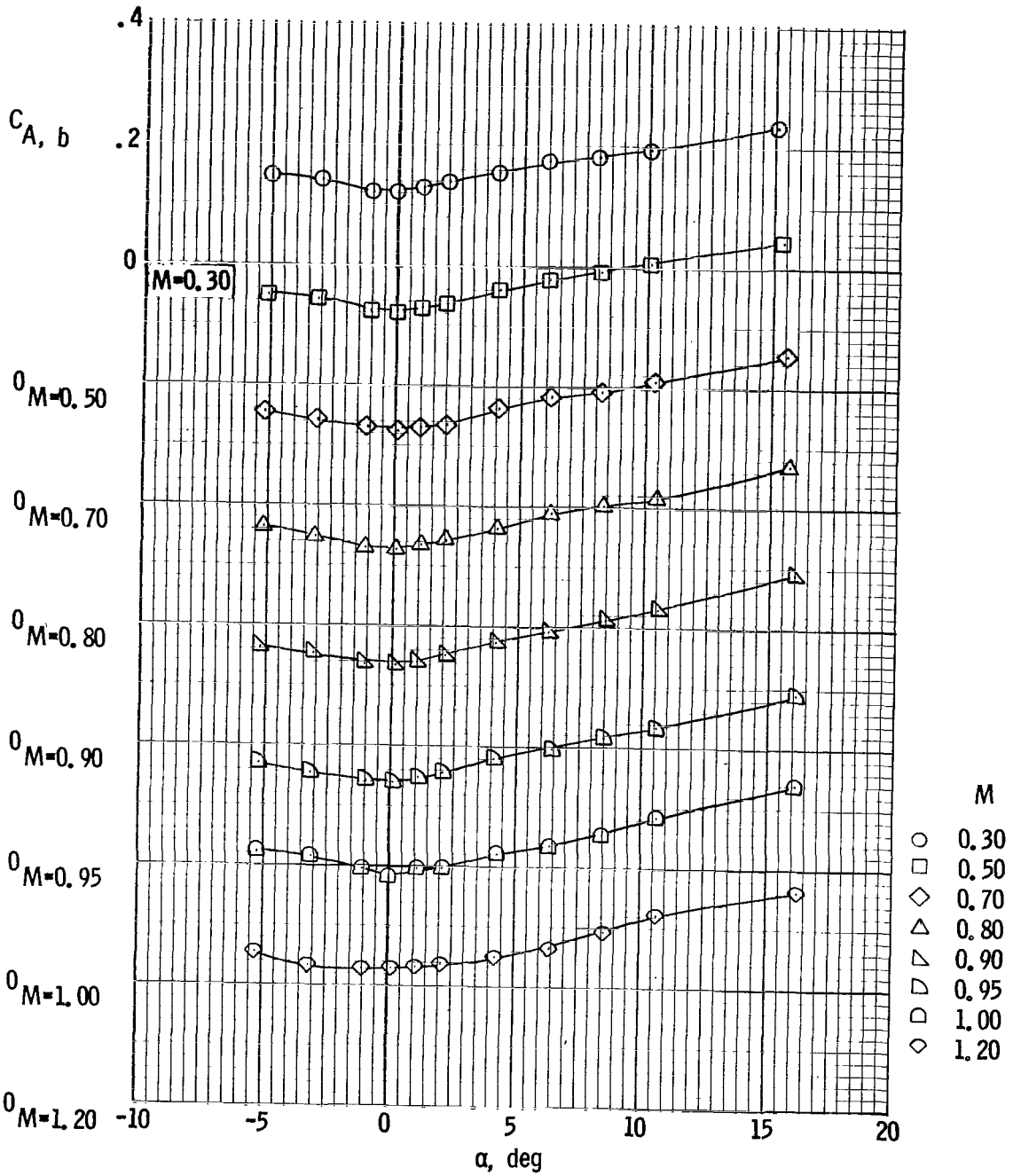

(f) Base axial-force coefficient.

Figure 13. - Concluded.

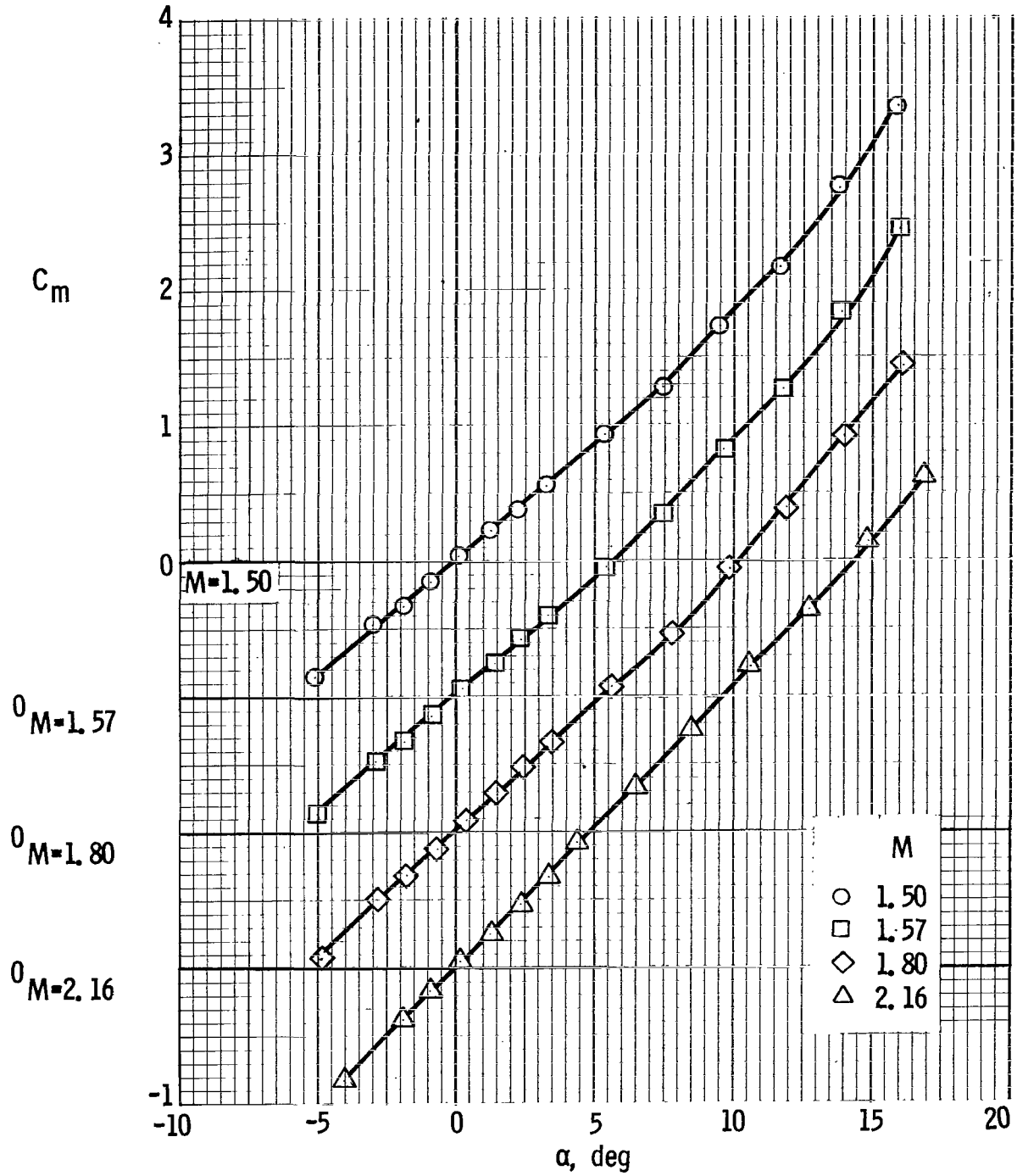

(a) Pitching-moment coefficient.

Figure 14. - Aerodynamic characteristics of configuration II with medium service module at Mach numbers from 1.50 to 2.16, fins off.

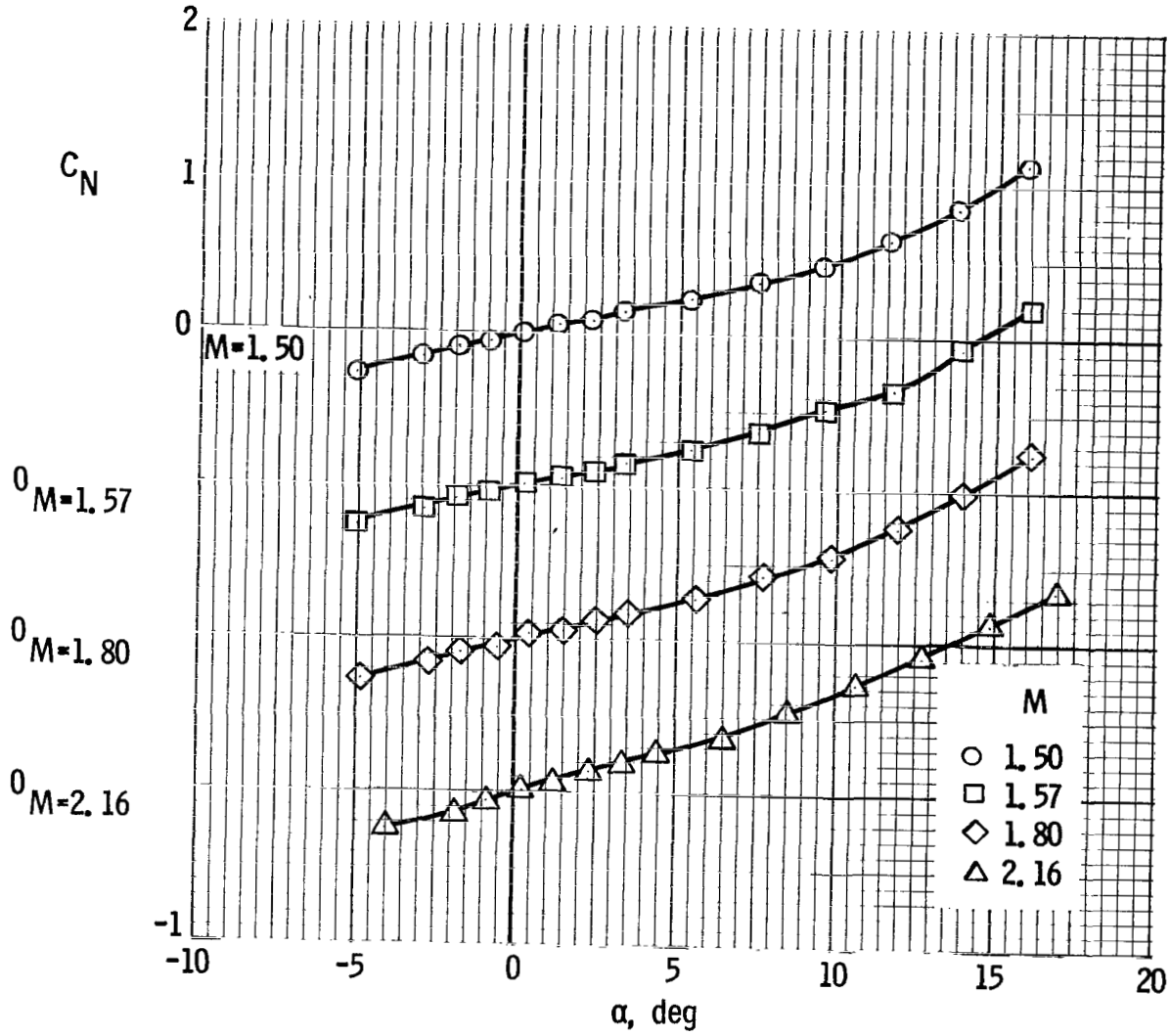

(b) Normal-force coefficient.

Figure 14. - Continued.

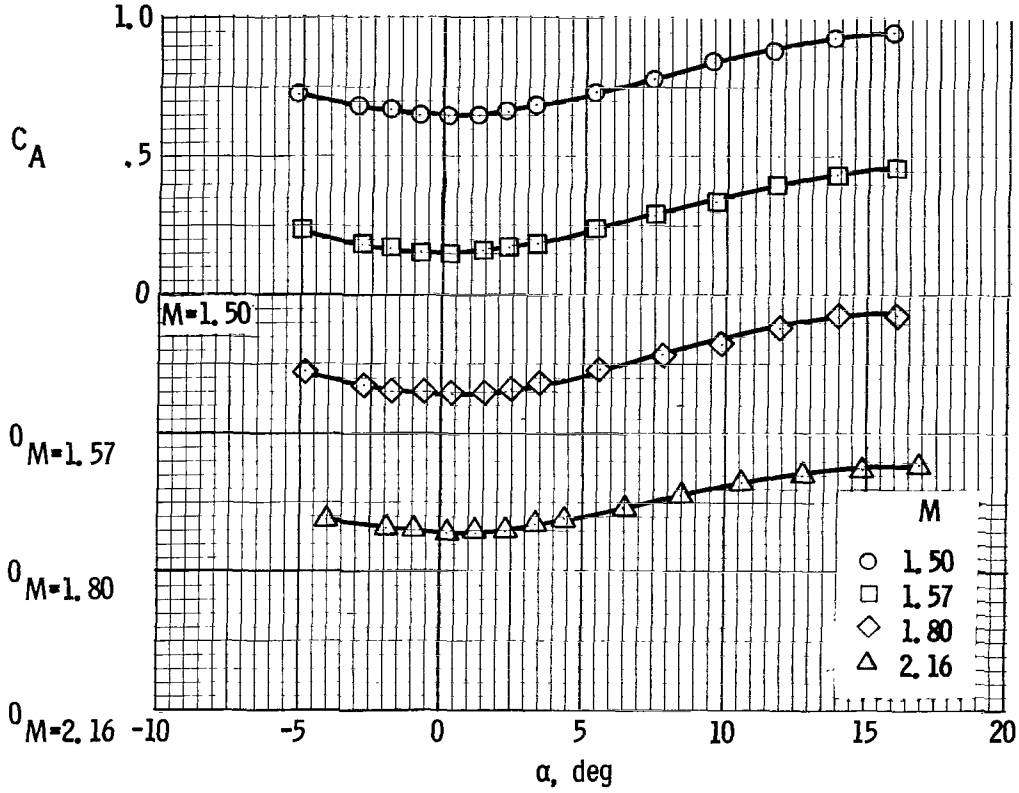

(c) Axial-force coefficient.

Figure 14. - Continued.

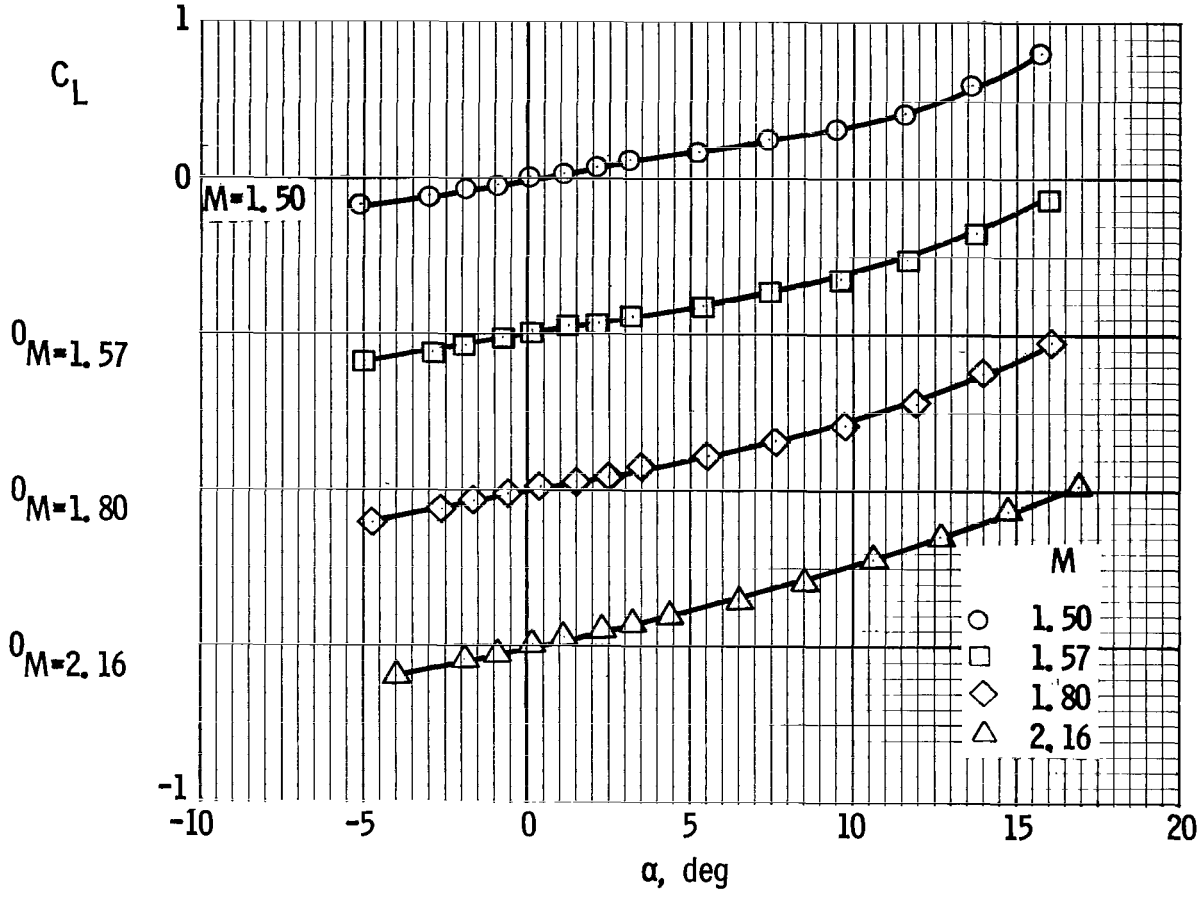

(d) Lift coefficient.

Figure 14. - Continued.

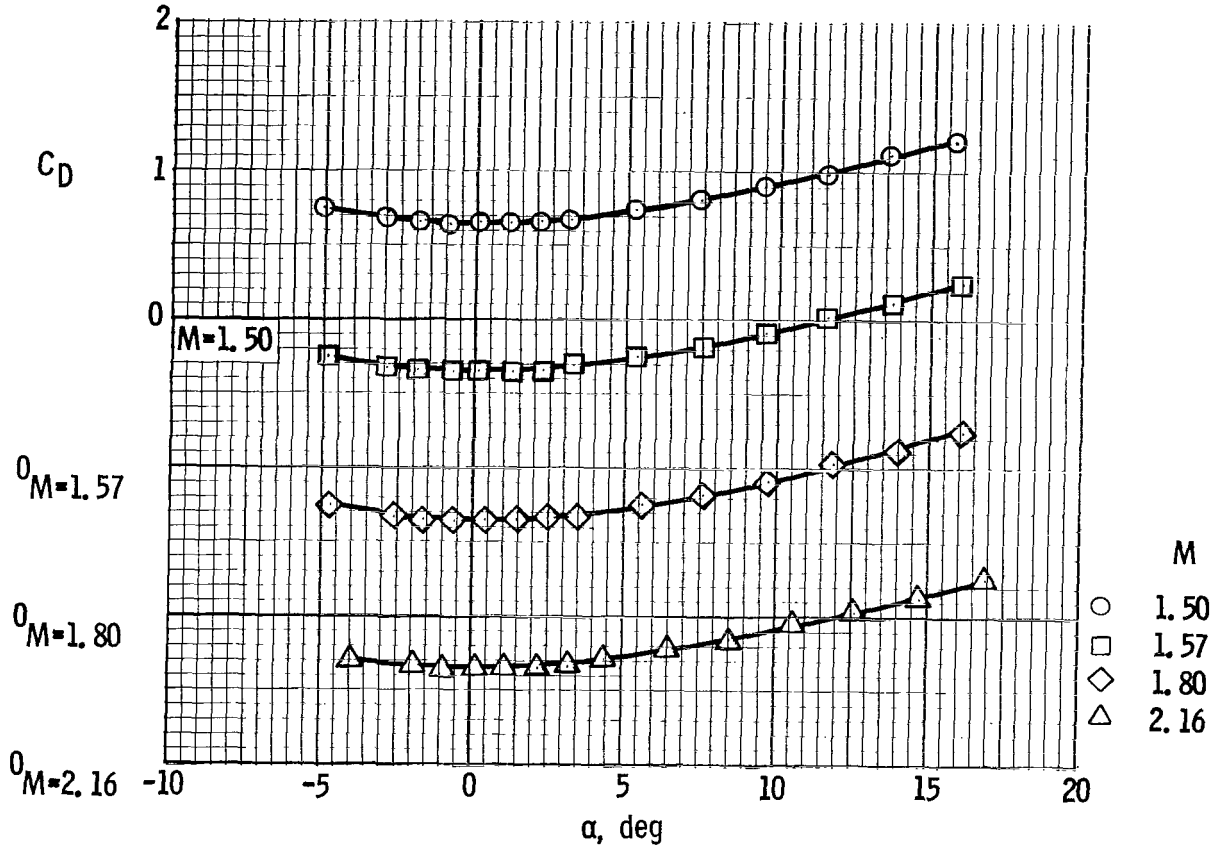

(e) Drag coefficient.

Figure 14. - Continued.

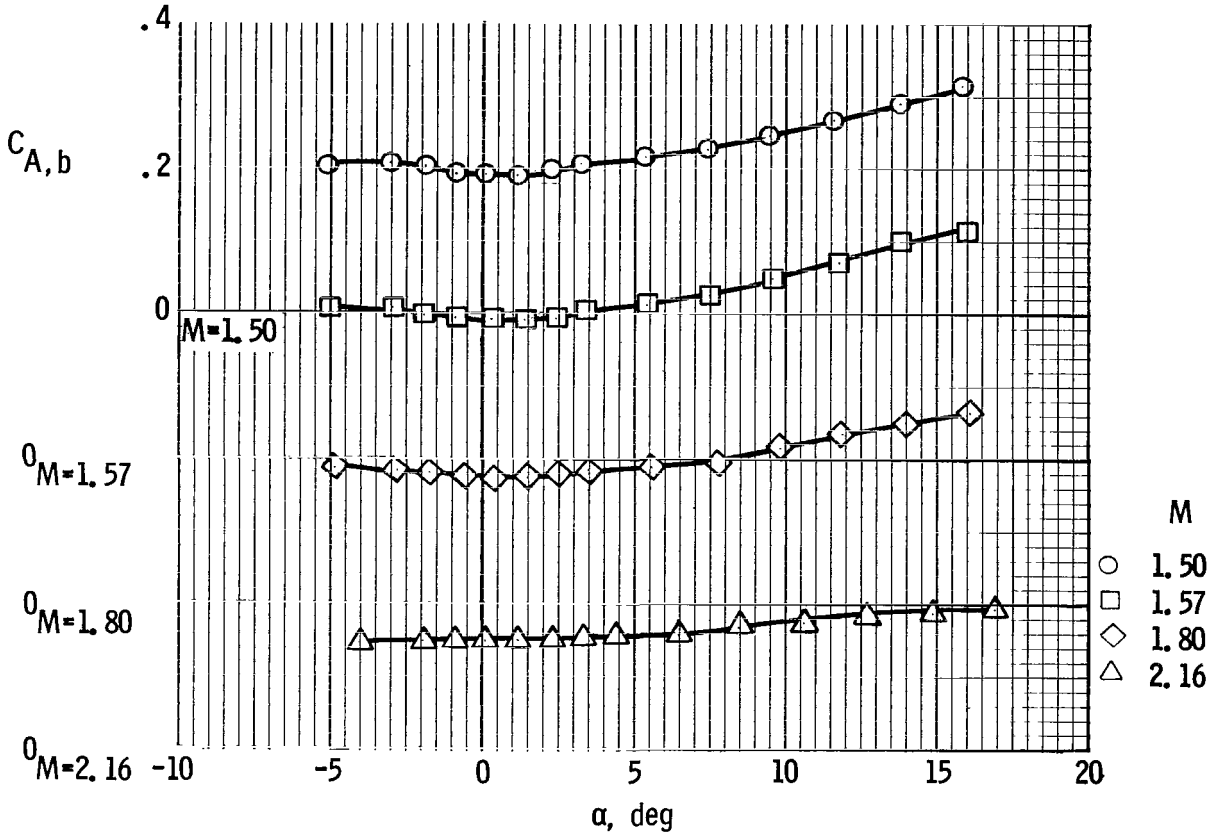

(f) Base axial-force coefficient.

Figure 14. - Concluded.

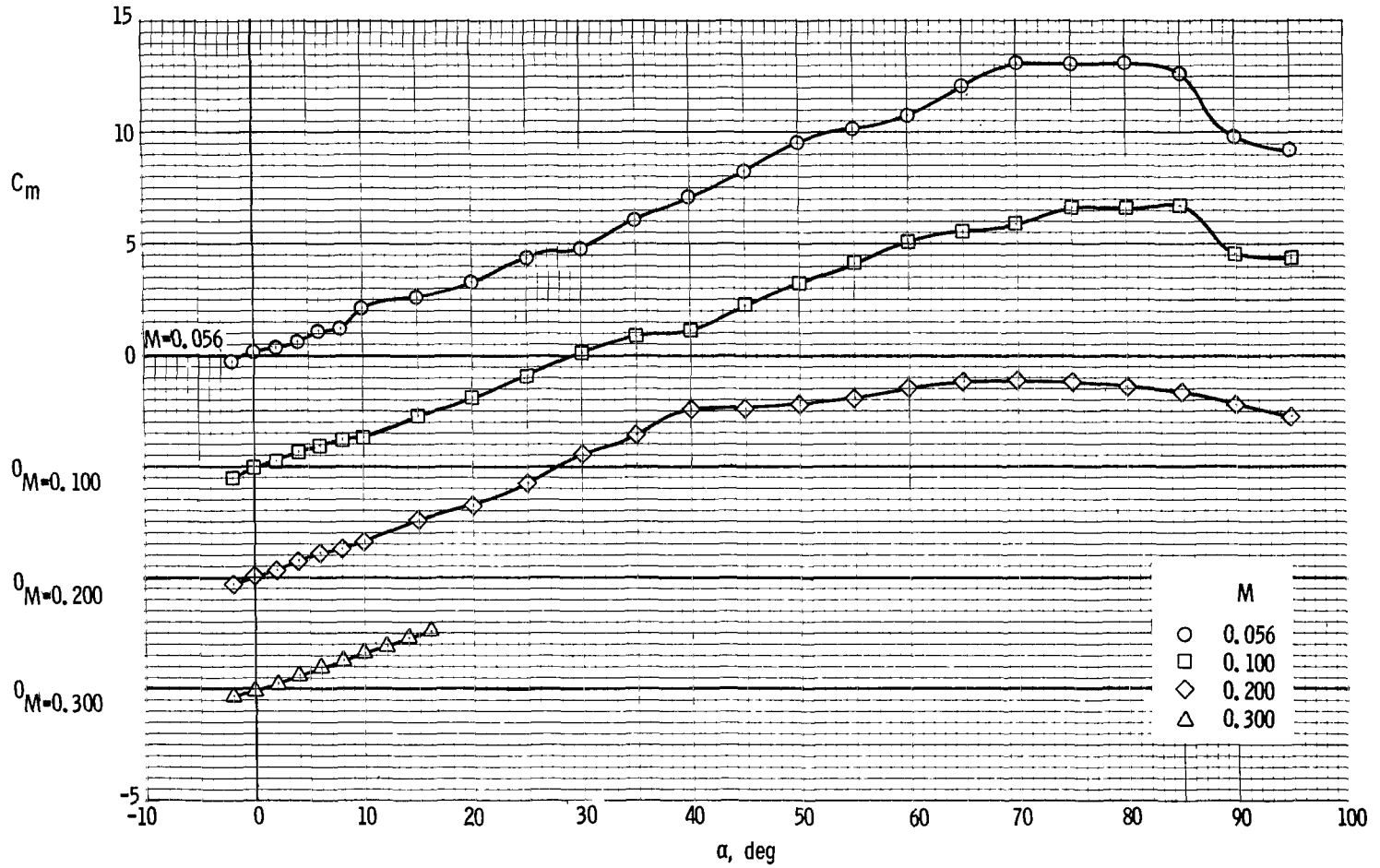

(a) Pitching-moment coefficient.

Figure 15. - Aerodynamic characteristics of configuration II with large fins and long service module at Mach numbers from 0.056 to 0.30.

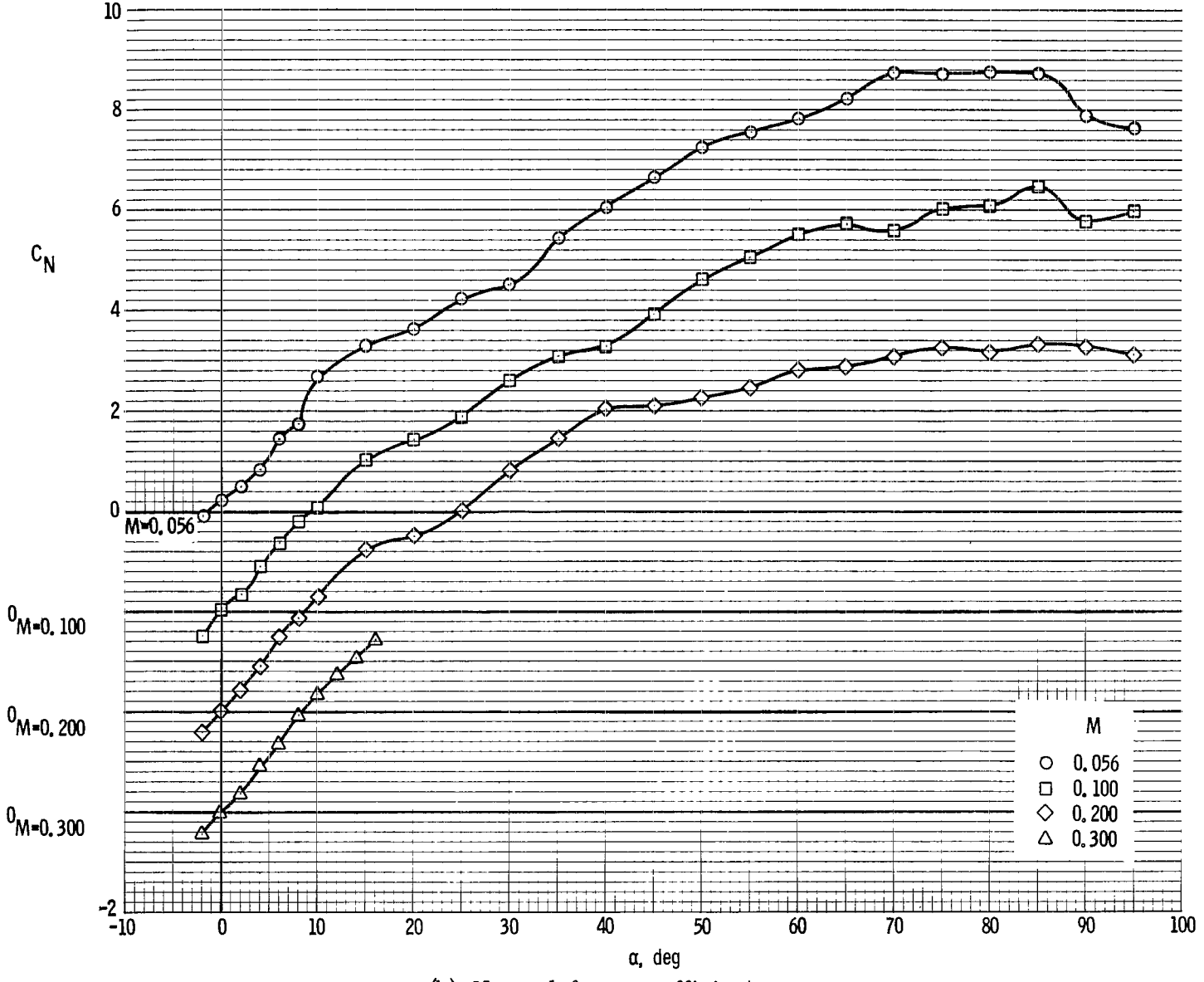

(b) Normal-force coefficient.

Figure 15. - Continued.

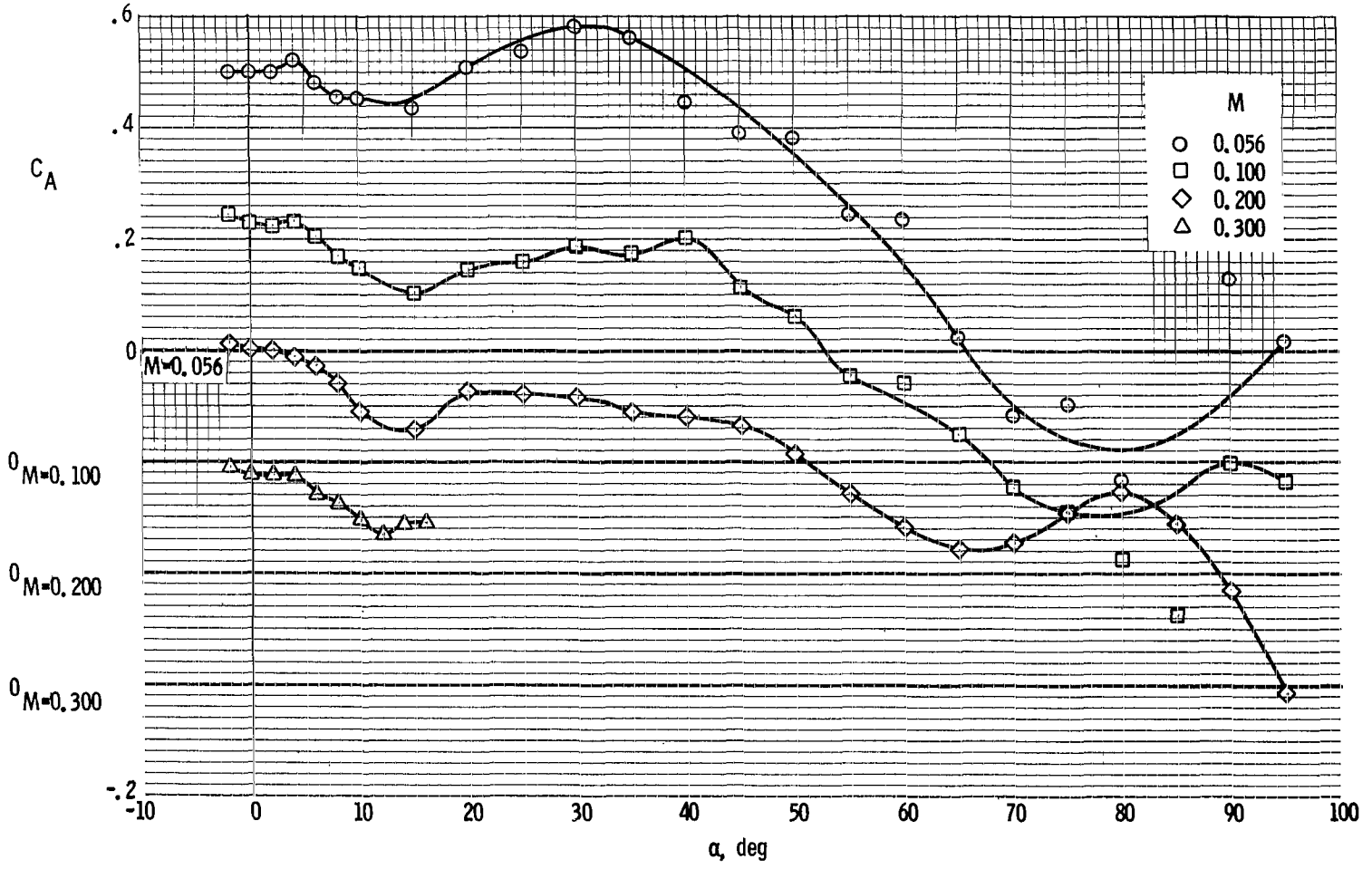

(c) Axial-force coefficient.

Figure 15. - Continued.

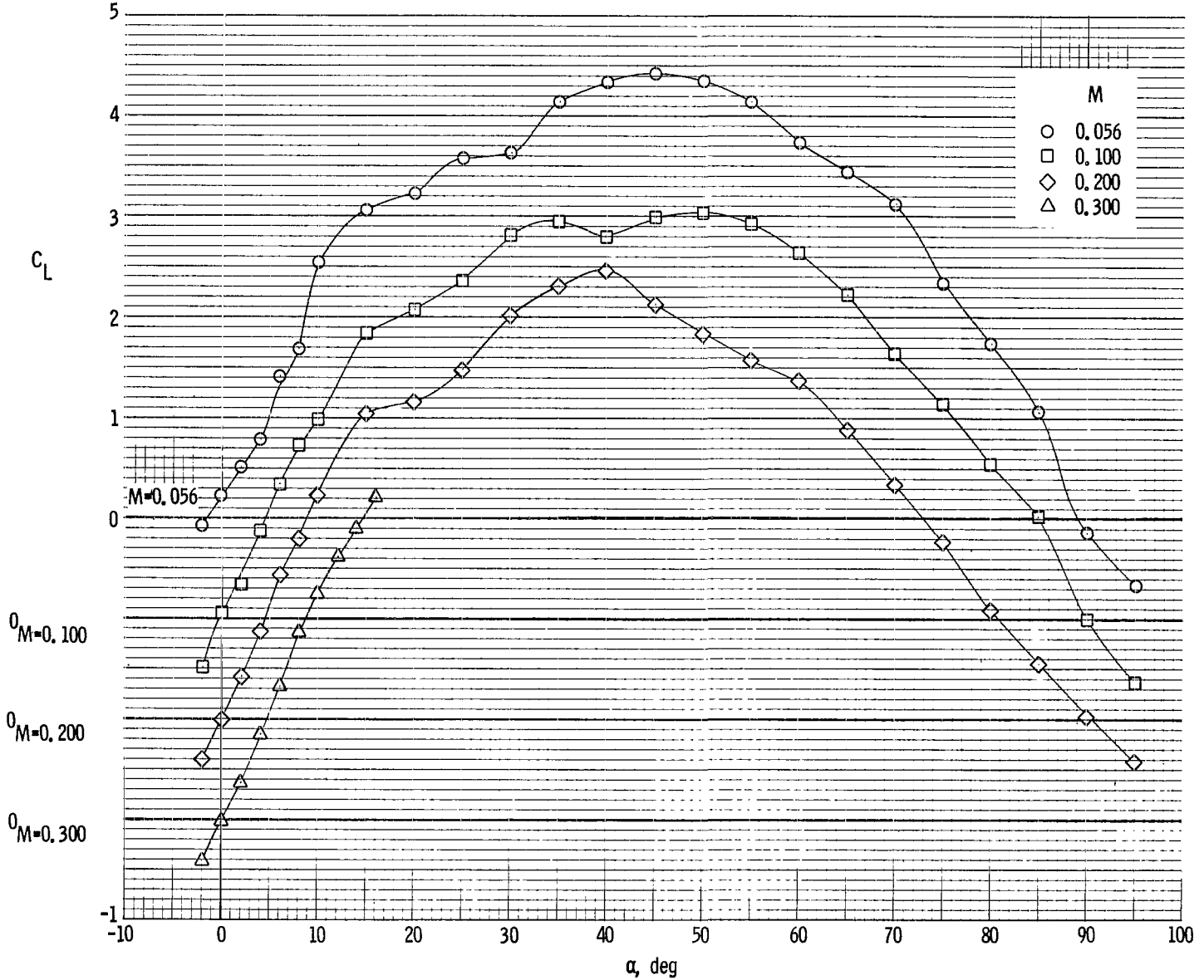

(d) Lift coefficient.

Figure 15. - Continued.

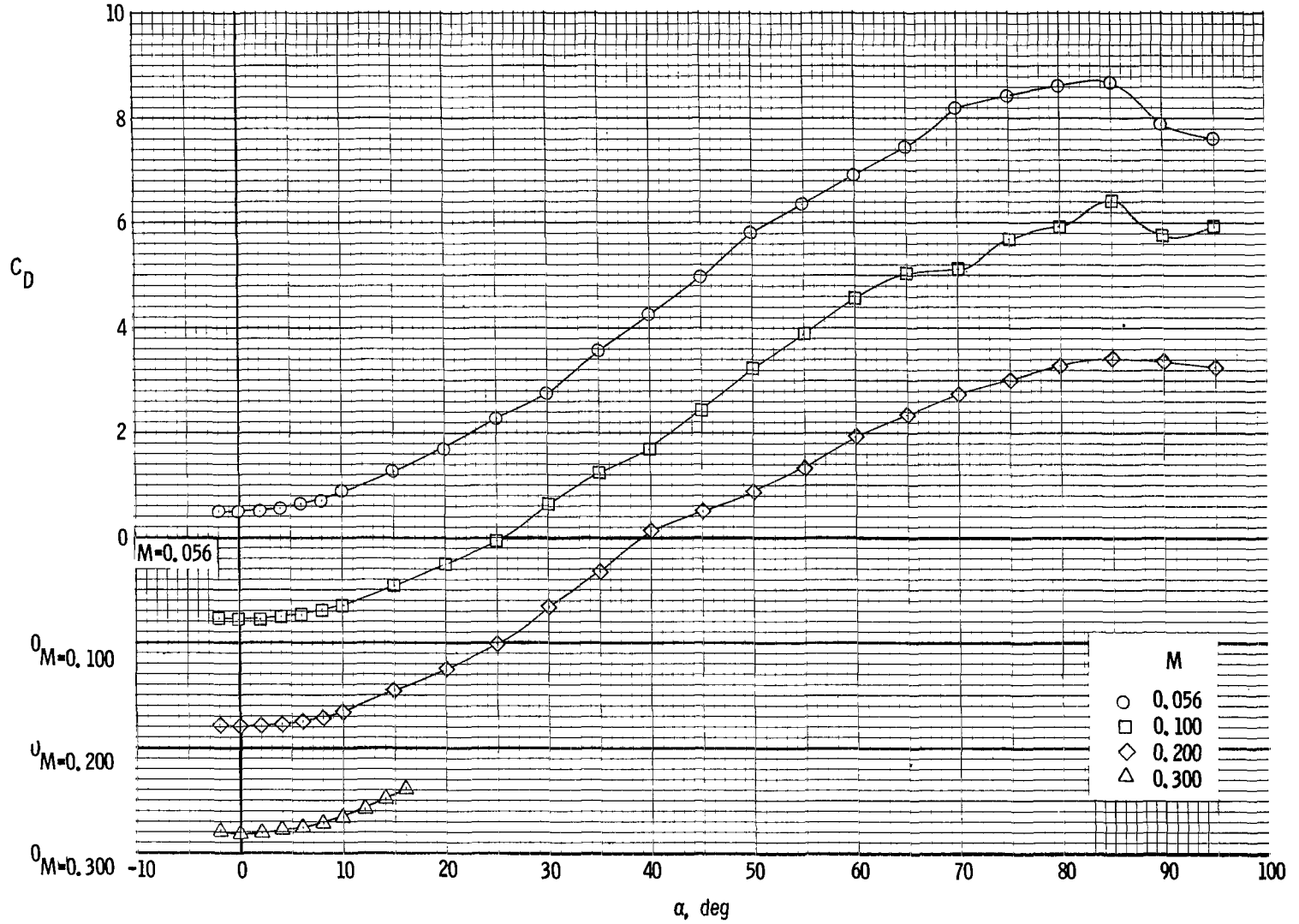

(e) Drag coefficient.

Figure 15. - Continued.

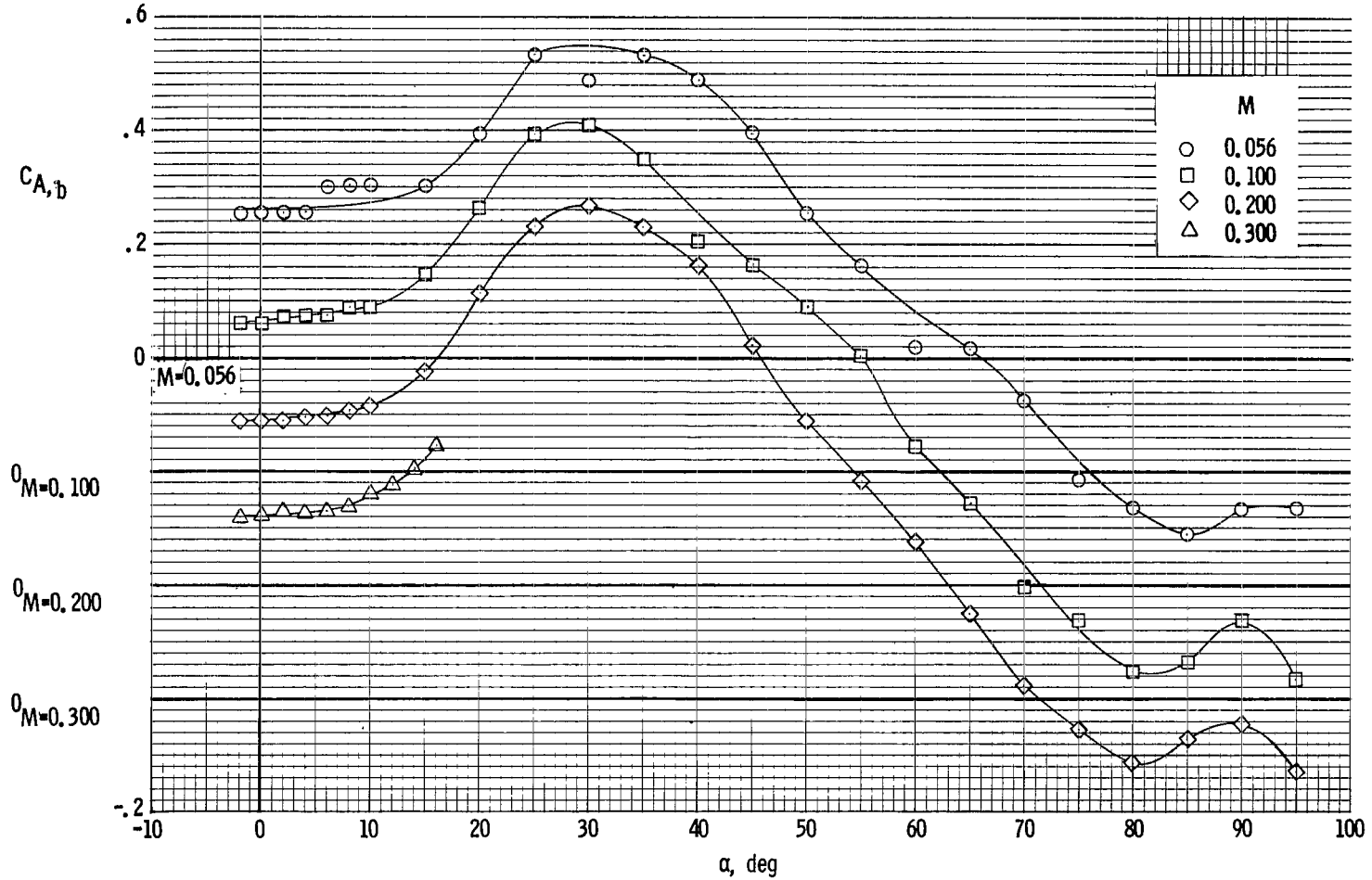

(f) Base axial-force coefficient.

Figure 15. - Concluded.

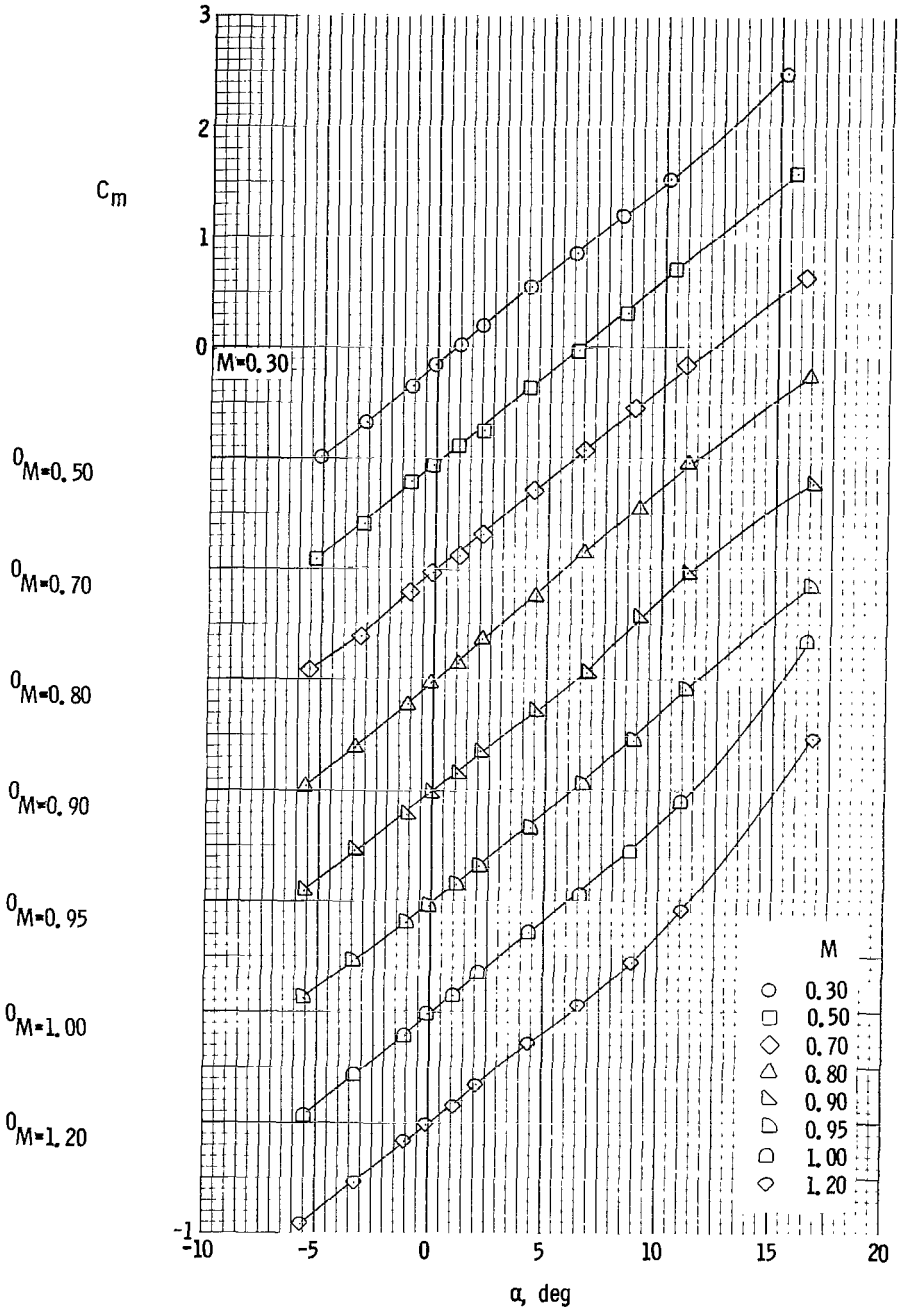

(a) Pitching-moment coefficient.

Figure 16. - Aerodynamic characteristics of configuration II with large fins and long service module at Mach numbers from 0.30 to 1.20.

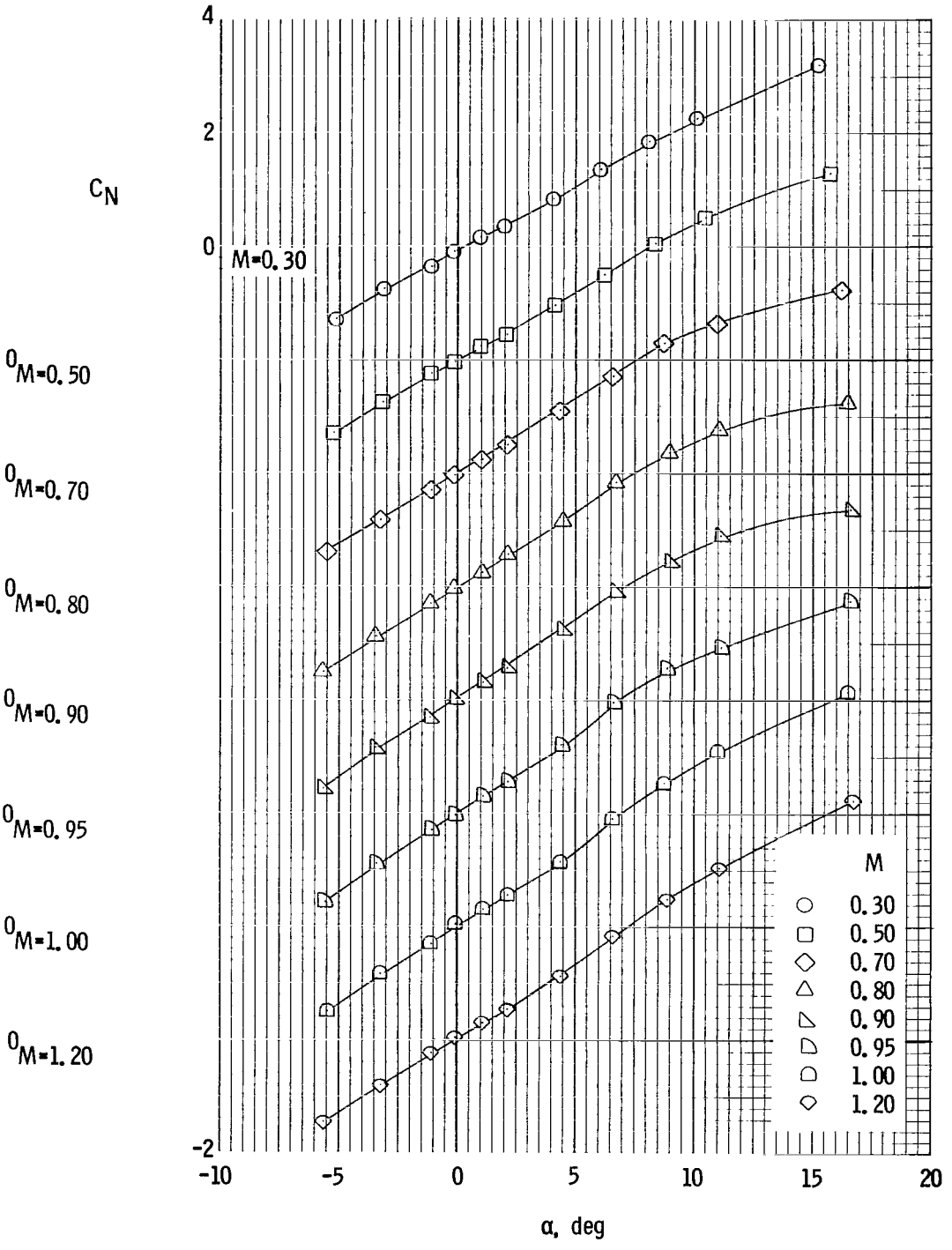

(b) Normal-force coefficient.

Figure 16. - Continued.

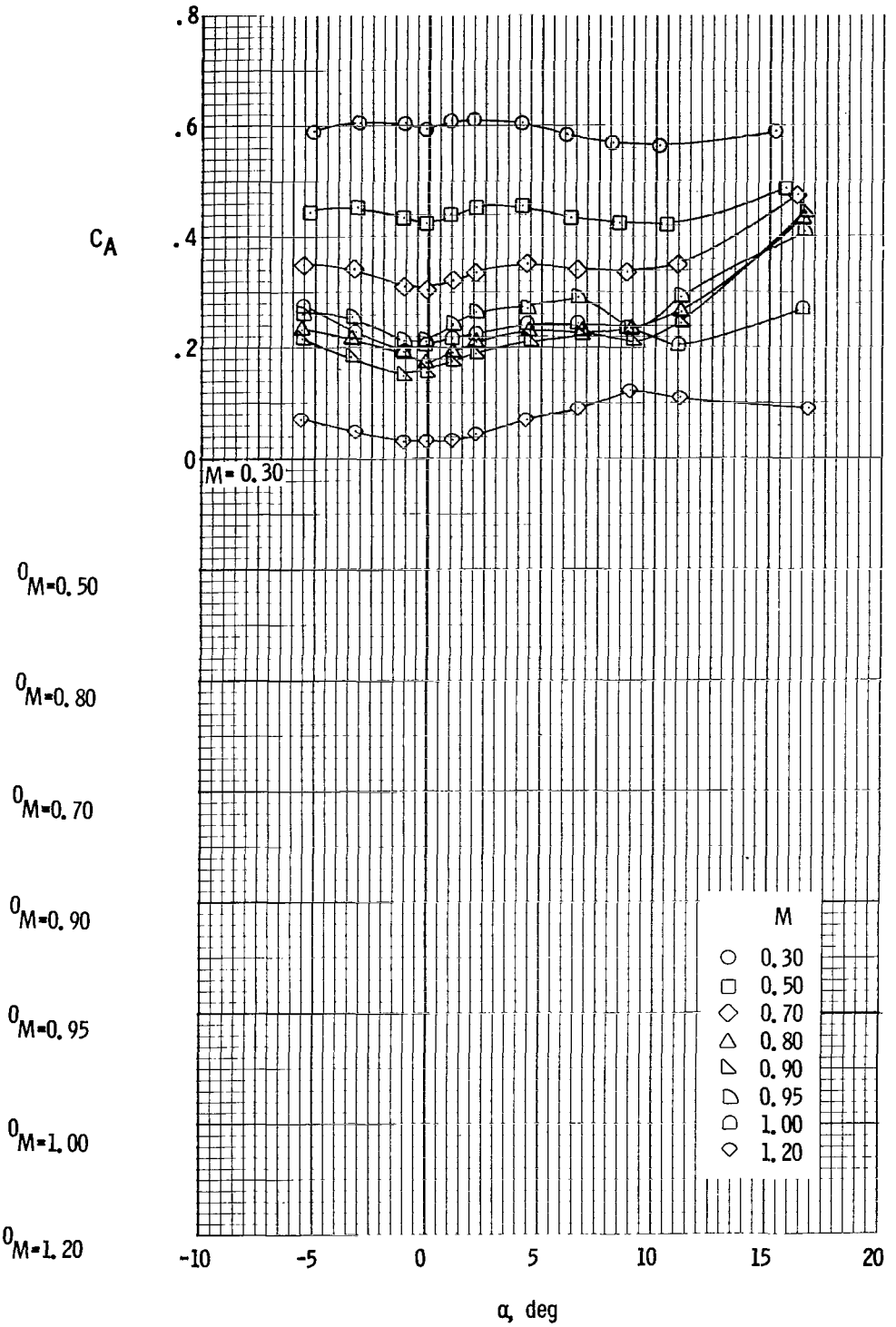

(c) Axial-force coefficient.

Figure 16. - Continued.

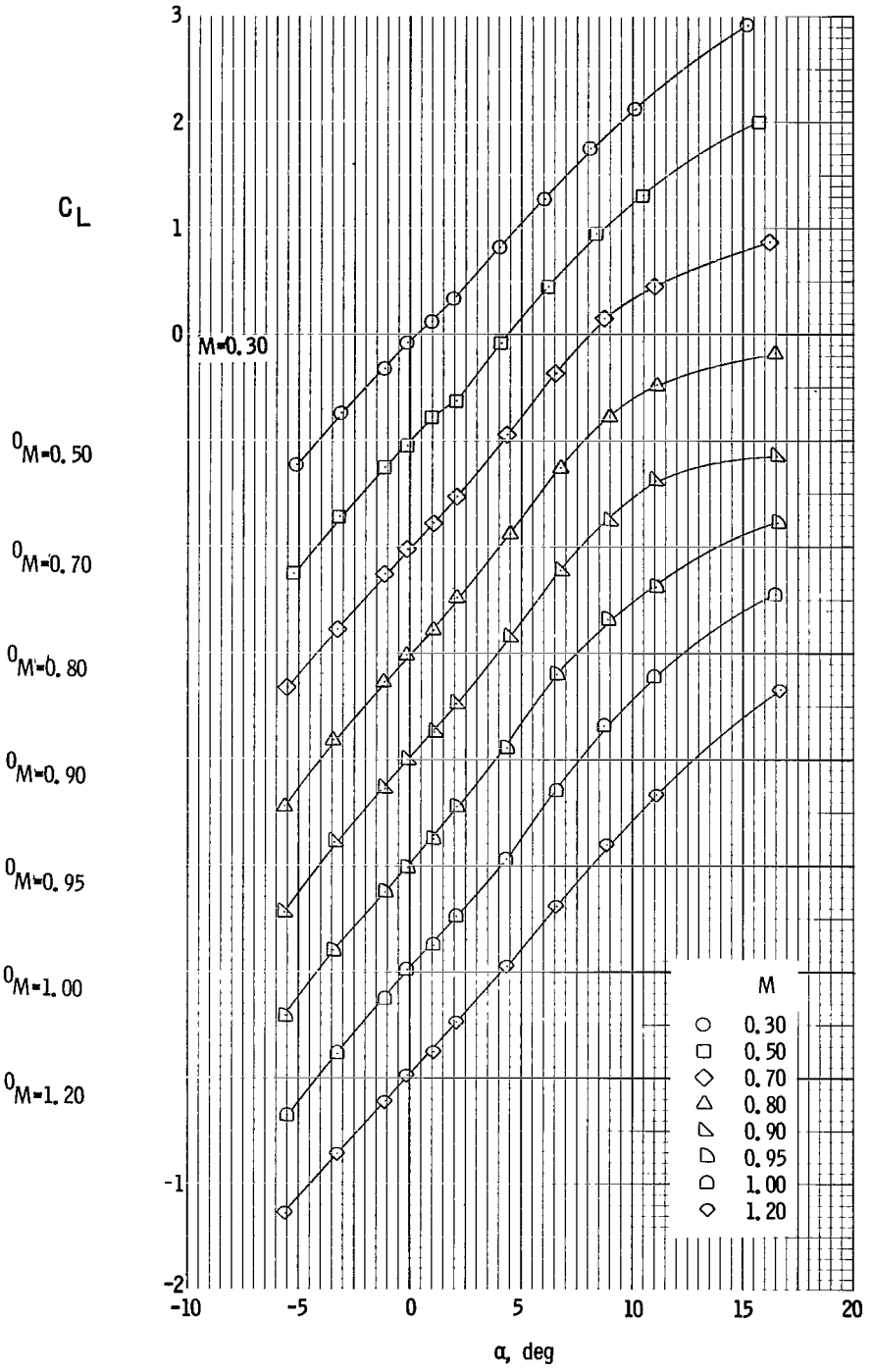

(d) Lift coefficient.

Figure 16. - Continued.

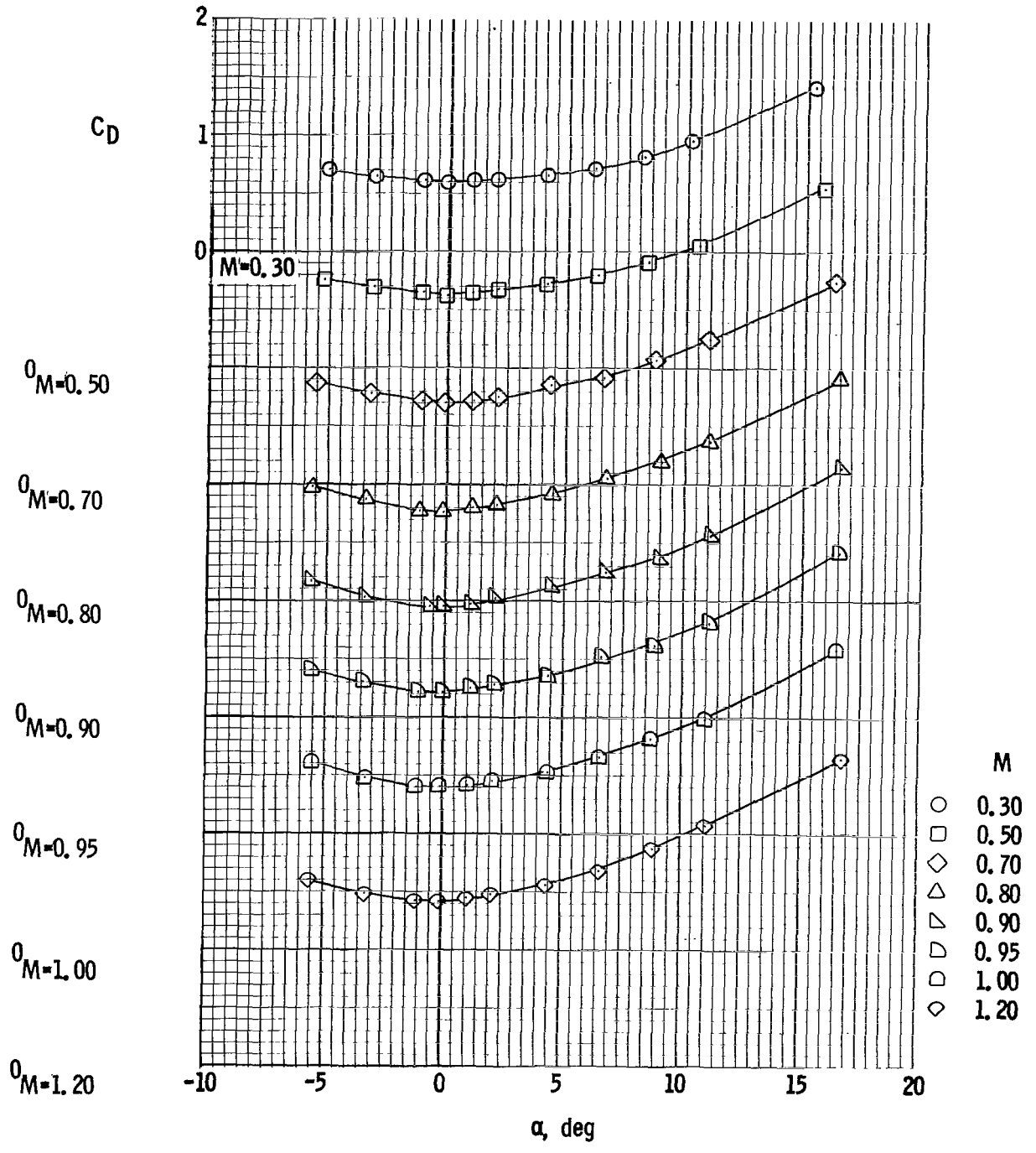

(e) Drag coefficient.

Figure 16. - Continued.

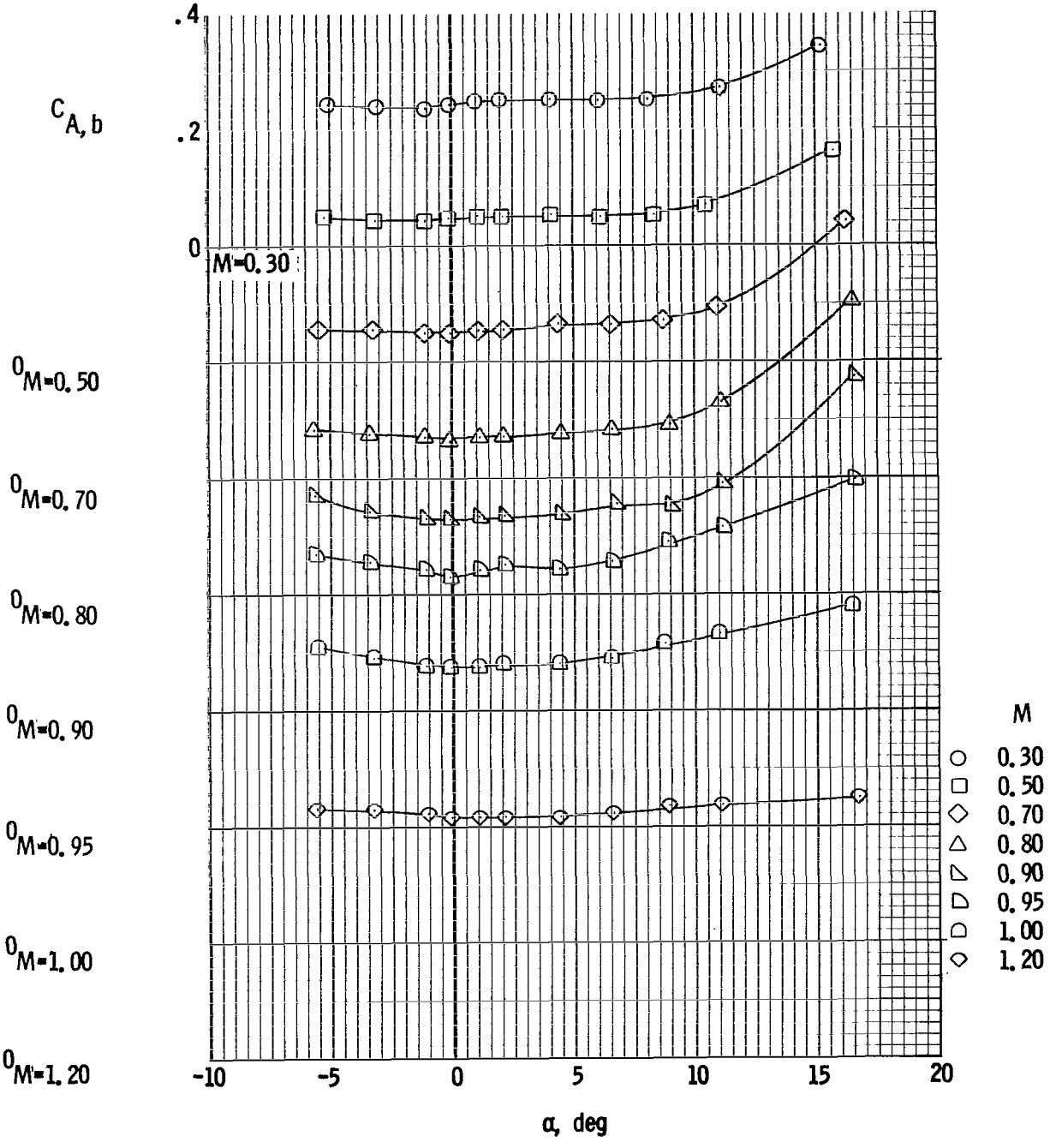

(f) Base axial-force coefficient.

Figure 16. - Concluded.

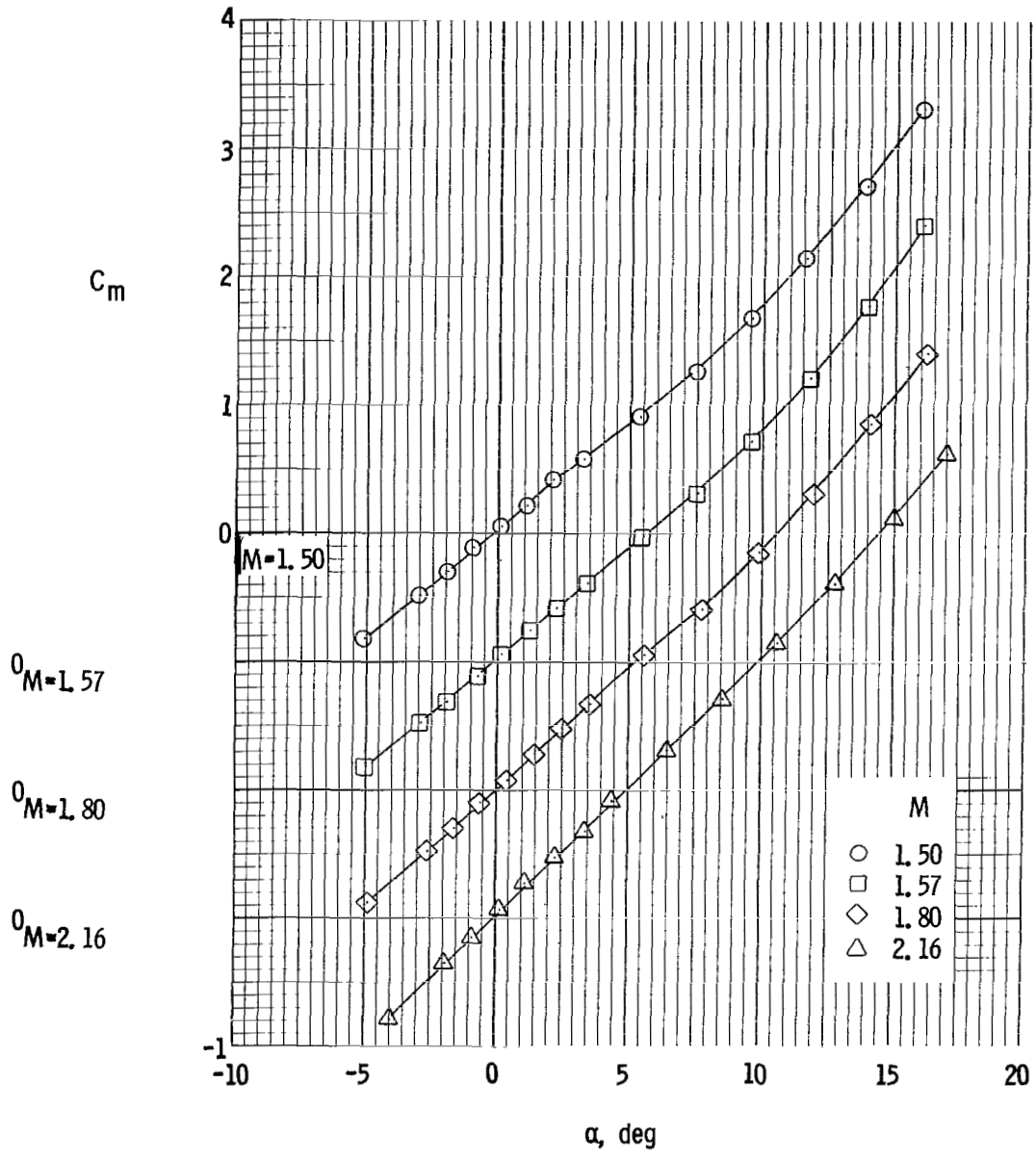

(a) Pitching-moment coefficient.

Figure 17. - Aerodynamic characteristics of configuration II with large fins and long service module at Mach numbers from 1.50 to 2.16.

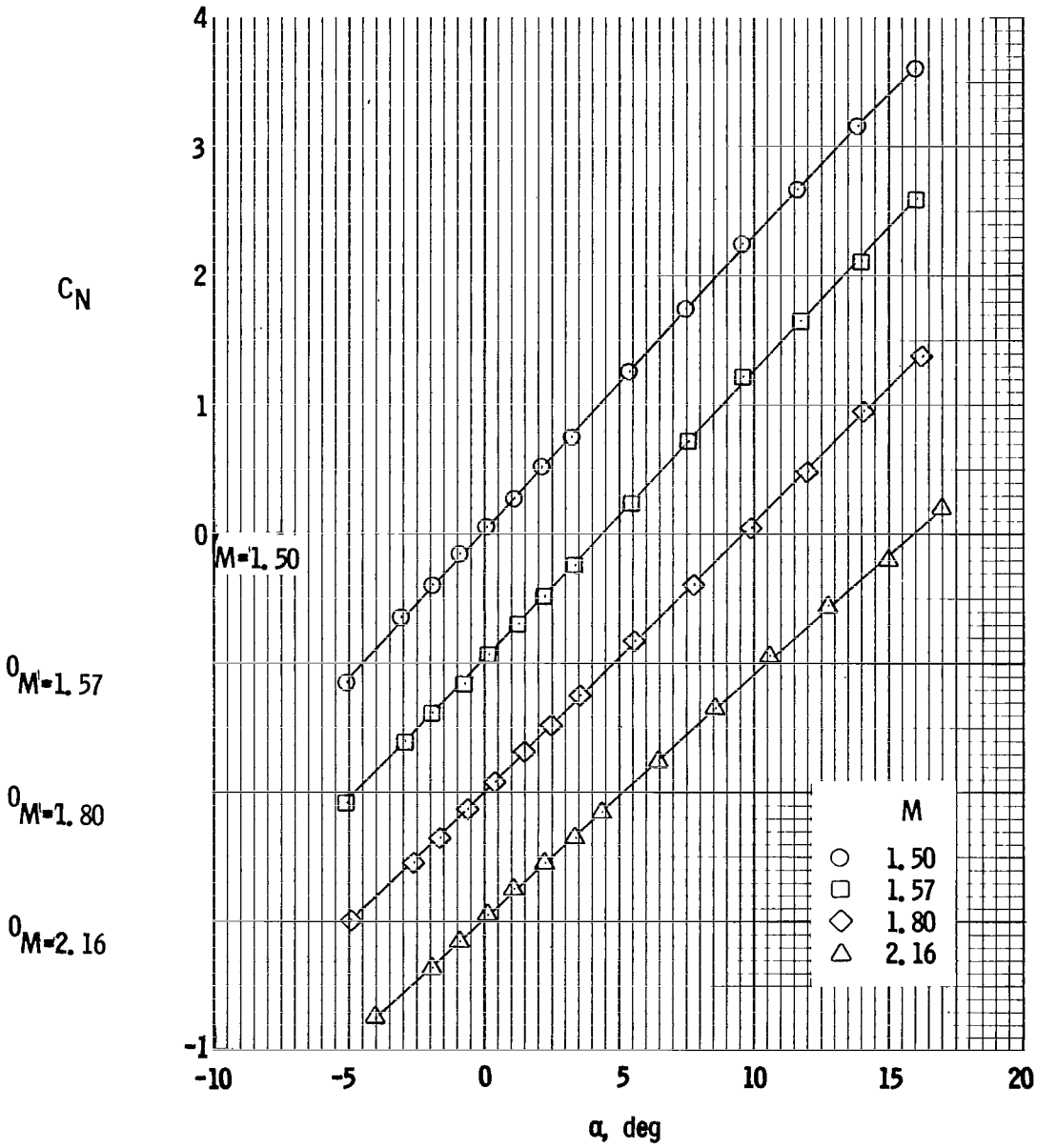

(b) Normal-force coefficient.

Figure 17. - Continued.

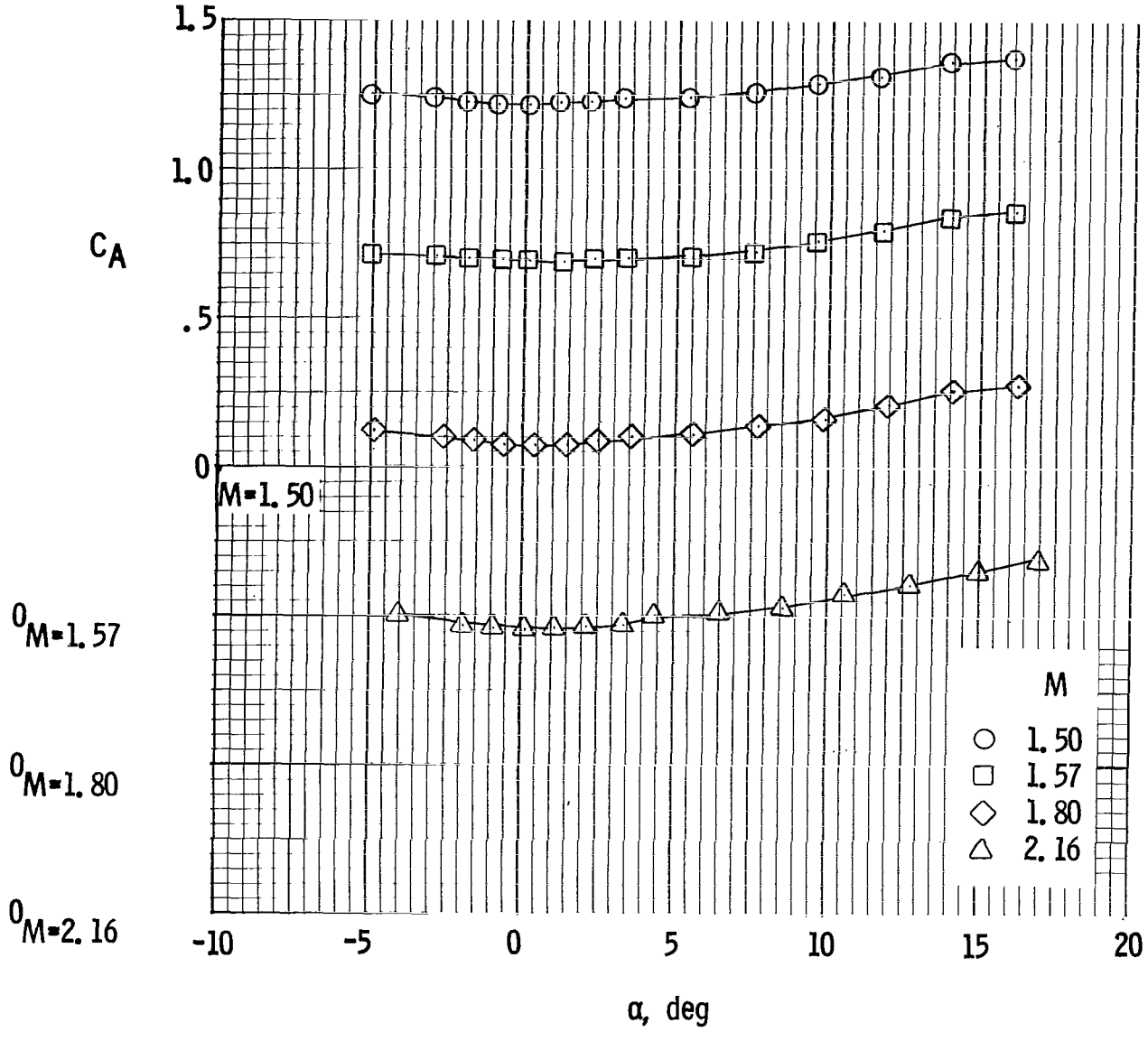

(c) Axial-force coefficient.

Figure 17. - Continued.

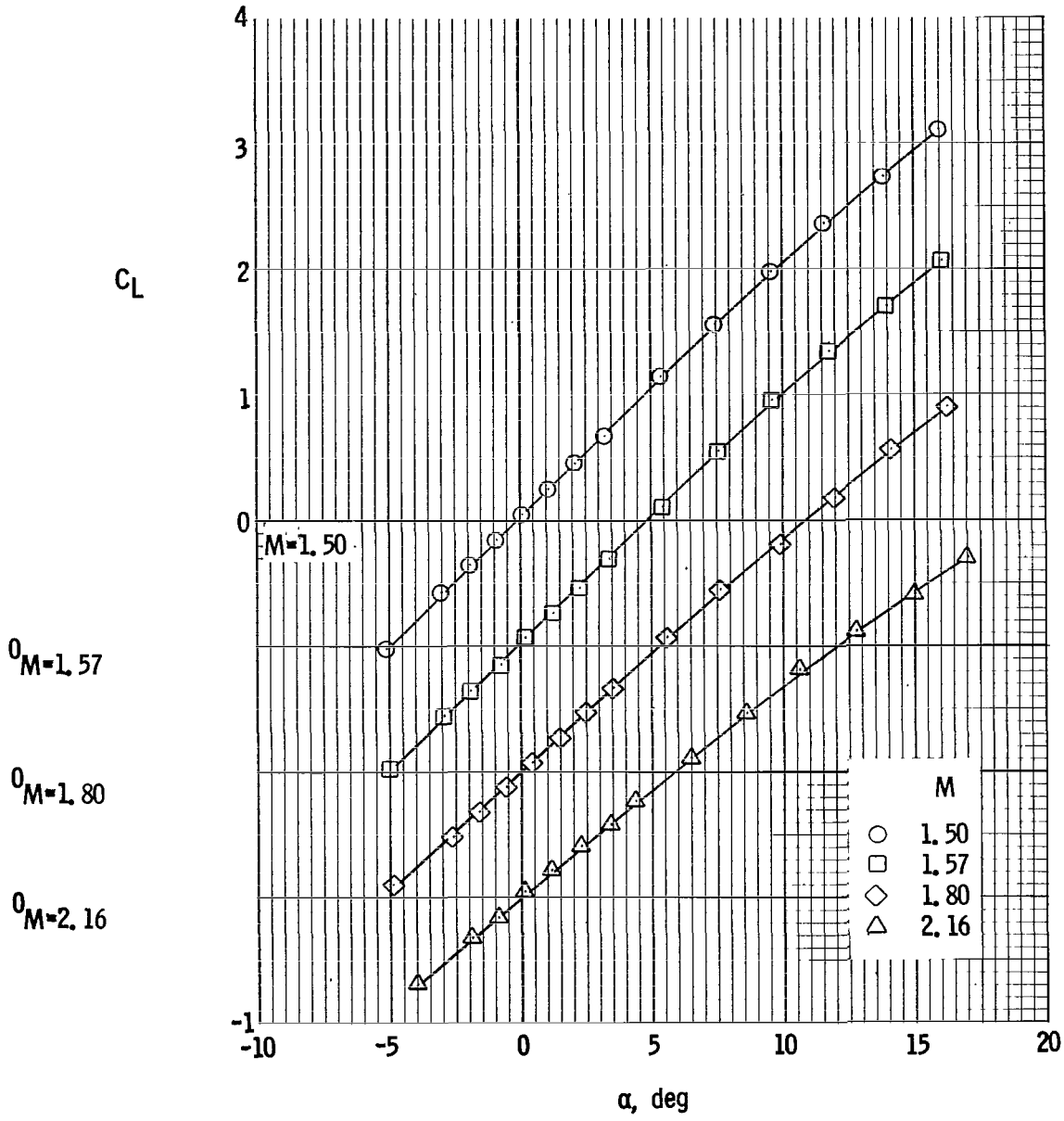

(d) Lift coefficient.

Figure 17. - Continued.

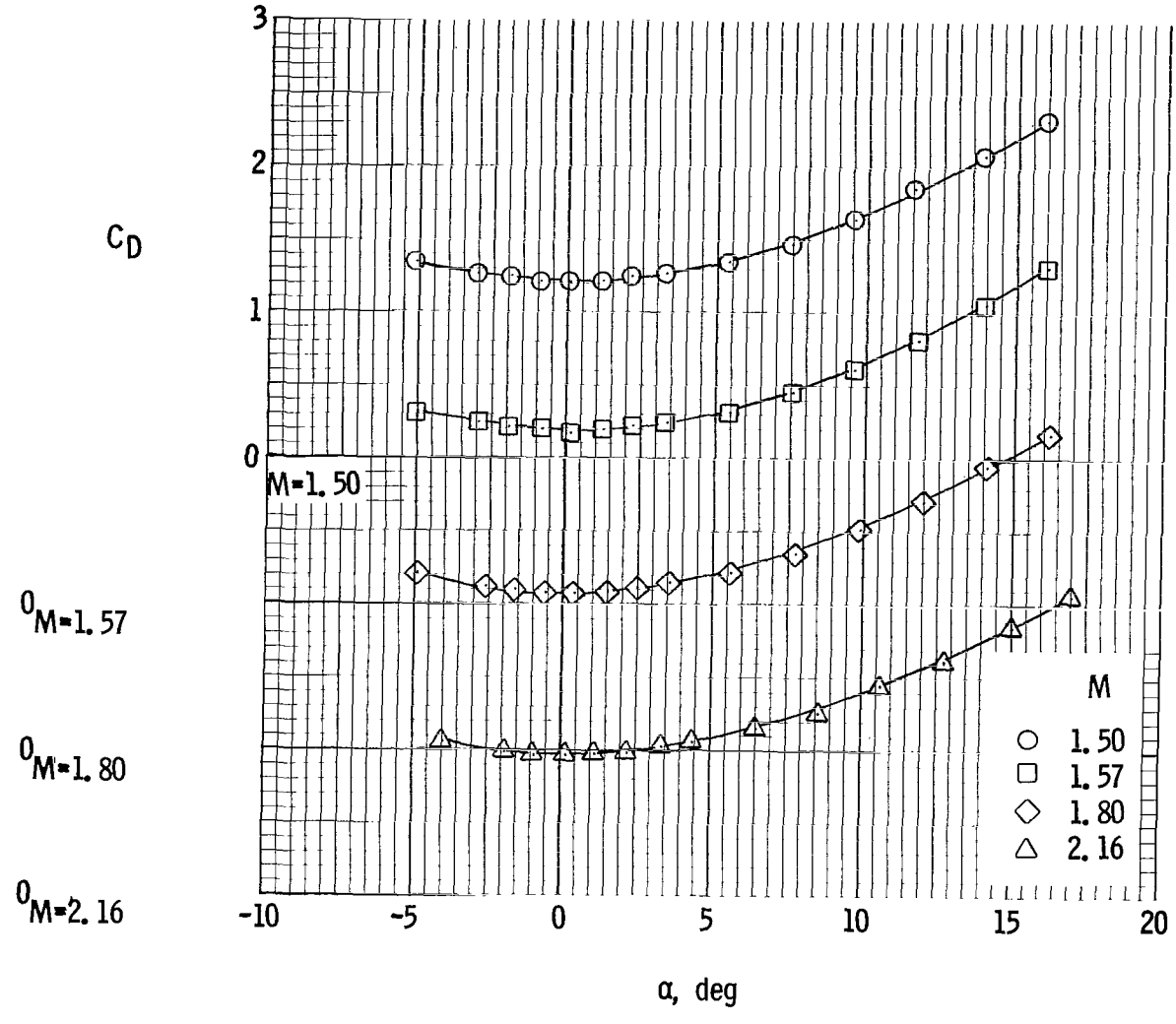

(e) Drag coefficient.

Figure 17. - Continued.

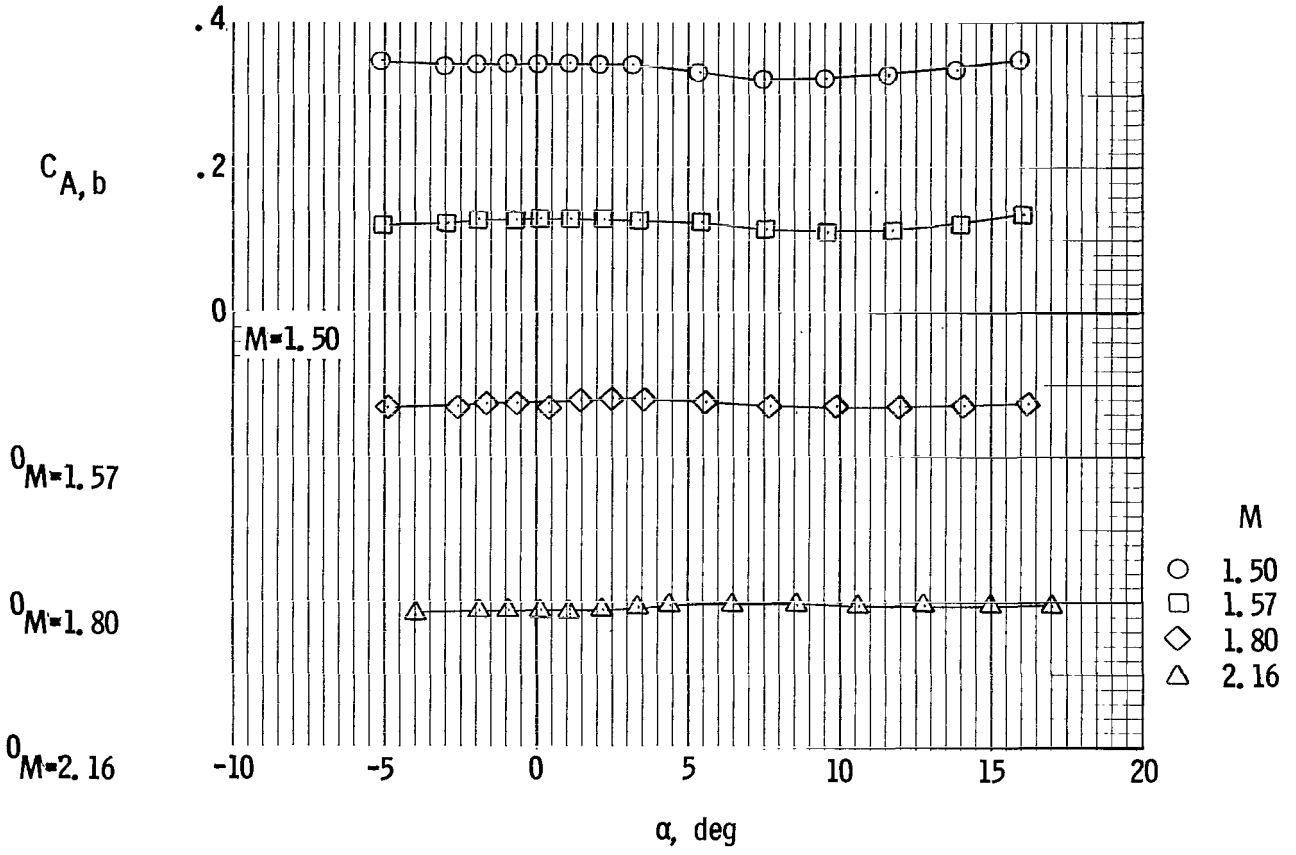

(f) Base axial-force coefficient.

(f) Base axial-force coefficient.

Figure 17. - Concluded.

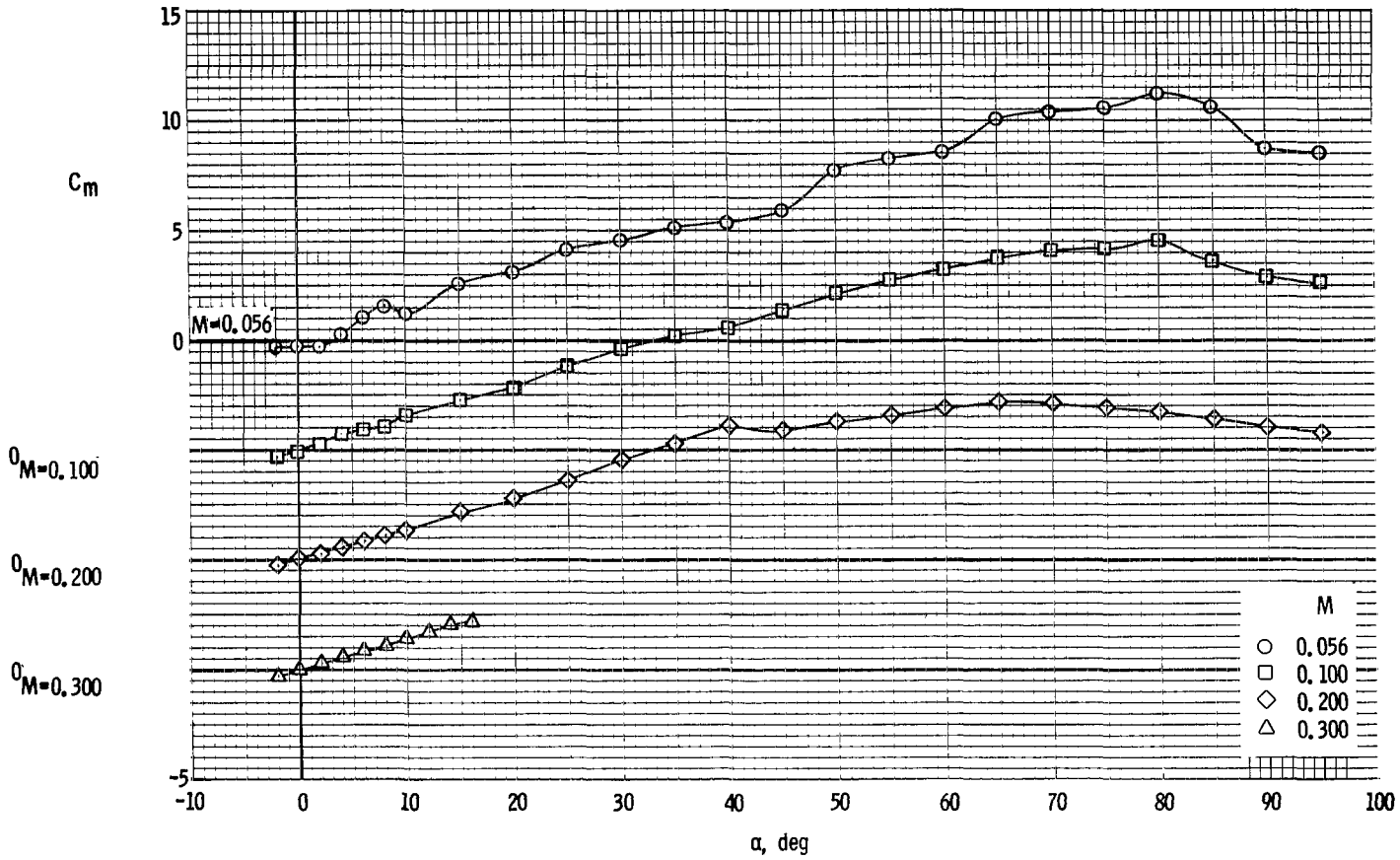

(a) Pitching-moment coefficient.

Figure 18. - Aerodynamic characteristics of configuration II with large fins and short service module at Mach numbers from 0.056 to 0.300.

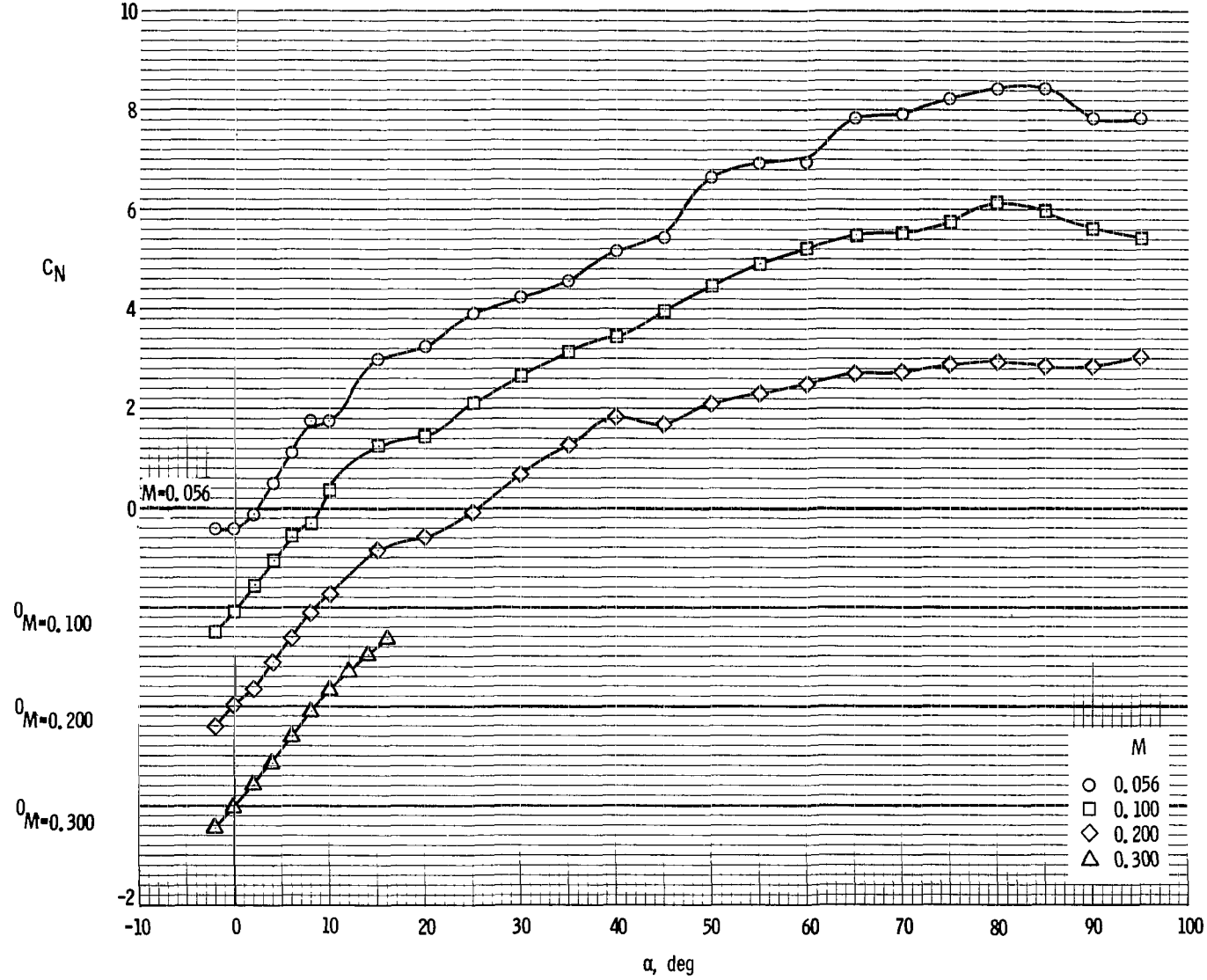

(b) Normal-force coefficient.

Figure 18. - Continued.

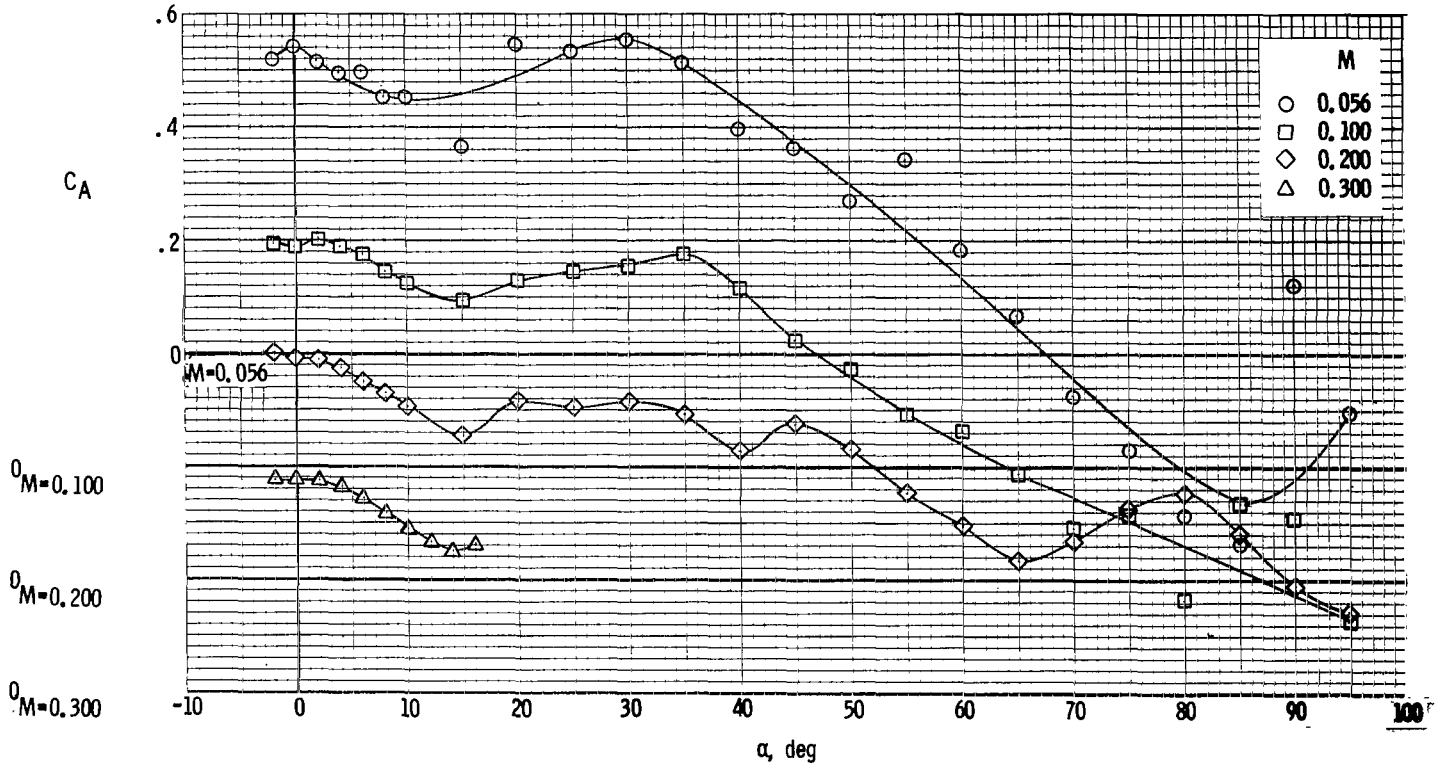

(c) Axial-force coefficient.

Figure 18. - Continued.

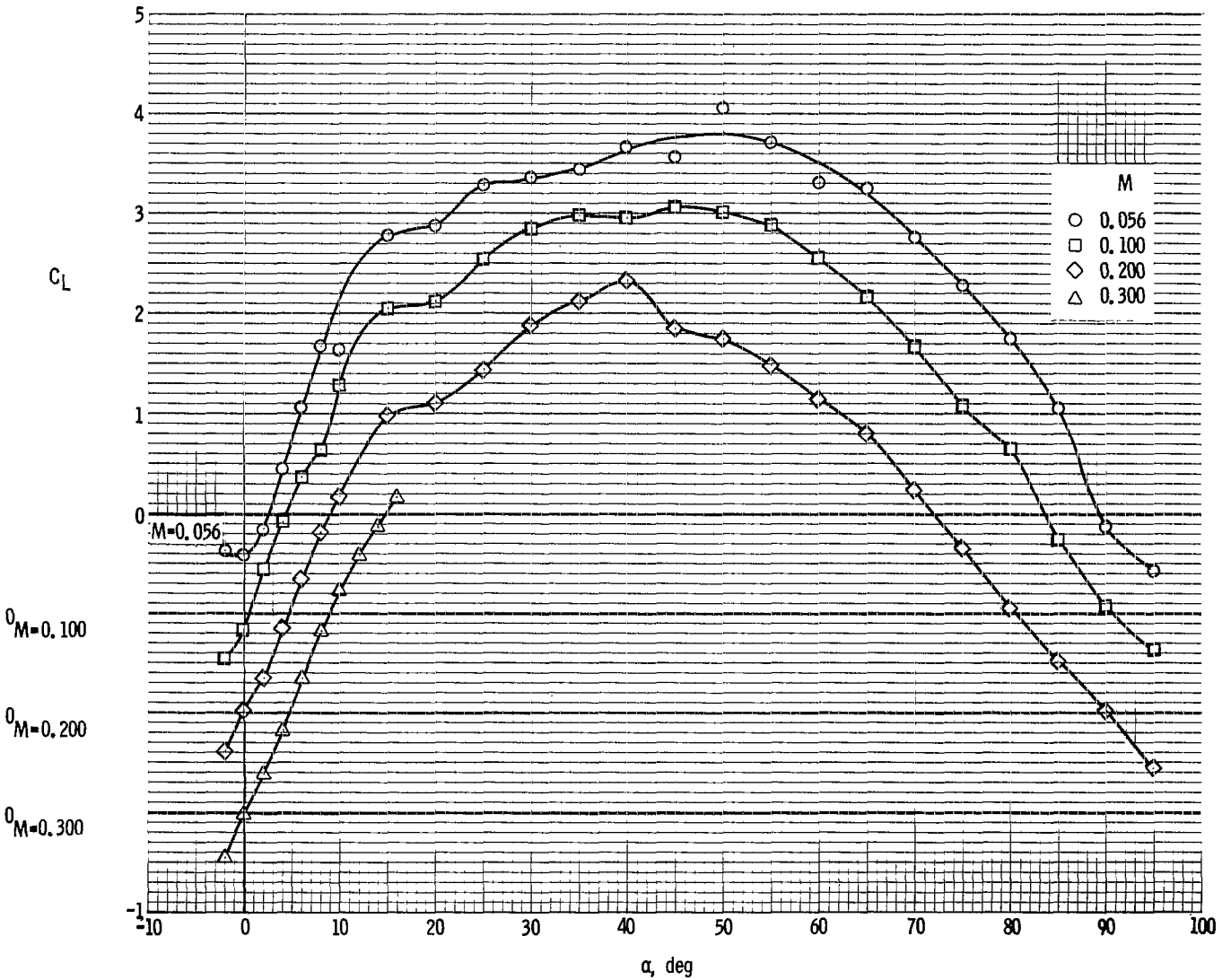

(d) Lift coefficient.

Figure 18. - Continued.

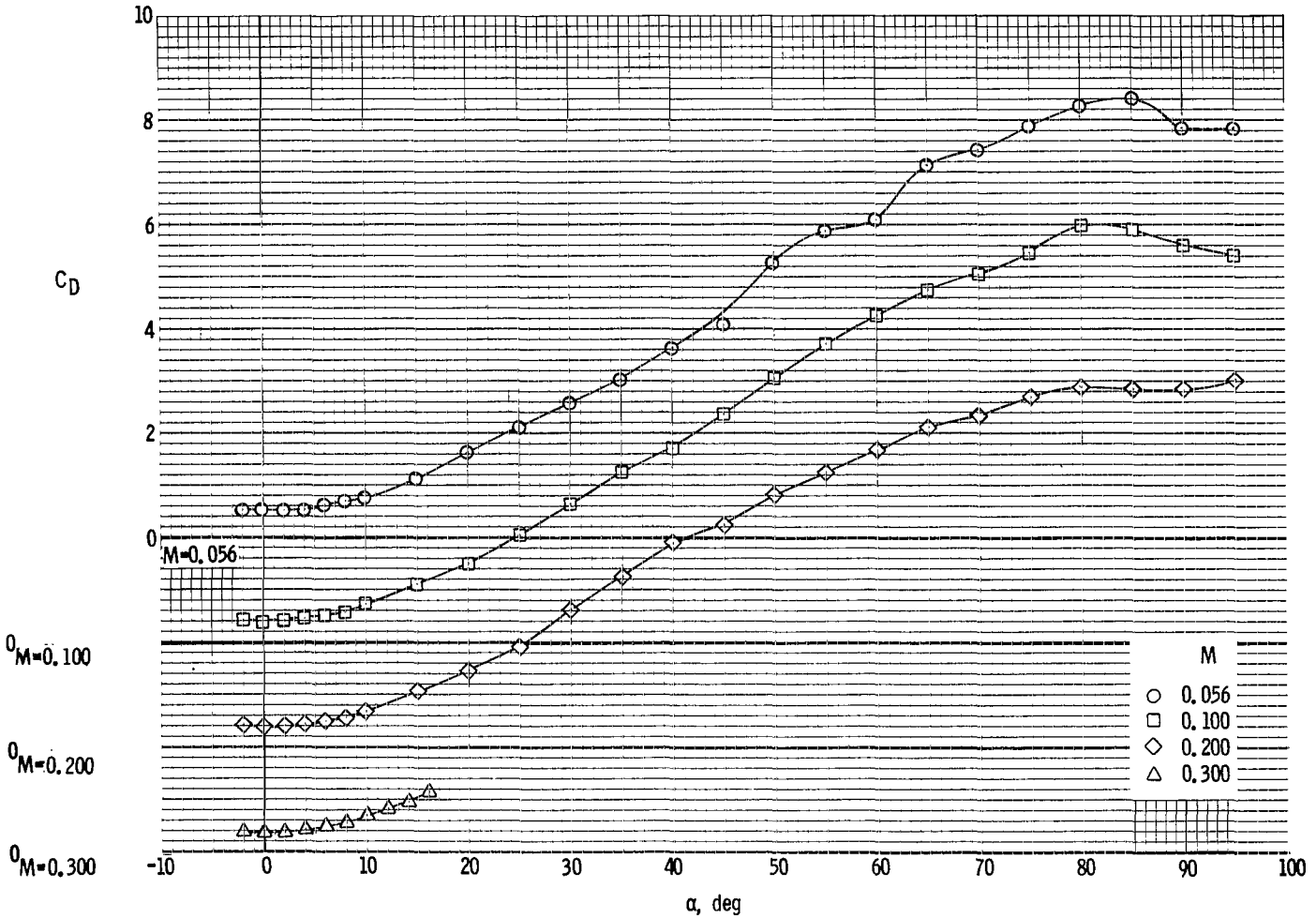

(e) Drag coefficient.

Figure 18. - Continued.

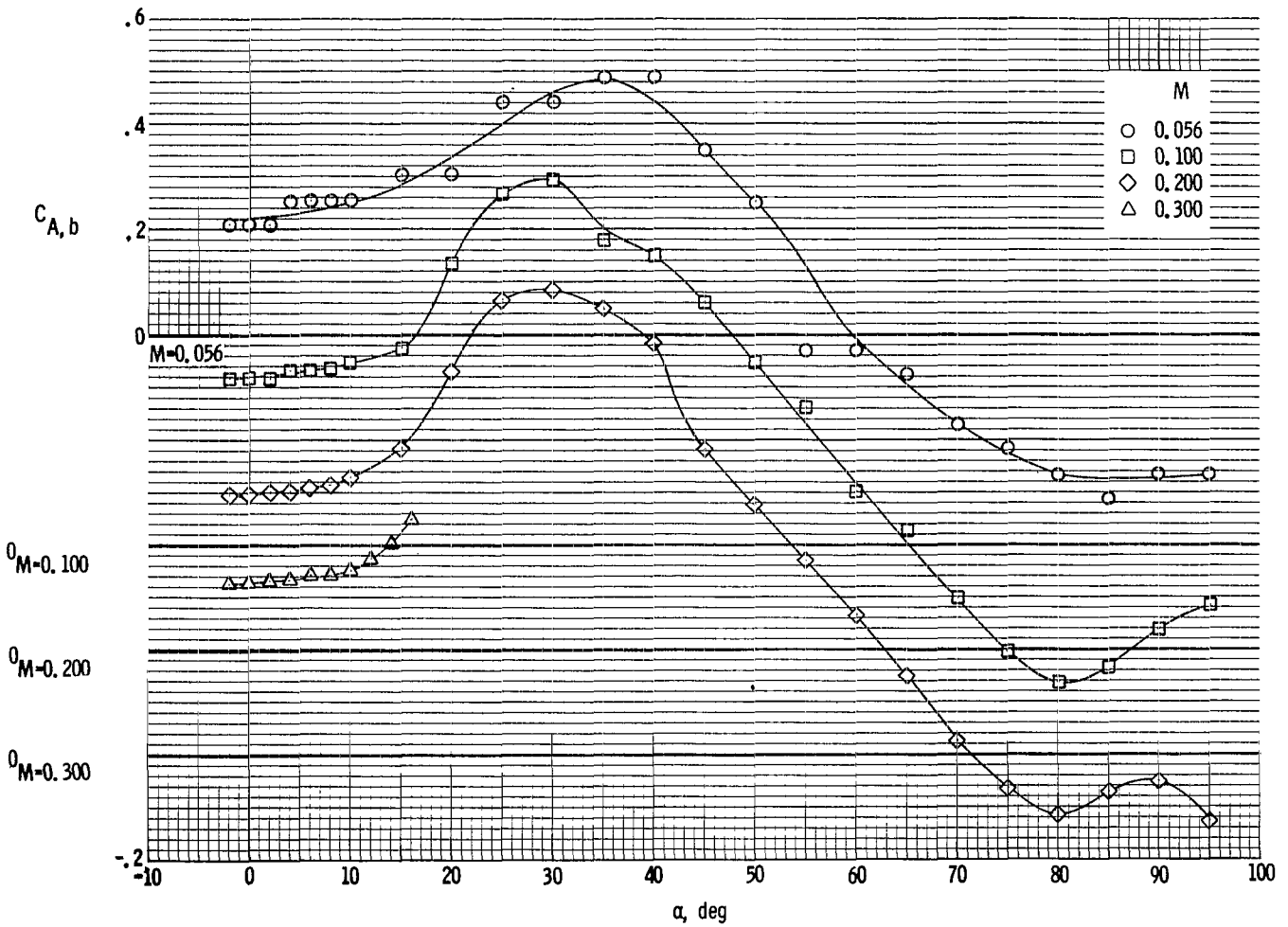

(f) Base axial-force coefficient.

Figure 18. - Concluded.

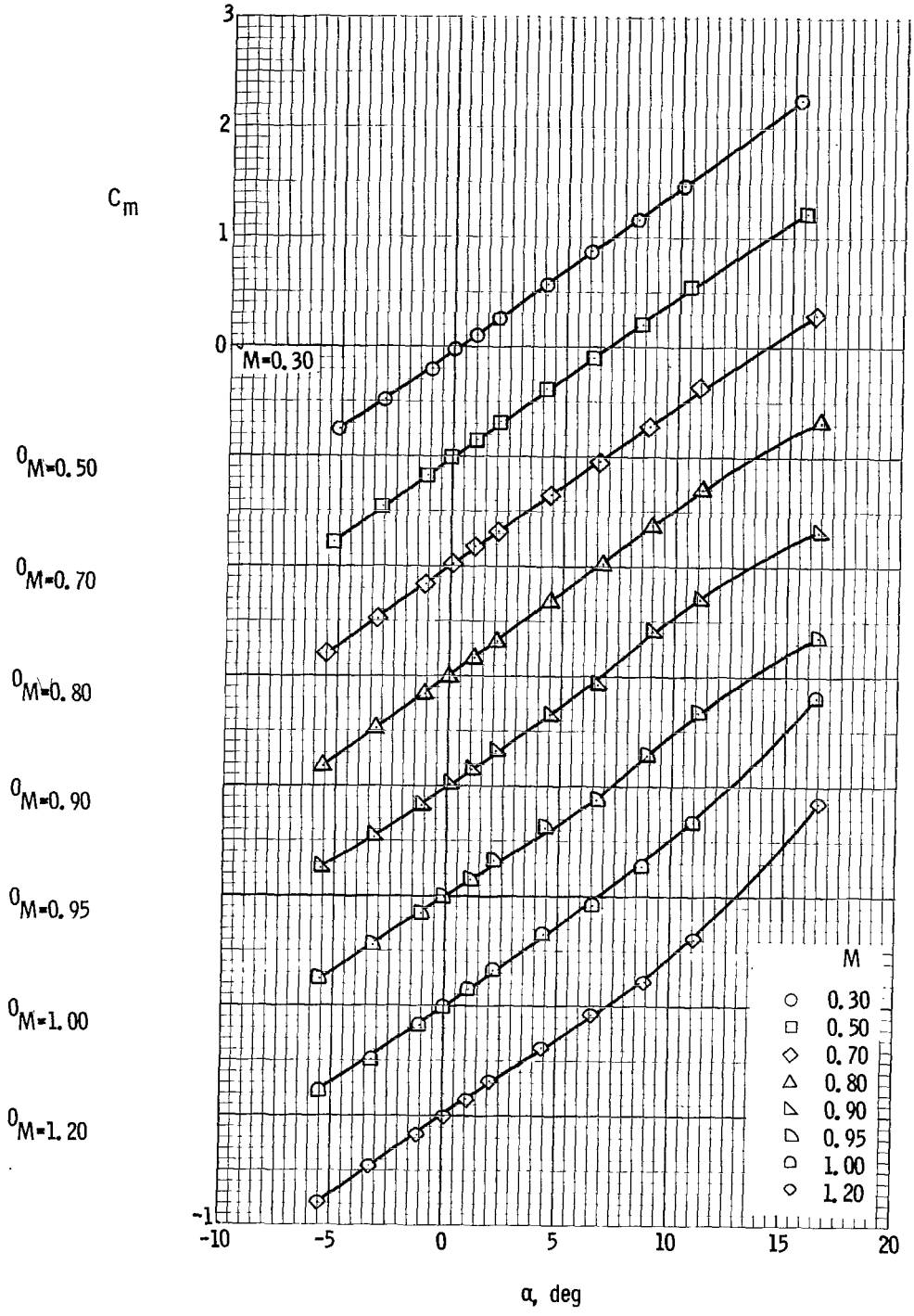

(a) Pitching-moment coefficient.

Figure 19. - Aerodynamic characteristics of configuration II with large fins and short service module at Mach numbers from 0.30 to 1.20.

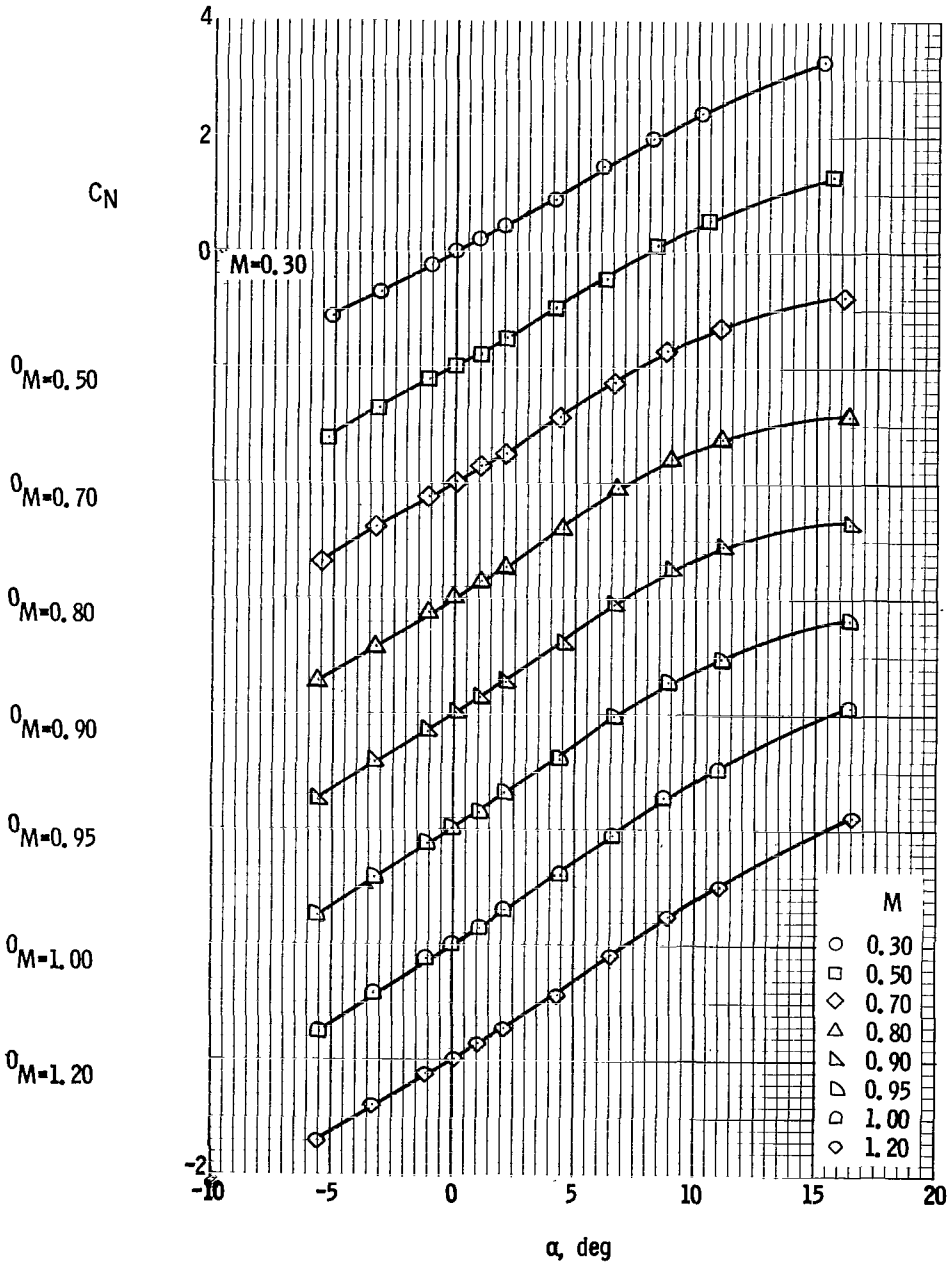

(b) Normal-force coefficient.

Figure 19. - Continued.

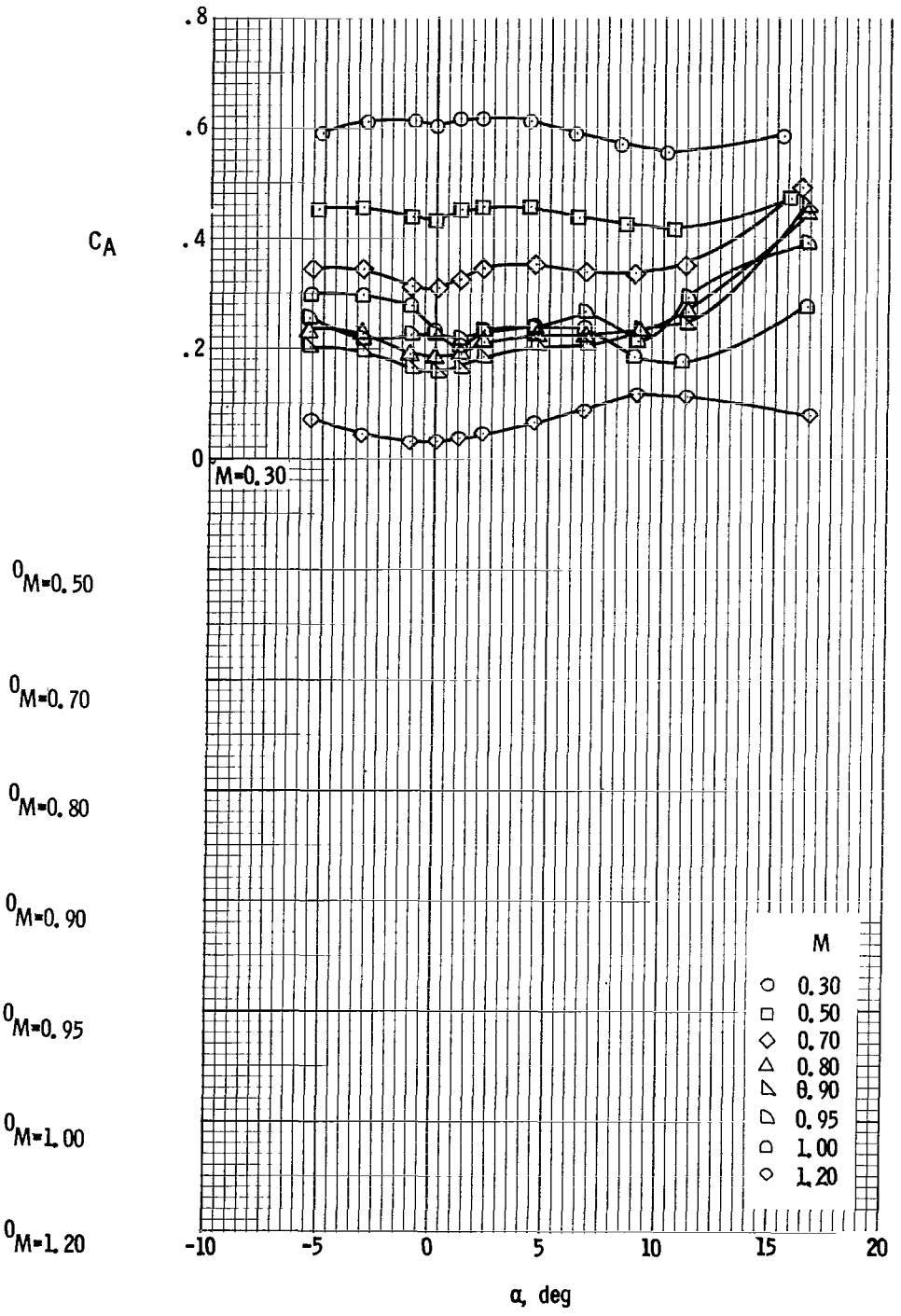

(c) Axial-force coefficient.

Figure 19. - Continued.

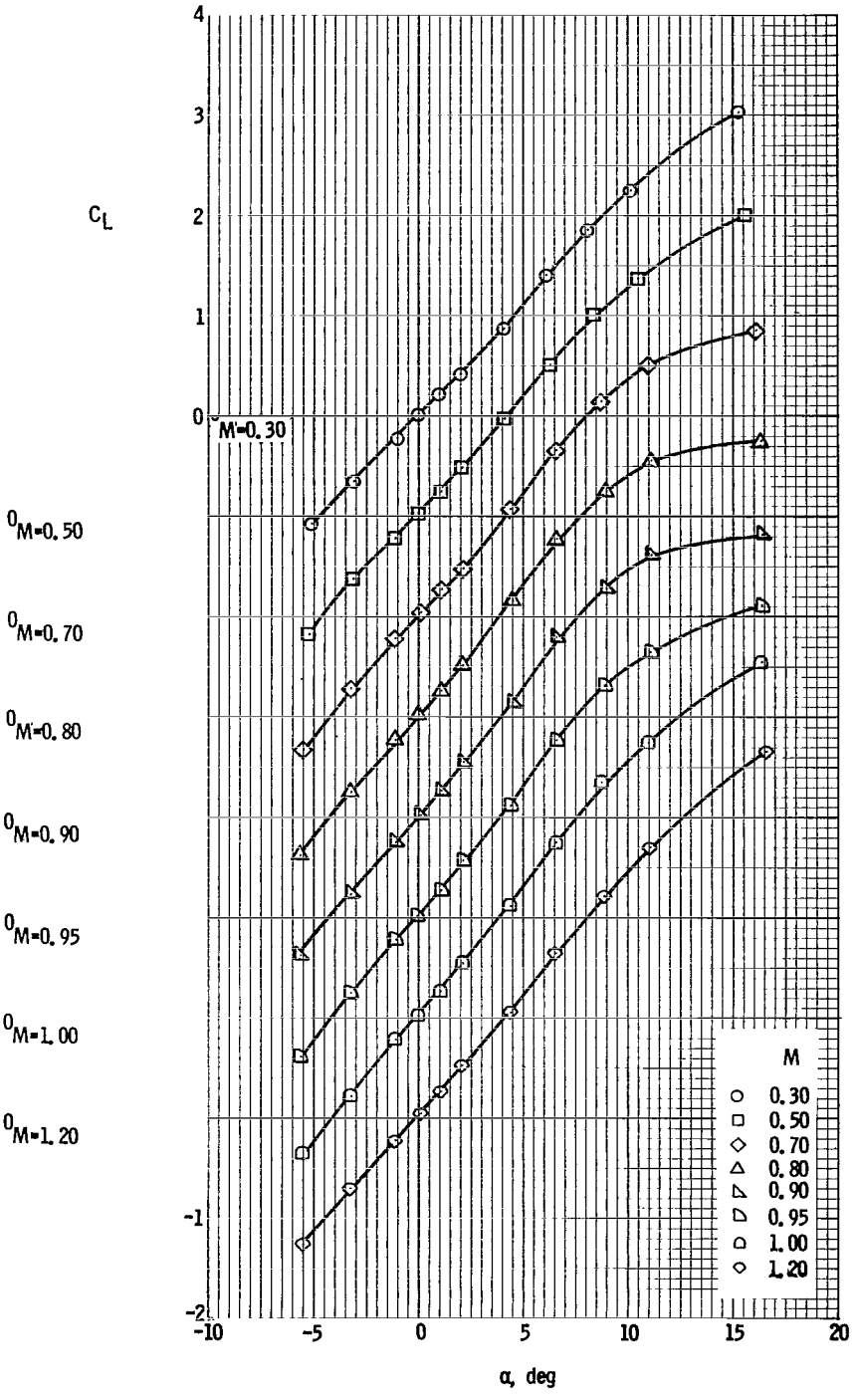

(d) Lift coefficient.

Figure 19. - Continued.

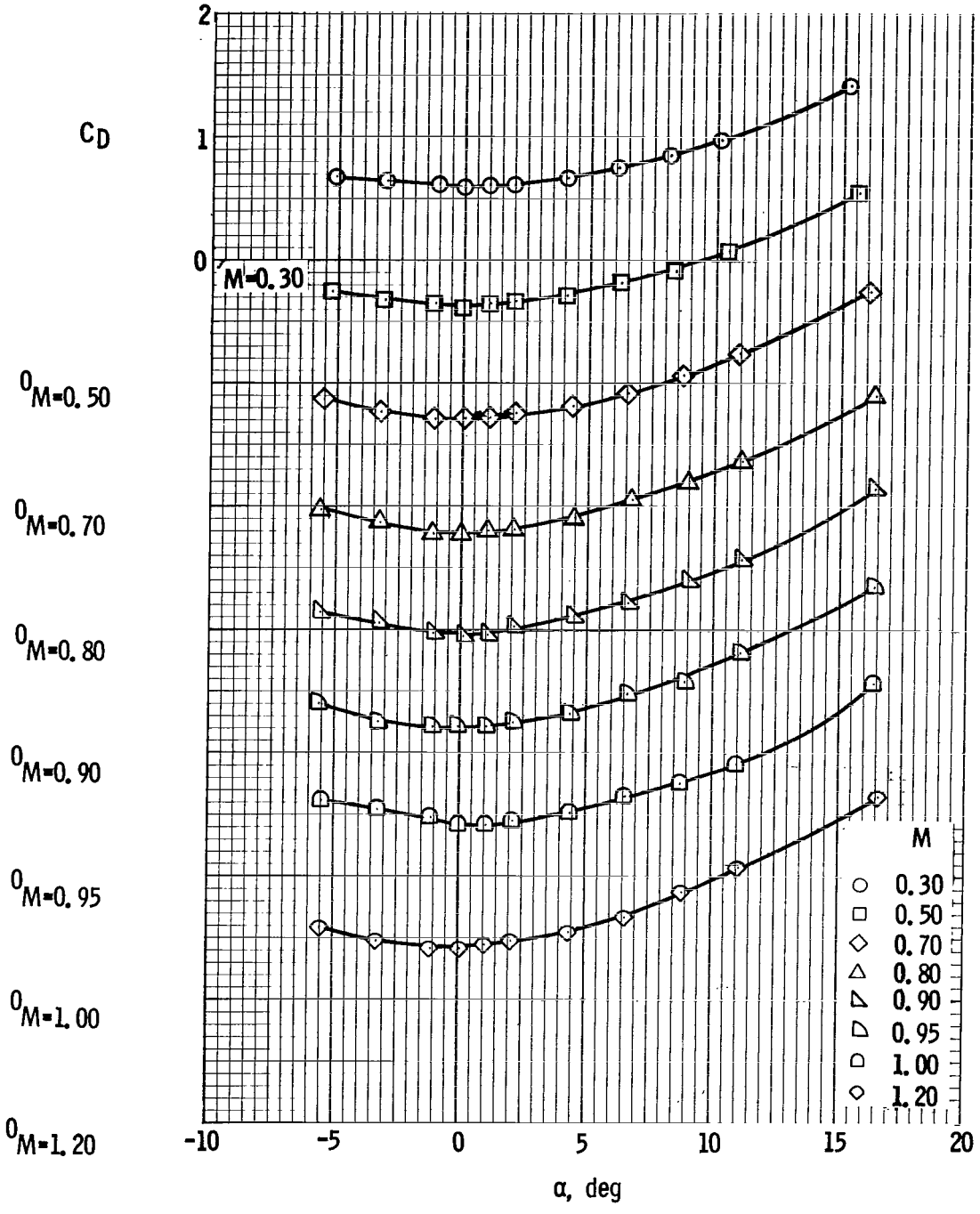

(e) Drag coefficient.

Figure 19. - Continued.

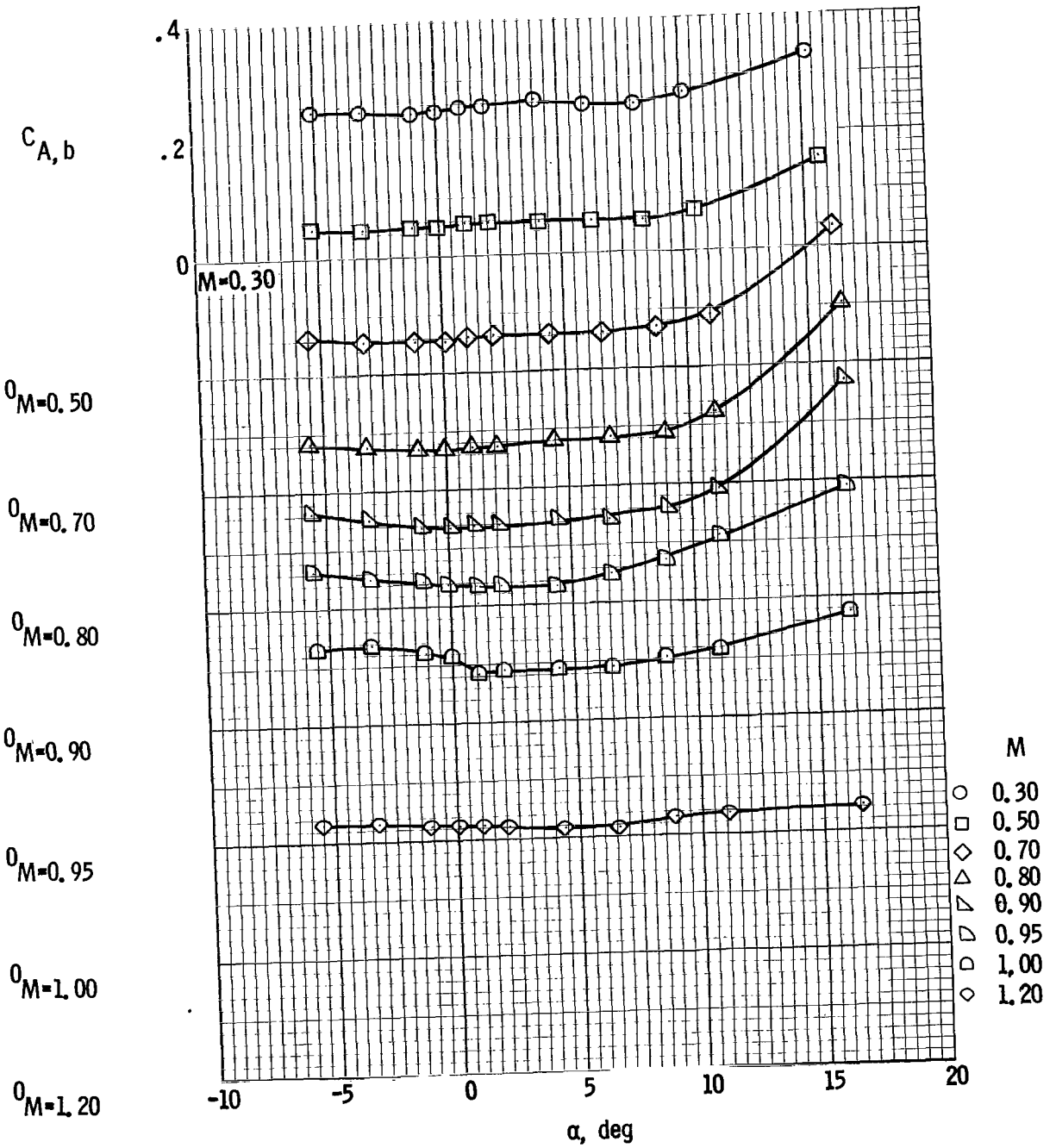

(f) Base axial-force coefficient.

Figure 19. - Concluded.

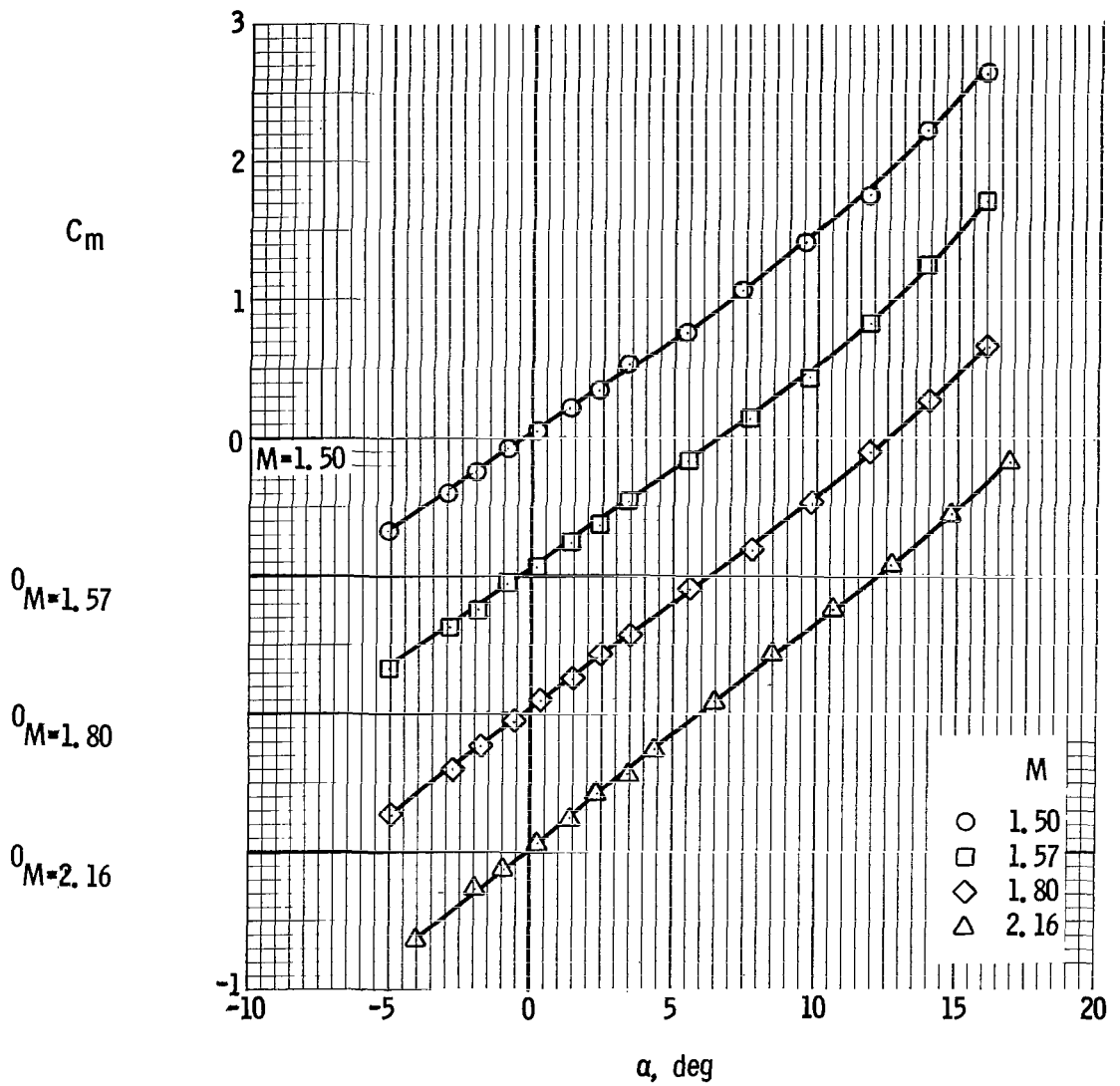

(a) Pitching-moment coefficient.

Figure 20. - Aerodynamic characteristics of configuration II with large fins and short service module at Mach numbers from 1.50 to 2.16.

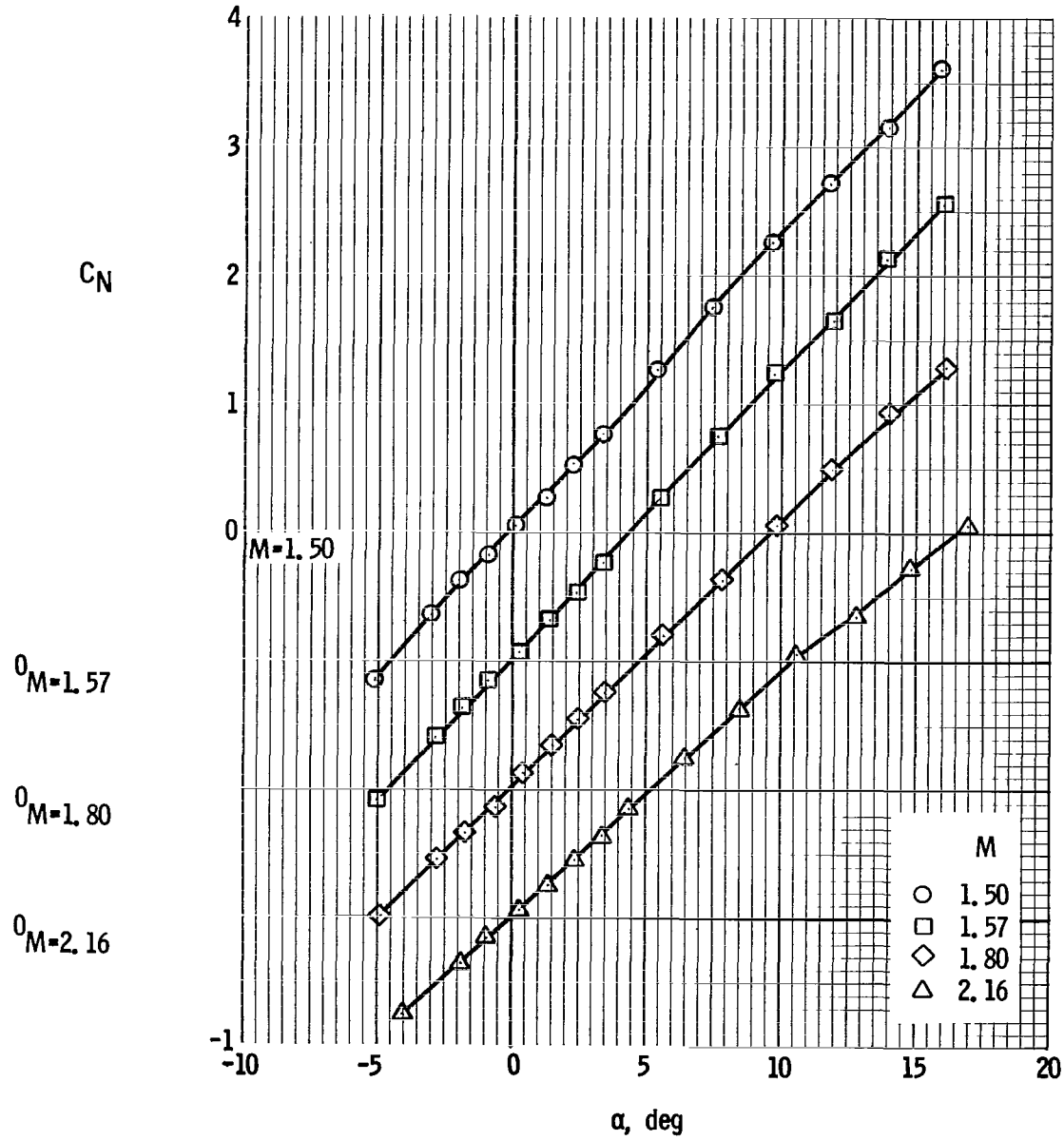

(b) Normal-force coefficient.

Figure 20. - Continued.

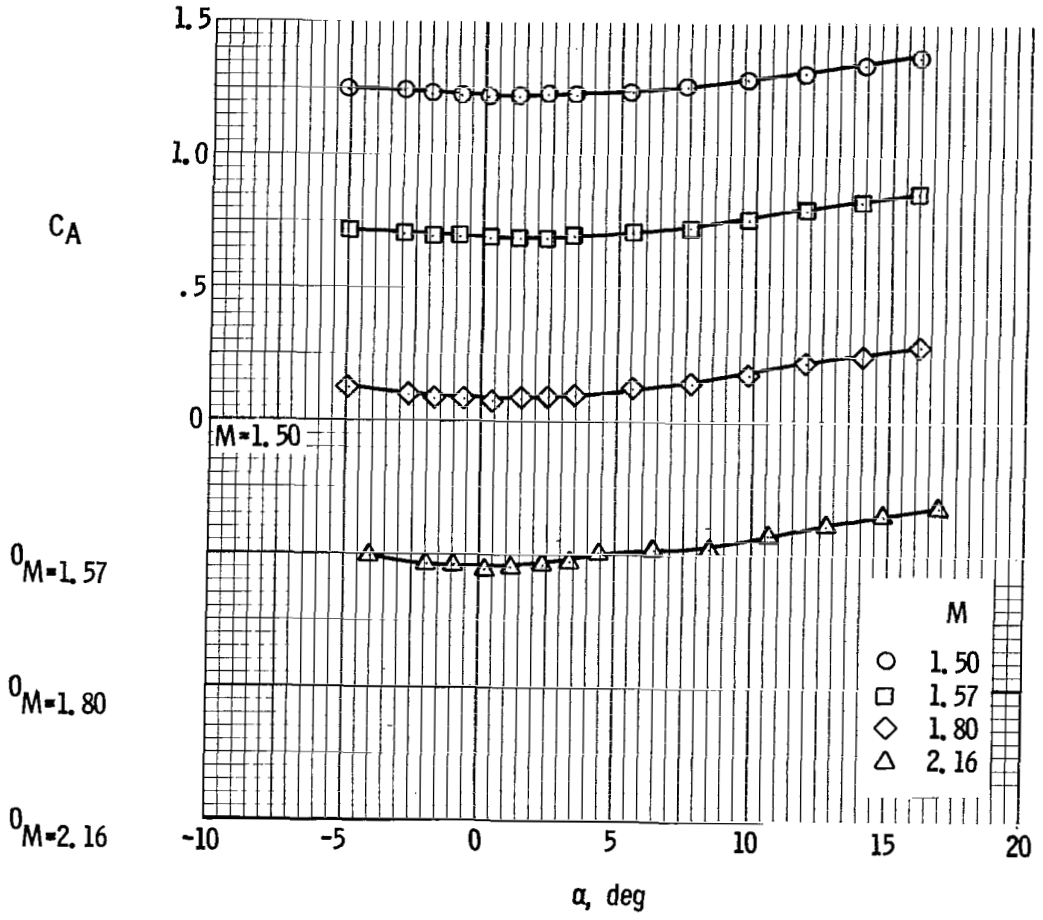

(c) Axial-force coefficient.

Figure 20. - Continued.

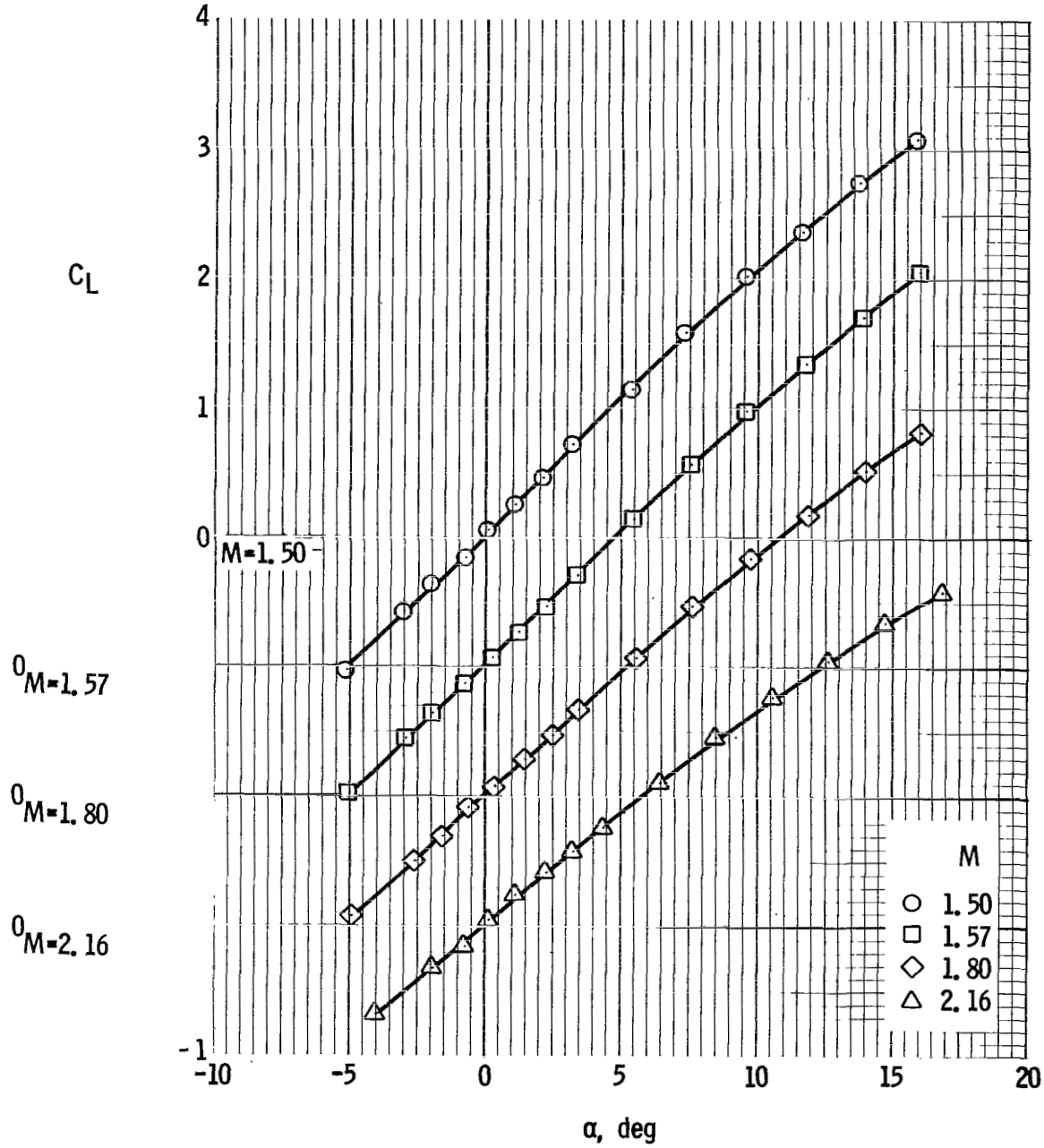

(d) Lift coefficient.

Figure 20. - Continued.

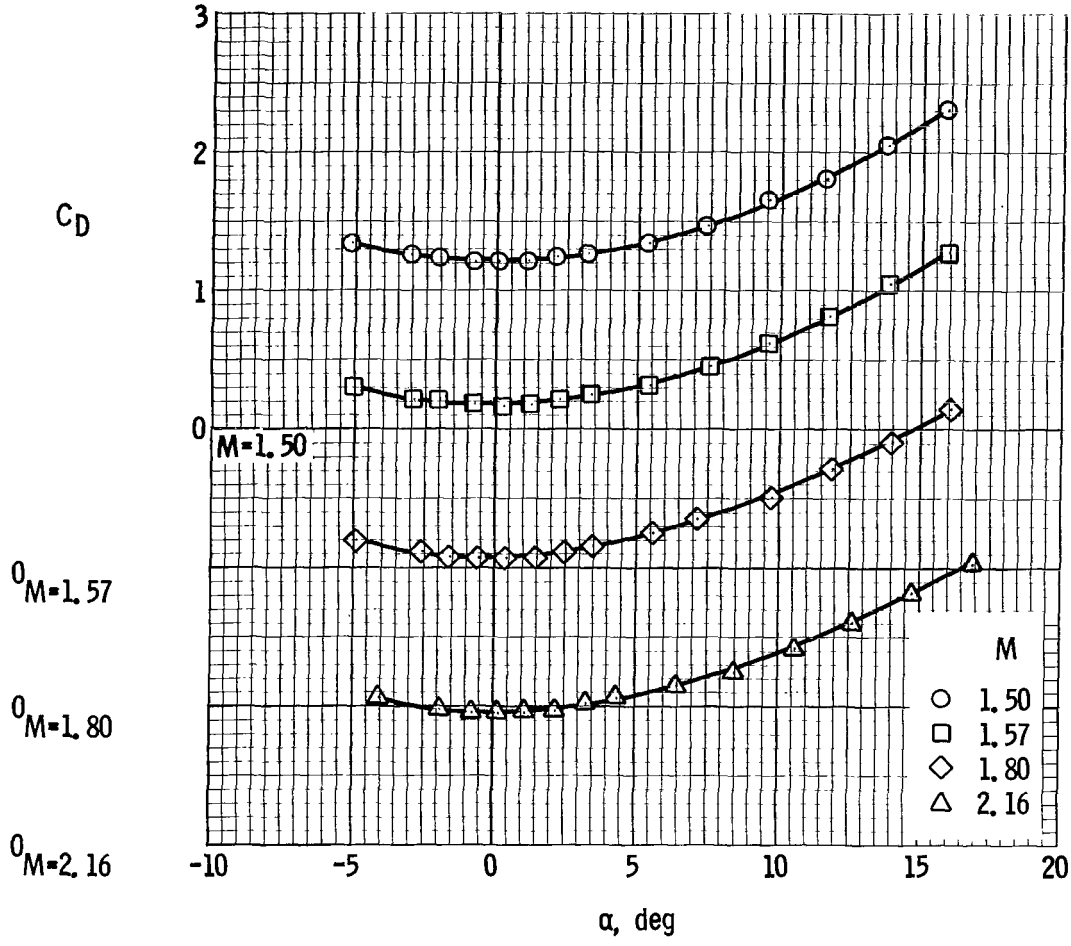

(e) Drag coefficient.

Figure 20. - Continued.

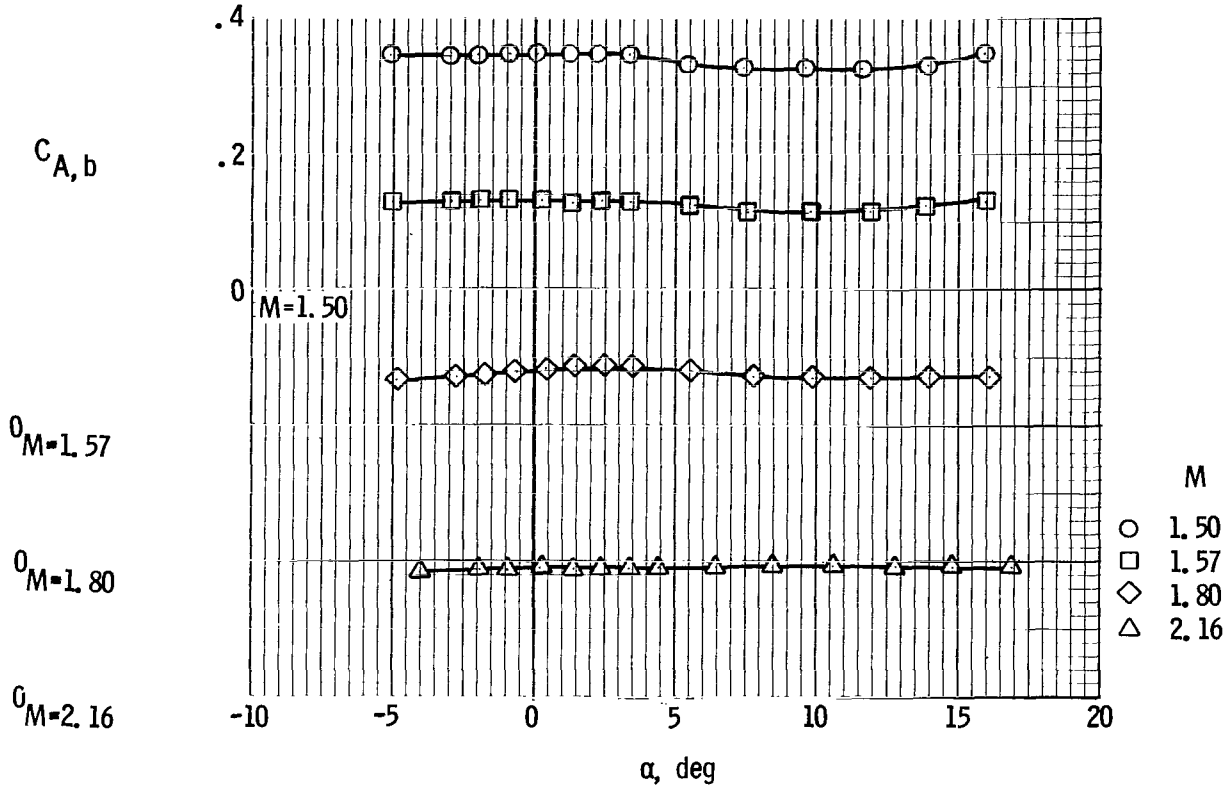

(f) Base axial-force coefficient.

Figure 20. - Concluded.

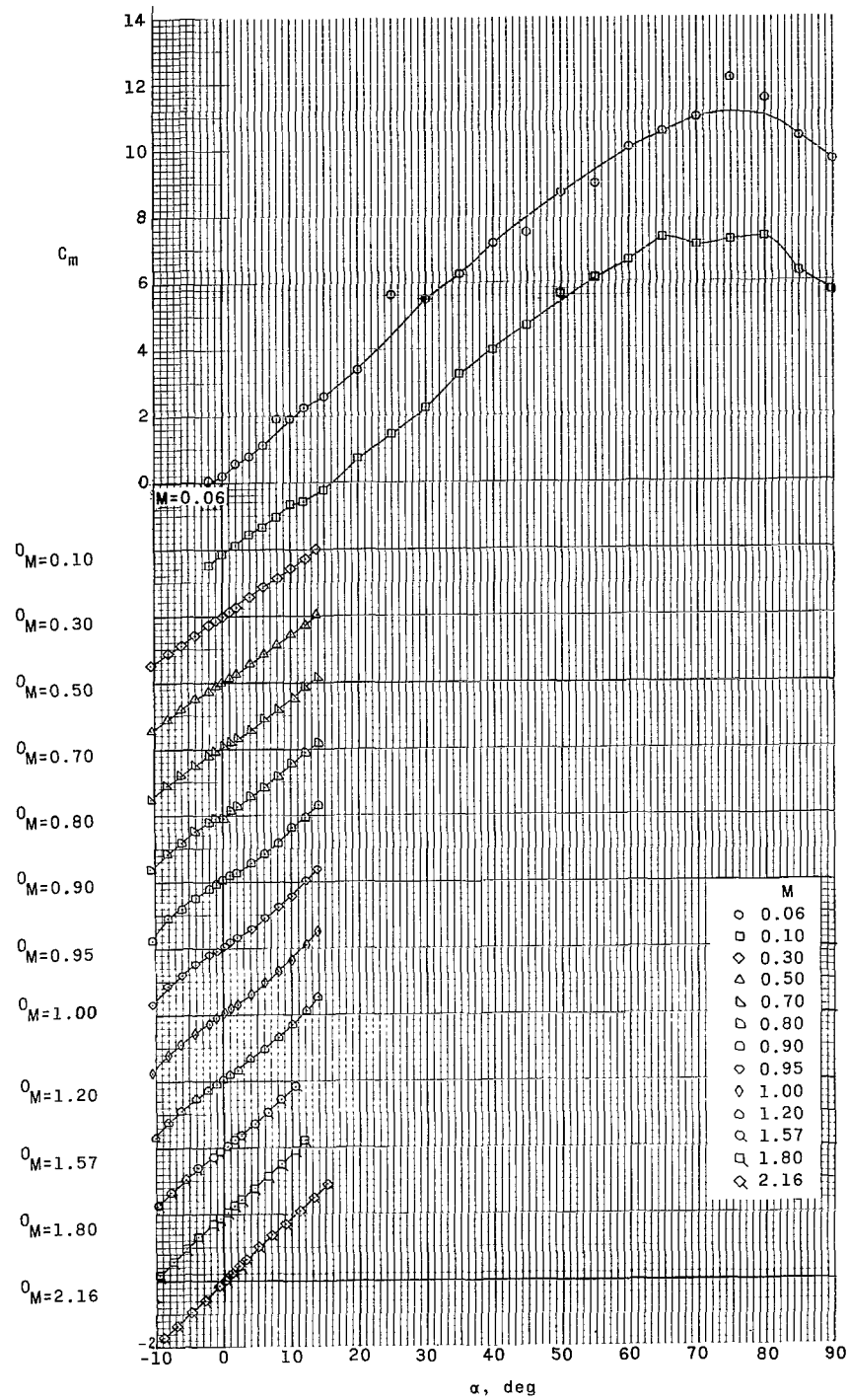

(a) Pitching-moment coefficient.

Figure 21. - Longitudinal aerodynamic characteristics of configuration III at Mach numbers from 0.056 to 2.16 (with a stabilizing disk mounted on the rocket motor; c.g. = X/D = 0; Z/D = 0; $\delta_f = 0°$).

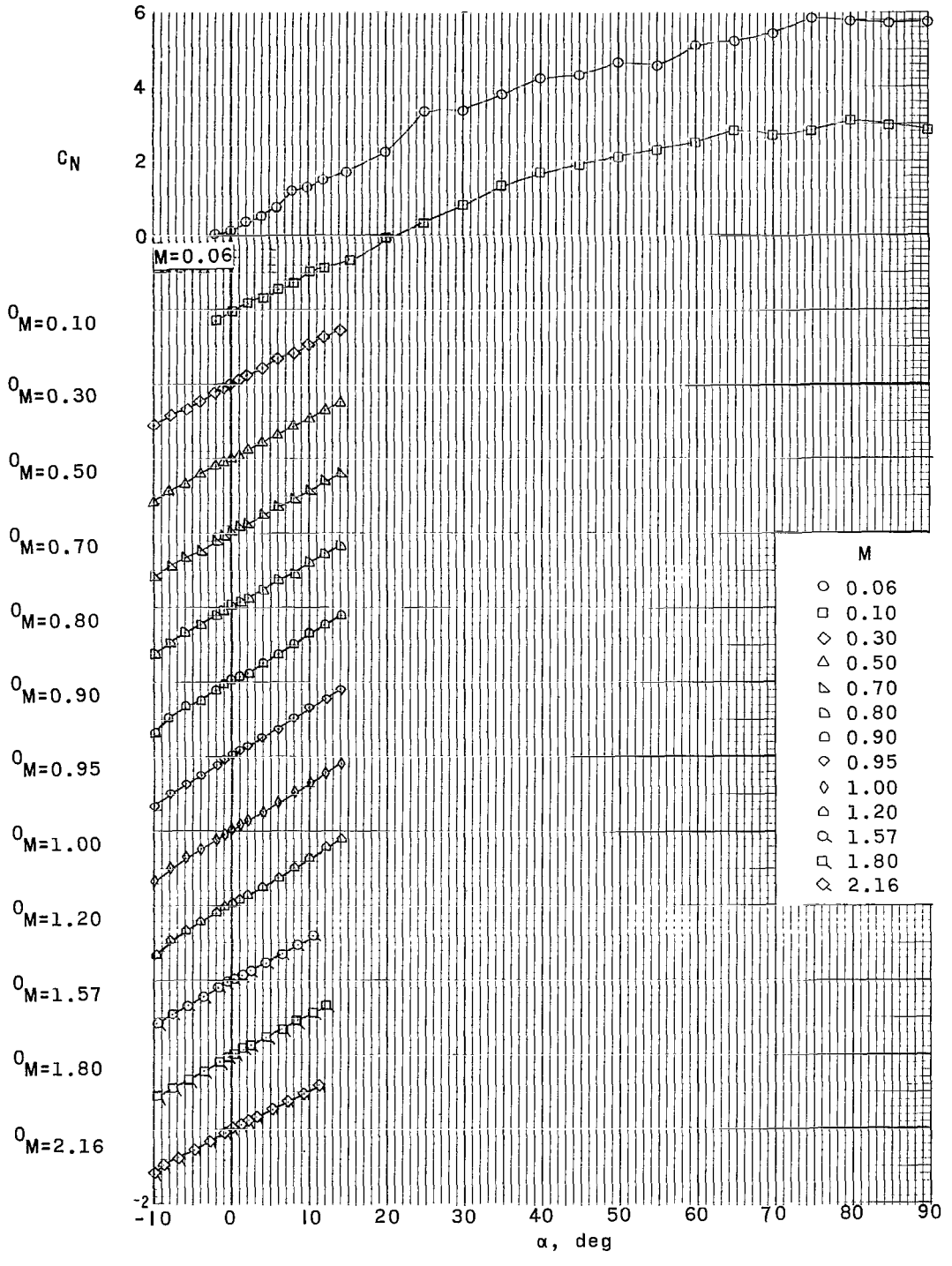

(b) Normal-force coefficient.

Figure 21. - Continued.

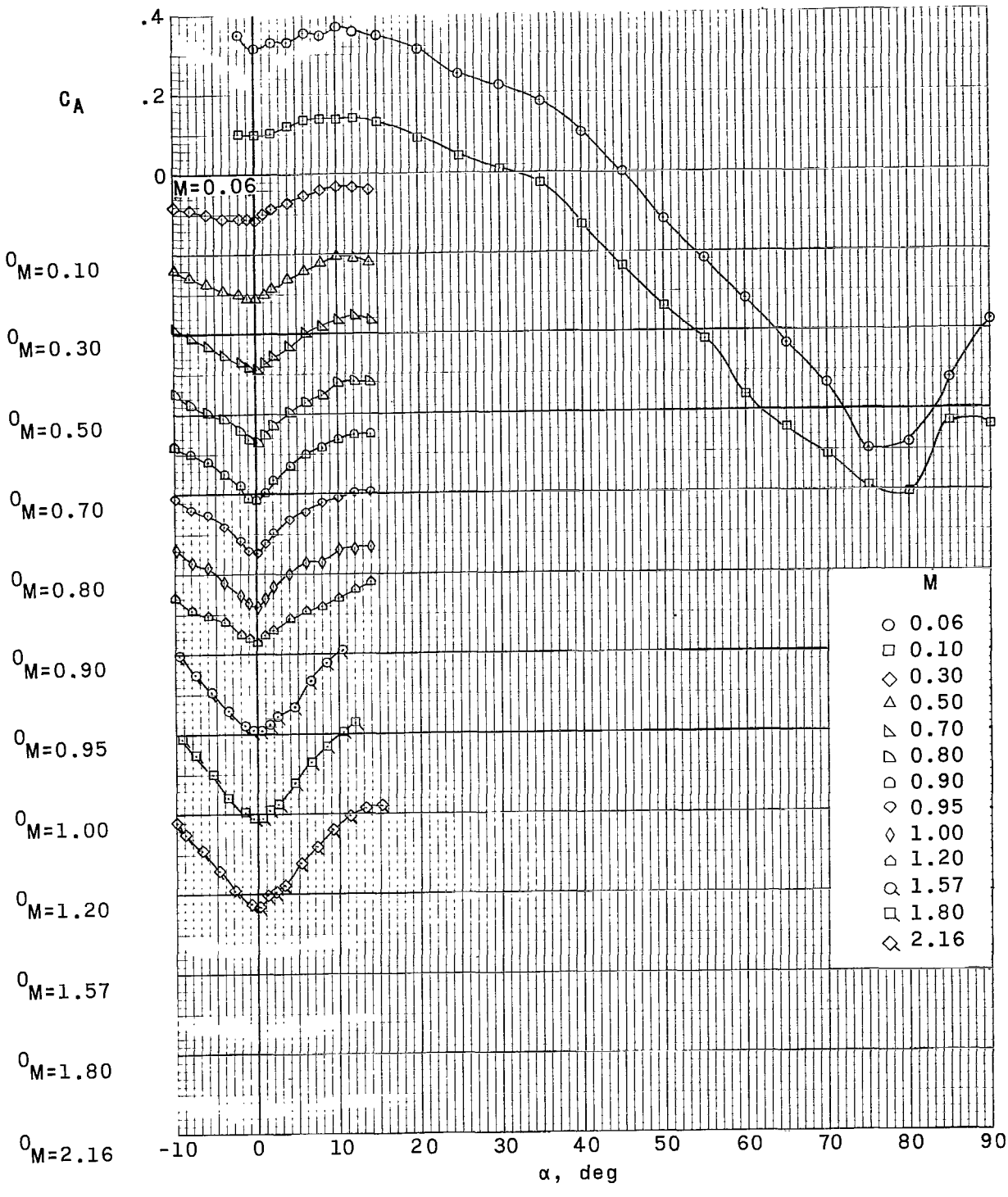

(c) Axial-force coefficient.

Figure 21. - Continued.

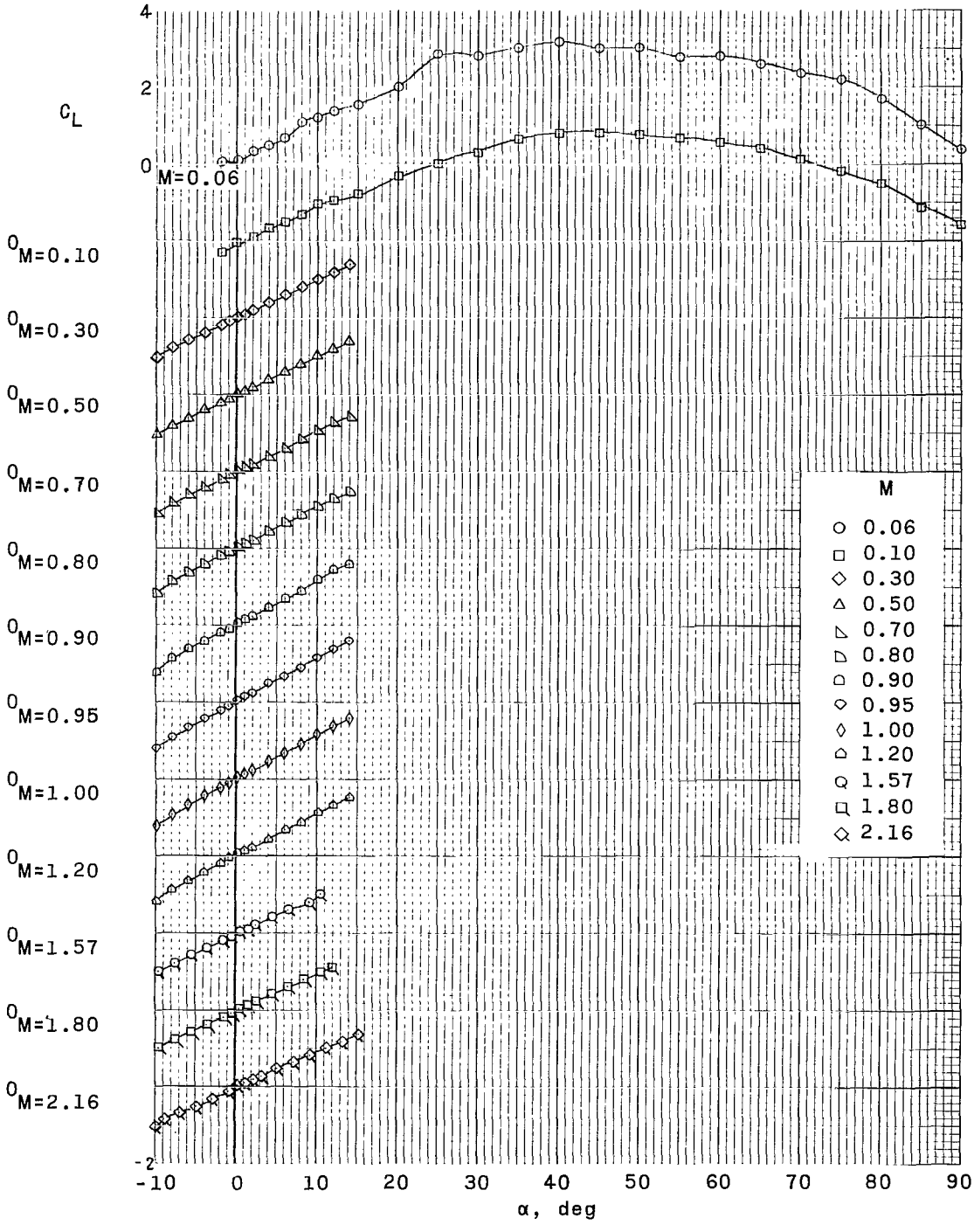

(d) Lift coefficient.

Figure 21.- Continued.

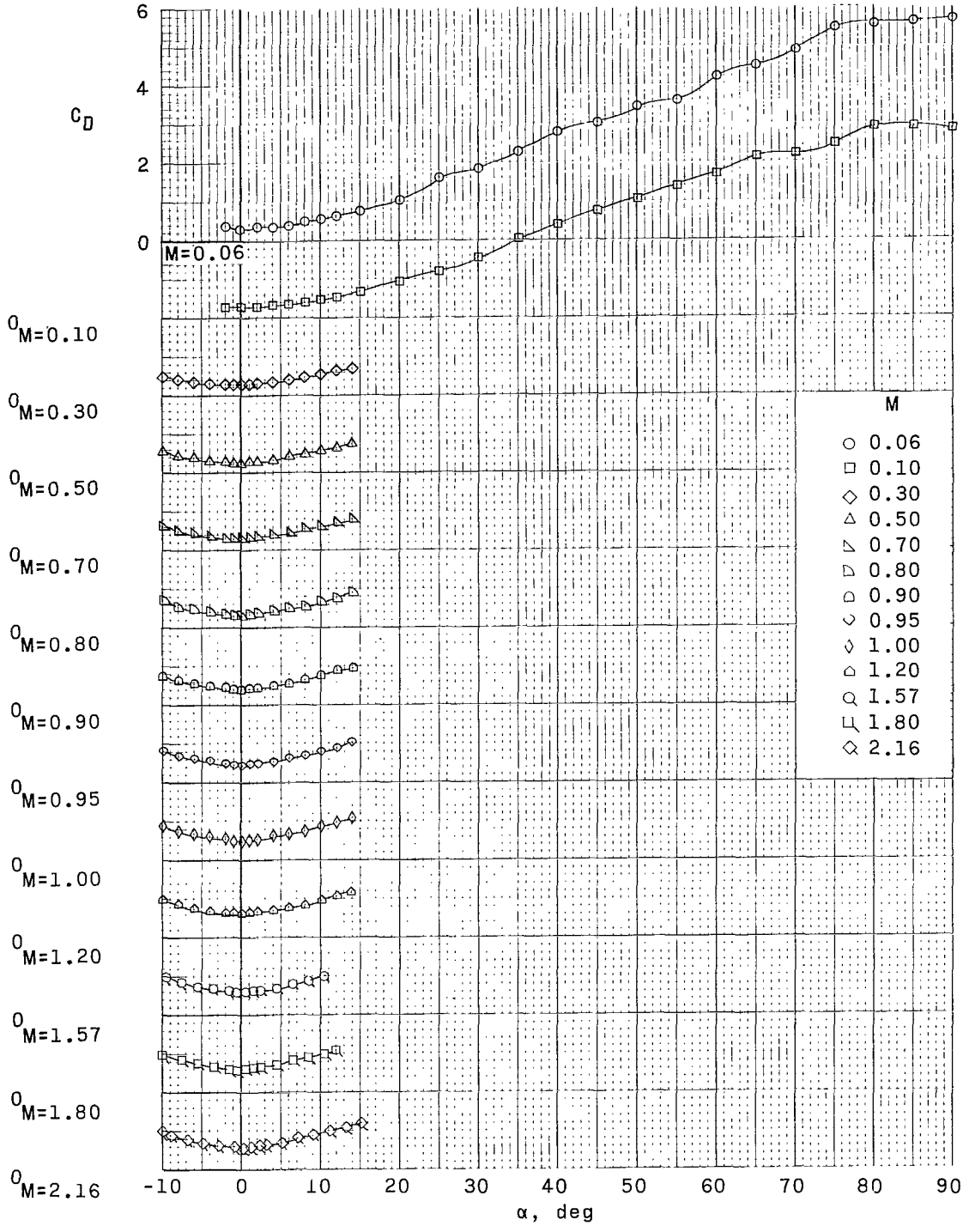

(e) Drag coefficient.

Figure 21. - Concluded.

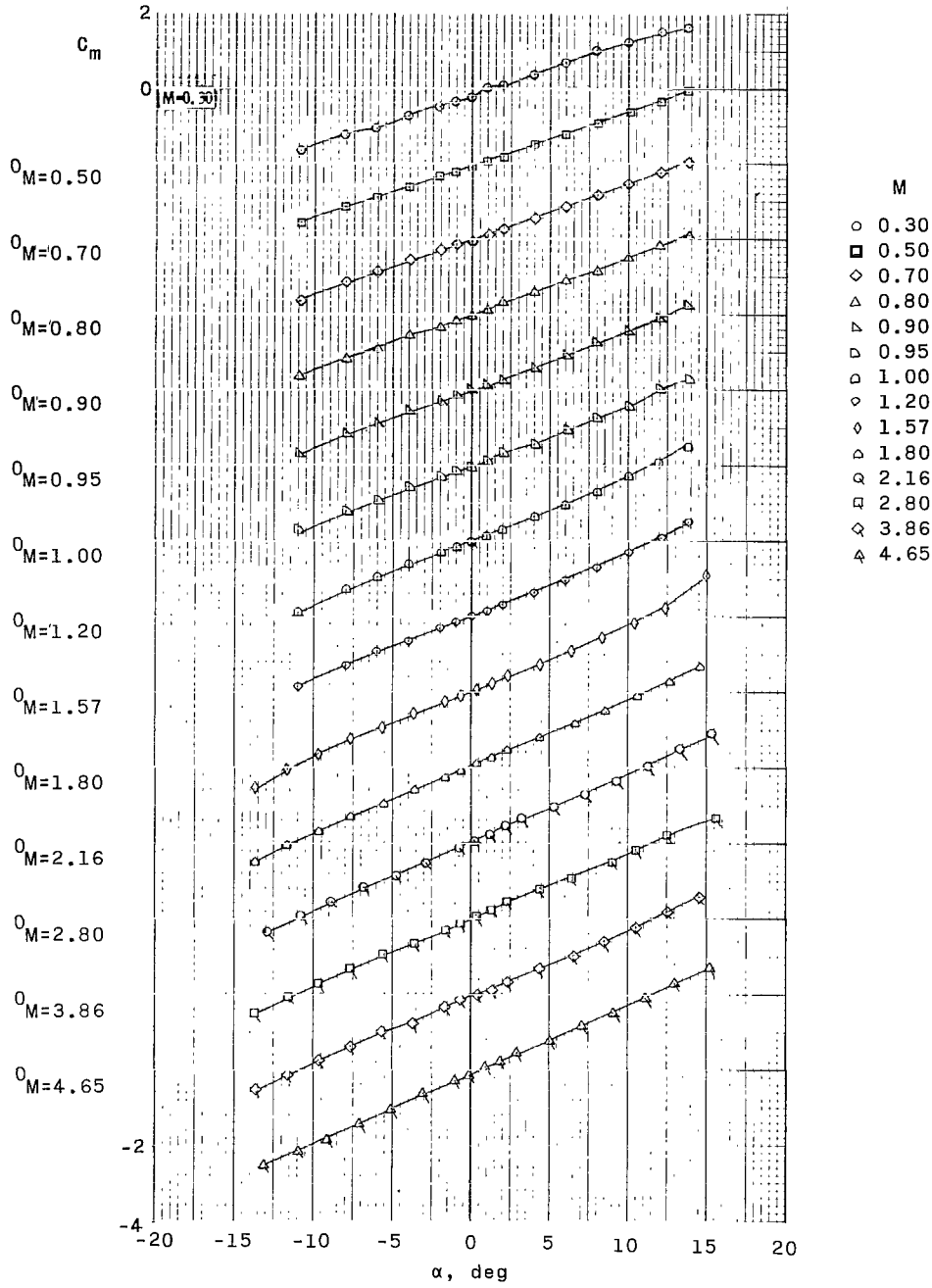

(a) Pitching-moment coefficient.

Figure 22.- Longitudinal aerodynamic characteristics of configuration III at Mach numbers from 0.30 to 4.65 (without stabilizing disk; c.g. = X/D = 0; Z/D = 0; $\delta_f = 0°$).

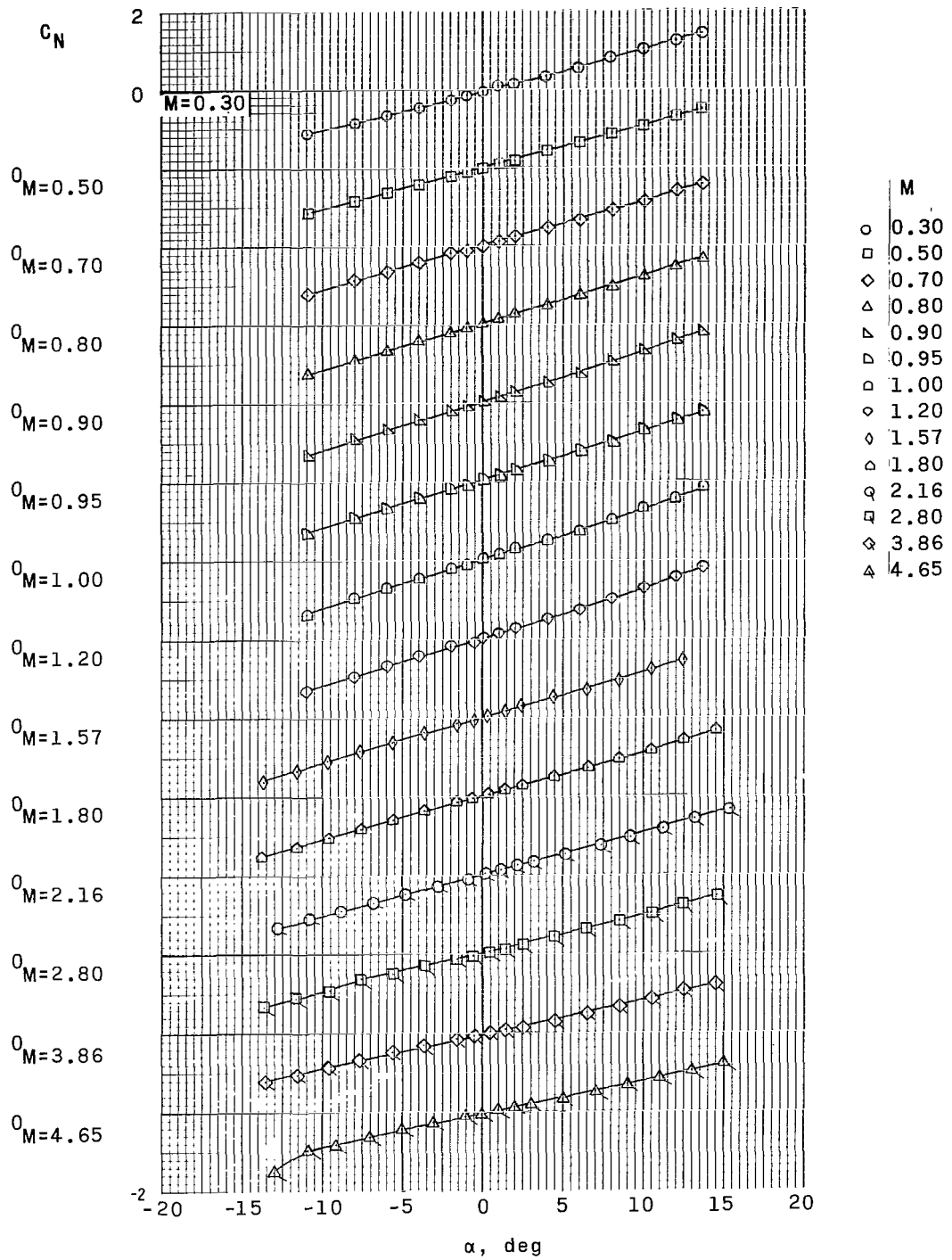

(b) Normal-force coefficient.

Figure 22. - Continued.

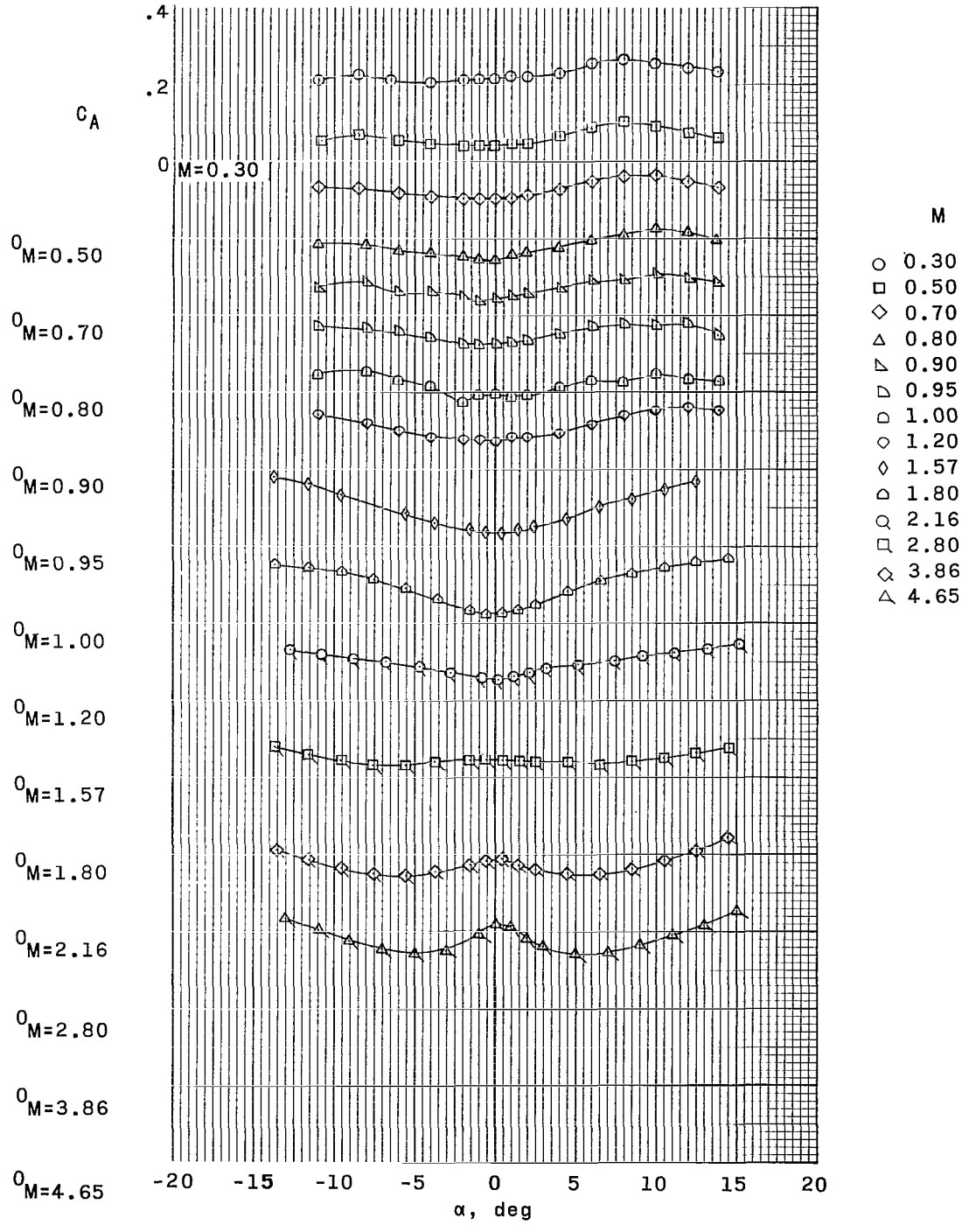

(c) Axial-force coefficient.

Figure 22. - Continued.

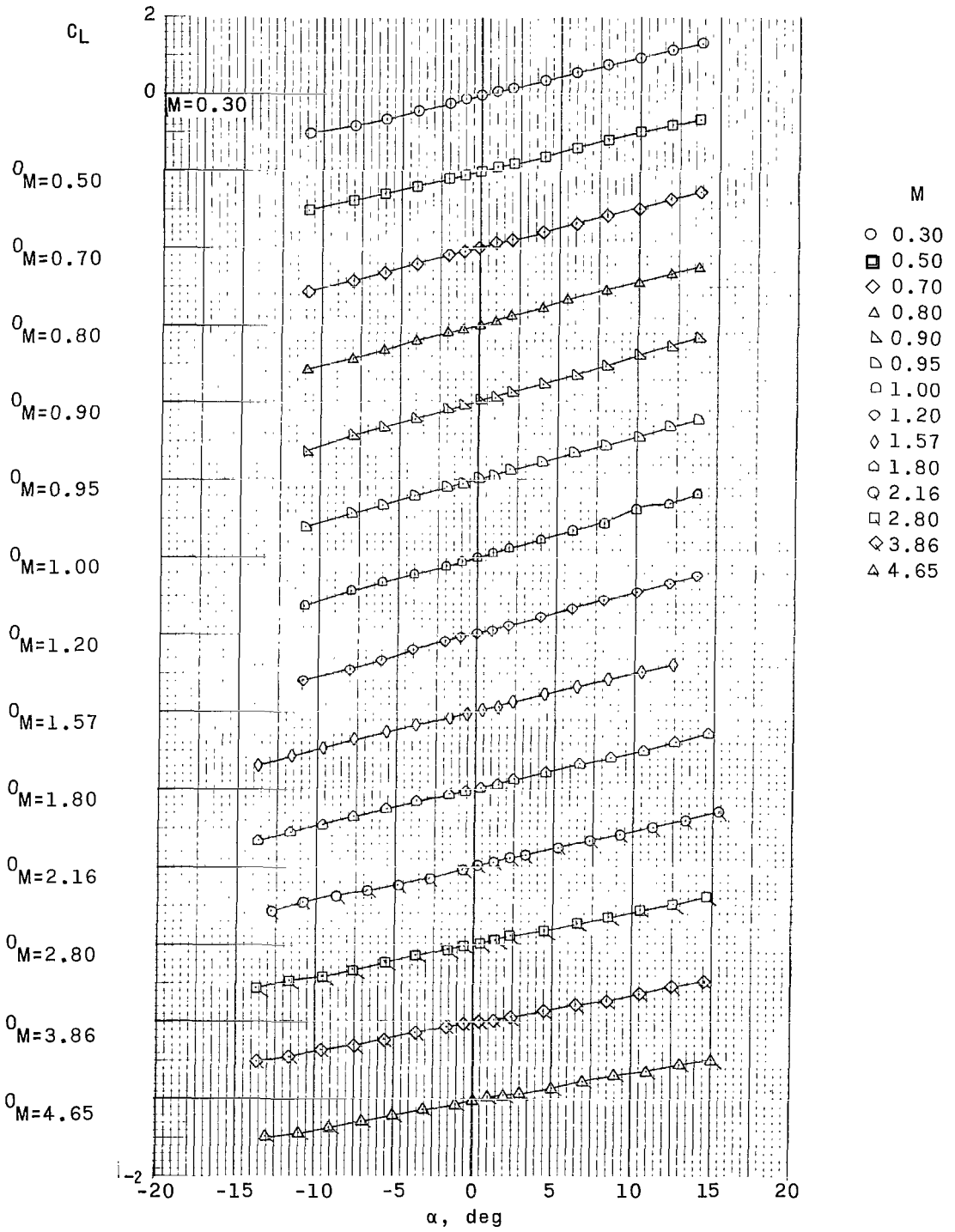

(d) Lift coefficient.

Figure 22. - Continued.

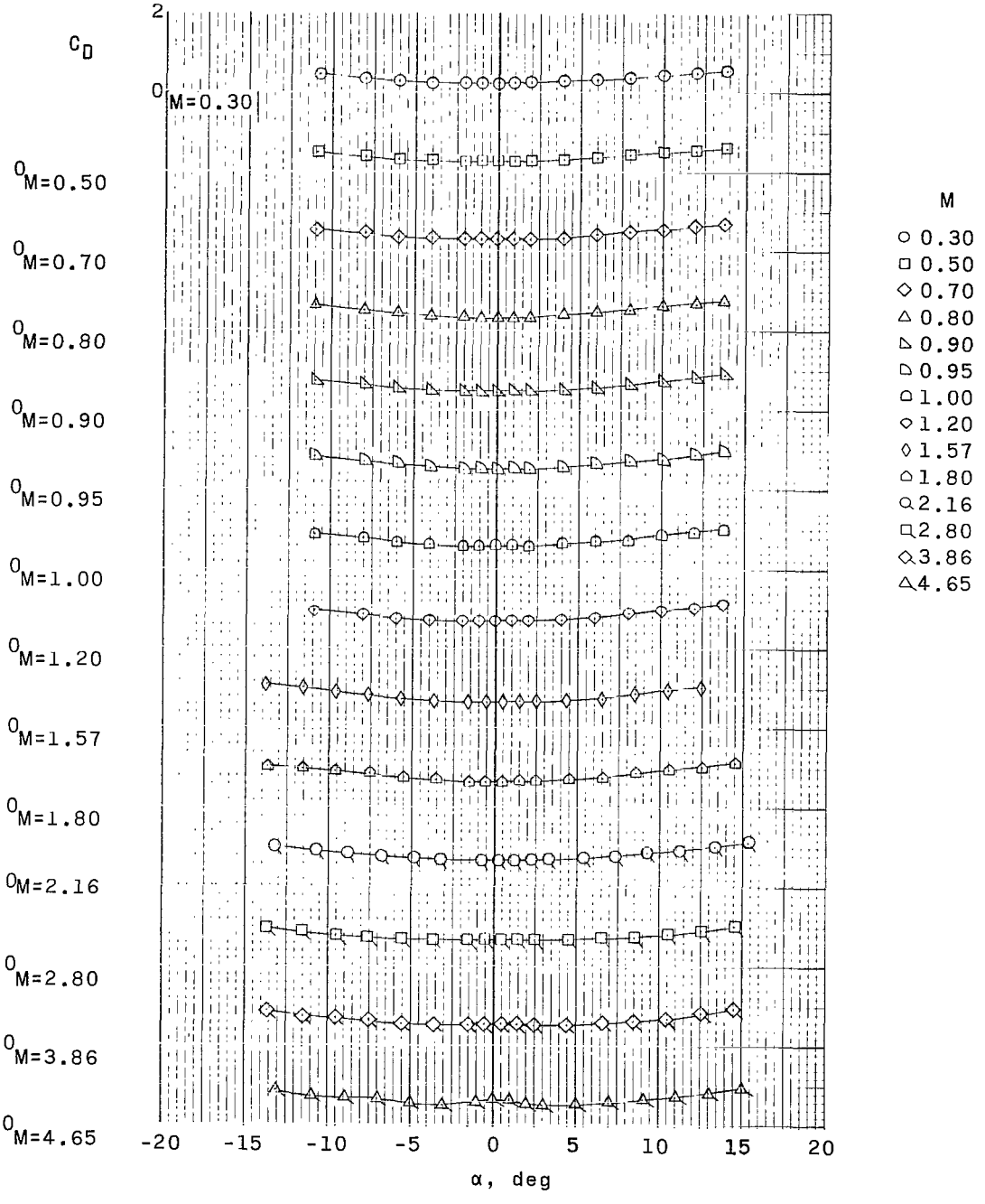

(e) Drag coefficient.

Figure 22. - Continued.

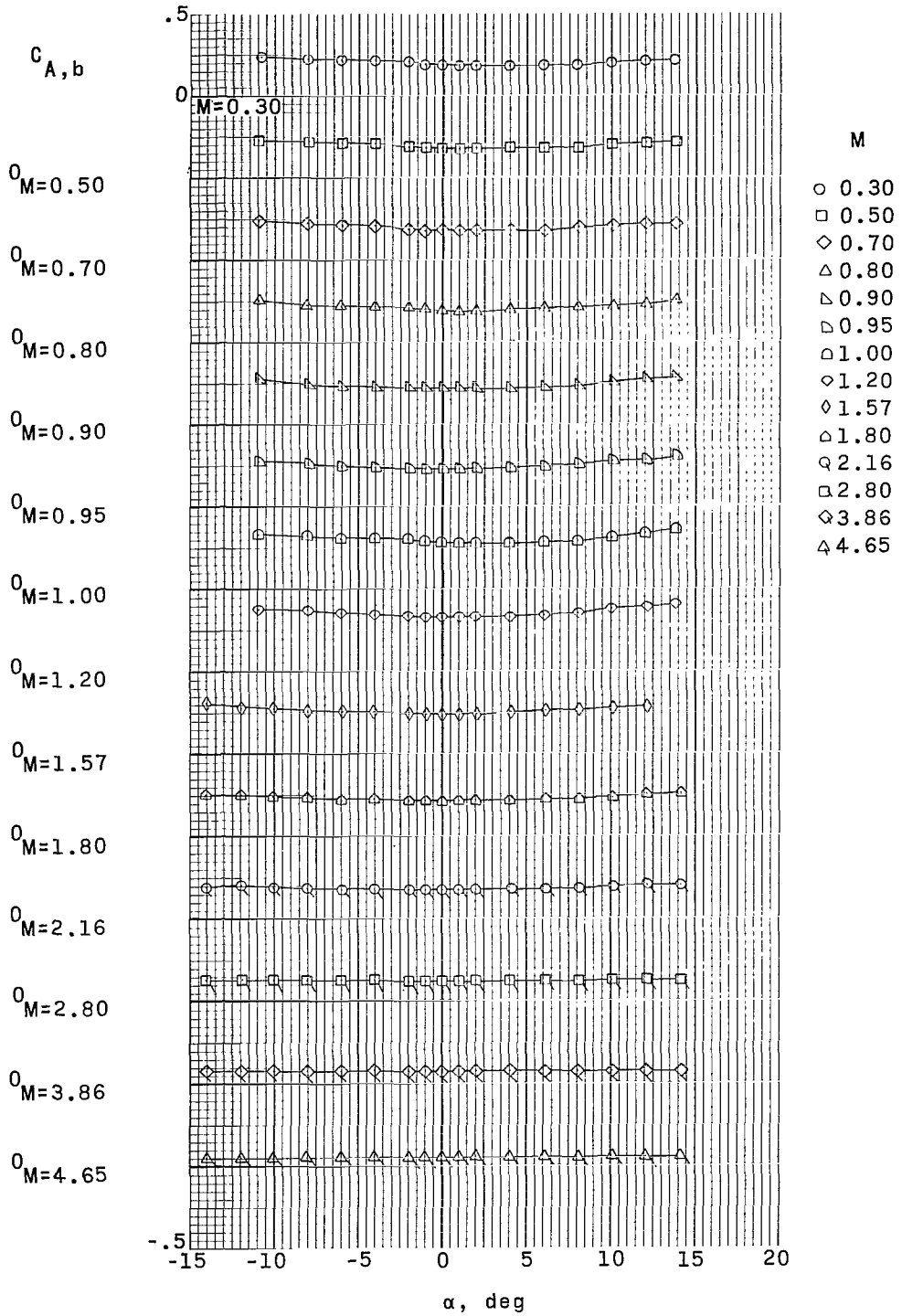

(f) Base axial-force coefficient.

Figure 22. - Concluded.

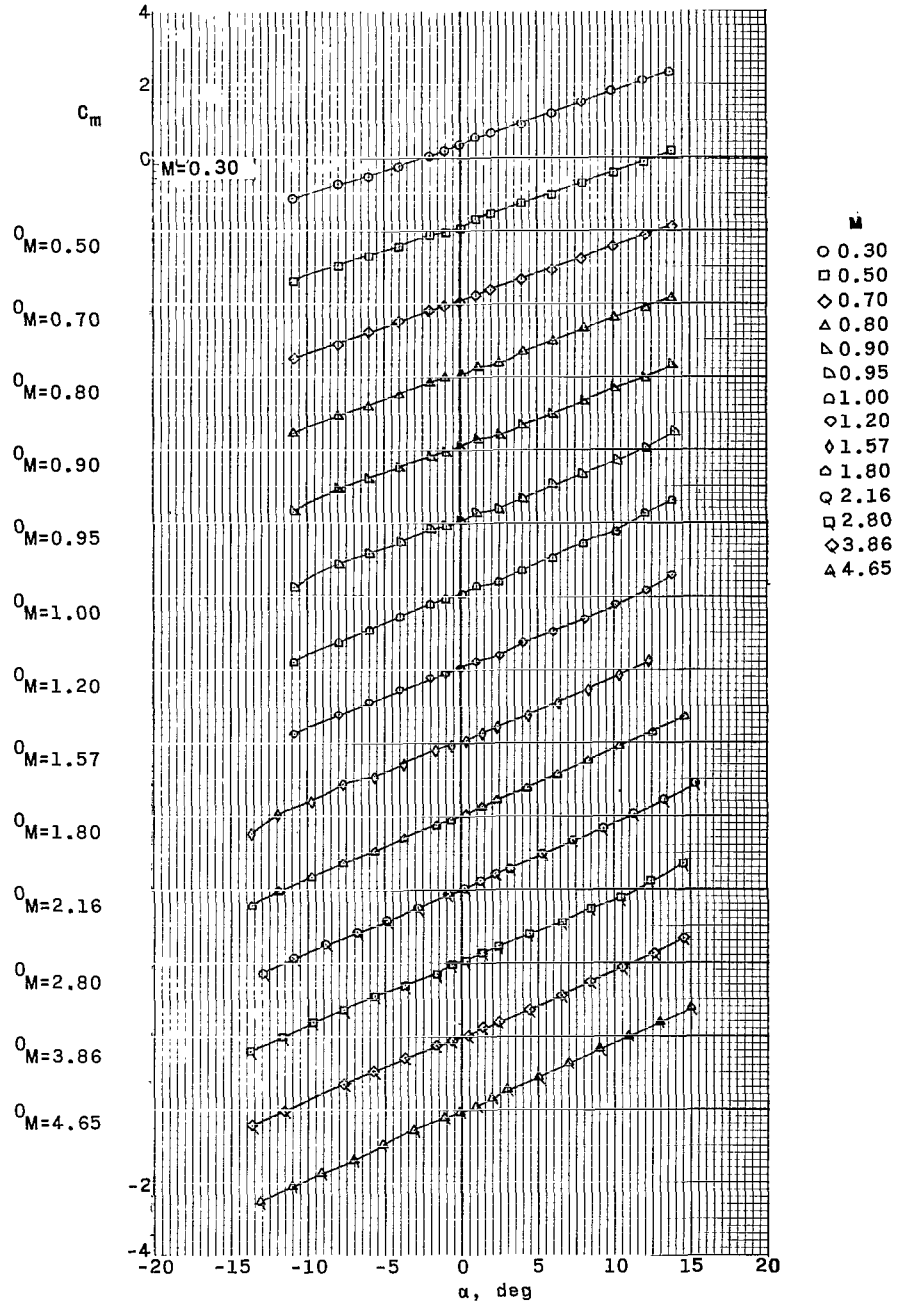

(a) Pitching-moment coefficient.

Figure 23. - Effect of deflection of trailing-edge control surfaces on longitudinal aerodynamic characteristics of configuration III at Mach numbers from 0.30 to 4.65 (c.g. = X/D = 0; Z/D = 0; $\delta_f = -5°$).

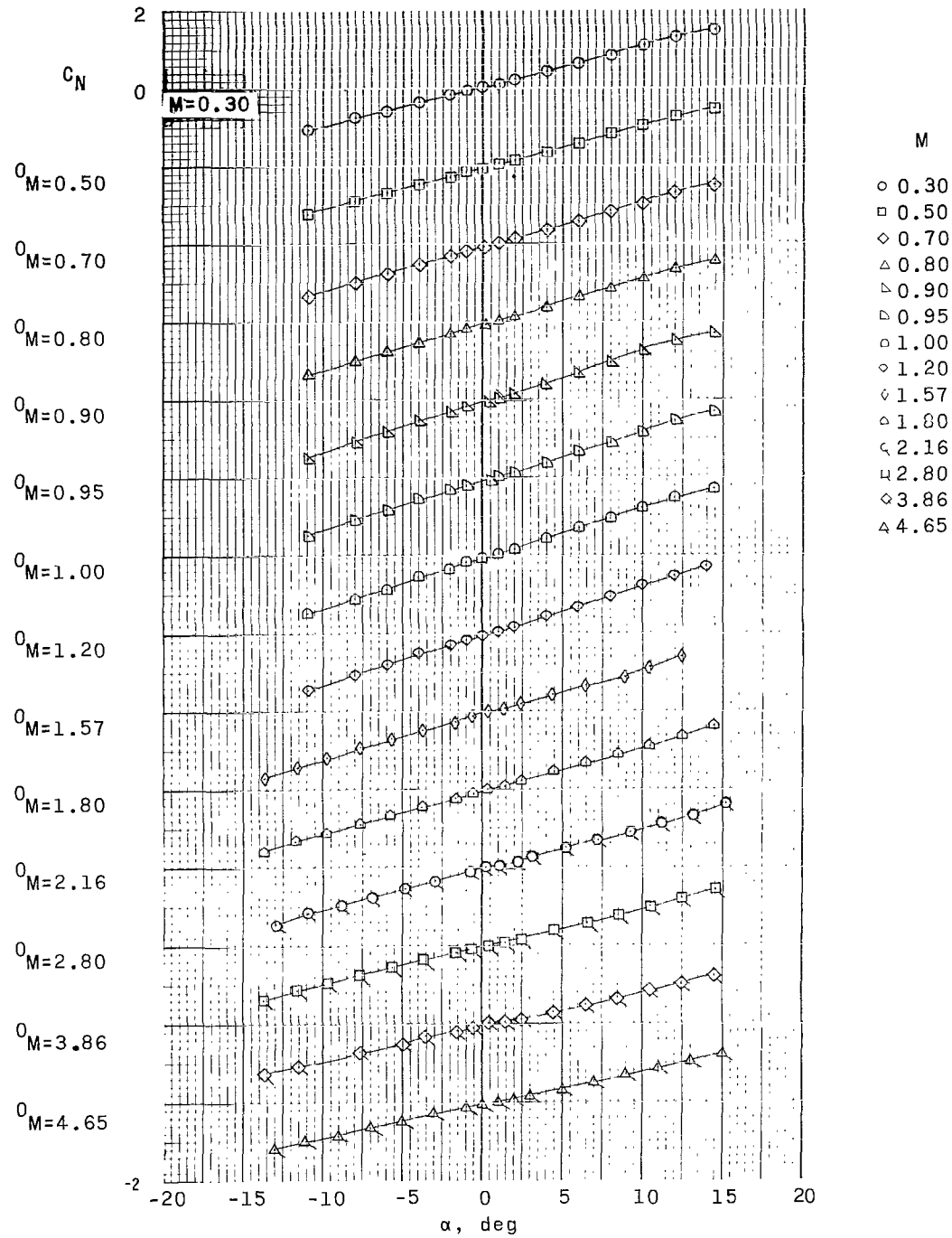

(b) Normal-force coefficient.

Figure 23. - Continued.

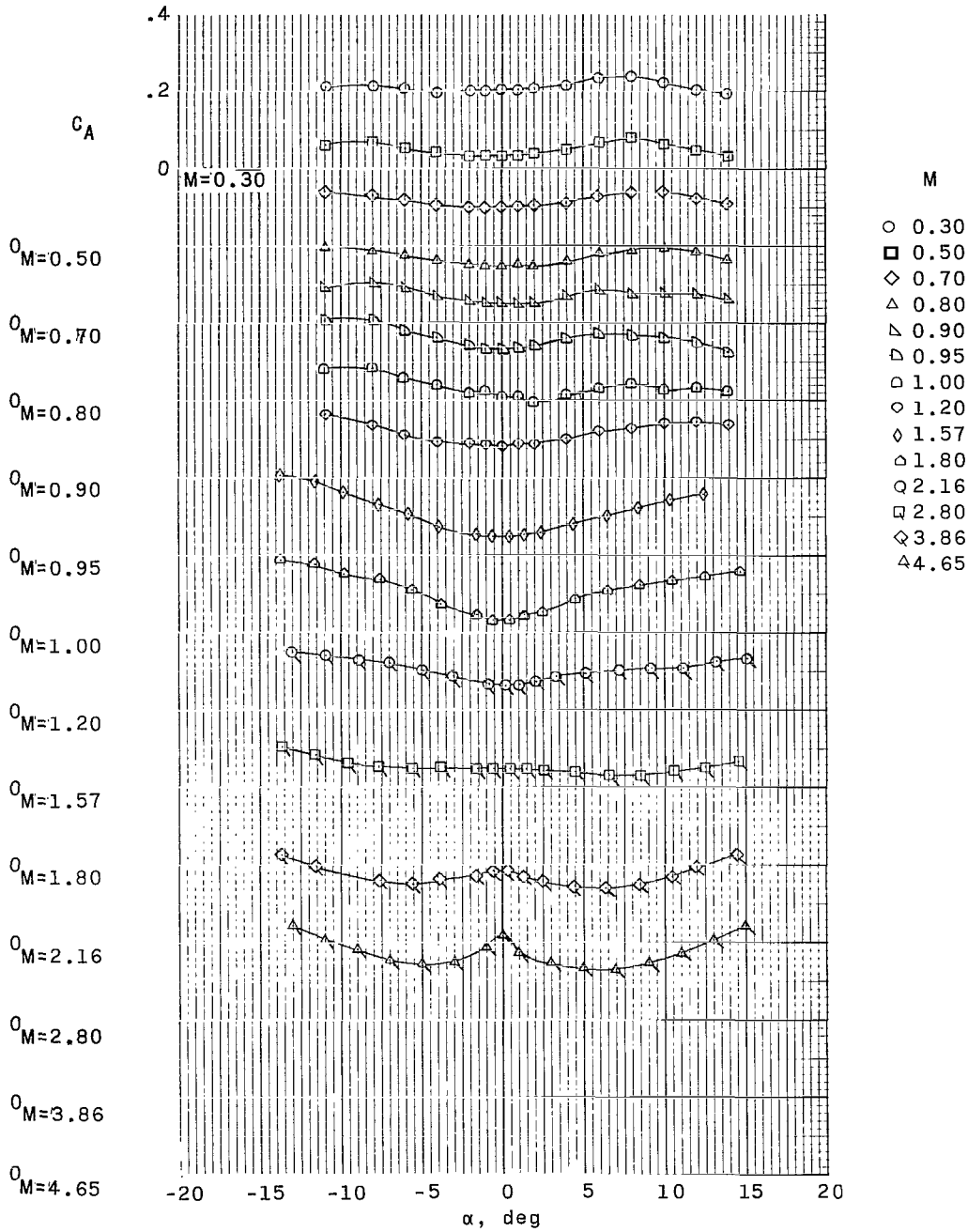

(c) Axial-force coefficient.

Figure 23. - Continued.

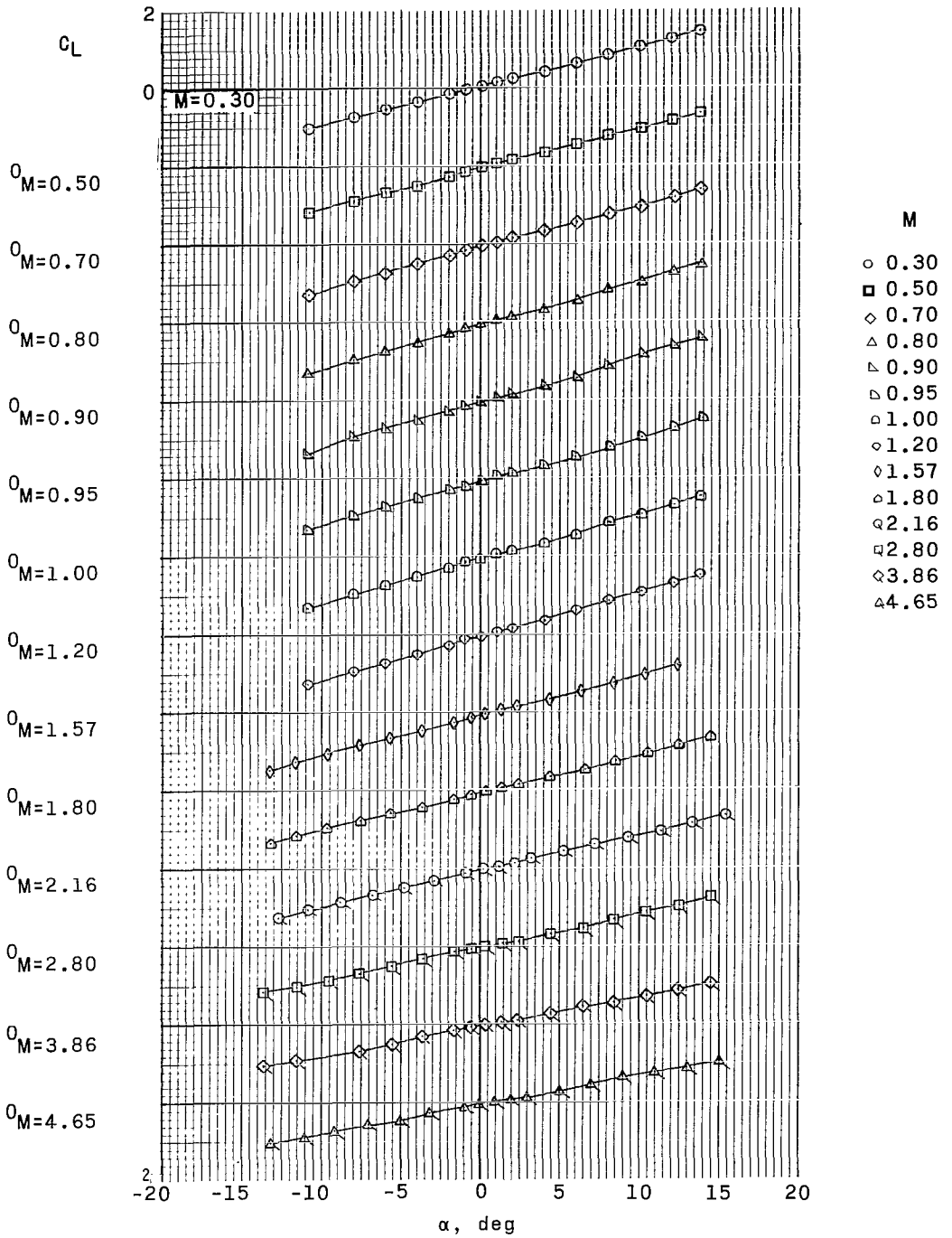

(d) Lift coefficient.

Figure 23. - Continued.

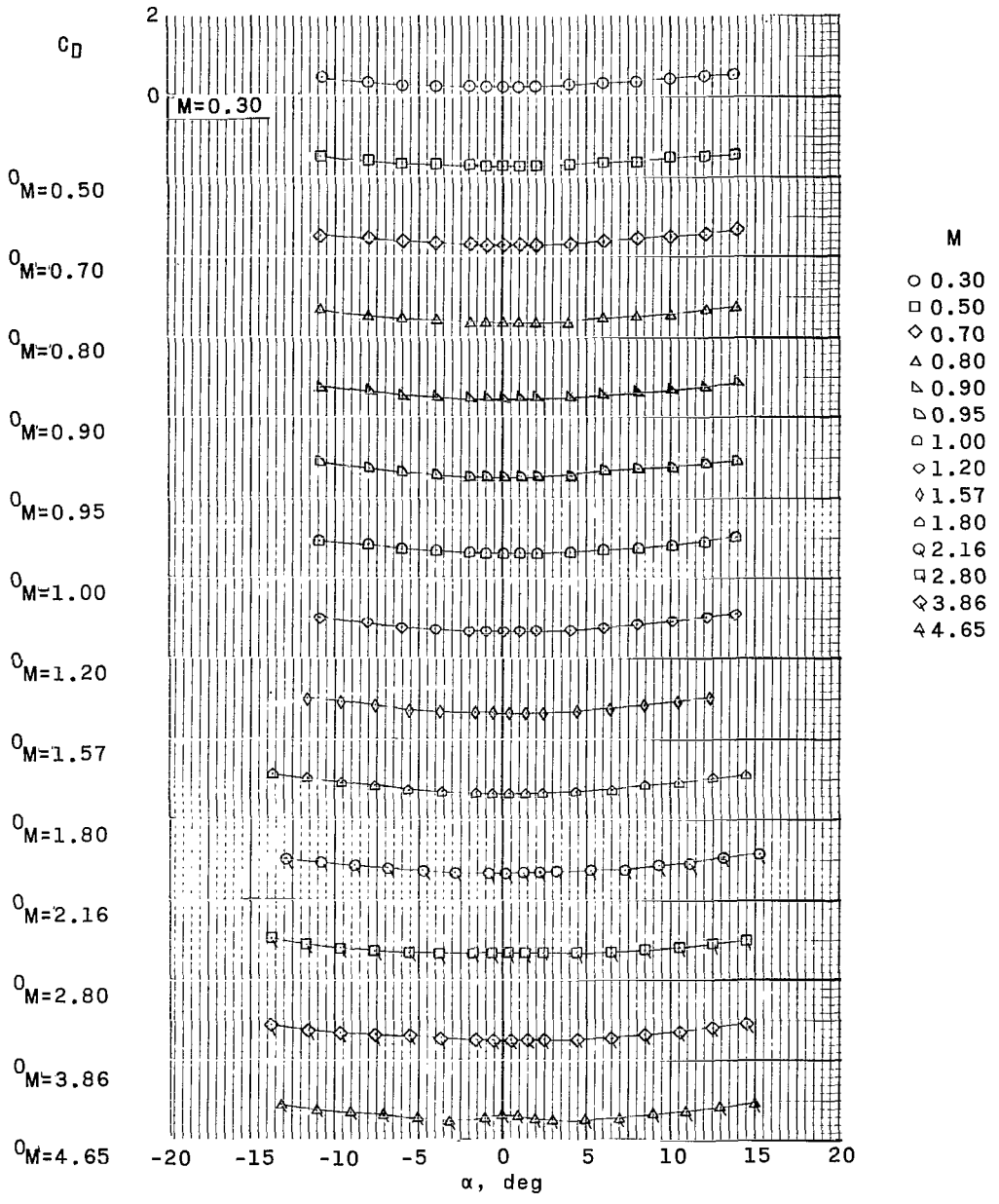

(e) Drag coefficient.

Figure 23. - Continued.

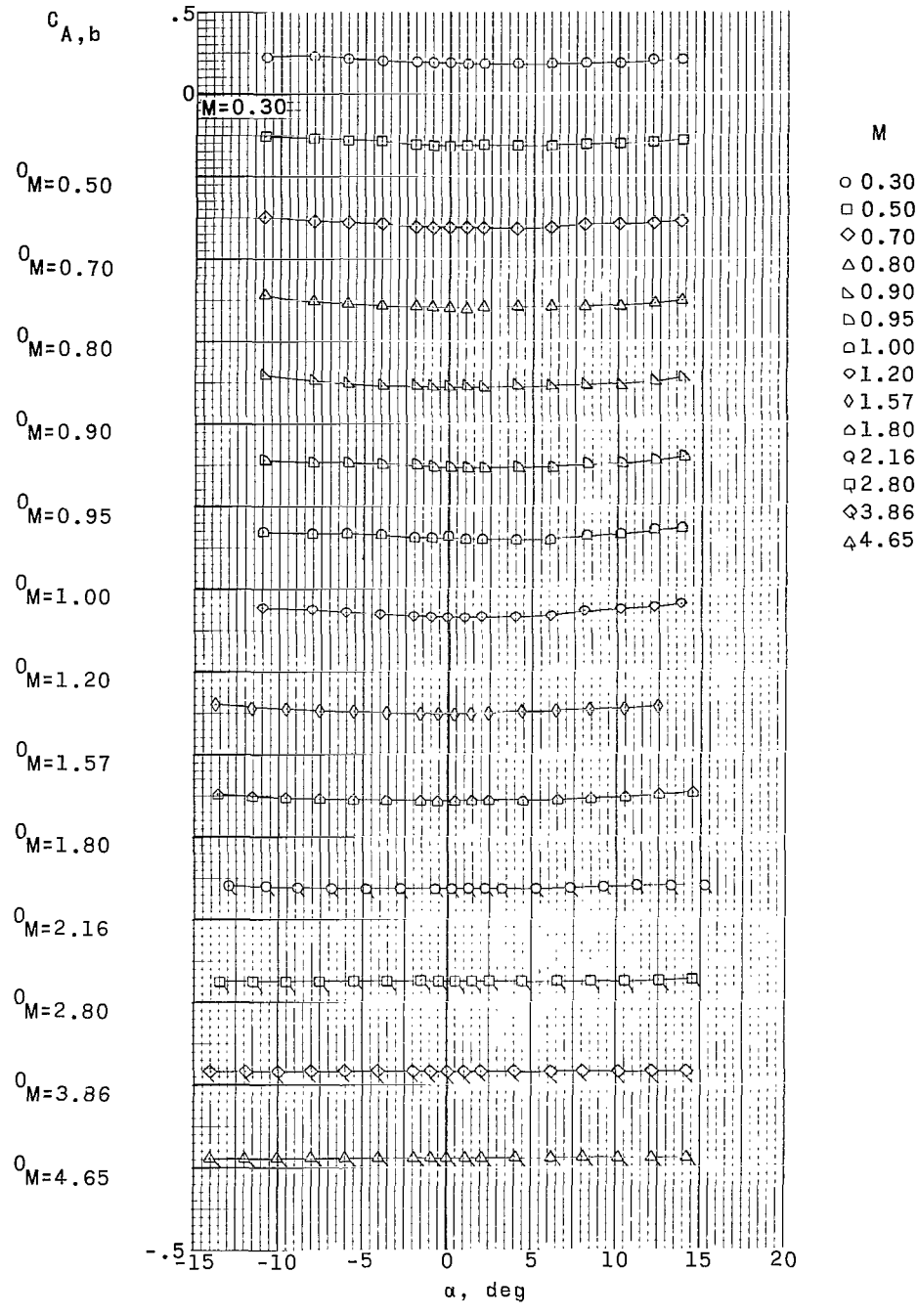

(f) Base axial-force coefficient.

Figure 23. - Concluded.

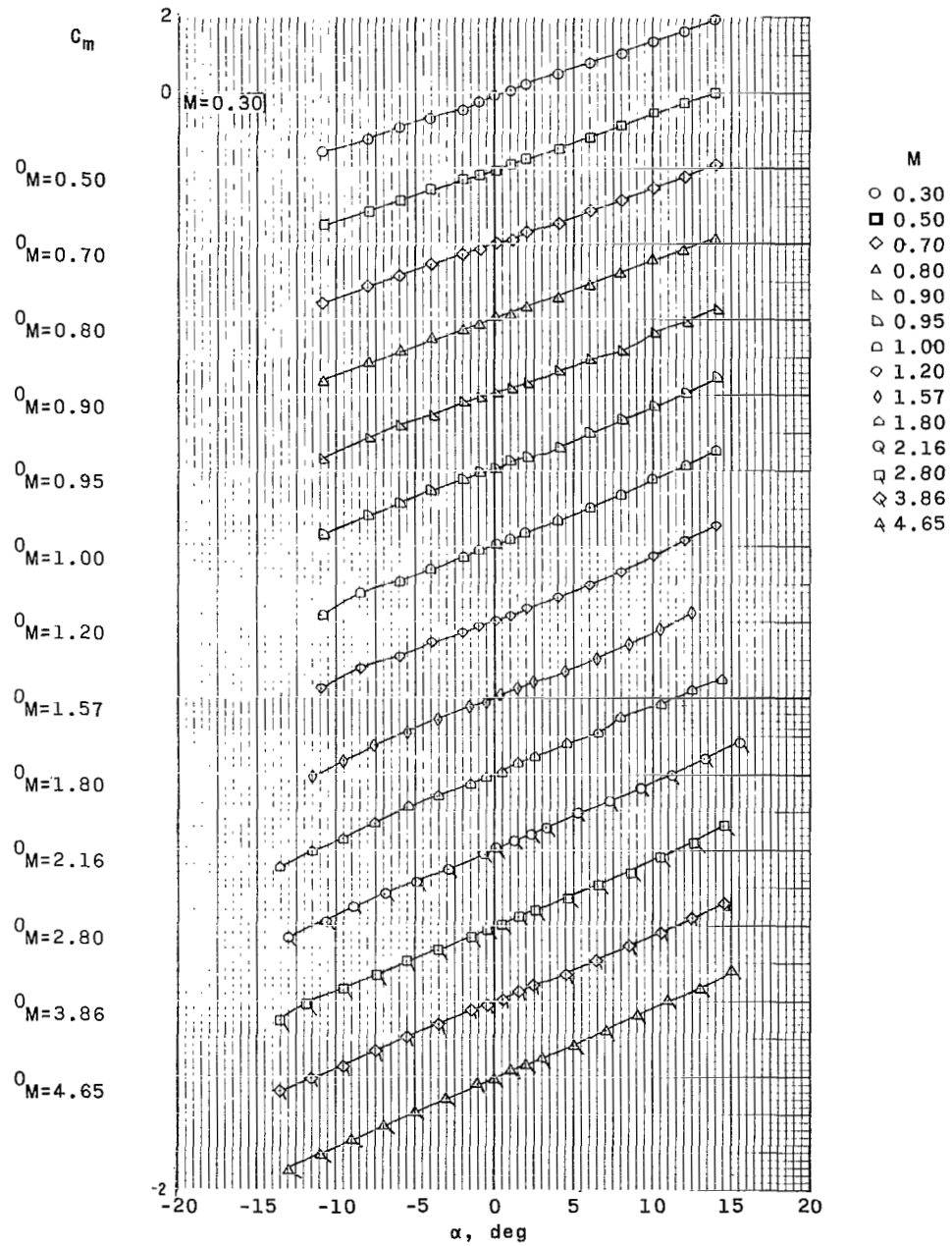

(a) Pitching-moment coefficient.

Figure 24.- Effect of deflection of trailing-edge control surfaces on longitudinal aerodynamic characteristics of configuration III (without stabilizing disk) at Mach numbers from 0.30 to 4.65 (c.g. = X/D = 0; Z/D = 0; $\delta_f = -10°$).

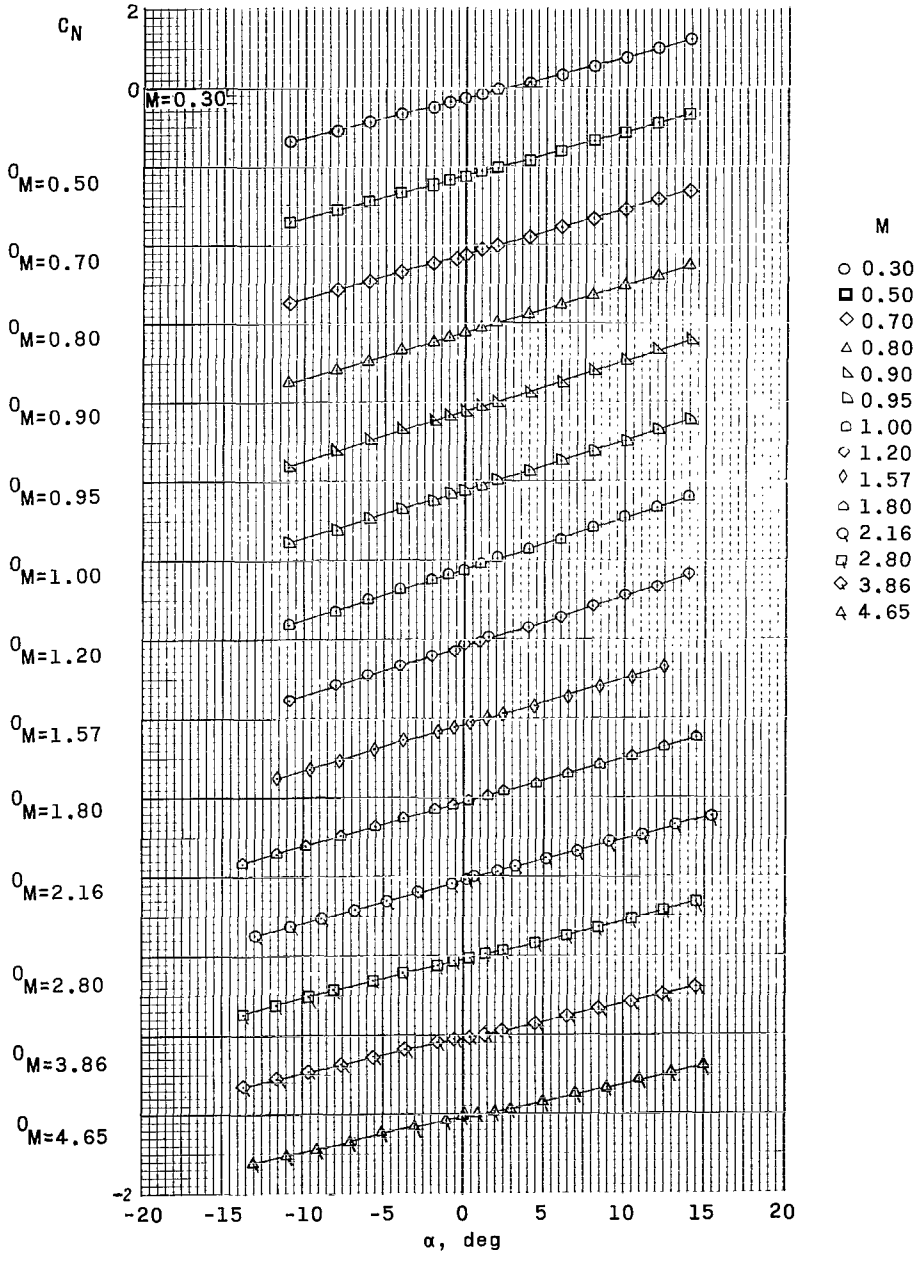

(b) Normal-force coefficient.

Figure 24. - Continued.

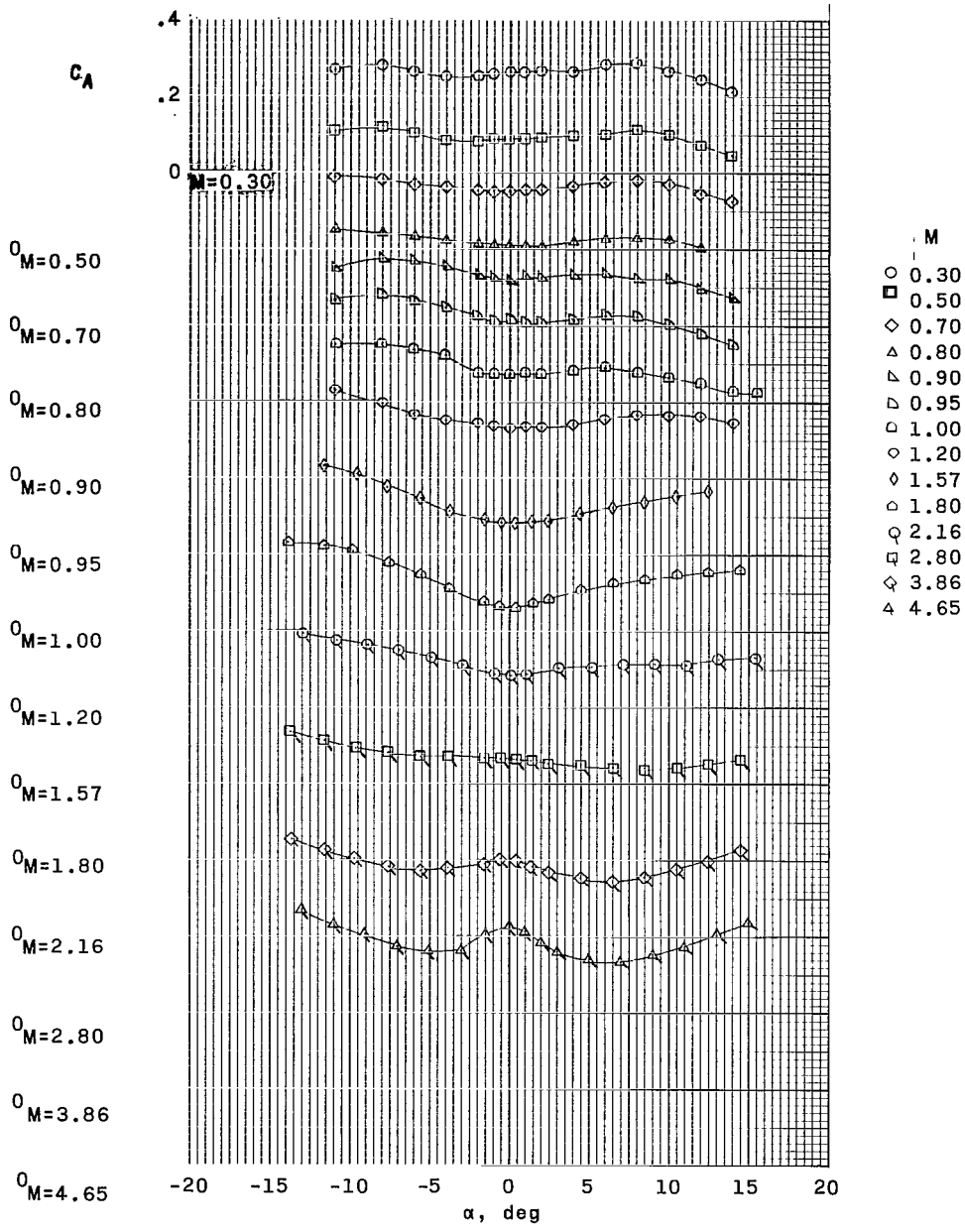

(c) Axial-force coefficient.

Figure 24. - Continued.

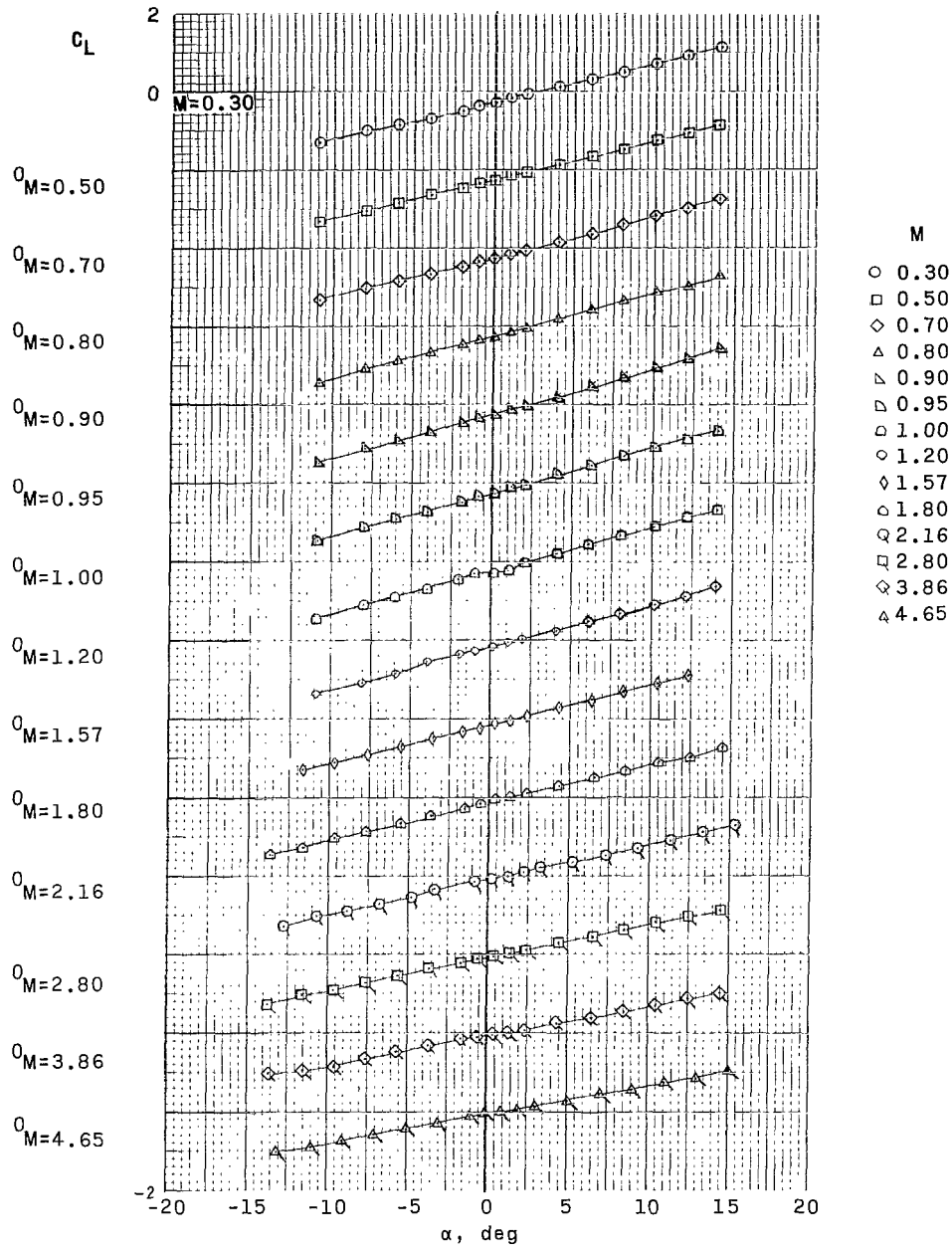

(d) Lift coefficient.

Figure 24. - Continued.

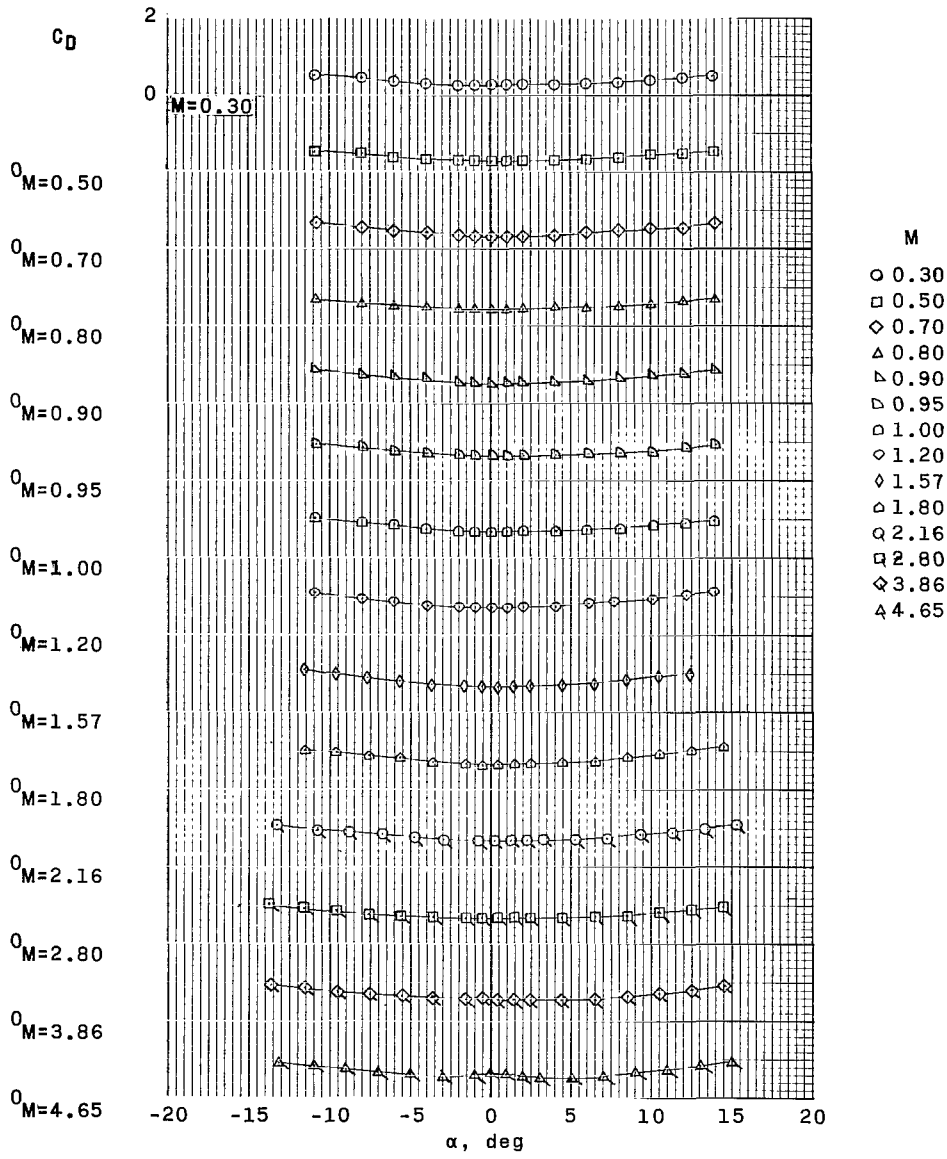

(e) Drag coefficient.

Figure 24. - Continued.

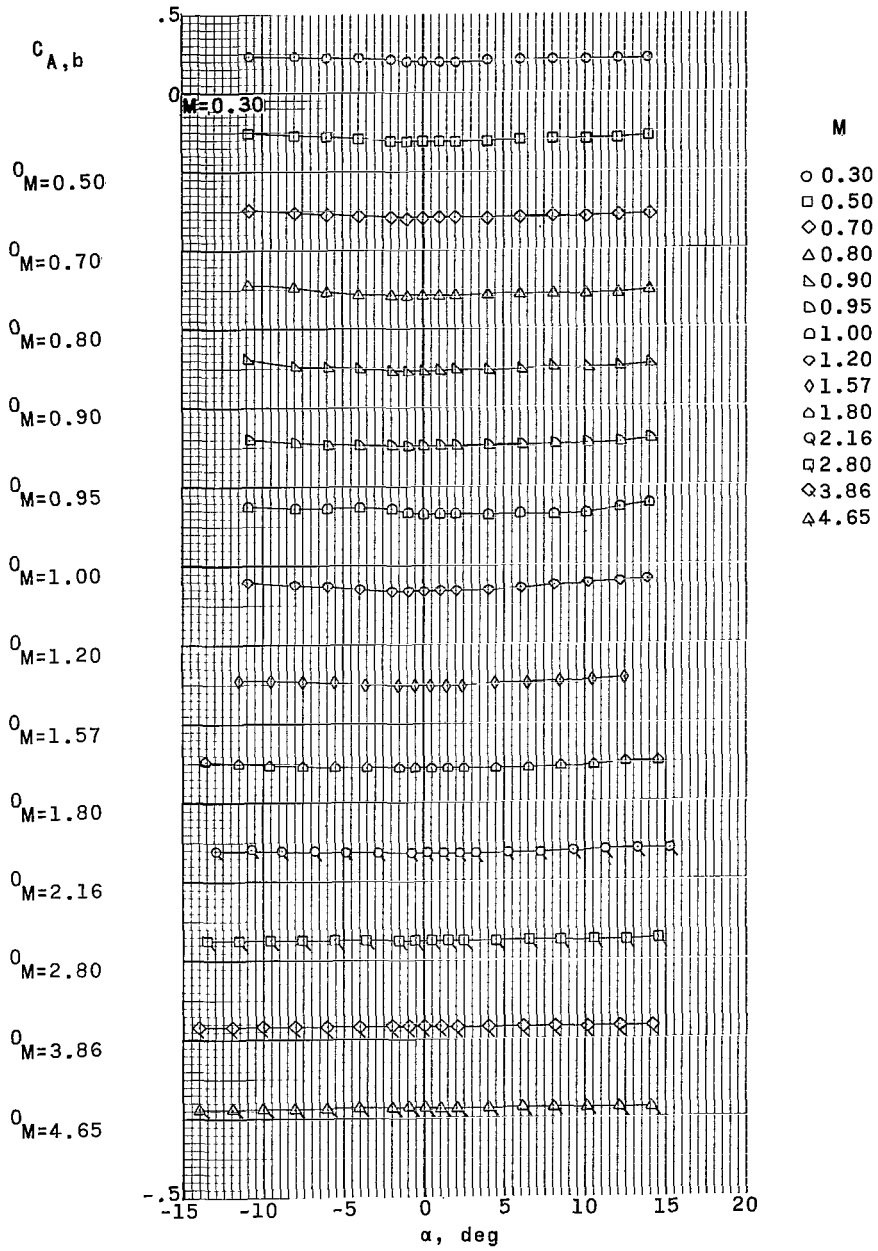

(f) Base axial-force coefficient.

Figure 24. - Concluded.

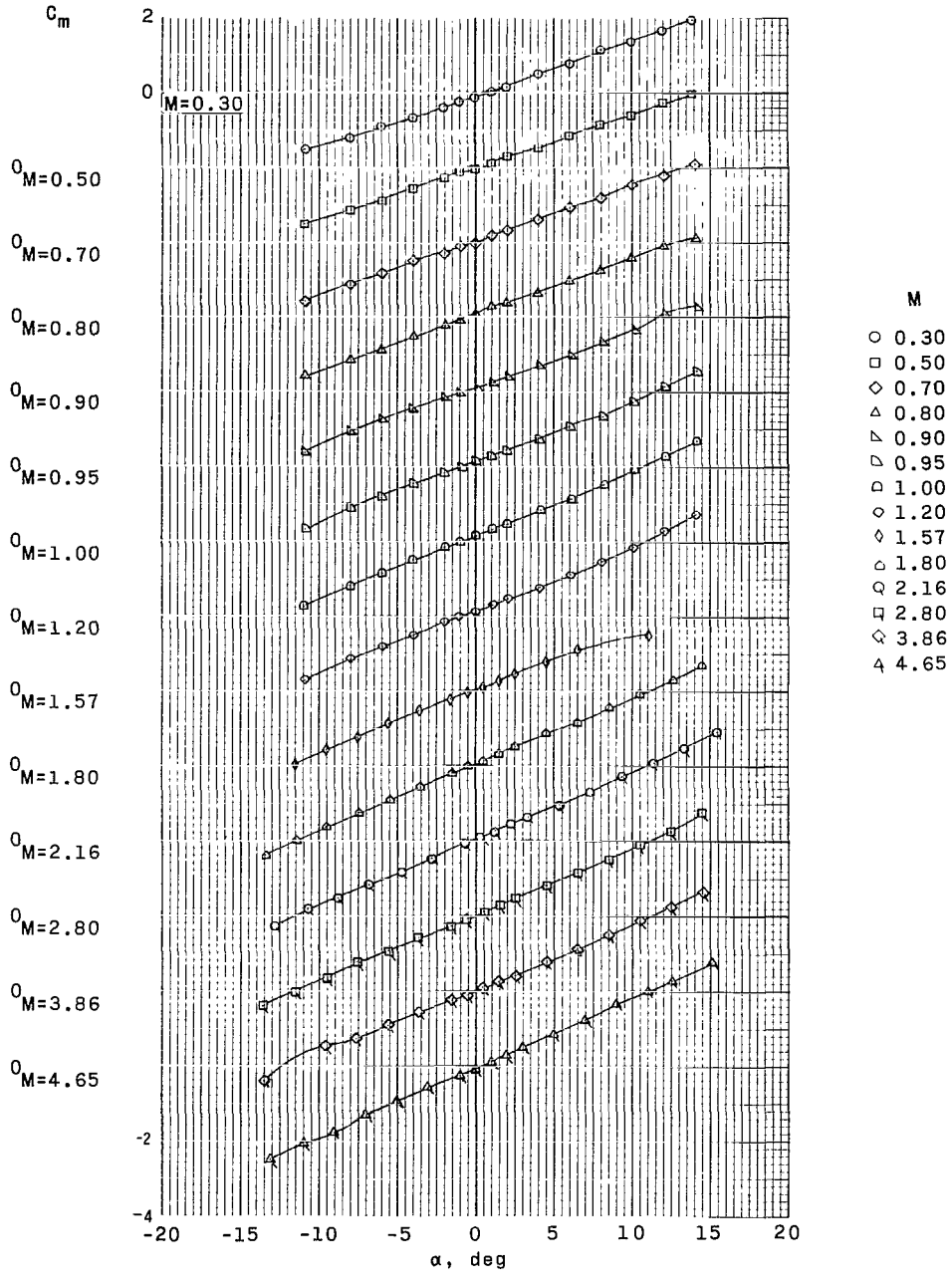

(a) Pitching-moment coefficient.

Figure 25. - Effect of deflection of trailing-edge control surfaces on longitudinal aerodynamic characteristics of configuration III (without stabilizing disk) at Mach numbers from 0.30 to 4.65 (c.g. = X/D = 0; Z/D = 0; δ_f = -20°).

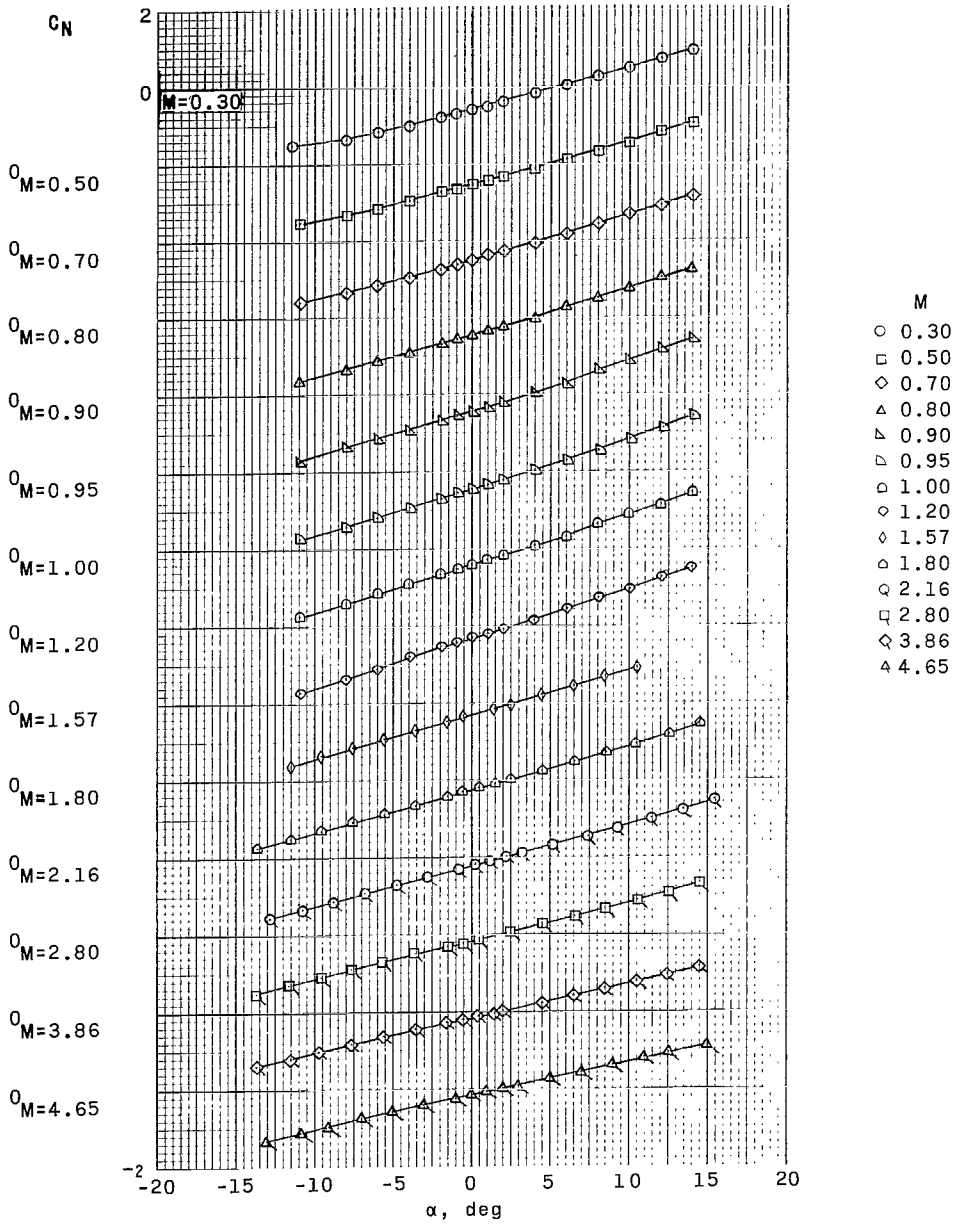

(b) Normal-force coefficient.

Figure 25. - Continued.

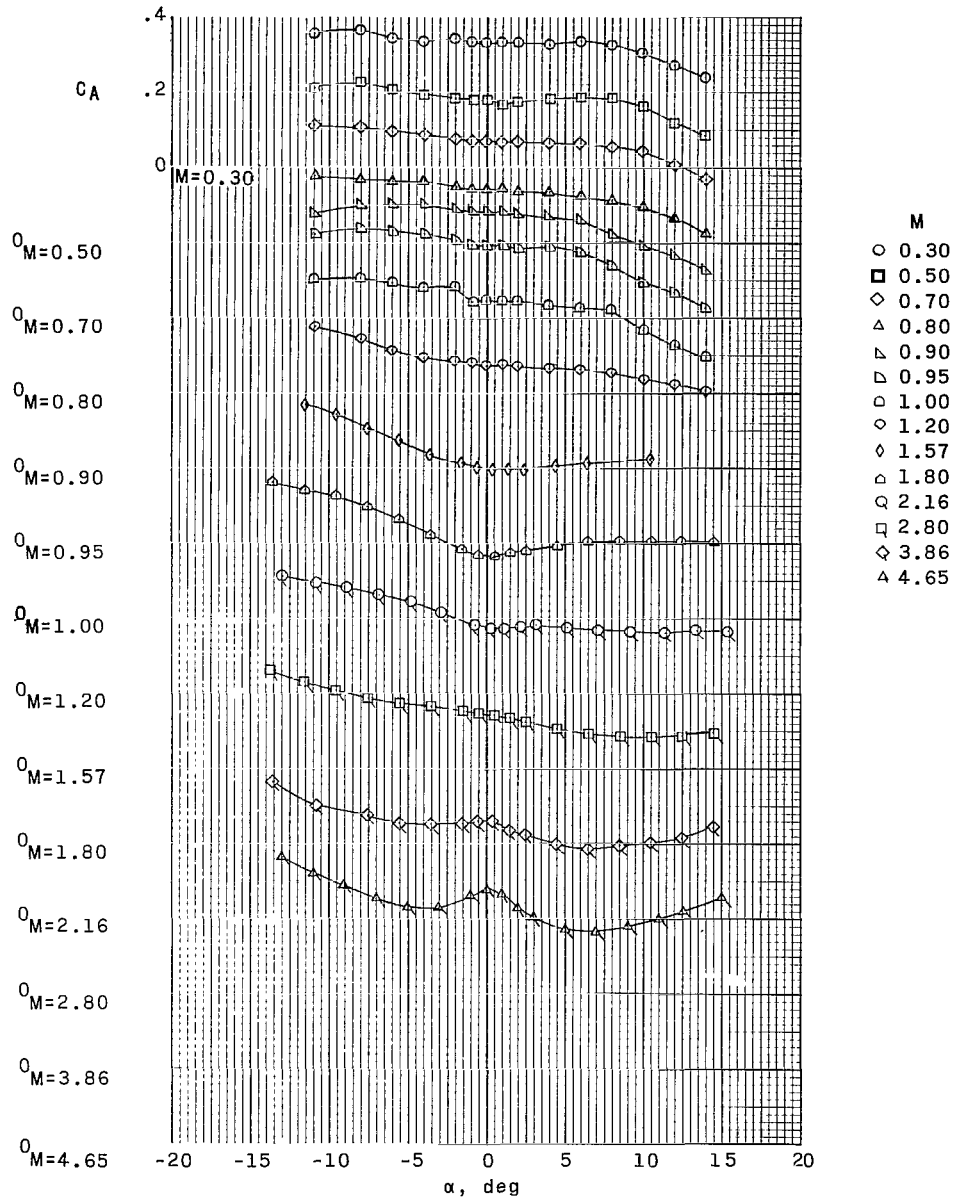

(c) Axial-force coefficient.

Figure 25. - Continued.

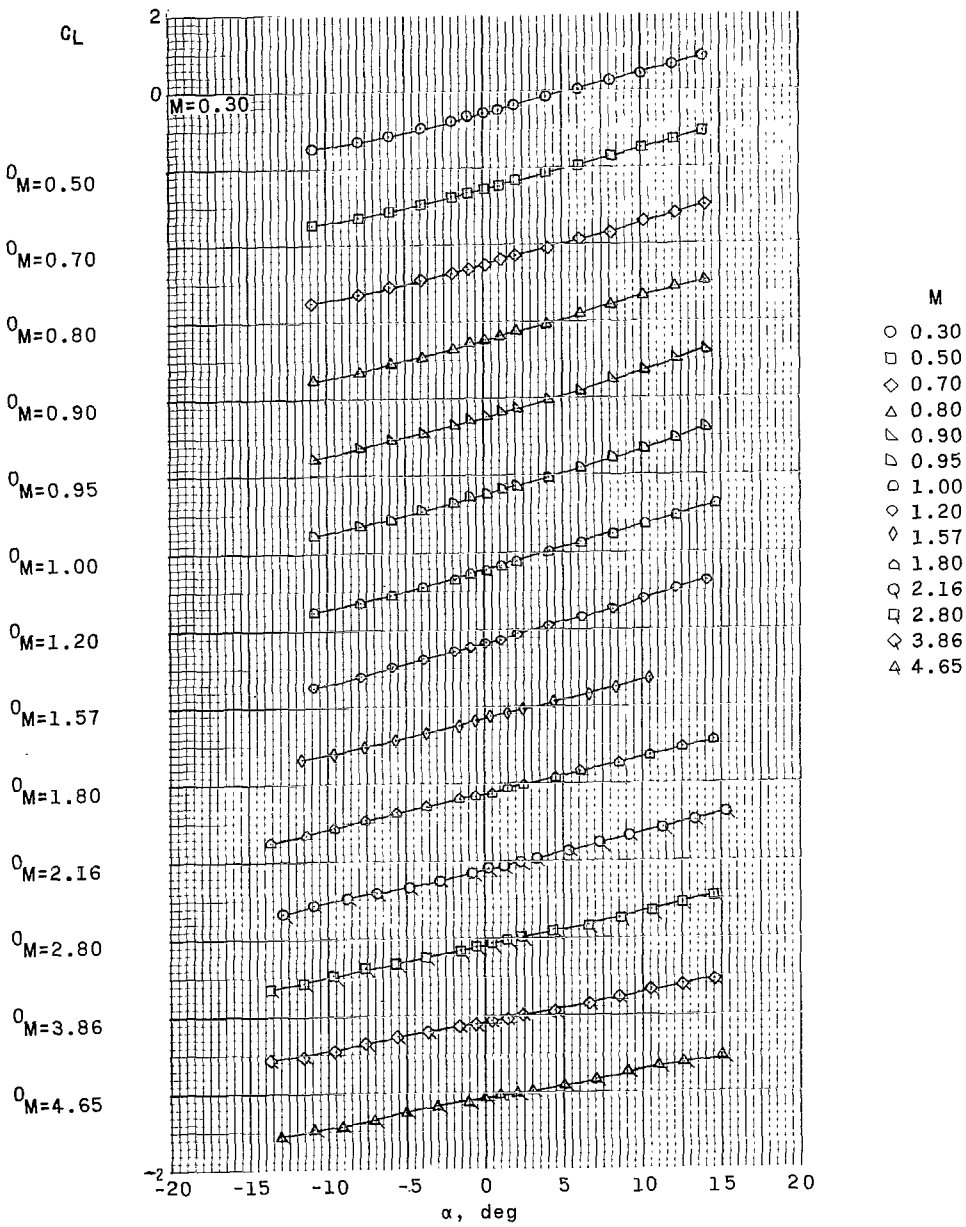

(d) Lift coefficient.

Figure 25. - Continued.

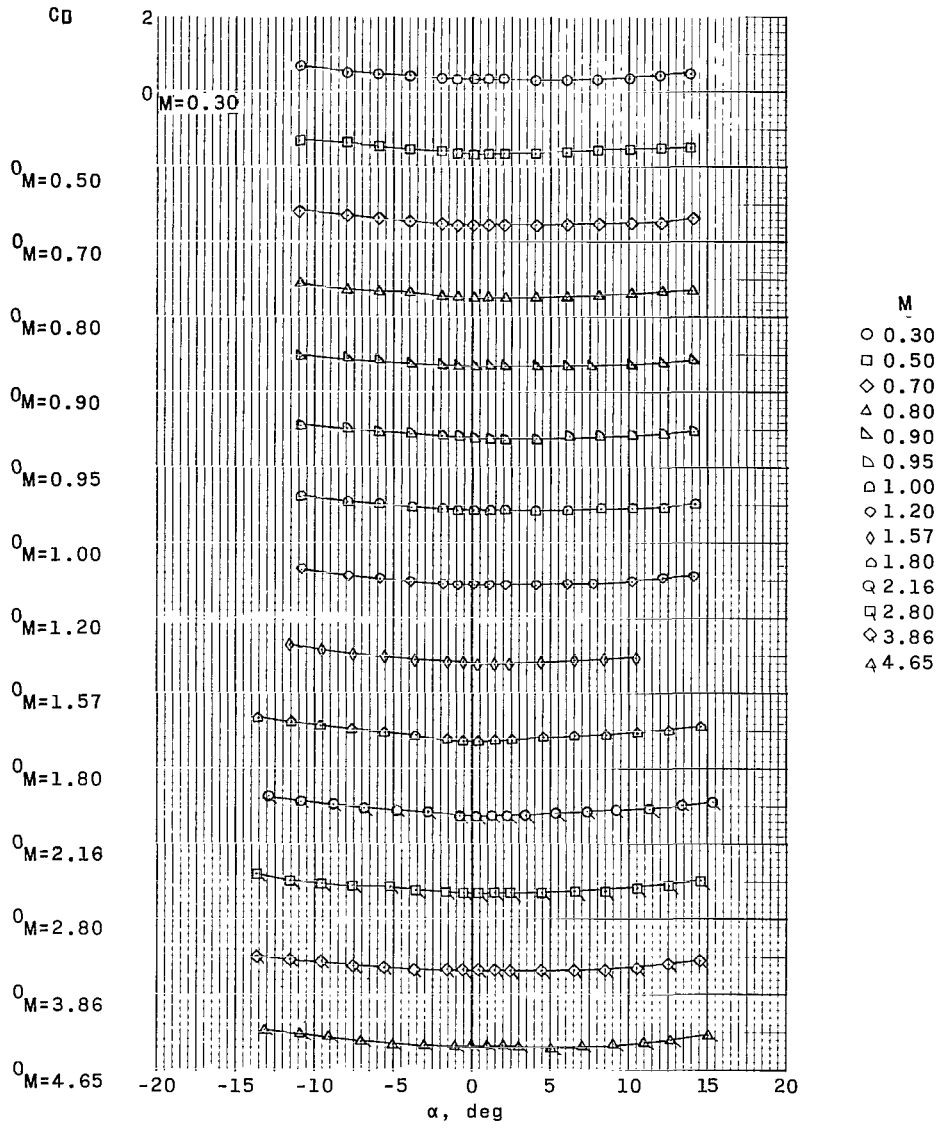

(e) Drag coefficient.

Figure 25. - Continued.

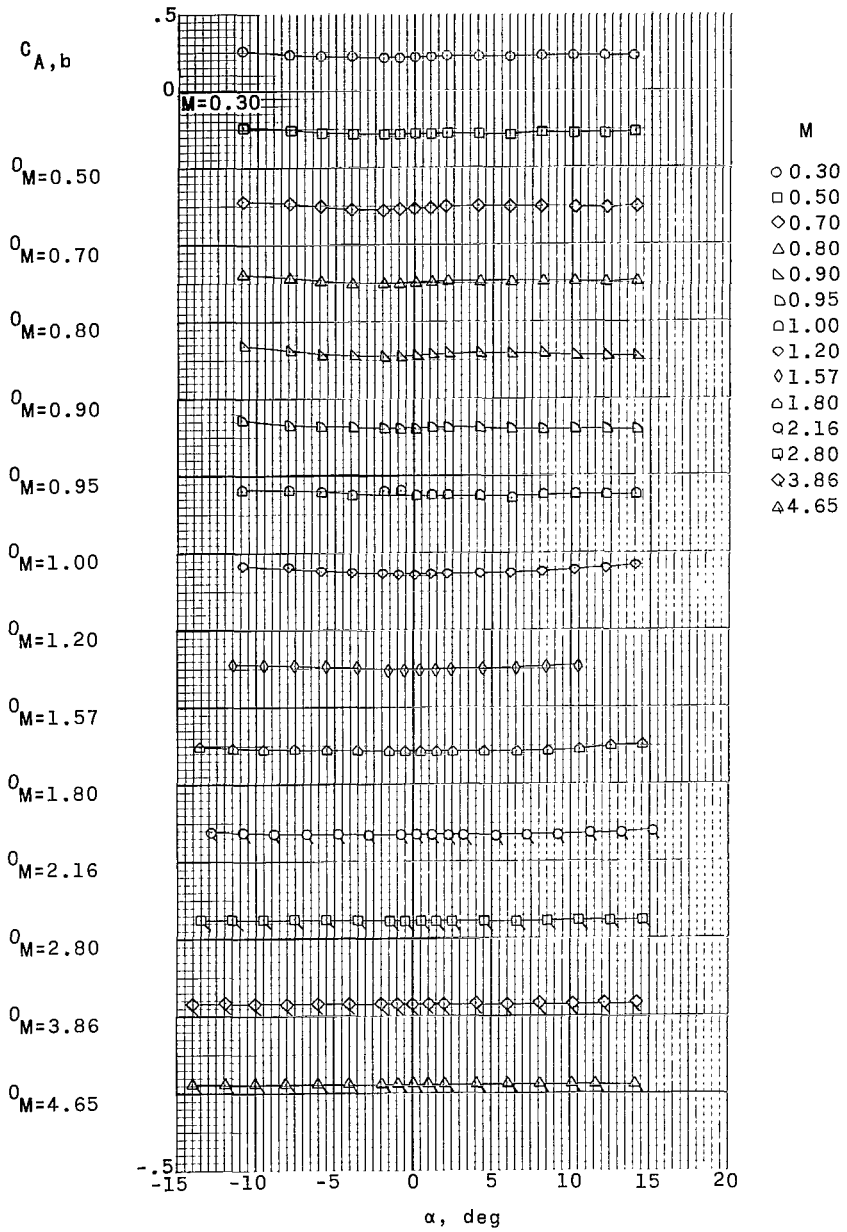

(f) Base axial-force coefficient.

Figure 25. - Concluded.

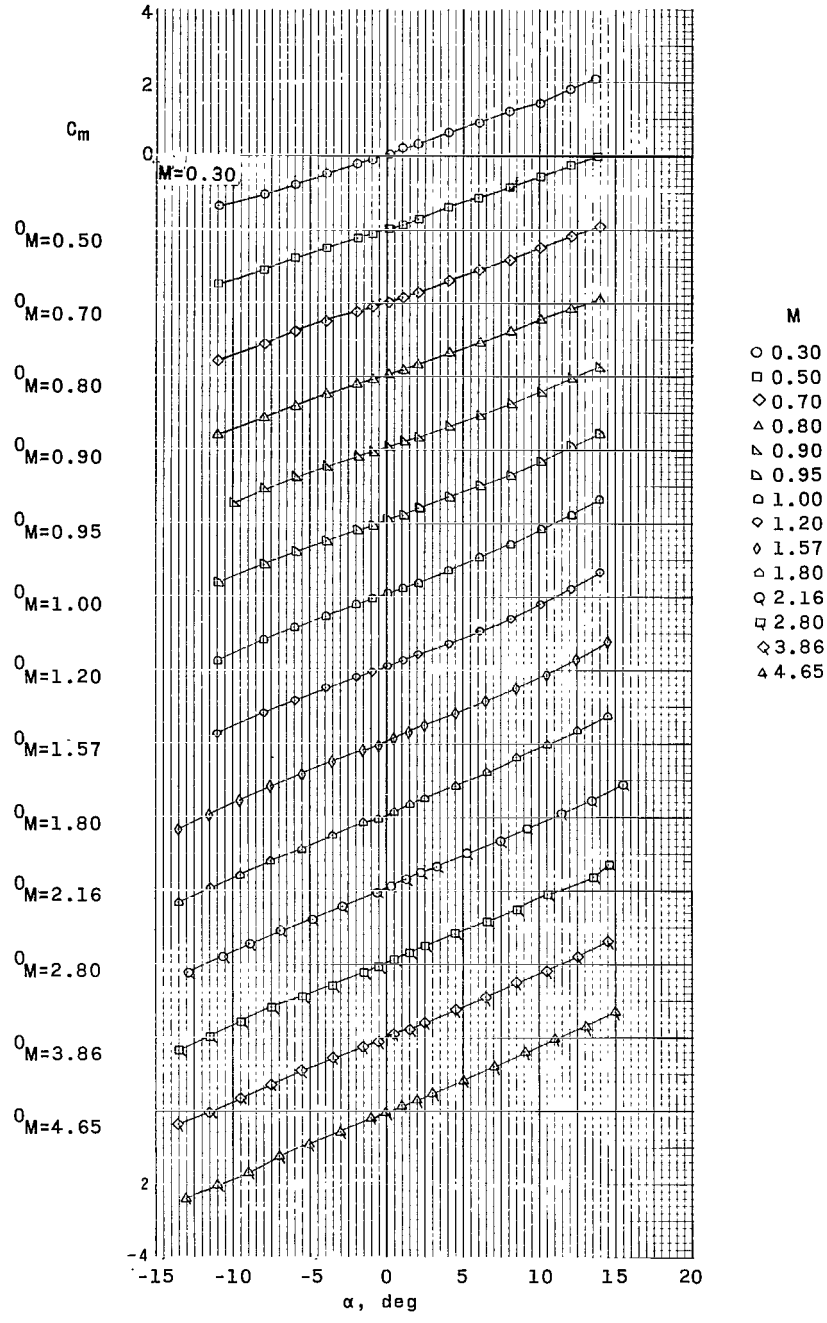

(a) Pitching-moment coefficient.

Figure 26. - Effect of deflection of trailing-edge control surfaces on longitudinal aerodynamic characteristics of configuration III (without stabilizing disk) at Mach numbers from 0.30 to 4.65 (c.g. = X/D = 0; Z/D = 0; δ_f = -30°).

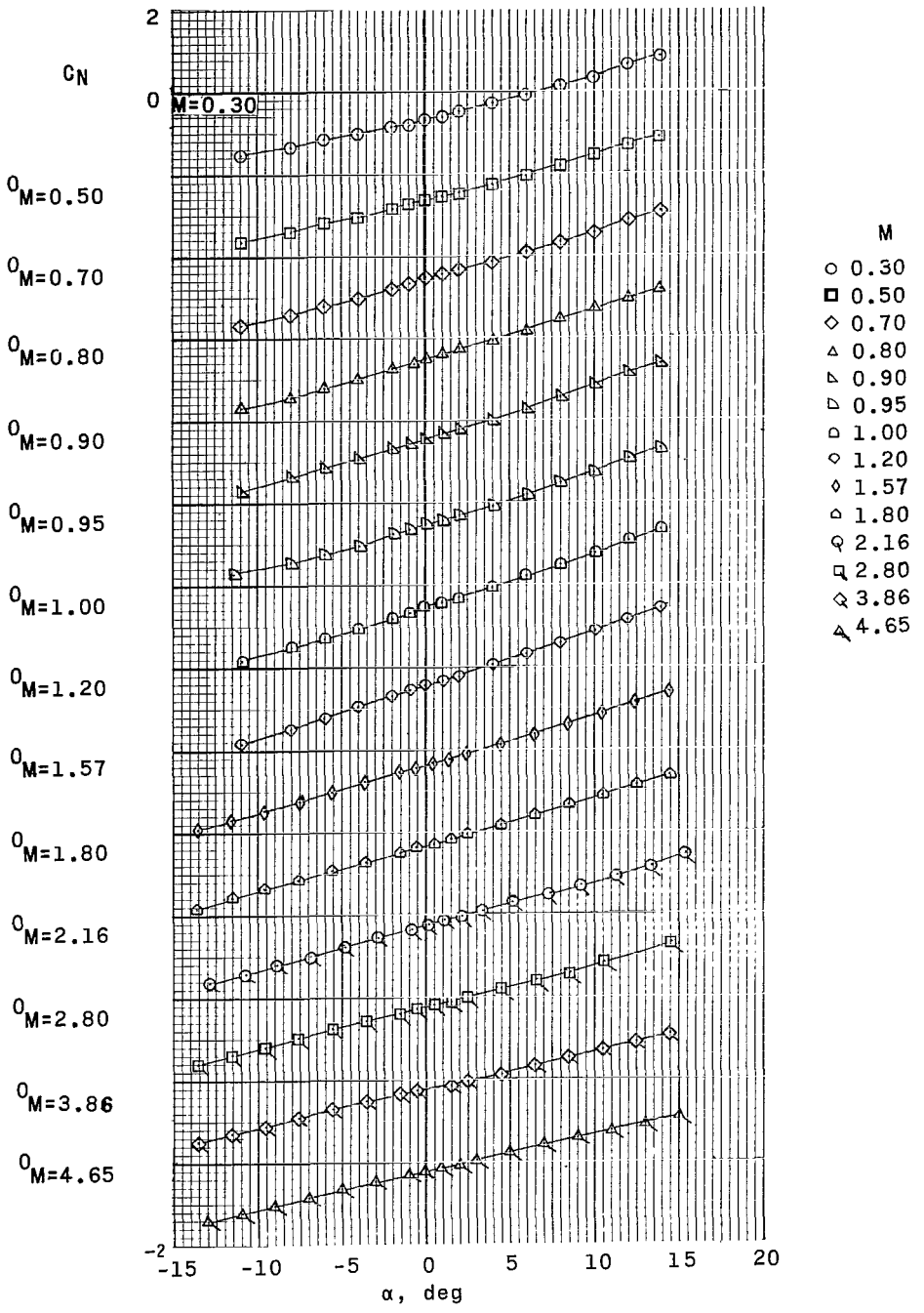

(b) Normal-force coefficient.

Figure 26. - Continued.

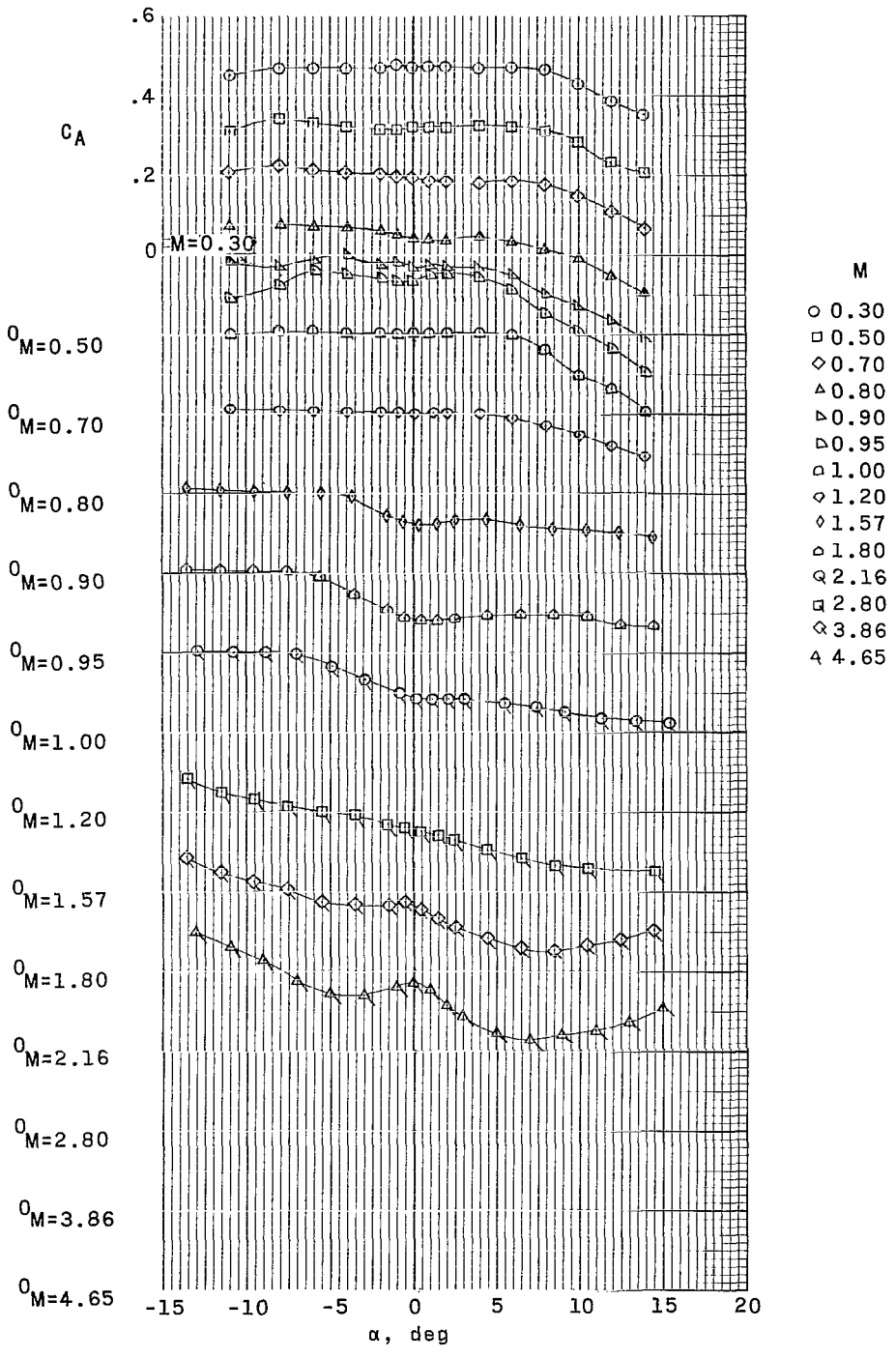

(c) Axial-force coefficient.

Figure 26. - Continued.

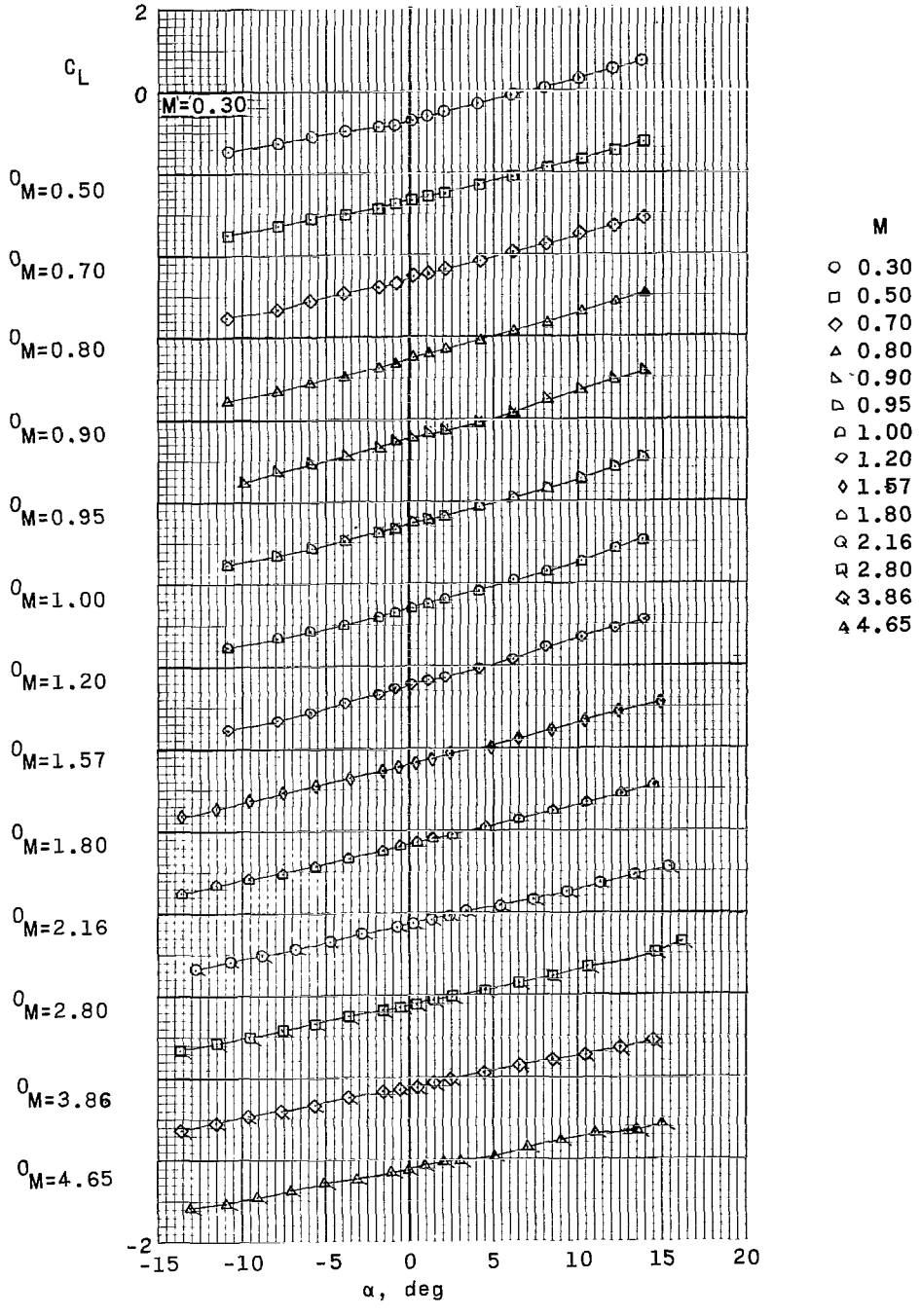

(d) Lift coefficient.

Figure 26. - Continued.

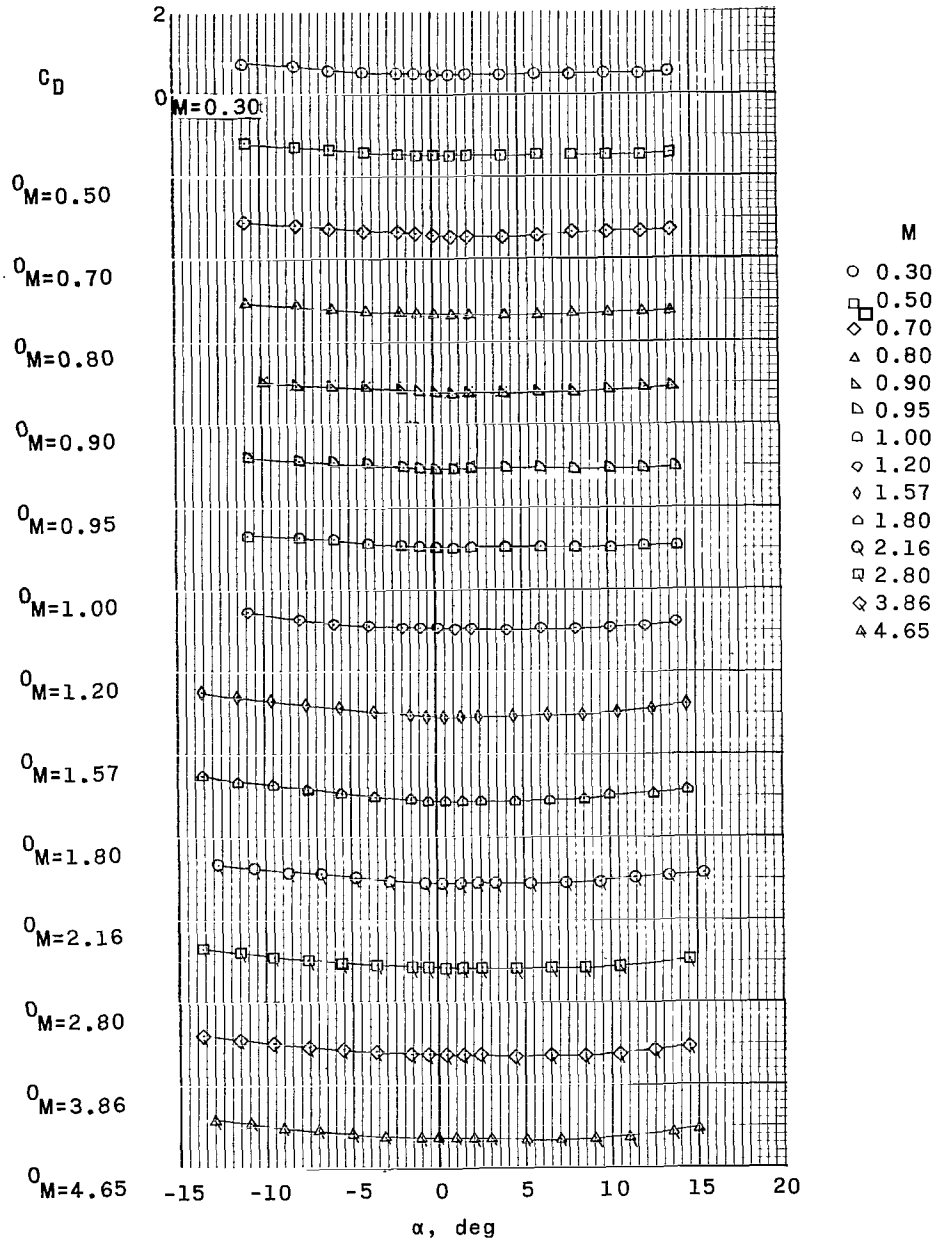

(e) Drag coefficient.

Figure 26. - Continued.

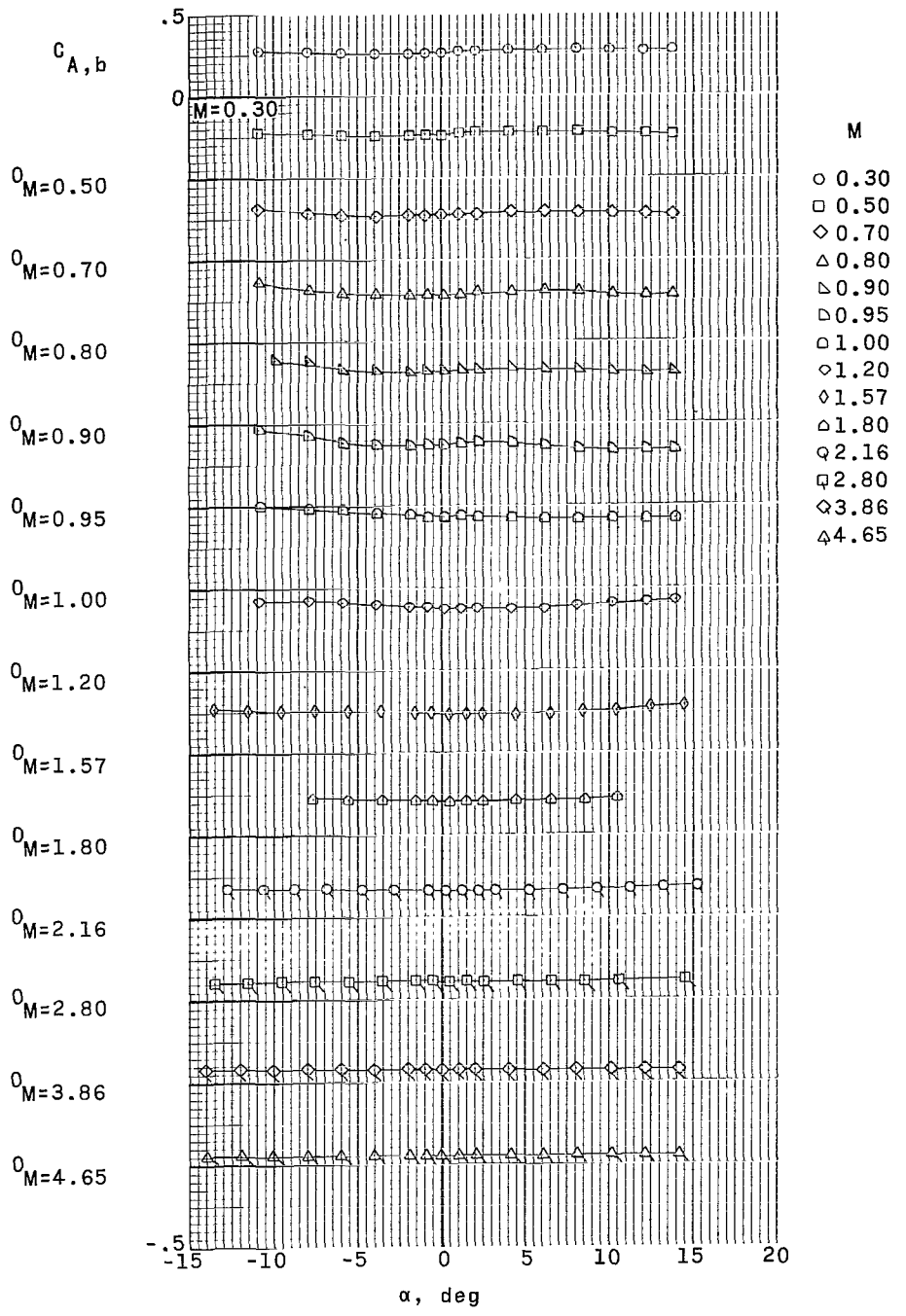

(f) Base axial-force coefficient.

Figure 26. - Concluded.

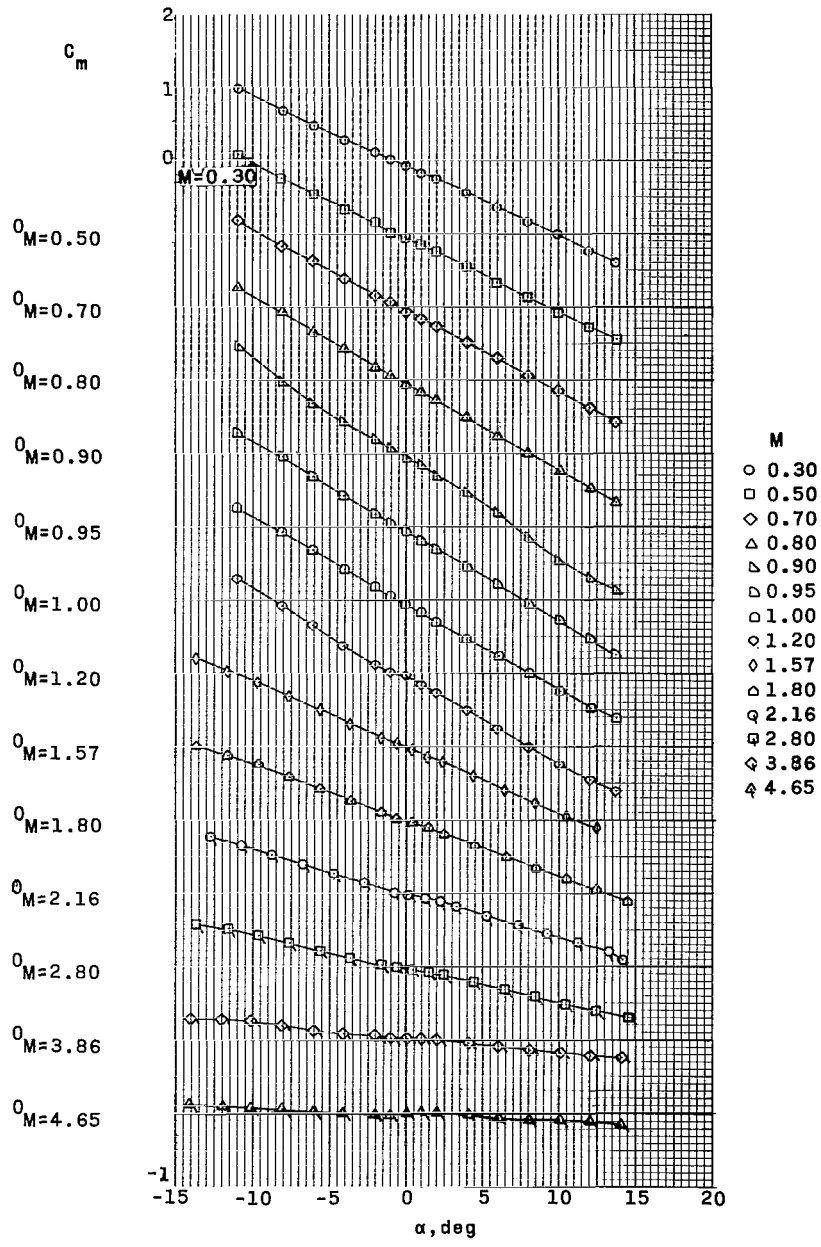

(a) $\delta_f = 0°$.

Figure 27. - Pitching-moment coefficient computed about a center-of-gravity location of X/D = 2.272; Z/D = 0 to show the effectiveness of the trailing-edge control surfaces for configuration III (without stabilizing disk).

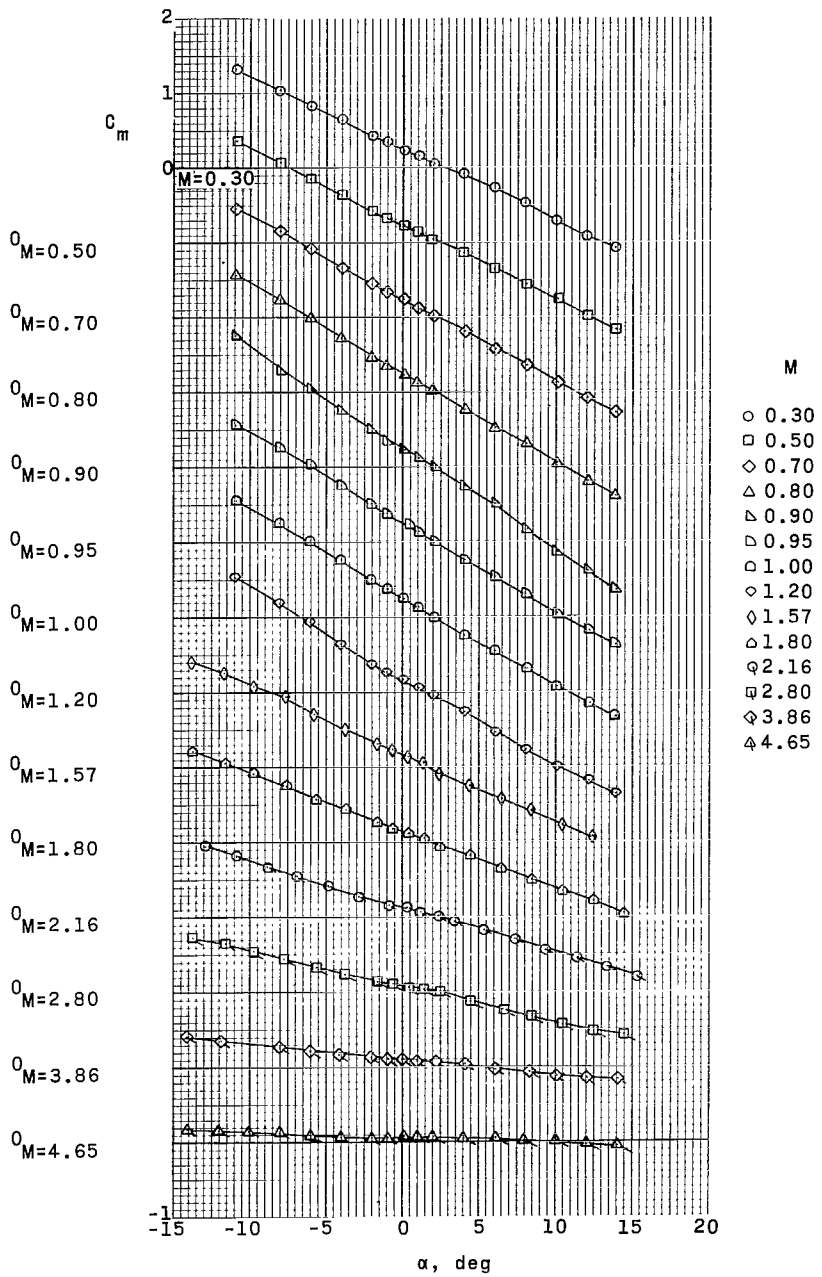

(b) $\delta_f = -5°$.

Figure 27. - Continued.

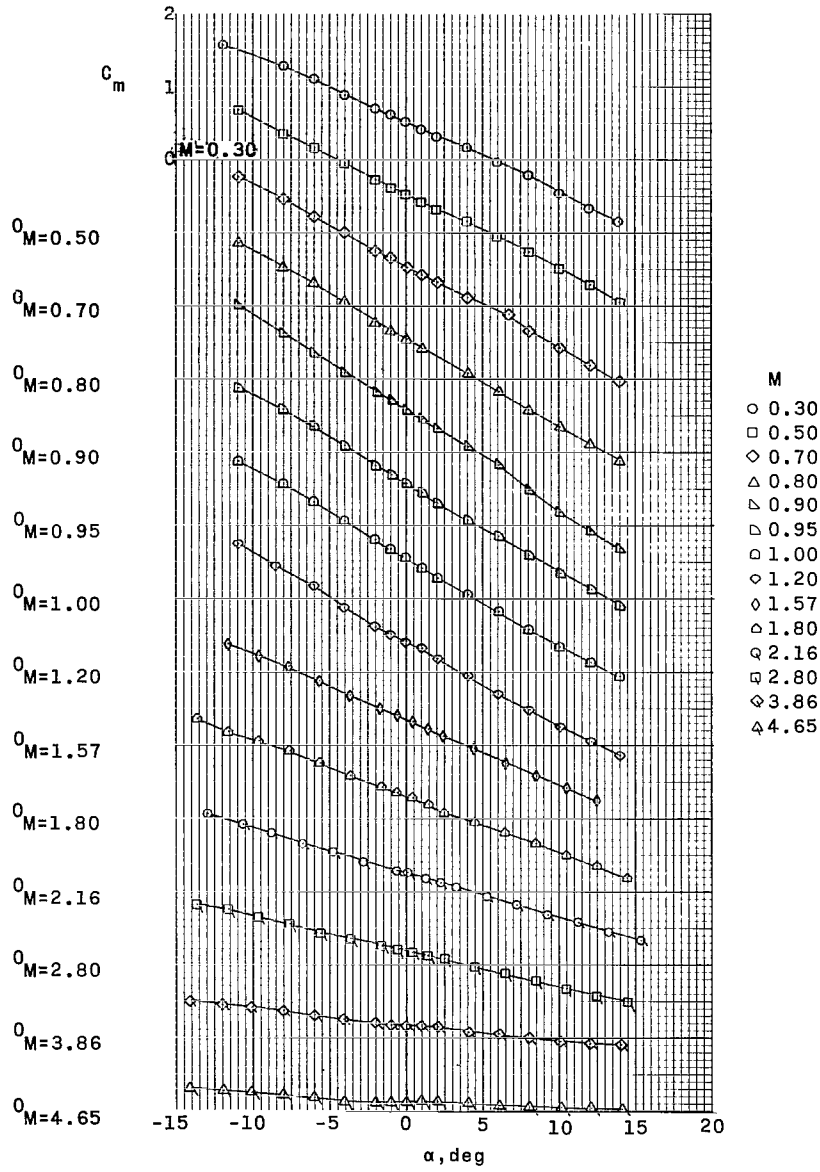

(c) $\delta_f = -10°$.

Figure 27. - Continued.

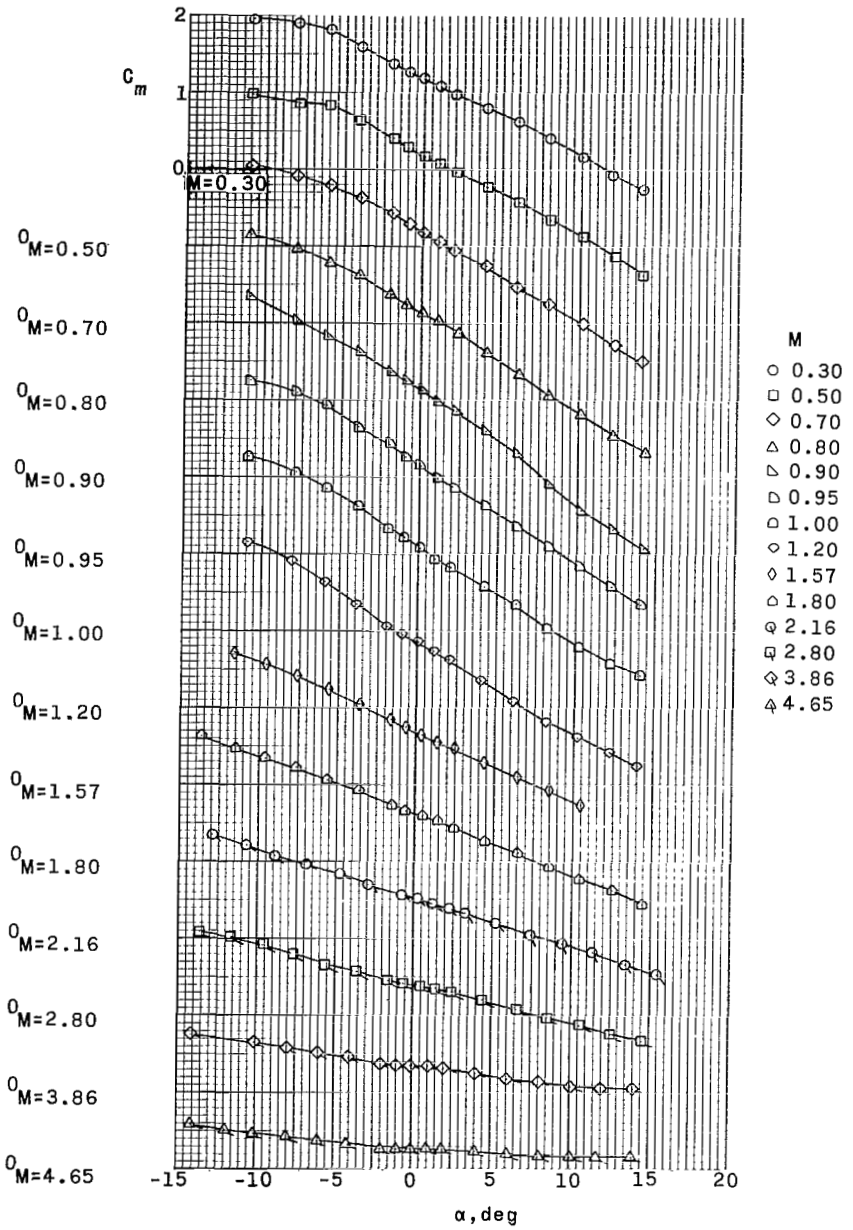

(d) $\delta_f = -20°$.

Figure 27. - Continued.

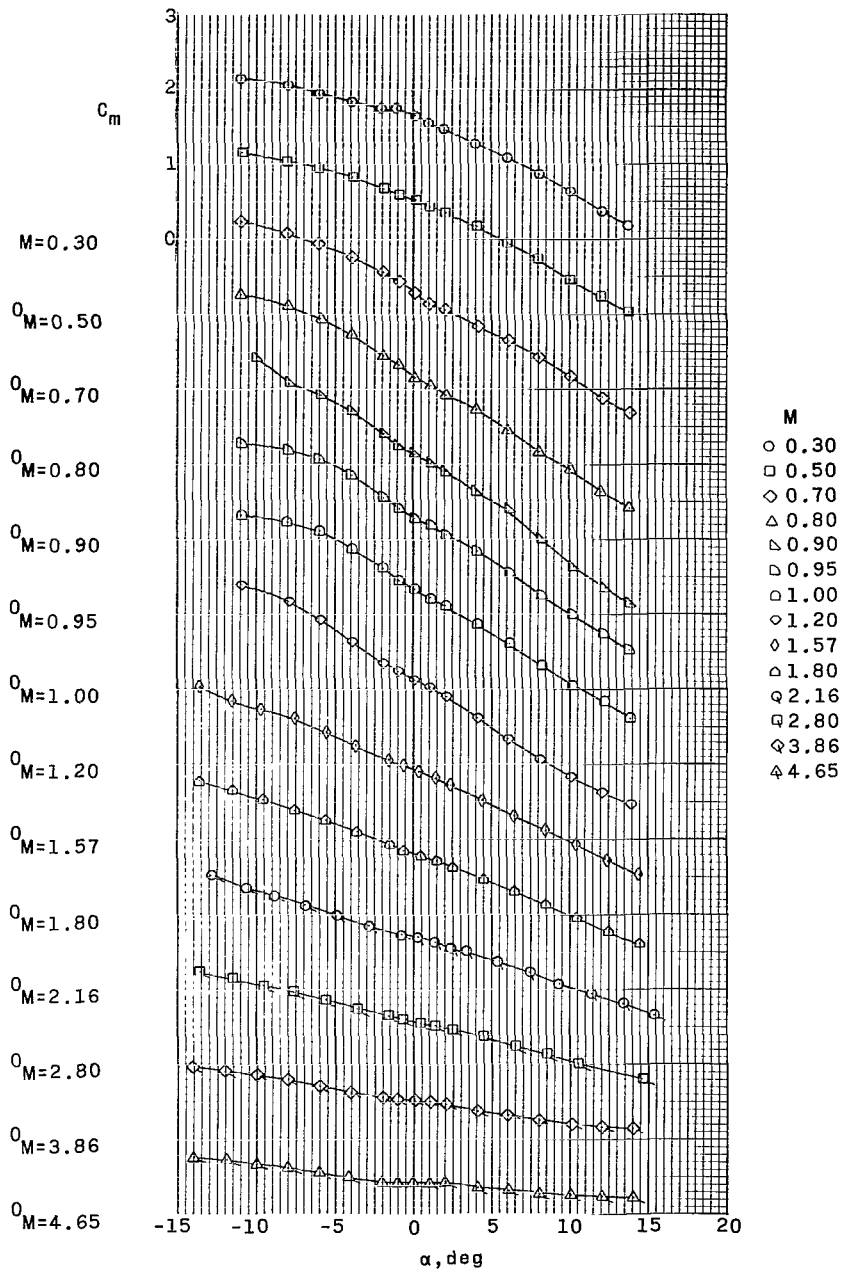

(e) $\delta_f = -30°$.

Figure 27. - Concluded.

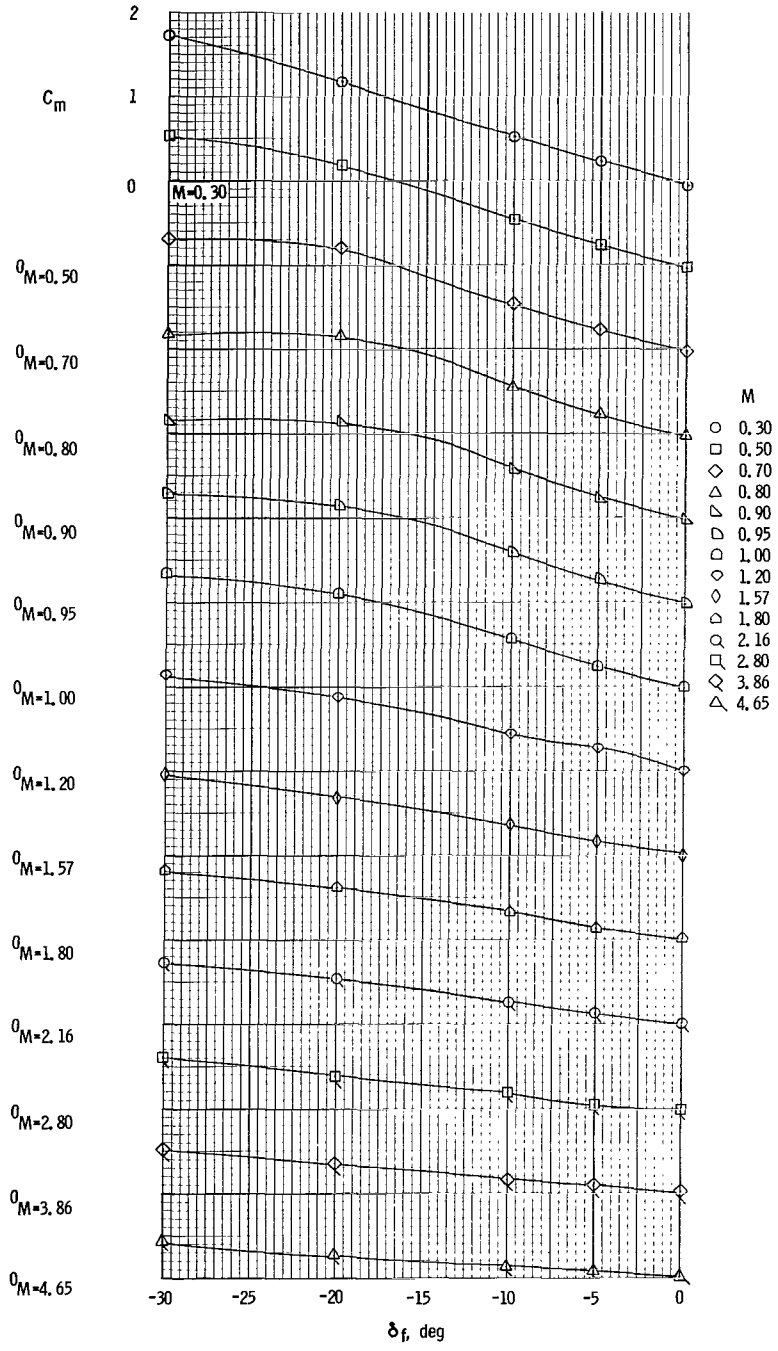

Figure 28. - Plot of pitching-moment coefficient versus control deflection for an angle of attack of 0° at the center-of-gravity location of X/D = 2.272; Z/D = 0 (α = 0°).

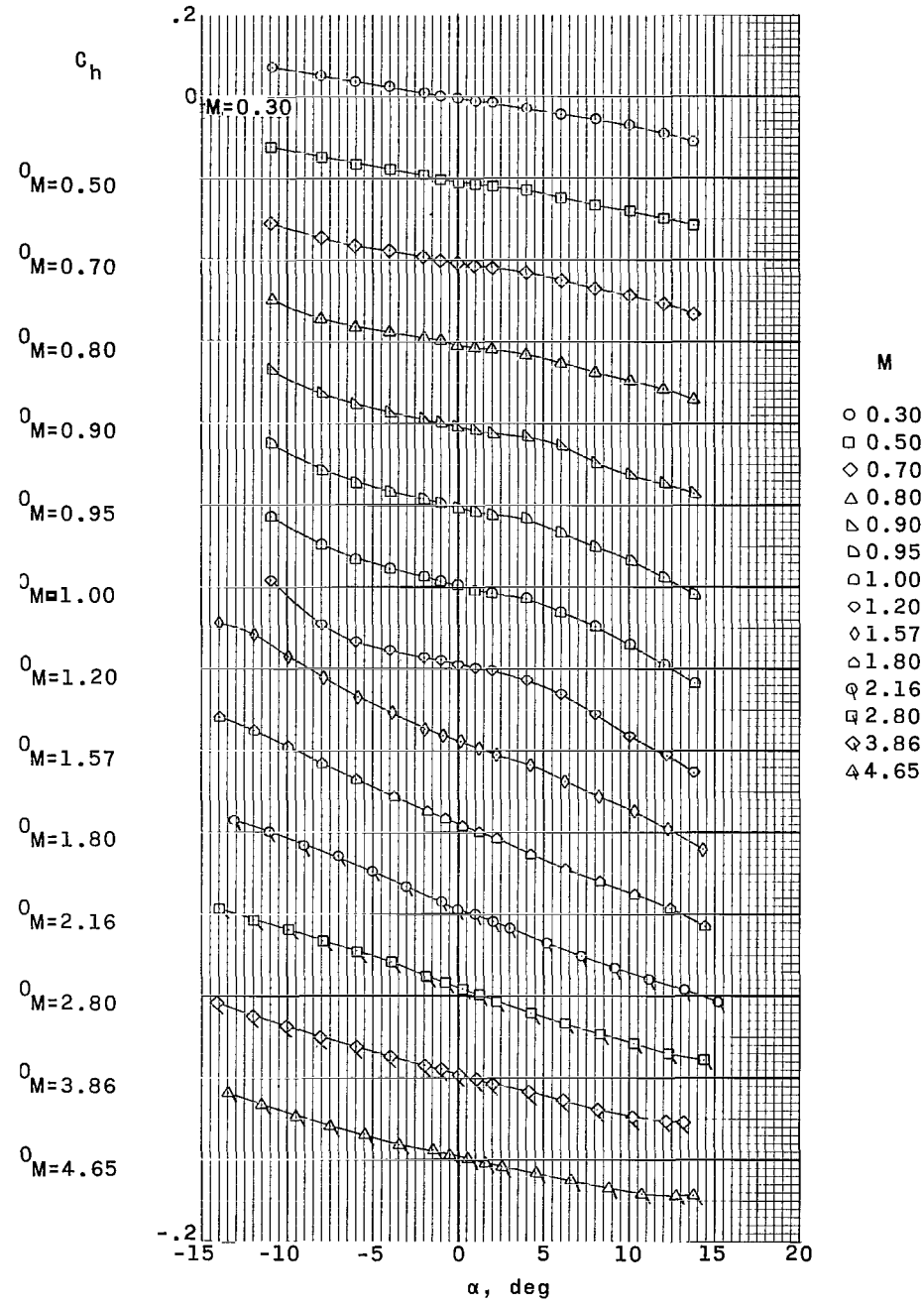

(a) $\delta_f = 0°$.

Figure 29. - Hinge-moment coefficient of the trailing-edge control surfaces for configuration III (without stabilizing disk).

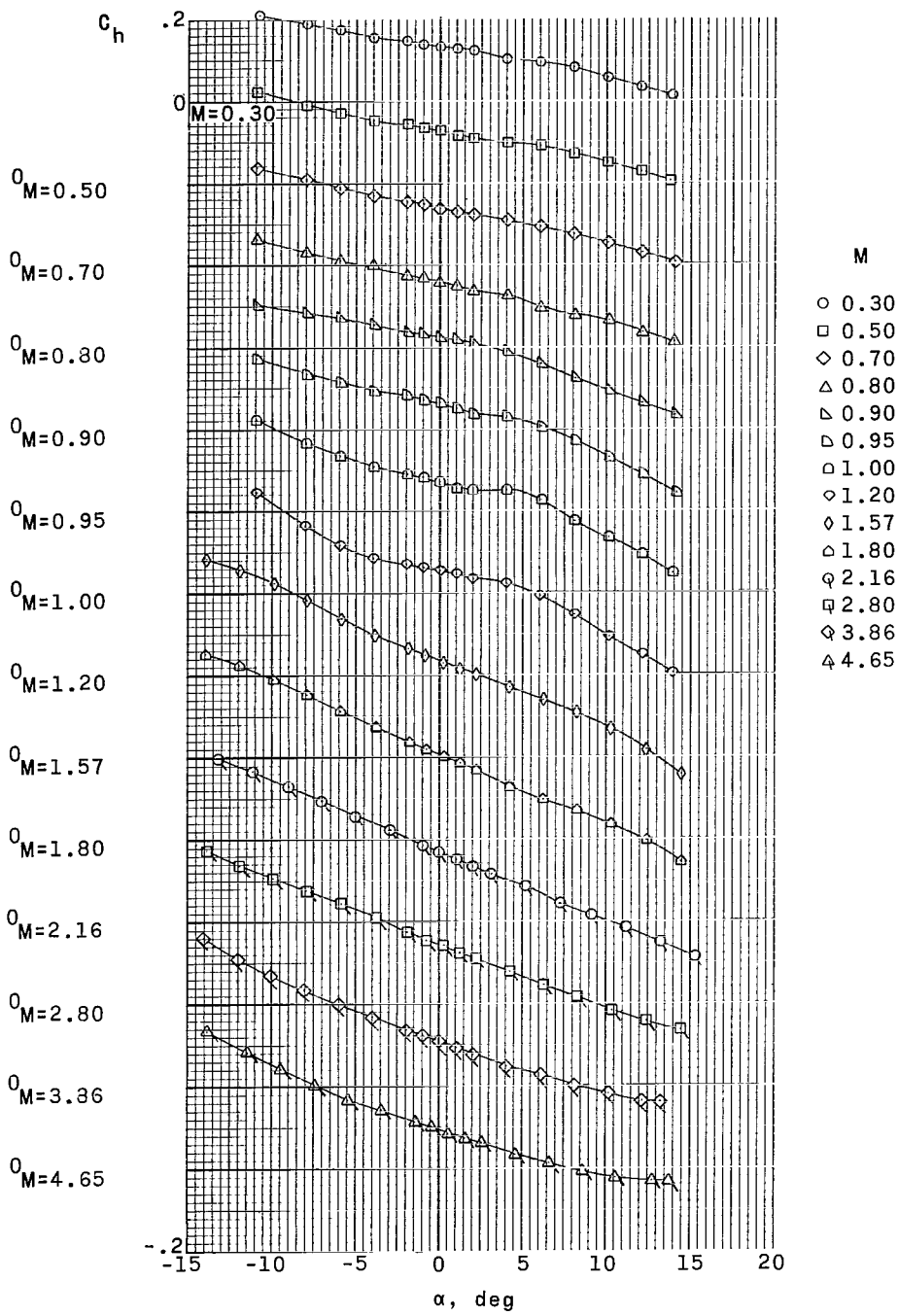

(b) $\delta_f = -10°$.

Figure 29. - Continued.

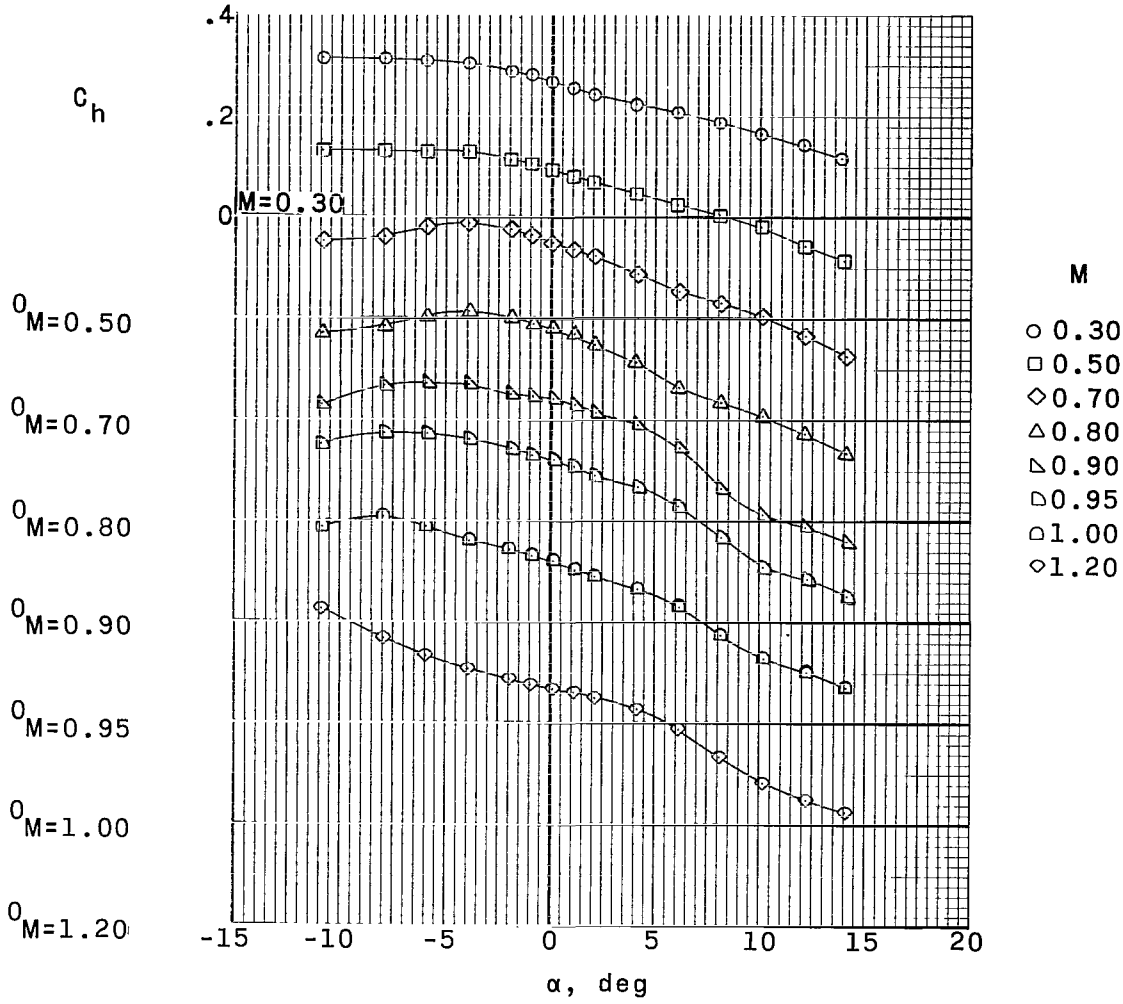

(c) $\delta_f = -20°$.

Figure 29.- Continued.

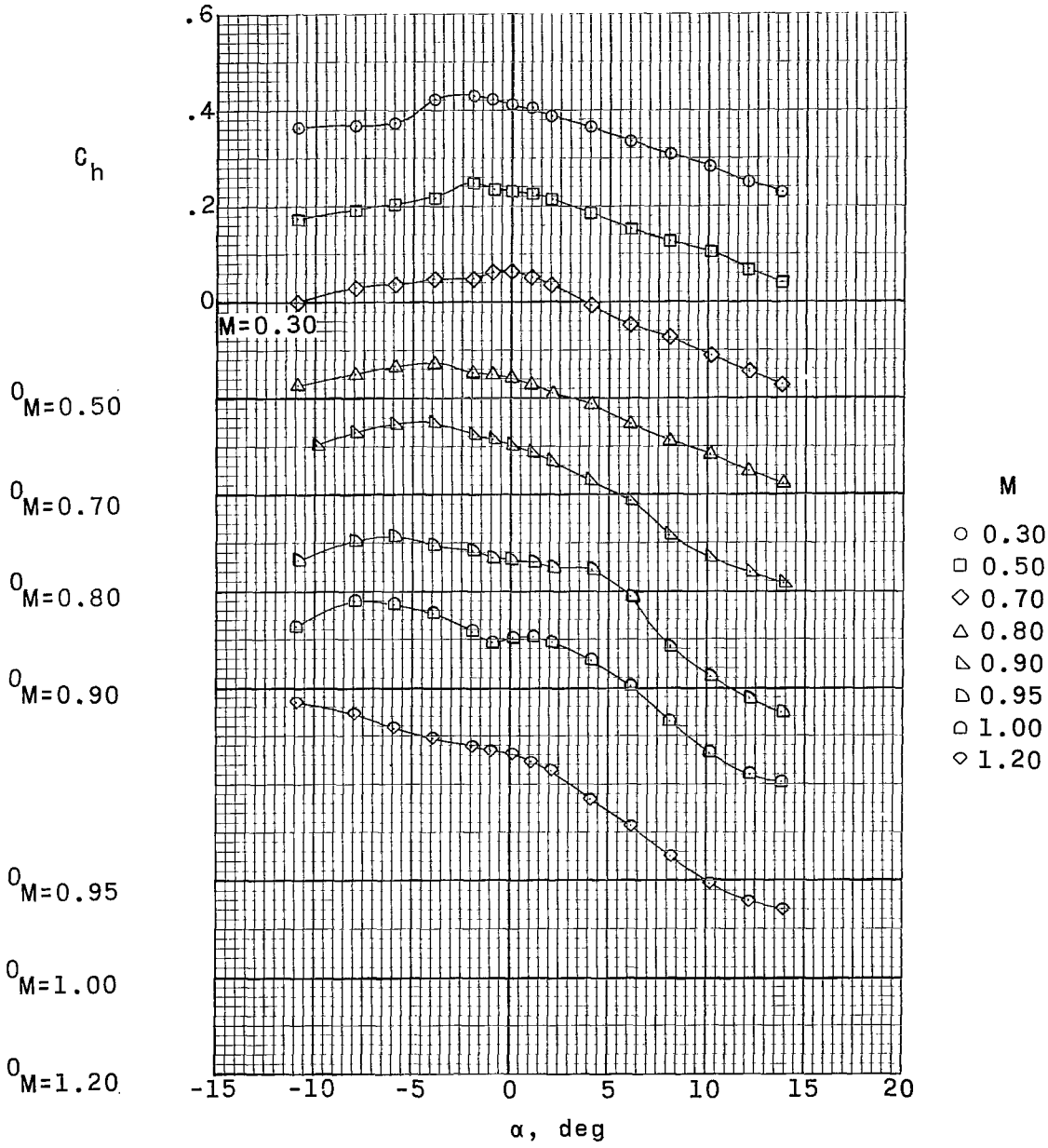

(d) $\delta_f = -30°$.

Figure 29. - Concluded.

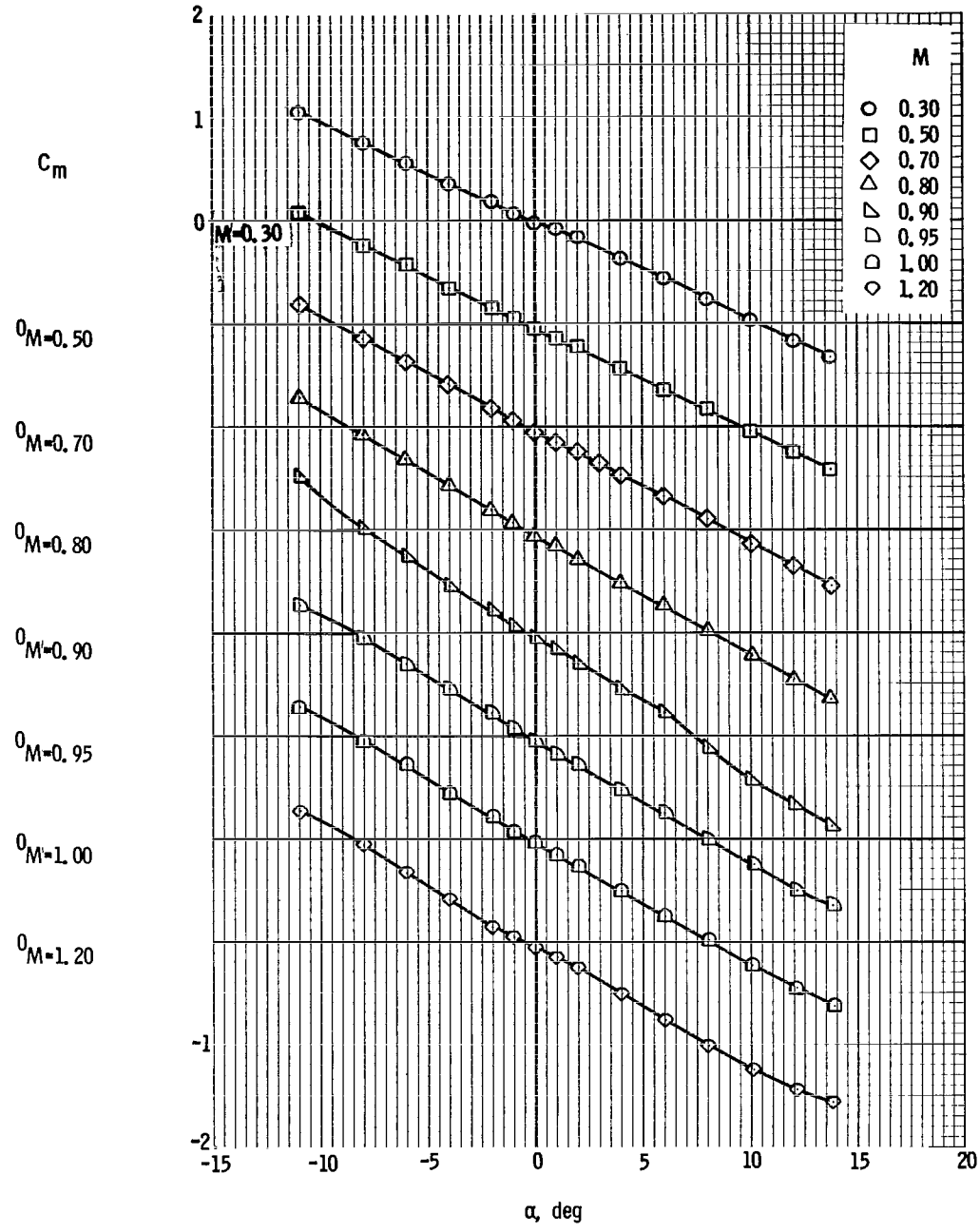

(a) Pitching-moment coefficient.

Figure 30. - Effect of differential deflection of trailing-edge control surfaces on longitudinal aerodynamic characteristics of configuration III (without stabilizing disk) at Mach numbers from 0.30 to 1.20 (c.g. = X/D = 0; Z/D = 0; $\delta_f = \pm 5°$).

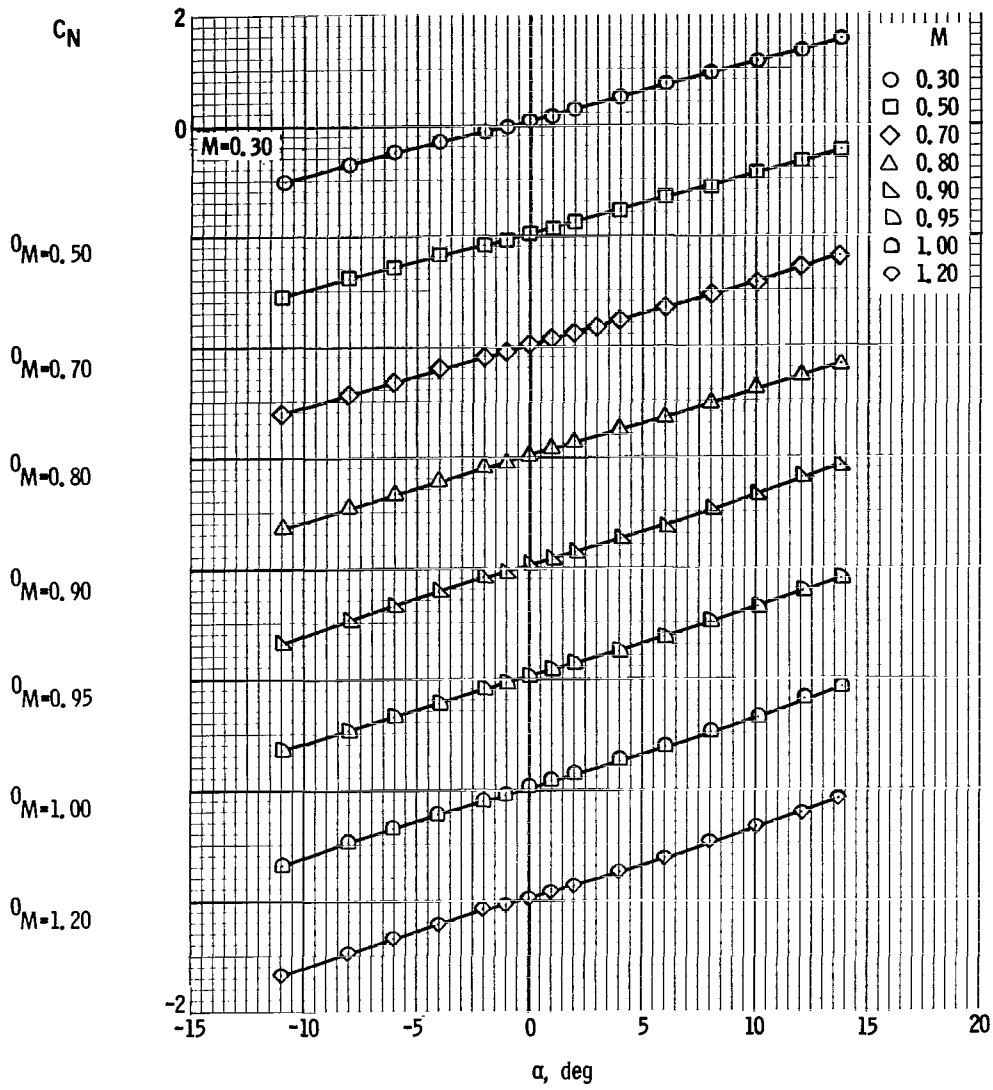

(b) Normal-force coefficient.

Figure 30. - Continued.

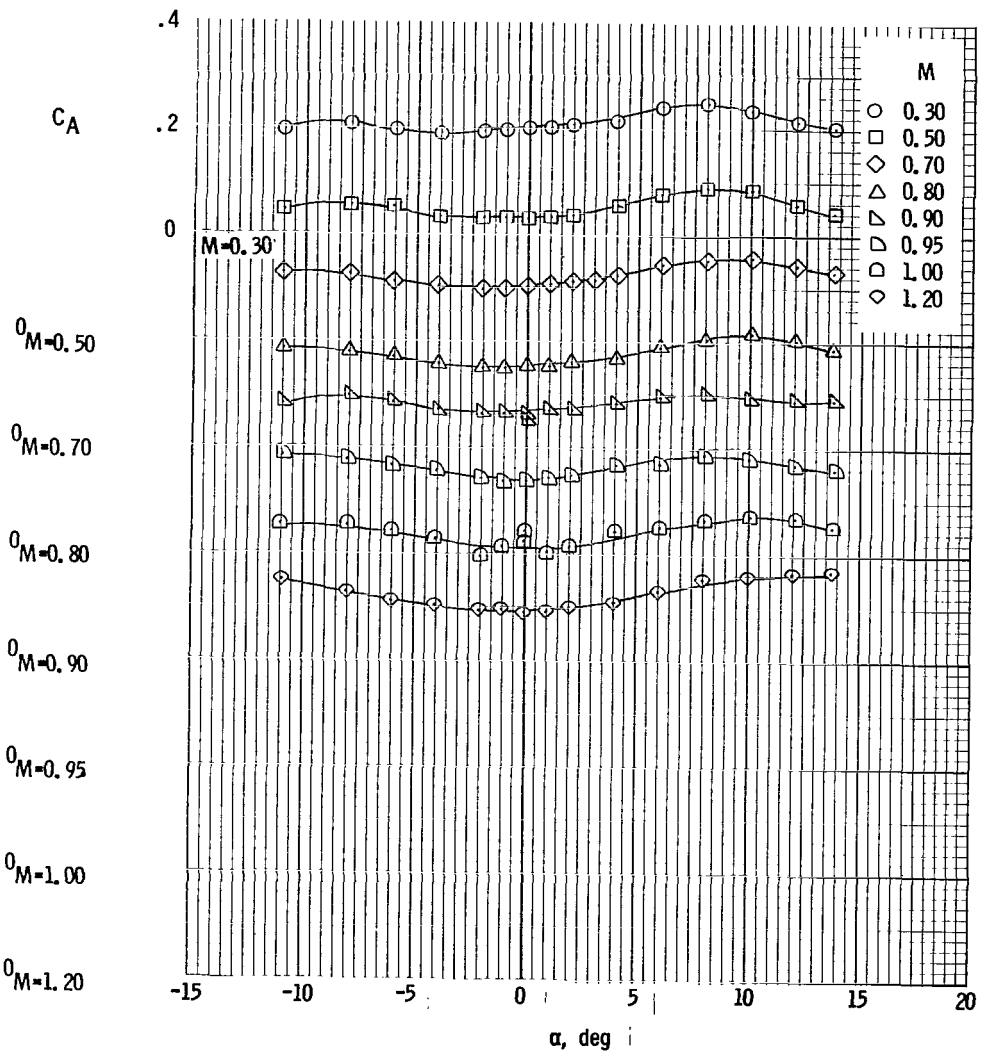

(c) Axial-force coefficient.

Figure 30. - Continued.

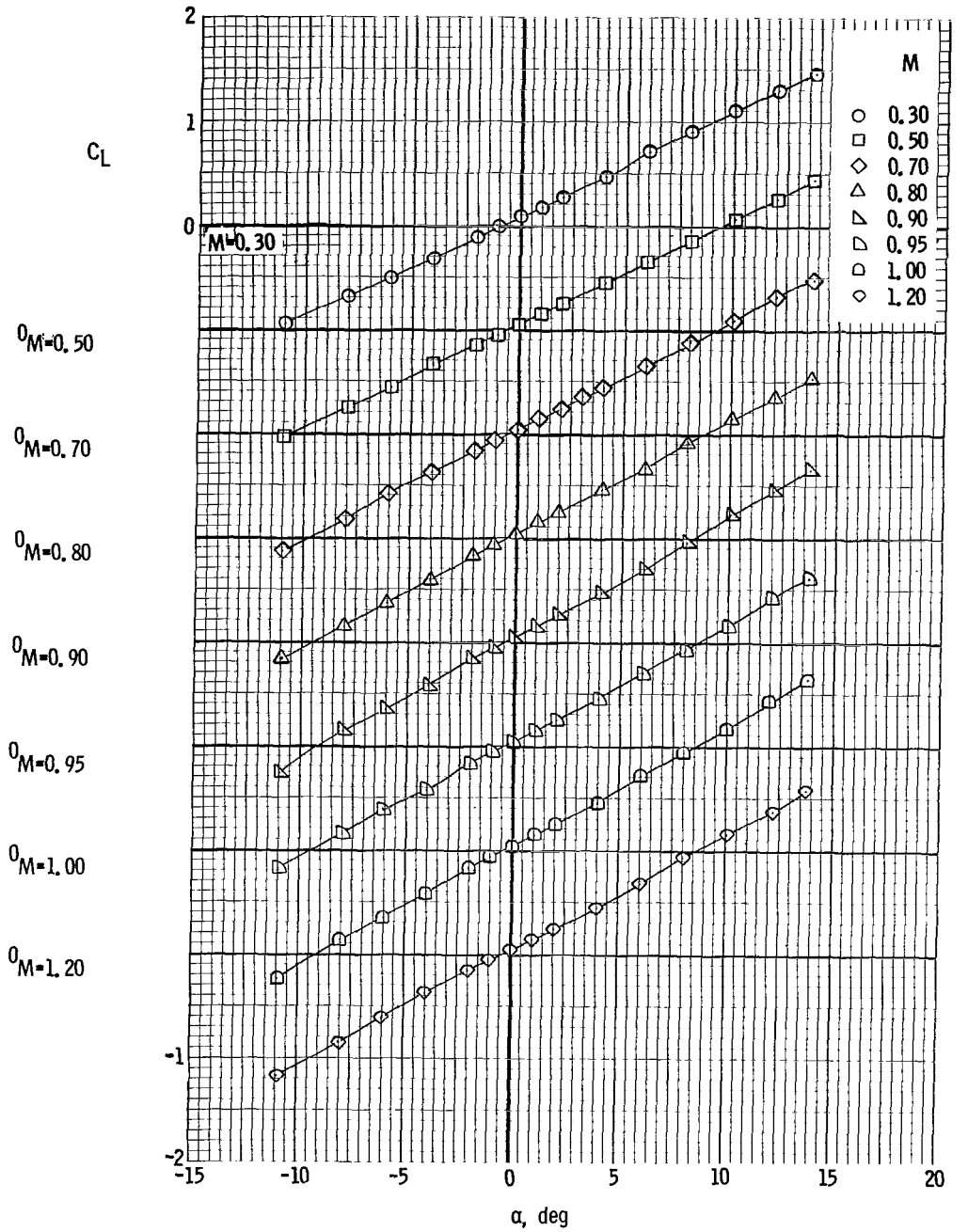

(d) Lift coefficient.

Figure 30. - Continued.

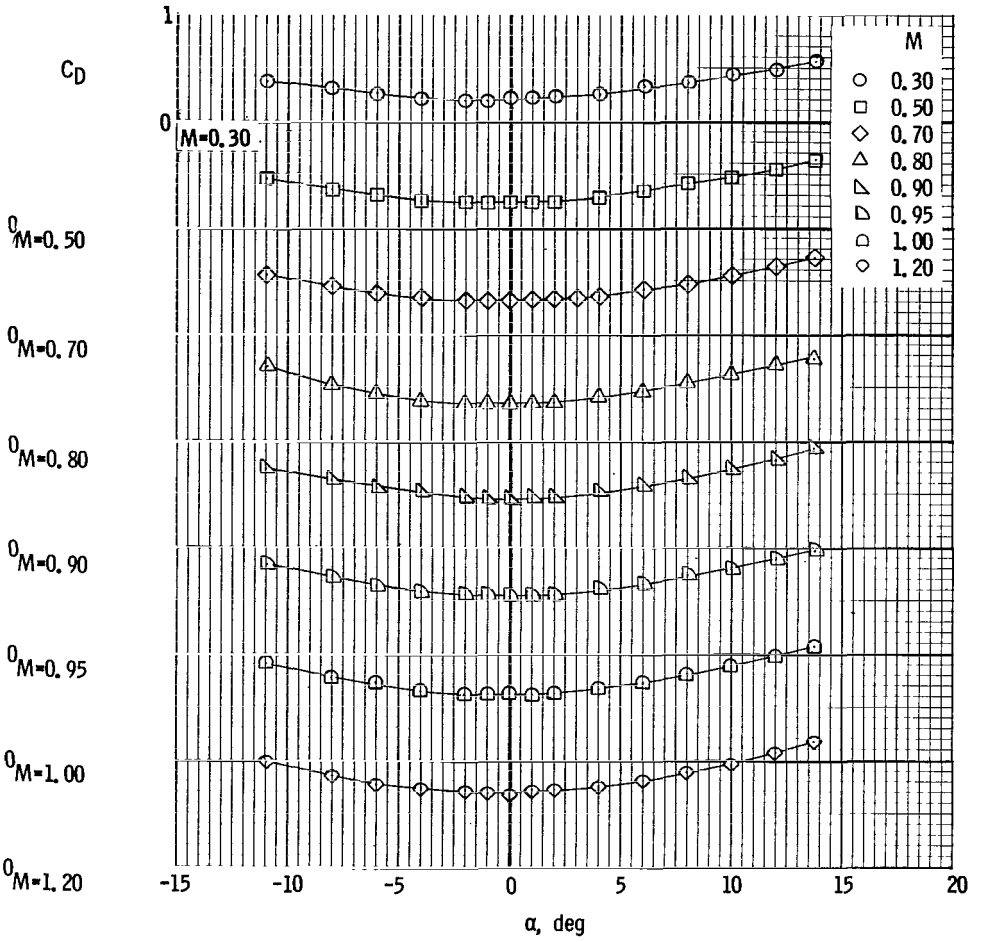

(e) Drag coefficient.

Figure 30. - Continued.

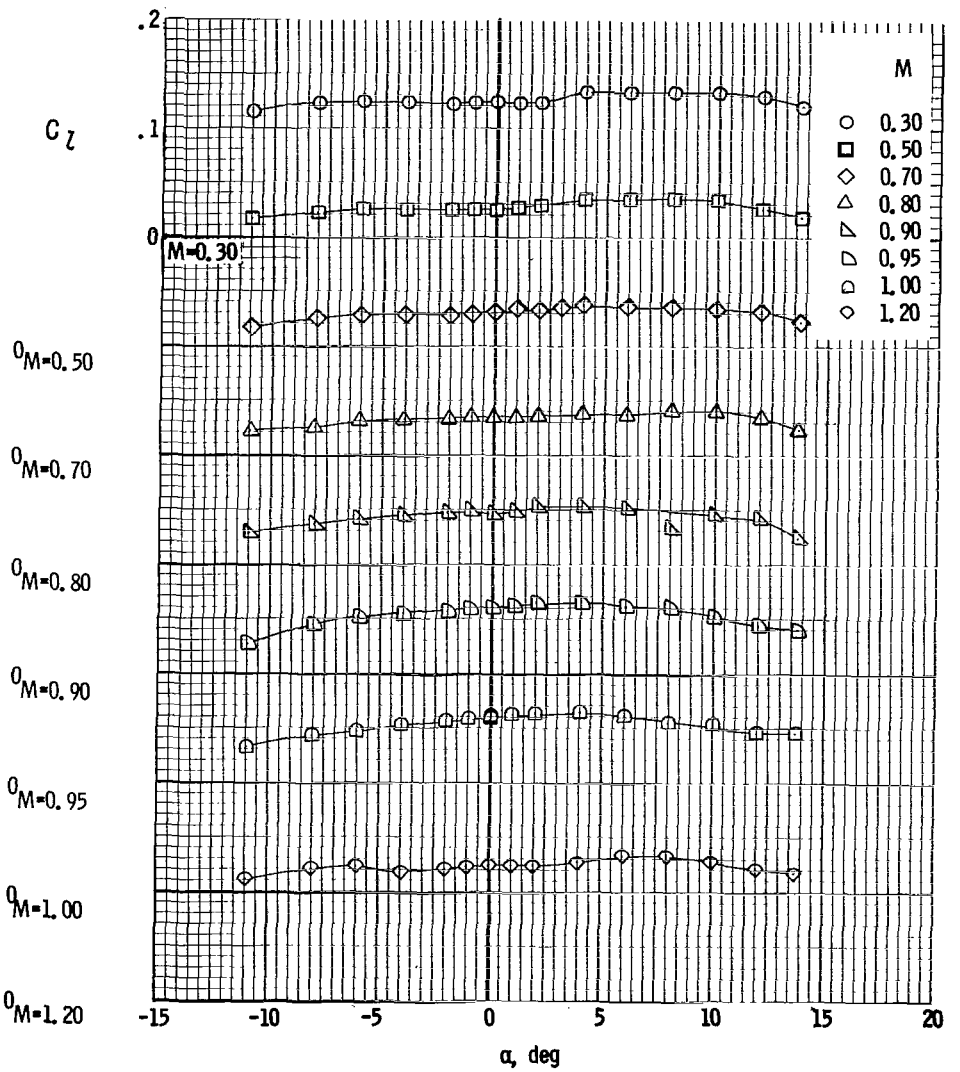

(f) Rolling-moment coefficient.

Figure 30. - Continued.

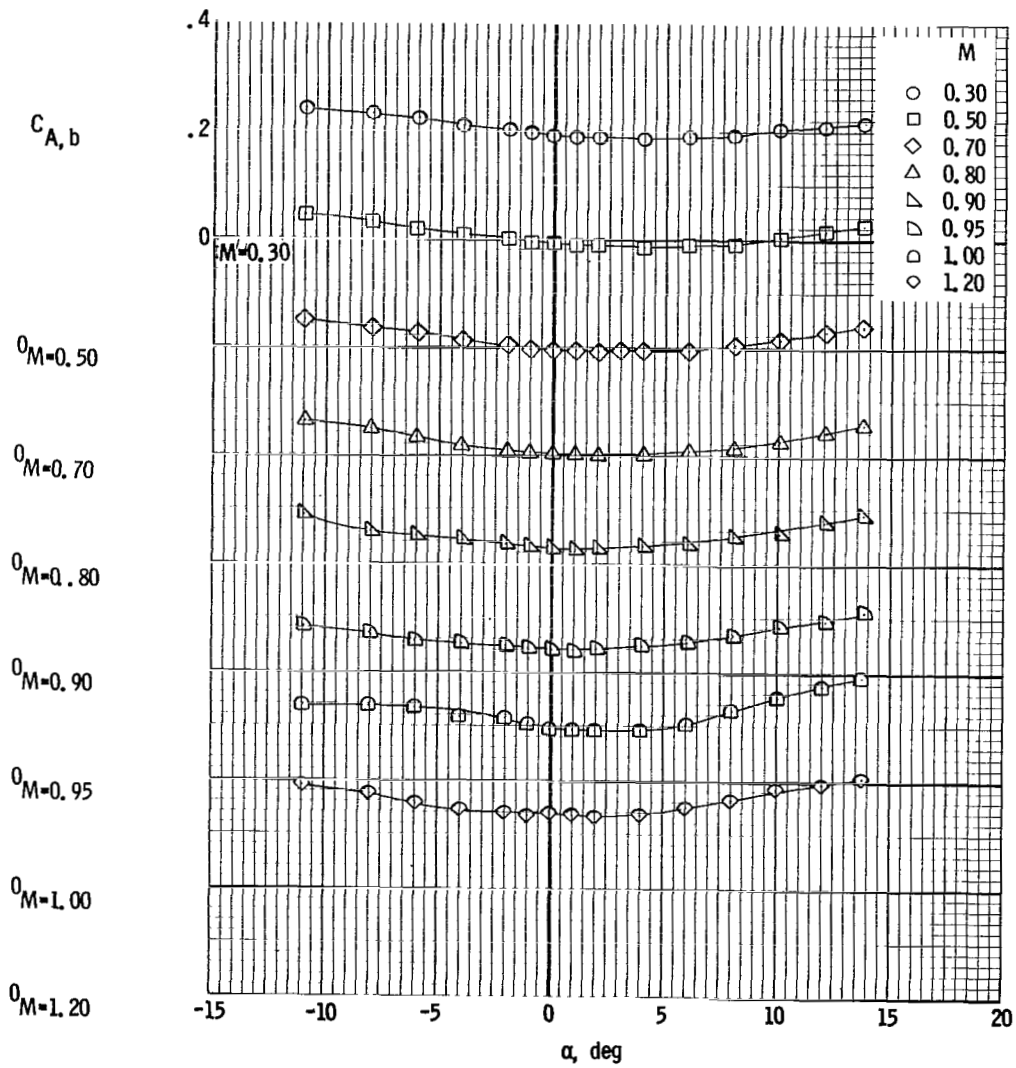

(g) Base axial-force coefficient.

Figure 30. - Concluded.

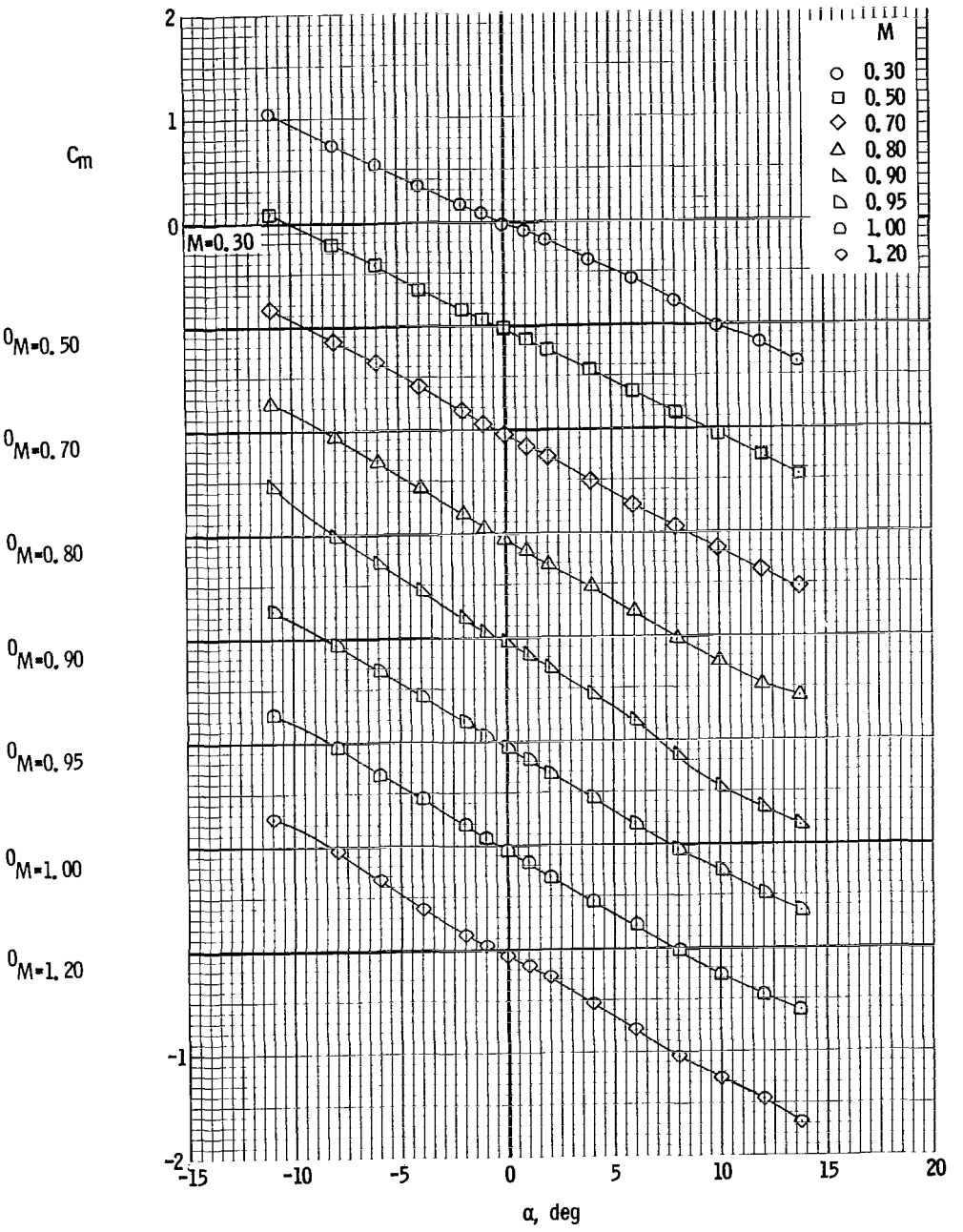

(a) Pitching-moment coefficient.

Figure 31. - Effect of differential deflection of trailing-edge control surfaces on longitudinal aerodynamic characteristics of configuration III (without stabilizing disk) at Mach numbers from 0.30 to 1.20 (c.g. = X/D = 0; Z/D = 0; $\delta_f = \pm 10°$).

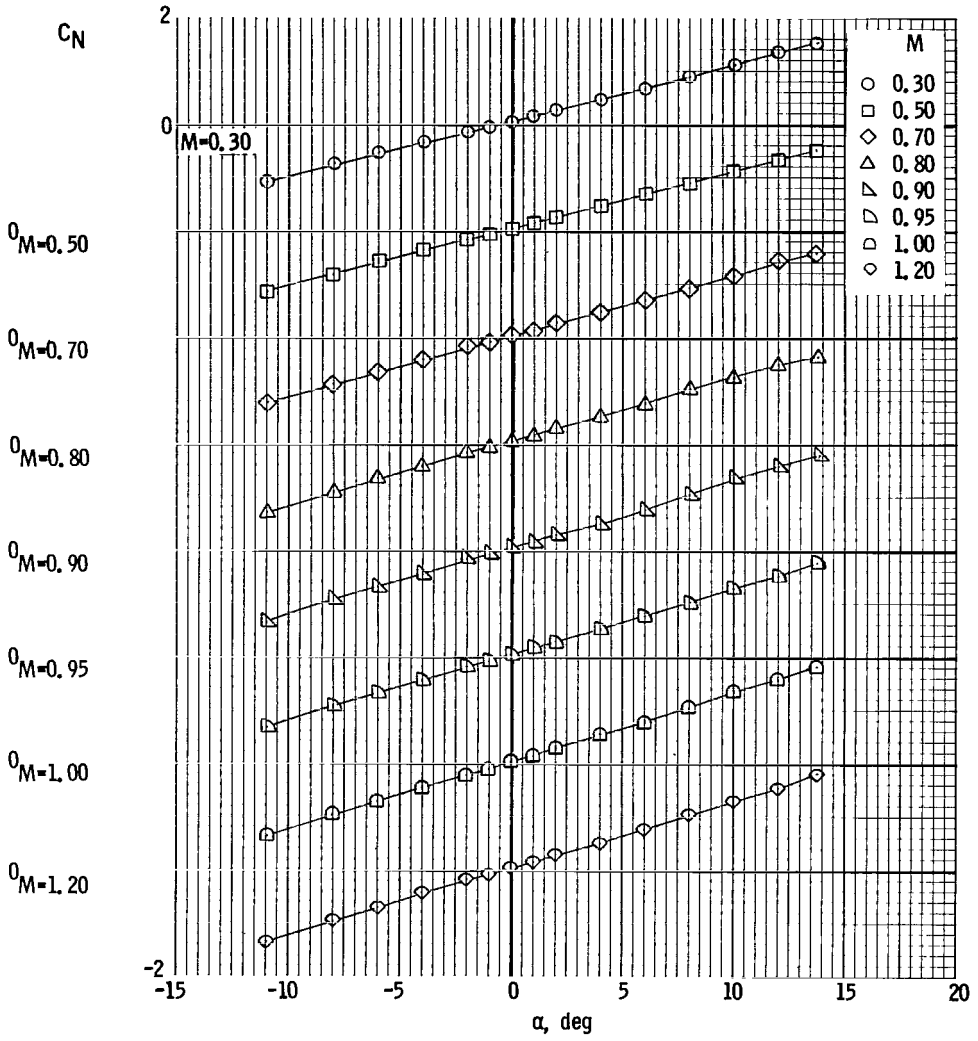

(b) Normal-force coefficient.

Figure 31. - Continued.

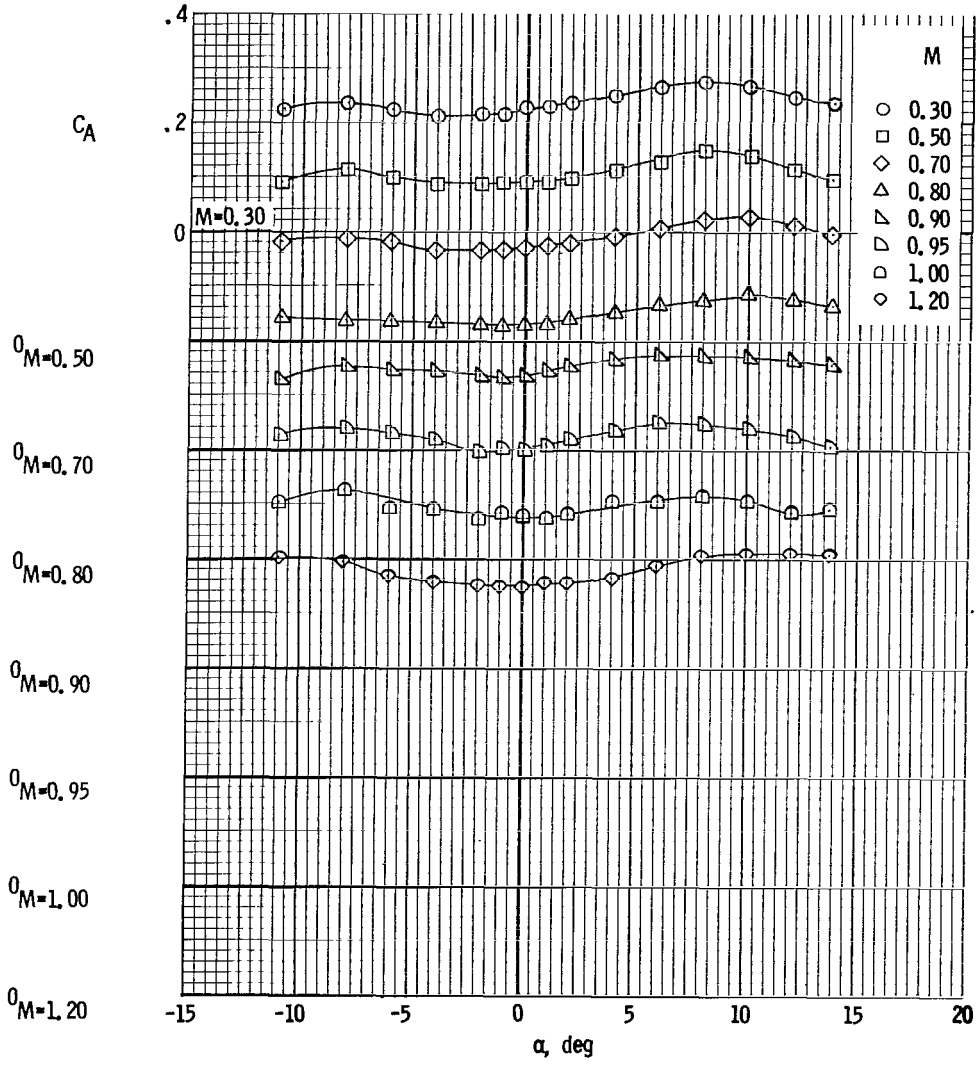

(c) Axial-force coefficient.

Figure 31. - Continued.

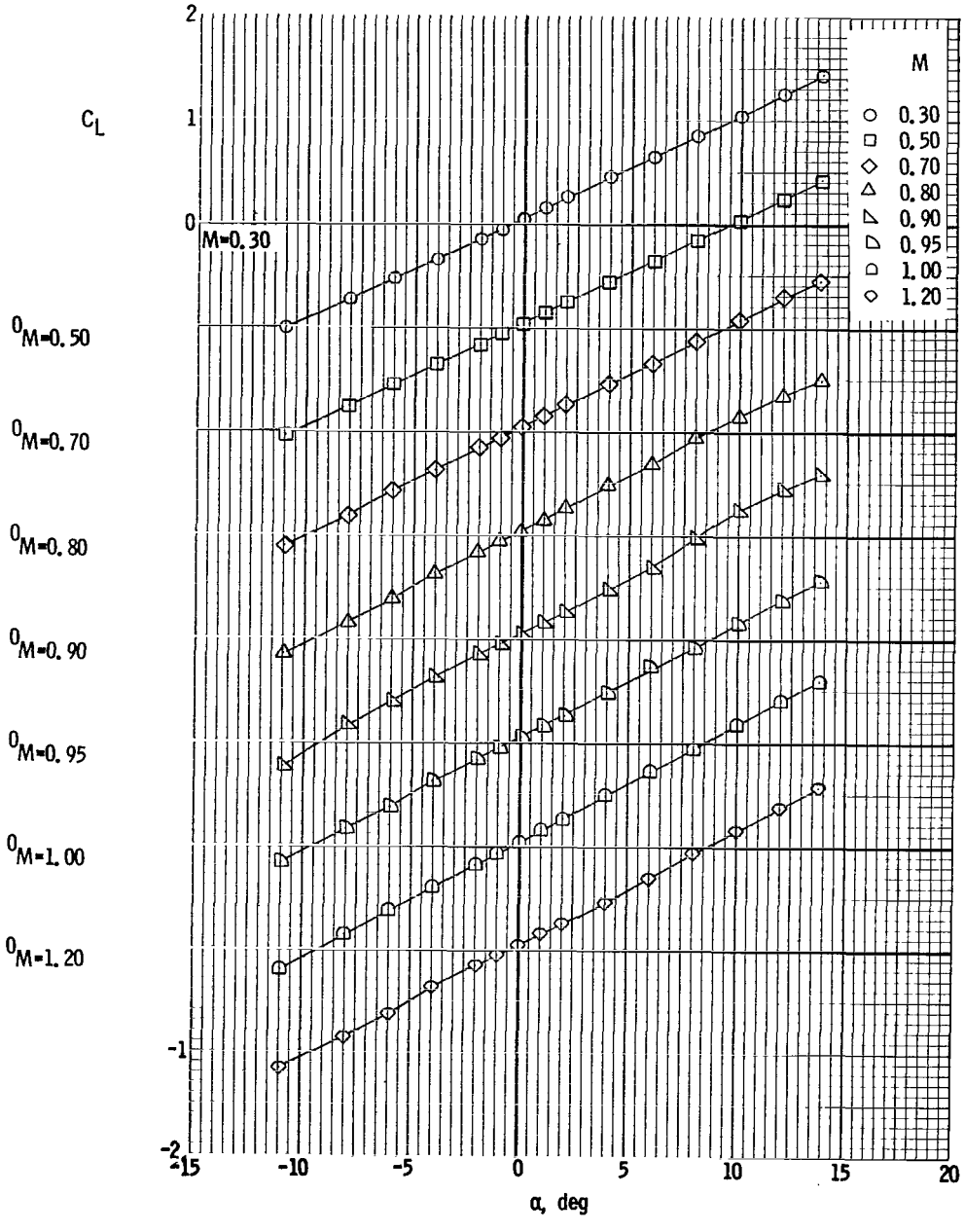

(d) Lift coefficient.

Figure 31. - Continued.

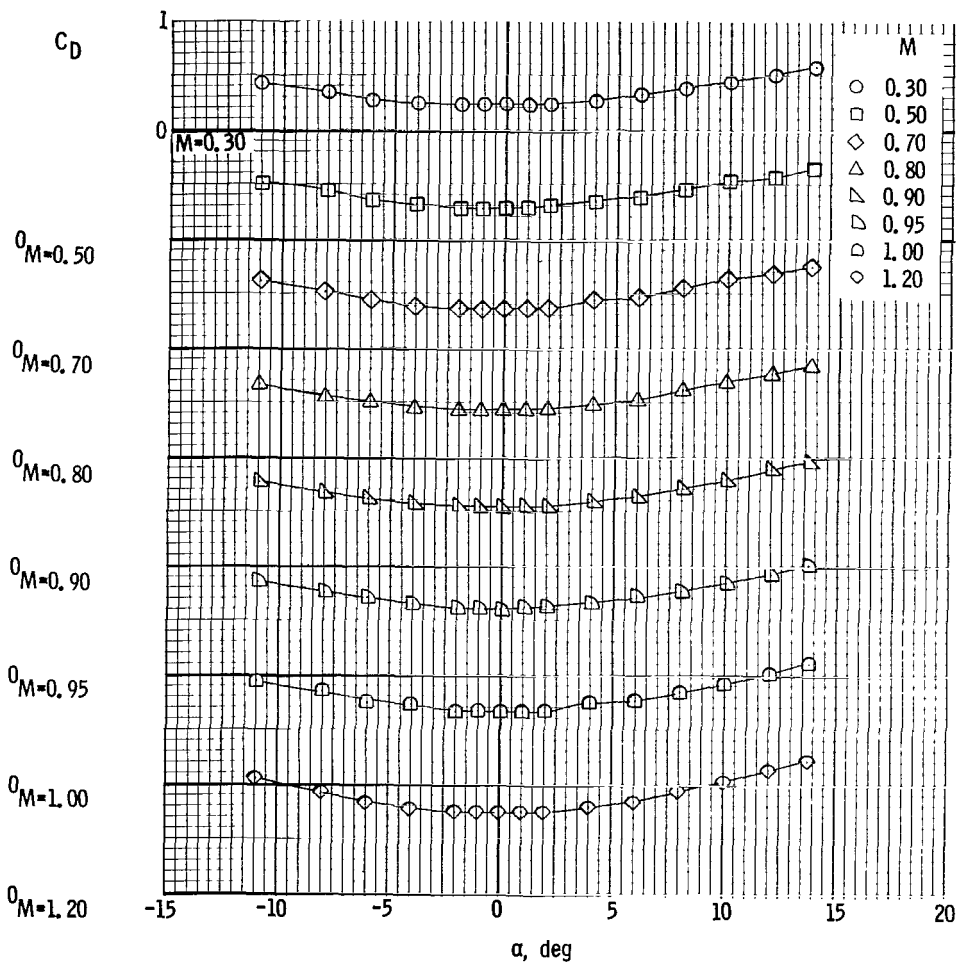

(e) Drag coefficient.

Figure 31. - Continued.

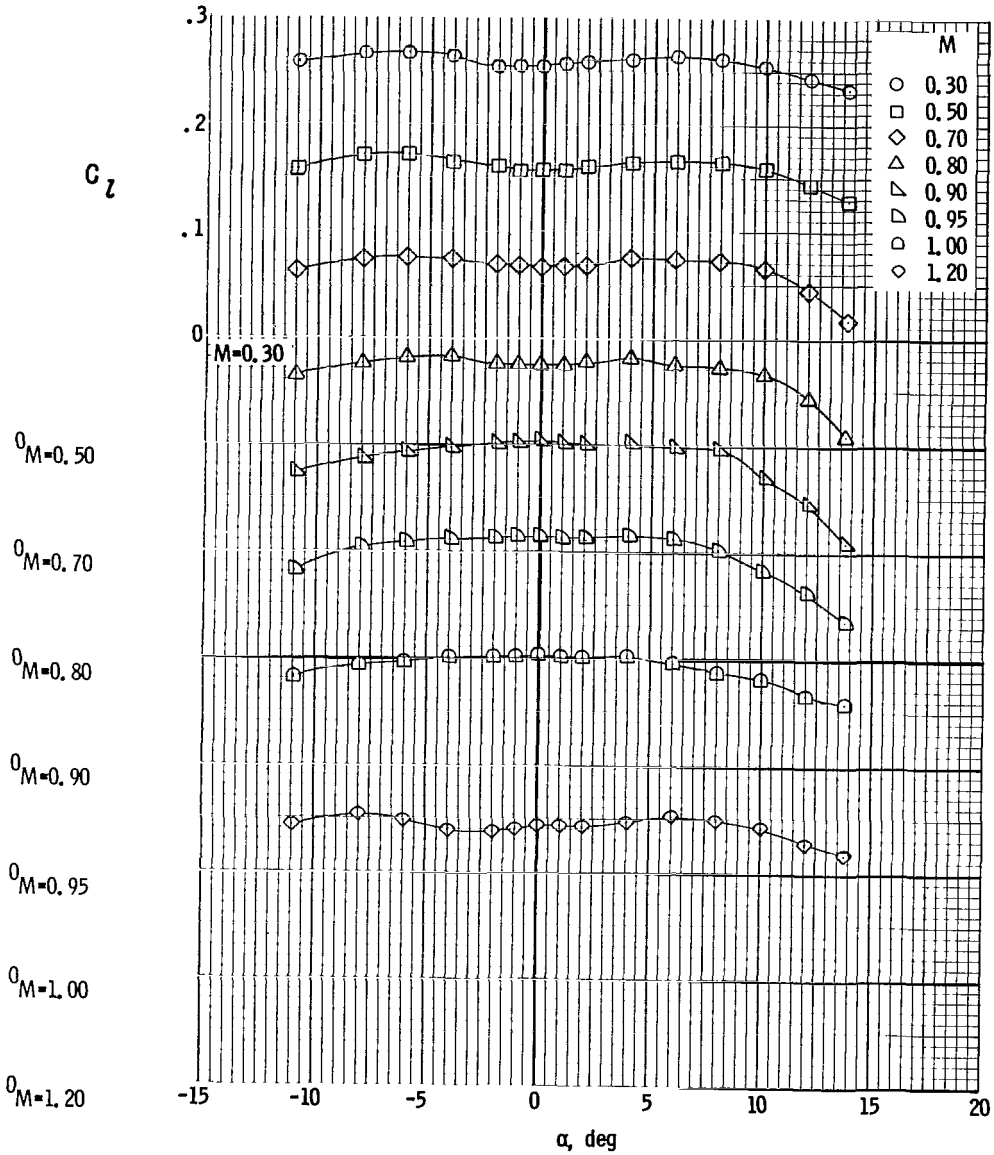

(f) Rolling-moment coefficient.

Figure 31. - Continued.

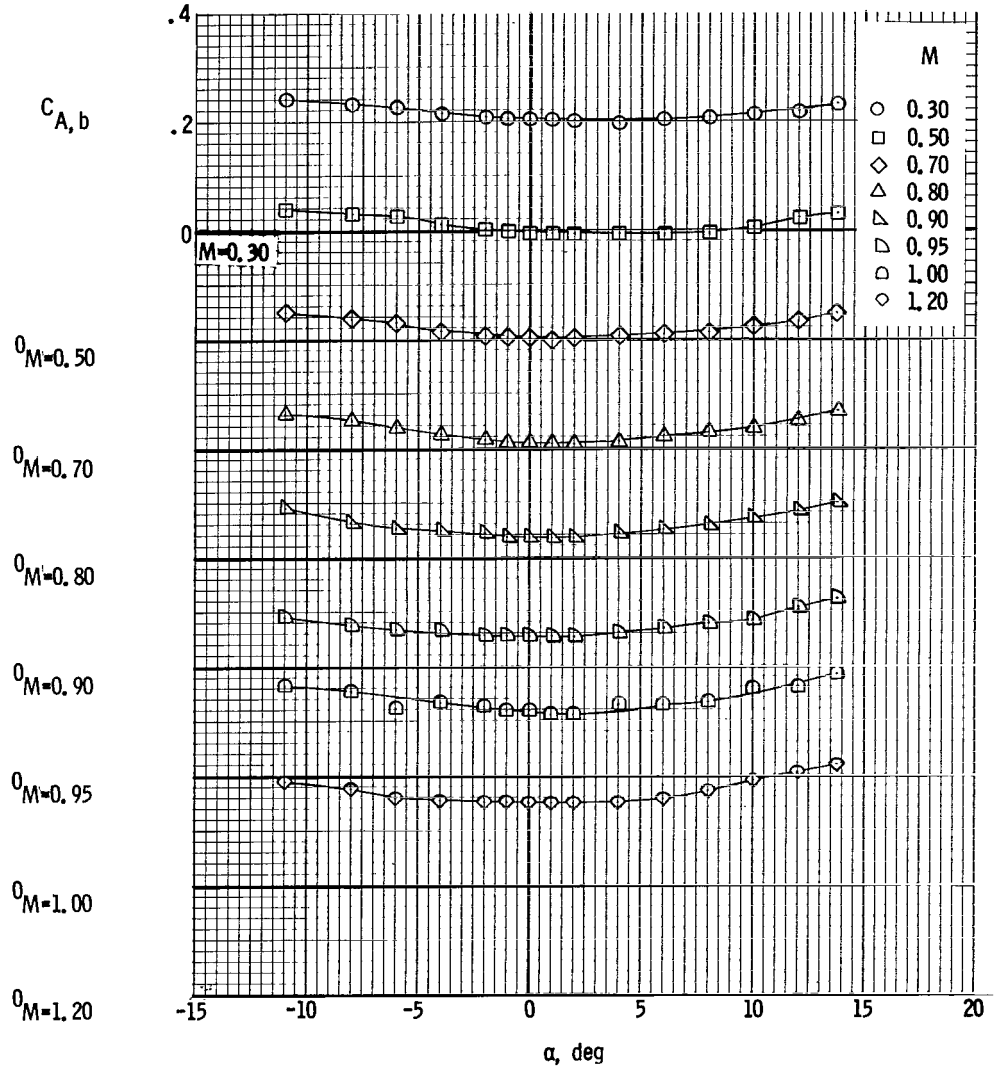

(g) Base axial-force coefficient.

Figure 31. - Concluded.

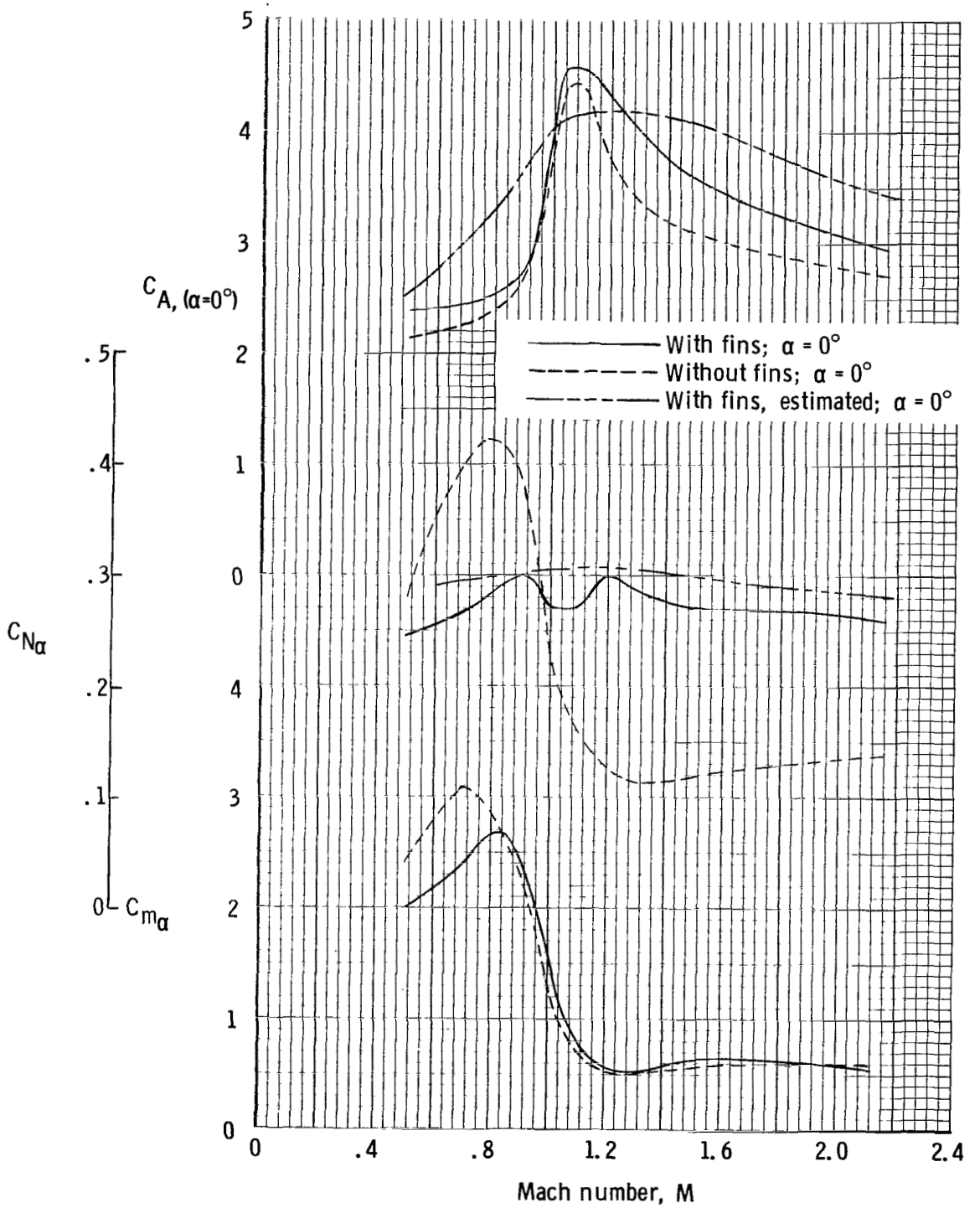

(a) $C_{A, \alpha=0°}$, C_{N_α}, and C_{m_α}.

Figure 32.- Summary of longitudinal-stability parameters for configuration I.

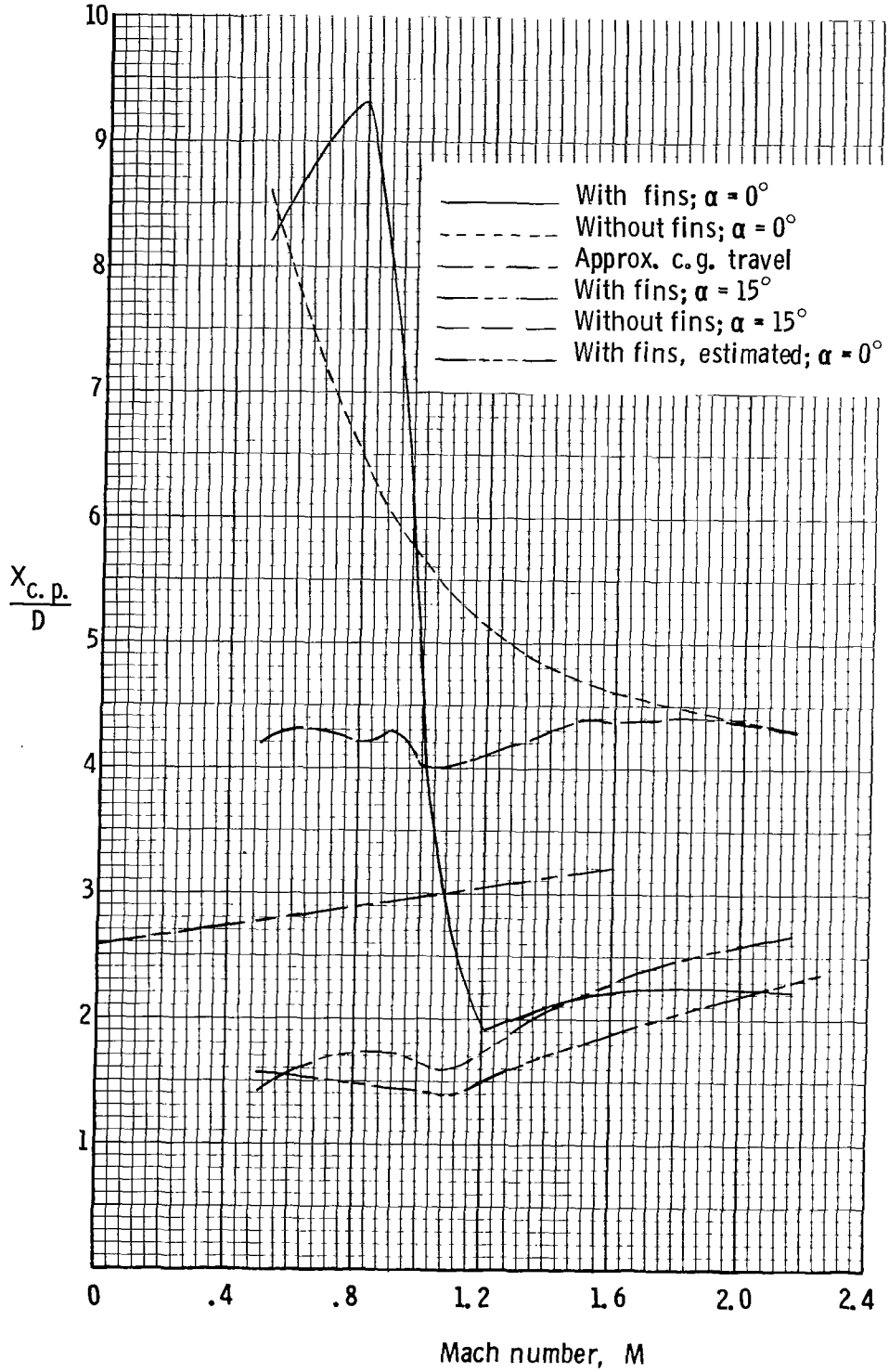

(b) $\frac{X_{c.p.}}{D}$.

Figure 32. - Concluded.

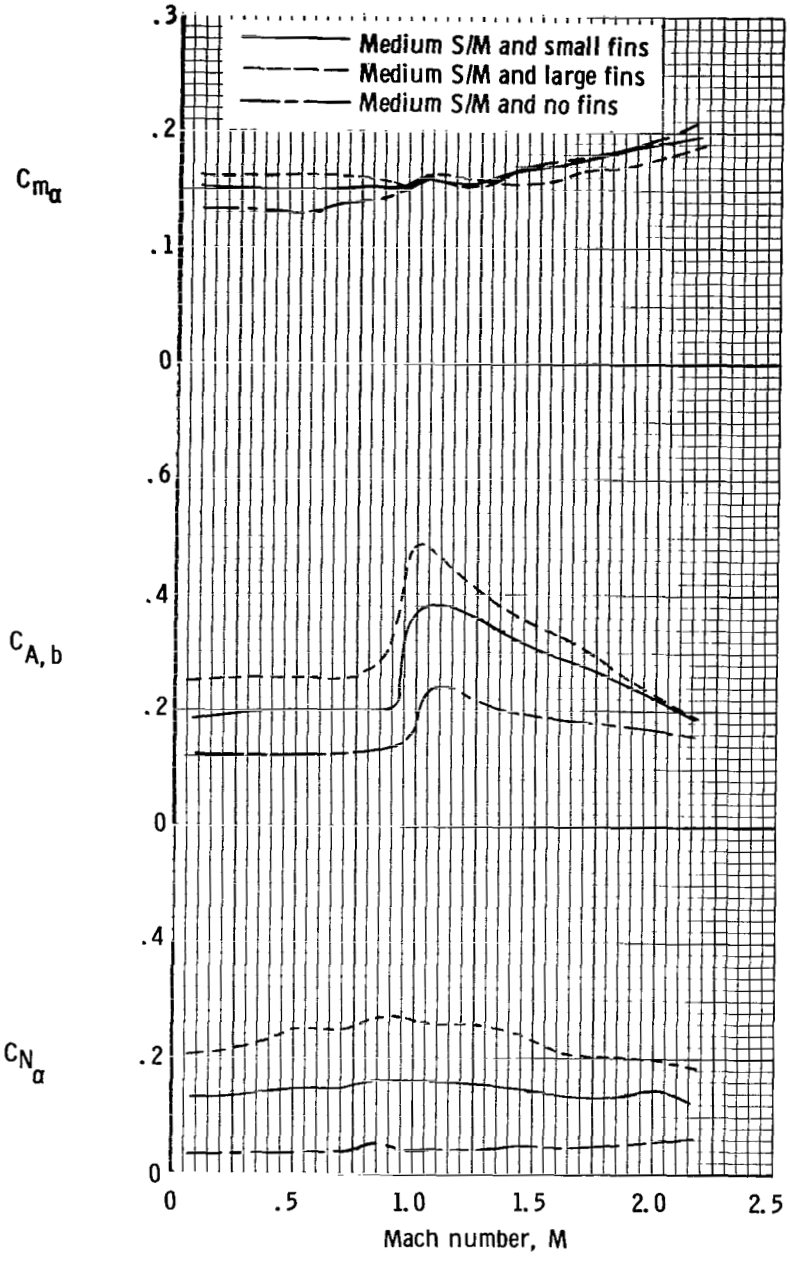

(a) C_{m_α}, $C_{A,b}$, C_{N_α}.

Figure 33. - Effect of booster fin size on configuration II with medium service module.

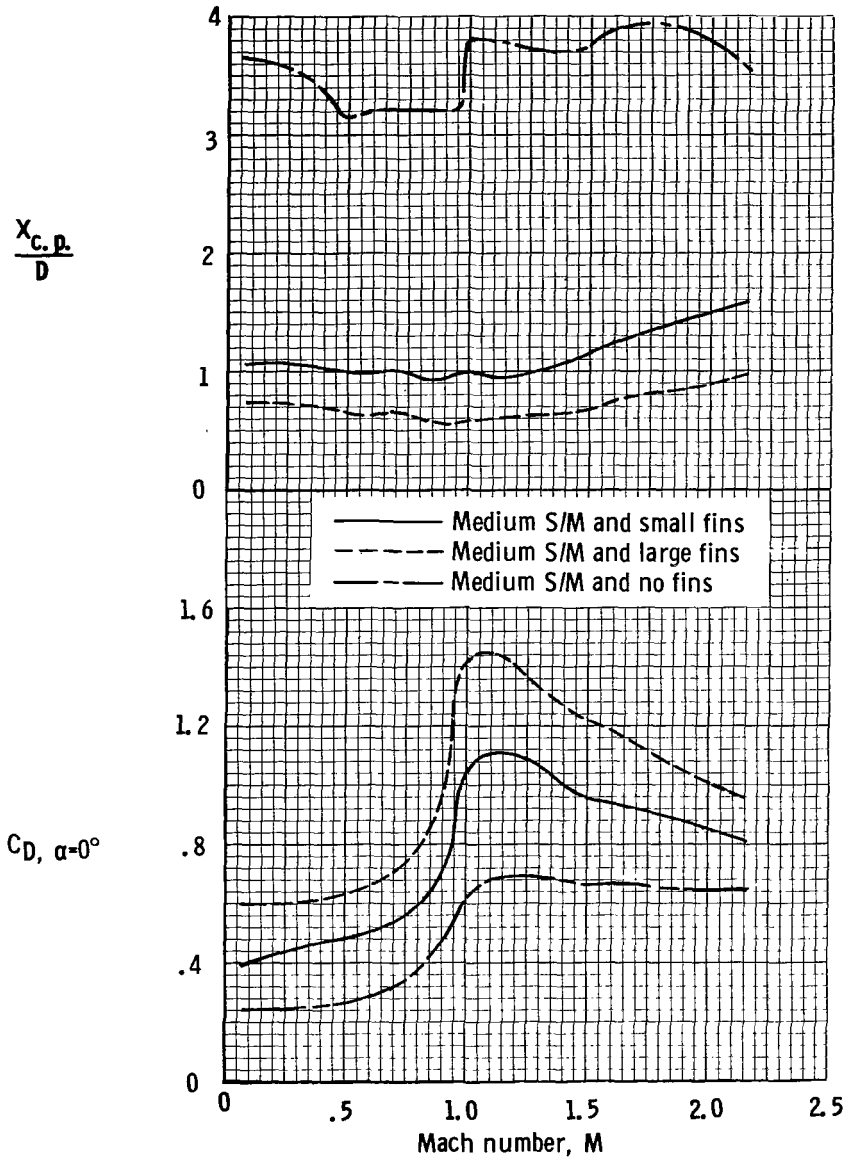

(b) $\frac{X_{c.p.}}{D}$, $C_{D,\ \alpha=0°}$.

Figure 33. - Concluded.

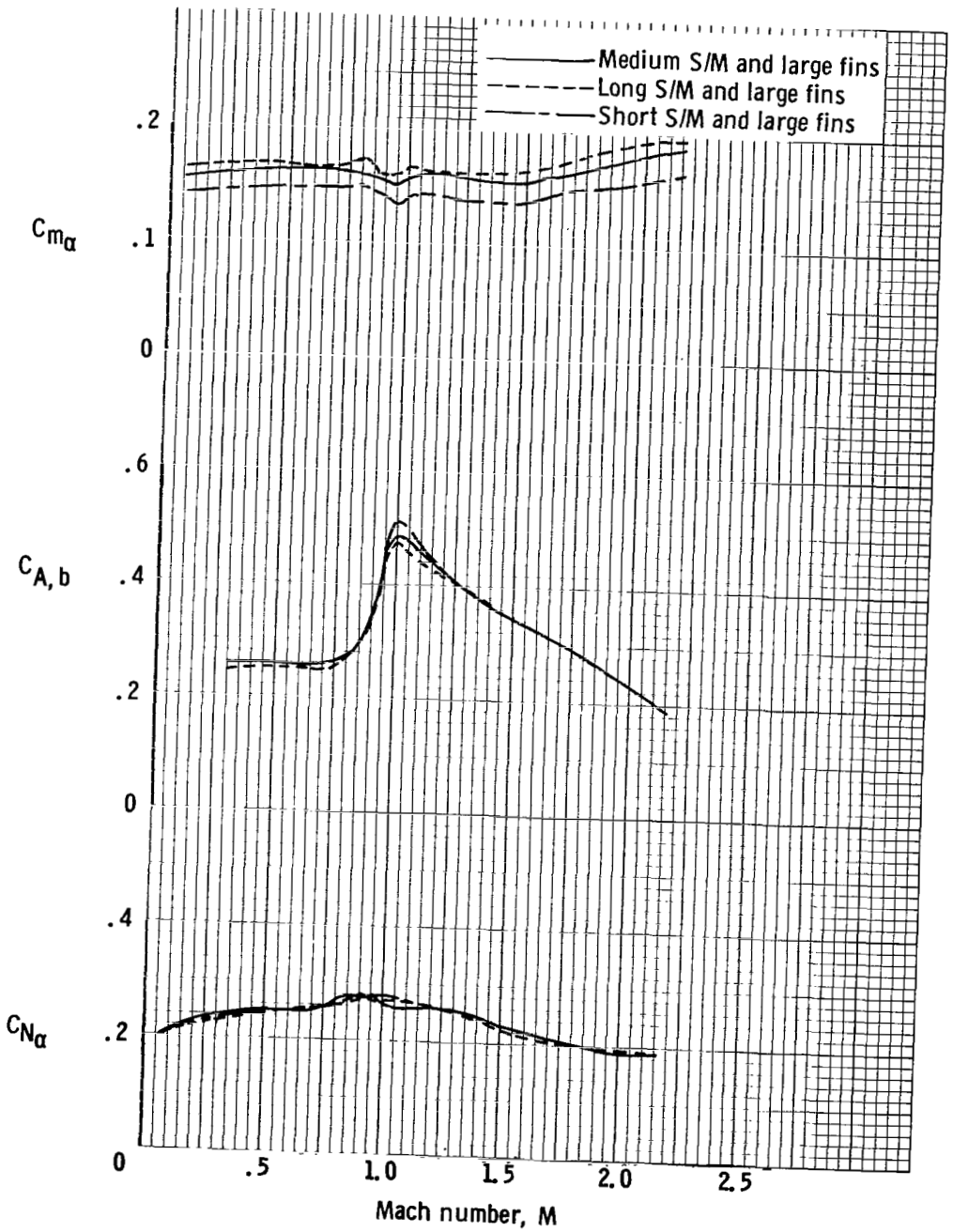

(a) C_{m_α}, $C_{A,b}$, and C_{N_α}.

Figure 34.- Effect of service module length on configuration II with large fins.

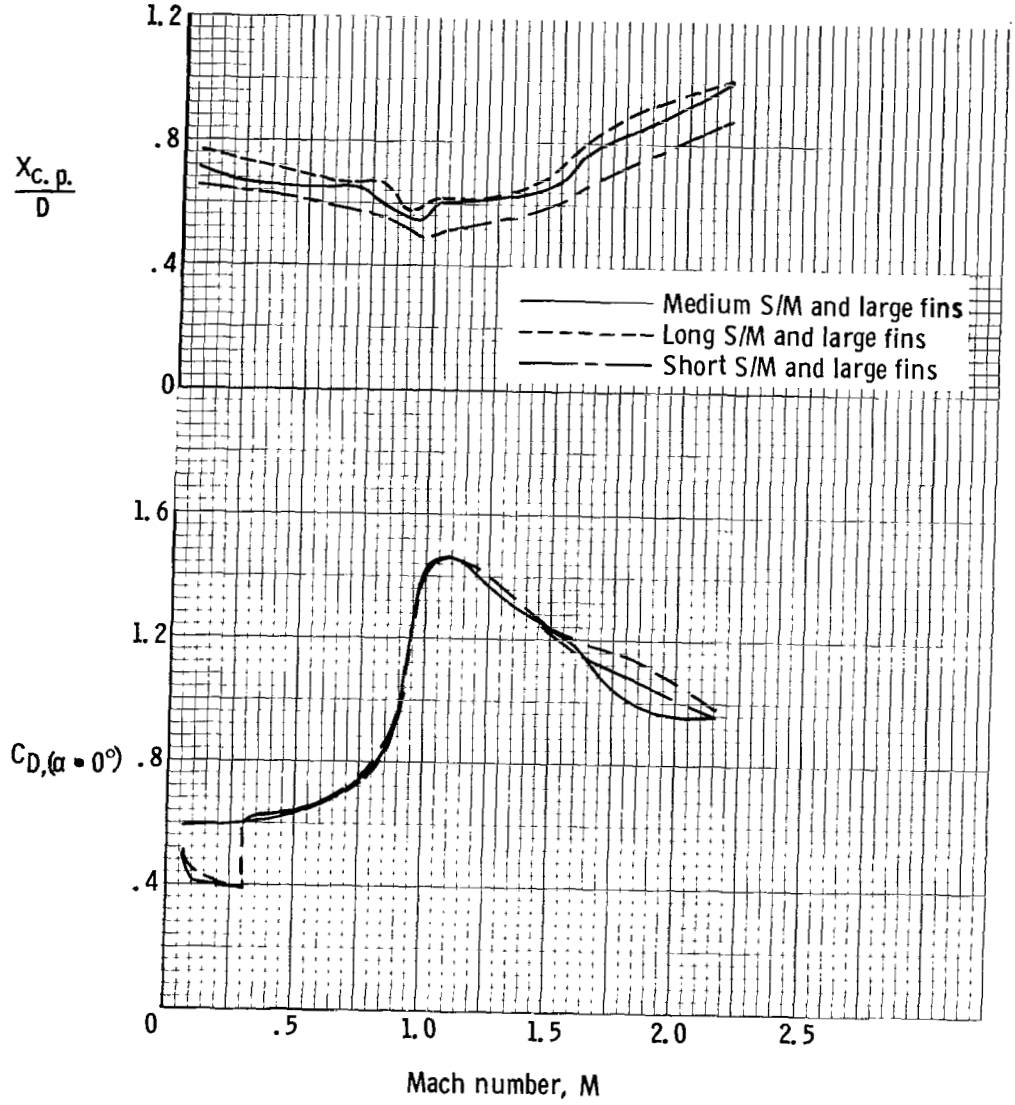

(b) $\frac{X_{c.p.}}{D}$ and $C_{D,\,(\alpha=0^\circ)}$.

Figure 34. - Concluded.

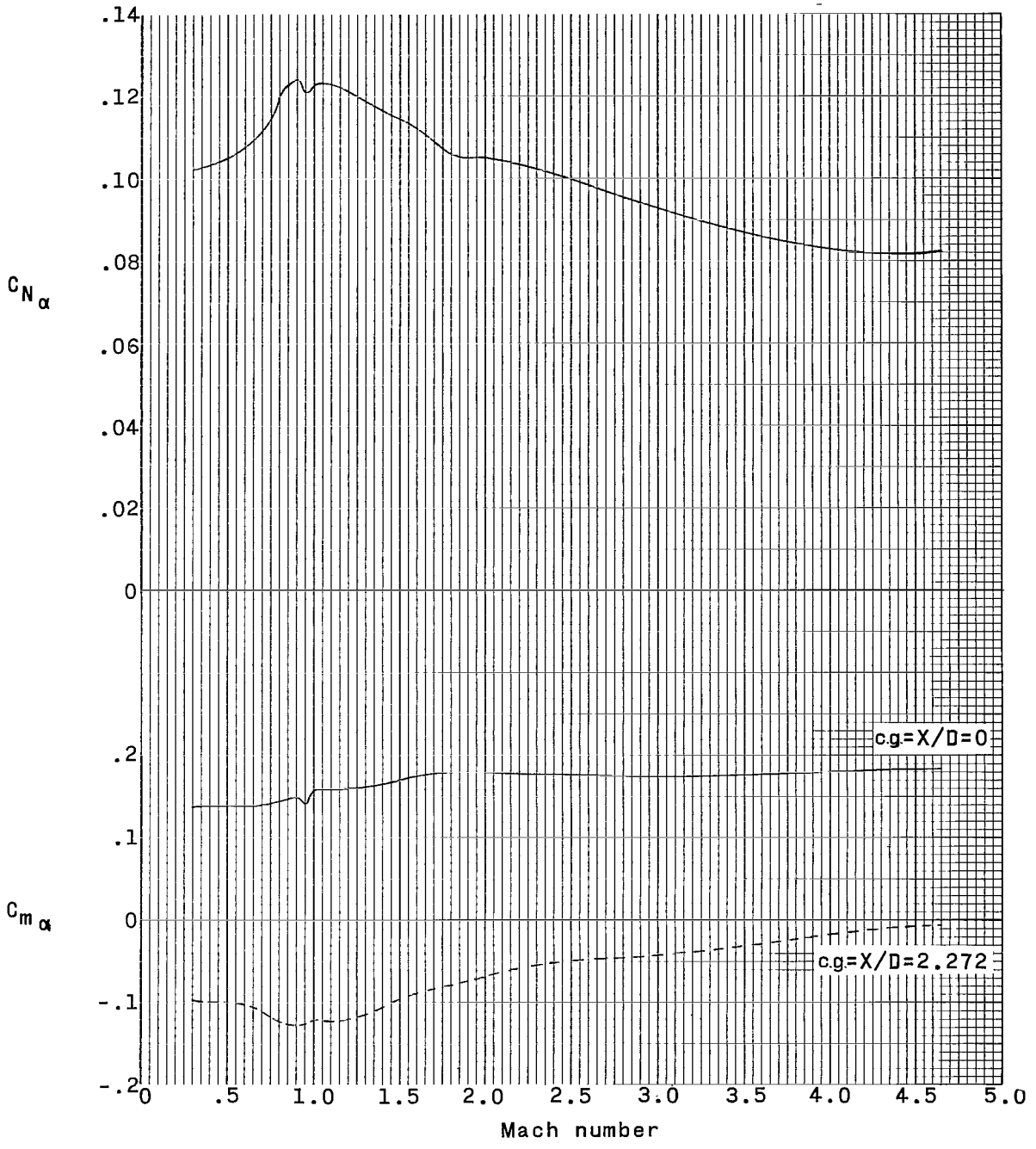

(a) C_{N_α} and C_{m_α}.

Figure 35. - Summary data for configuration III without the stabilizing disk on the rocket motor $(\delta_f = 0°)$.

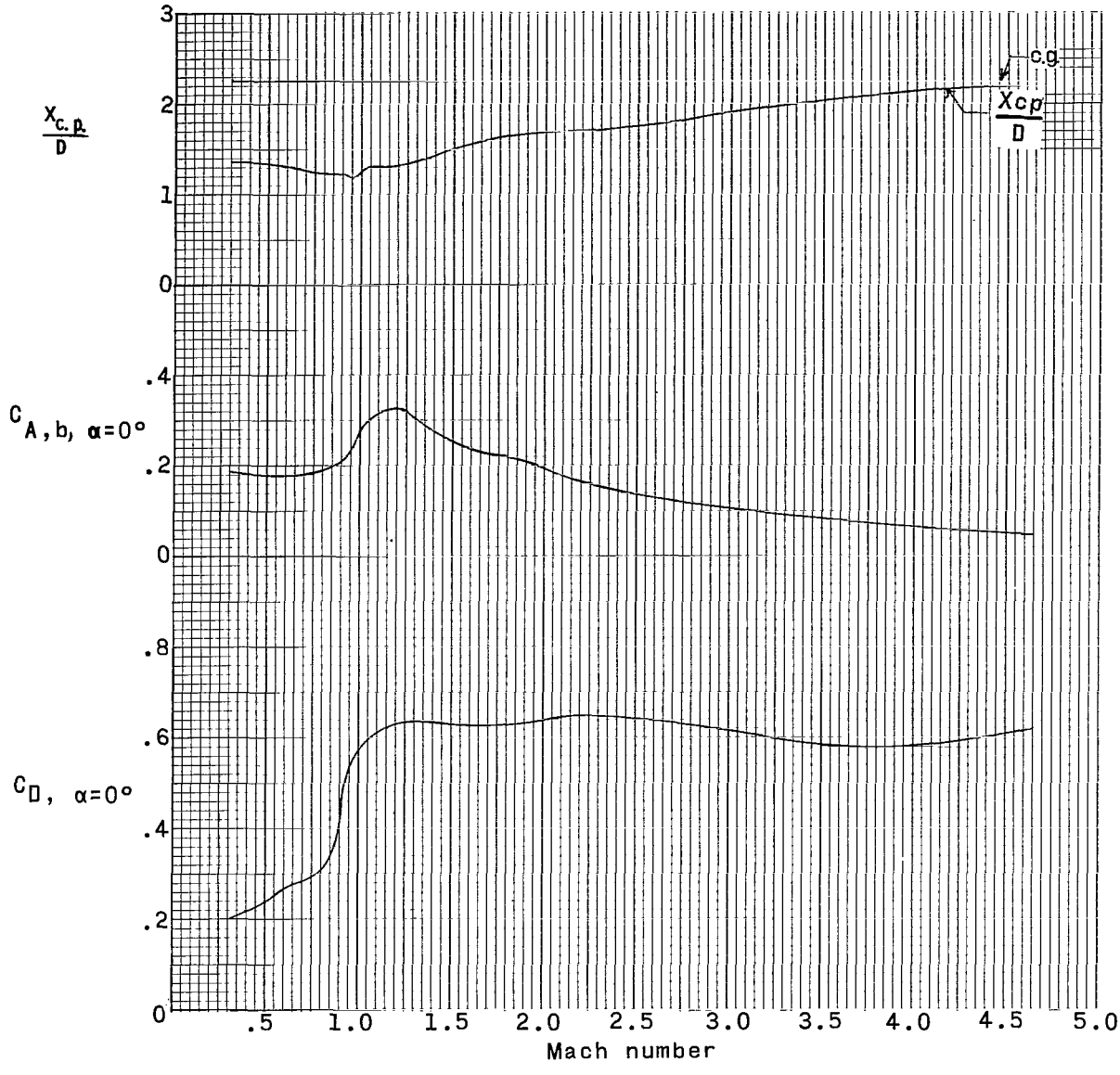

(b) $\frac{X_{c.p.}}{D}$, $C_{A,b,(\alpha=0°)}$, and $C_{D,(\alpha=0°)}$.

Figure 35. - Concluded.

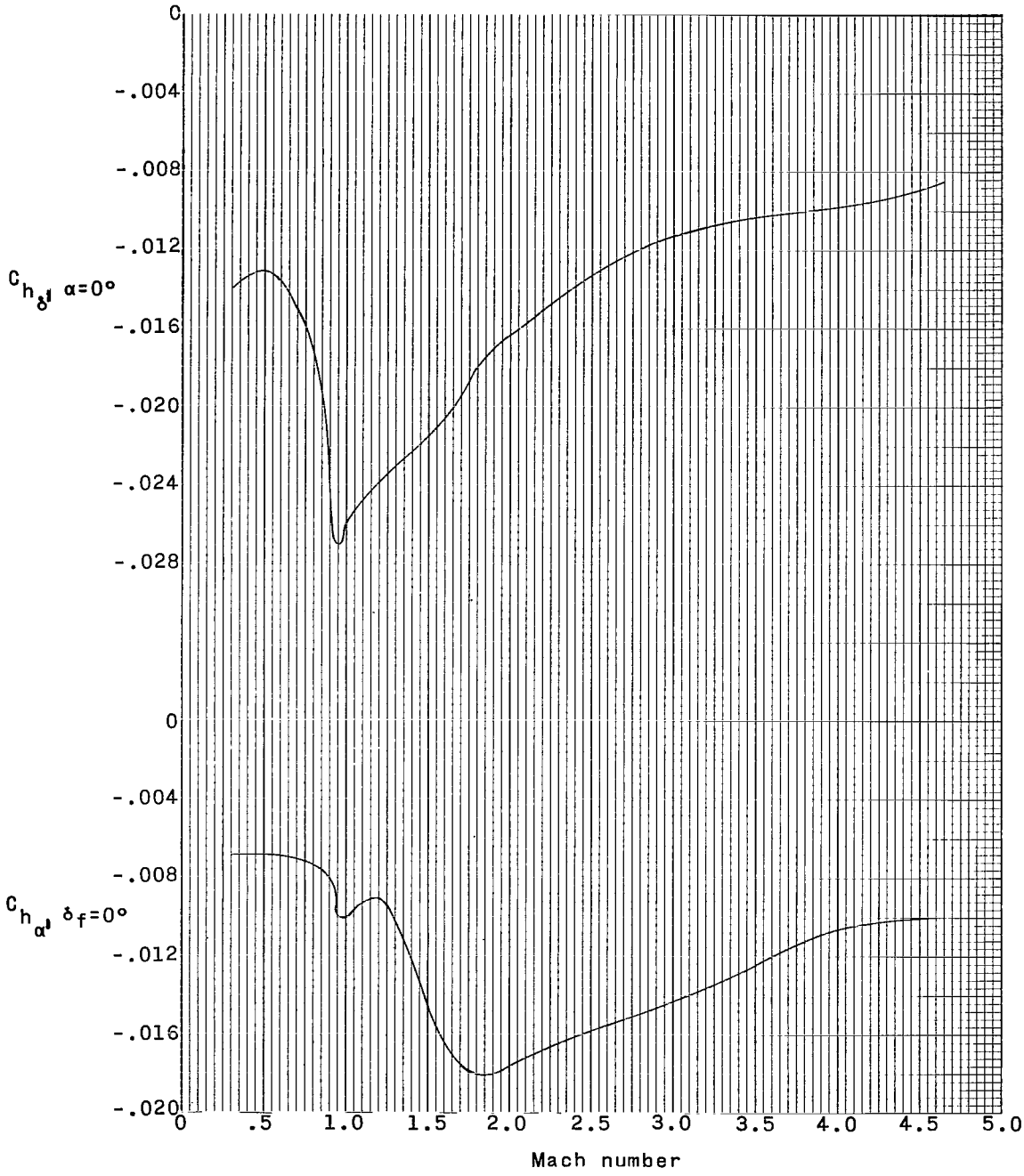

Figure 36.- Summary data of hinge-moment coefficient for configuration III (without stabilizing disk).

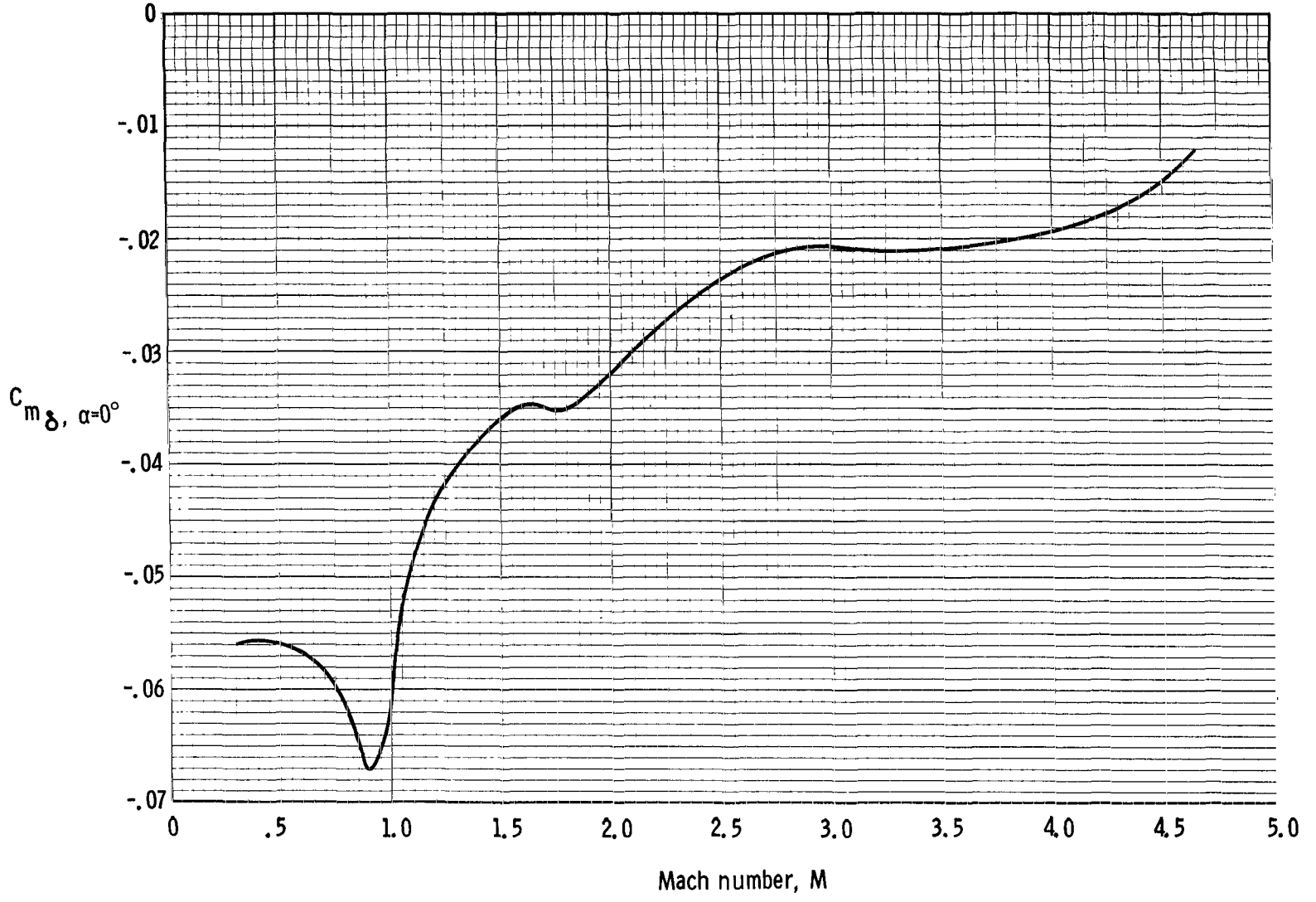

Figure 37. - Summary data of trailing-edge control-surface effectiveness for configuration III (without stabilizing disk).

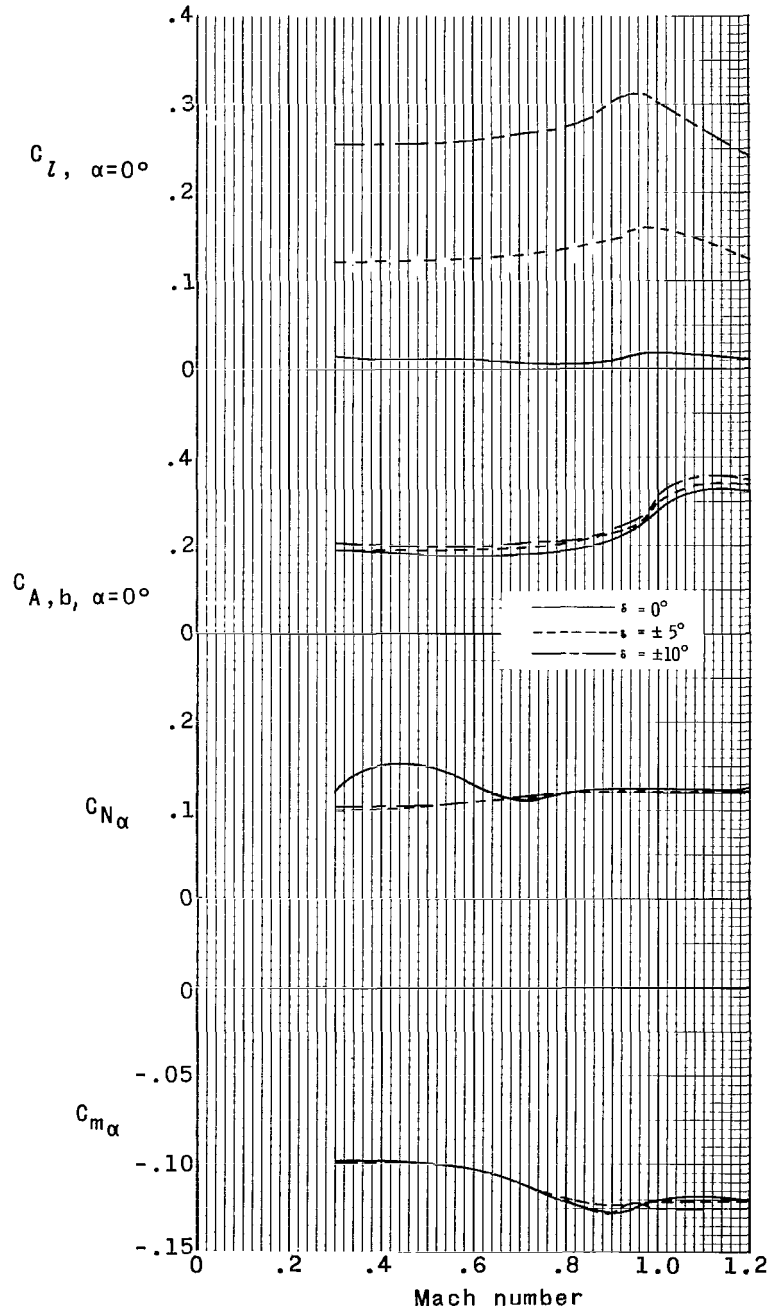

Figure 38.- Summary data for differential deflection of trailing-edge control surfaces for configuration III (without stabilizing disk).

"The aeronautical and space activities of the United States shall be conducted so as to contribute . . . to the expansion of human knowledge of phenomena in the atmosphere and space. The Administration shall provide for the widest practicable and appropriate dissemination of information concerning its activities and the results thereof."

—NATIONAL AERONAUTICS AND SPACE ACT OF 1958

NASA SCIENTIFIC AND TECHNICAL PUBLICATIONS

TECHNICAL REPORTS: Scientific and technical information considered important, complete, and a lasting contribution to existing knowledge.

TECHNICAL NOTES: Information less broad in scope but nevertheless of importance as a contribution to existing knowledge.

TECHNICAL MEMORANDUMS: Information receiving limited distribution because of preliminary data, security classification, or other reasons.

CONTRACTOR REPORTS: Scientific and technical information generated under a NASA contract or grant and considered an important contribution to existing knowledge.

TECHNICAL TRANSLATIONS: Information published in a foreign language considered to merit NASA distribution in English.

SPECIAL PUBLICATIONS: Information derived from or of value to NASA activities. Publications include conference proceedings, monographs, data compilations, handbooks, sourcebooks, and special bibliographies.

TECHNOLOGY UTILIZATION PUBLICATIONS: Information on technology used by NASA that may be of particular interest in commercial and other non-aerospace applications. Publications include Tech Briefs, Technology Utilization Reports and Notes, and Technology Surveys.

Details on the availability of these publications may be obtained from:

SCIENTIFIC AND TECHNICAL INFORMATION DIVISION

NATIONAL AERONAUTICS AND SPACE ADMINISTRATION

Washington, D.C. 20546